The HST/LCO Measurement of the Mean Flux of the Extragalactic Background Light (3000–8000Å)

Thesis by

Rebecca A. Bernstein

In Partial Fulfillment of the Requirements
for the Degree of
Doctor of Philosophy

California Institute of Technology
Pasadena, California

1998
(Submitted October 28, 1997)

Acknowledgements

Various terms of endearment are commonly used to refer to advisors at Caltech; "Fearless Leader" is my favorite of these. In my case, I think Fearless Leaders is an understatement. I would like to thank my advisors for having the faith in me to take on this project. There were many sizable obstacles to even starting this thesis, and I very much appreciate the time and energy that they put into making this thesis even logistically possible. In addition, this work would never have been completed in a single (reasonable) graduate career if they hadn't had the foresight to get the observational programs underway so early in my time at Caltech. Moreover, I thank Barry and Wendy for innumerable valuable discussions along the way.

I would like to the Caltech astronomy department, particularly Roger Blandford, for financial support during my first year in graduate school and for supporting my decission to undertake this project. I would also like to thank Carnegie Observatories and directors Leonard Searle and Gus Oemler for supporting this thesis at LCO and for letting me move to Carnegie when it seemed appropriate. The commitment of time and resources on the part of both institutions is very much appreciated.

A number of people who had made no official commitment and to this work were also very generous with their time and energy:

Many thanks to Steve Shectman for the two word comments that have led to entire sections of this thesis.

Thanks to Julianne for taking the data used to measure the pixel scale, and for listening to all the horrific details of the analysis and calibration before I worked them out. I hope it didn't cause lasting depression.

Thanks to Randy for following the 20 pages of instructions that I gave him for taking the 40–inch data in November 1995. He laughed at me, but he did it like it was a matter of life and death. It may have been that for me, but certainly wasn't for him.

Thanks to Ian Thompson for his patience in fielding obscure questions about CCDs in general and his electronics in particular. He also measured the slit width for me. The only random luck I have encountered during the course of this thesis was that he was on the mountain in November 1995. I also owe a special thanks both to Ian and the rest of the LCO troop for running the sort of observatory at which this measurement could be made. I'd also like to thank Ian for extensive use of his unabridged dictionary.

Many thanks to John Trauger for making his lab available for CTE tests and for spending several afternoons puzzling about trapped electrons.

Thanks to Doug Van Orsow, who was our program coordinator at STScI. In fact, I'm surprised he had time to be anyone else's during Cycle 5. Thanks for all the tables of moon position and shadow–entry times, and especially for getting our program scheduled during the 3 day windows that I requested.

At STScI, Harry Ferguson, Ralph Bohlin, Stefano Casertano, Tony Keyes and Larry Petro were very helpful with regard to details of WFPC2 and FOS. Harry not only spent a lot of time discussing the WFPC2 dark glow, but he also provided an excellent introduction to the details on WFPC2 calibration and the actual time–line of events for an exposure. Tony Keyes and Larry Petro spent a few hours on the phone with me between meetings trying to work out the best way to get data on a 23 mag/arcsec^2 source with the FOS. Sylvia Baggett and Ed Smith also learned to dread my phone calls, but they were extremely helpful with the WFPC2 and FOS, respectively. Good thing Carnegie has Caller ID Blocking.

Finally, immeasurable thanks are due to my people, who know who they are and for what they're being thanked.

Abstract

We present the first detection of the optical extragalactic background light (EBL) at 3000, 5500, and 8000Å using simultaneous observations taken from Hubble Space Telescope (HST) and the du Pont 2.5 m telescope at Las Campanas Observatory (LCO). The total background flux of the night sky was measured from space using the Wide Field Planetary Camera 2 (WFPC2), thereby avoiding terrestrial airglow which is the dominant foreground component from the ground and the primary obstacle in previous efforts to measure the EBL. Foregrounds which contribute to the surface brightness of the night sky from HST are zodiacal light and diffuse galactic light. We have measured the absolute surface brightness of the zodiacal light using spectrophotometry taken with the du Pont 2.5 m telescope at LCO and using the Faint Object Spectrograph (FOS) on HST. We minimize the contribution from diffuse galactic light by conducting the measurement in a target field with a low column density of galactic dust and neutral hydrogen, both of which are traced by 100μm emission in the IRAS maps. The small remaining galactic contribution has been modeled using known correlations between the diffuse thermal emission from the dust at 100μm and the diffuse optical light due to starlight scattered off the same dust. Because galaxies brighter than $V = 23$ AB mag are statistically poorly sampled in the WFPC2 field of view, we define the EBL as the total flux from objects fainter than $V = 23$ AB mag. We find the following mean levels for the EBL as a function of wavelength (in units of ergs $\mathrm{s^{-1}cm^{-2}sr^{-1}Å^{-1}}$, with 1 σ *rms* errors): I_λ(3000Å)=4.0 ($\pm$1.9)$\times 10^{-9}$, I_λ(5500Å)=2.8 ($\pm$0.8)$\times 10^{-9}$, I_λ(8000Å)=2.3 ($\pm$0.6)$\times 10^{-9}$, with systematic errors of 1–2$\times 10^{-9}$ at each wavelength. The total flux detected at each wavelength is at least 2–3 times the integrated flux in published galaxy counts. The implications of this detection are discussed.

Contents

List of Figures

List of Tables

Chapter 1 Introduction

While the concern might be considered naive today, early astronomers considered the fact that night sky is dark to be a paradox with significant cosmological implications and of considerable interest (see Harrison 1990). The apparent contradiction as expressed by Olbers is based on the supposition that in a static universe filled with stars in concentric shells, the $1/r^2$ distance to a shell and the r^2 surface area of that shell will cancel, so that the surface area of the sky should be as bright as the center of the Sun. Olbers' Paradox, simply that the night sky is dark, is in part explained by redshifting of light out of the optical, by the expansion of the Universe, and by the finite speed of light. The strongest effect which resolves the problem, however, was clearly stated 1964 by Harrison in terms of the conservation of energy and the finite lifetimes of stars: the stars would need to shine for the full Hubble time for the paradox to exist at all.

The solution given by Harrison is a clear exposition of the factors which influence the extragalactic contribution to the surface brightness of the night sky. While Olbers' Paradox is outdated, the surface brightness of isotropic backgrounds at all wavelengths is well recognized today as a powerful cosmological test. The extragalactic background light (EBL) at UV and optical wavelengths comes from young stellar populations at all redshifts. The surface brightness of the optical EBL, the integrated light from all extragalactic sources, is low principally because the lifetimes of galaxies and stars are finite. The EBL is also affected by cosmological models and the expansion of the Universe, however these effects play a relatively minor role. The utility of the EBL as a cosmological tool is then principally as a probe of galaxy formation and evolution. The star formation history of the Universe, the metal production rate, the ionizing flux at all redshifts, and the total baryon density are all addressed by a measurement of the EBL.

The EBL is often discussed theoretically as flux from all luminous, extragalactic objects. Observationally, however, this is not a useful definition because astronomical observations are made in finite regions of the sky. As an extreme example of the impracticality of this definition, imagine the difference in the inferred level EBL based on observations of the "background" level in a 5 arcmin^2 region of the sky in the direction of M81 as compared a 5 arcmin^2 region of "blank" sky such as the Hubble Deep Field (Williams et al. 1996). A more useful definition of the EBL for observational purposes includes only the flux from all objects which are statistically well represented in a surface area defined by the field of view of the observations. In this work, a relatively small field of view (roughly 4.5 arcmin^2), imposes a natural bright–end cut-off of $V \sim 23$ AB mag (see §2.3). Comparisons between the integrated flux in detected–object studies (galaxy counts or redshift surveys) and with other measurements of the EBL should be made with this definition in mind.

While Olbers' Paradox is that the night sky is dark, the extragalactic component is, ironically, much darker than he knew. The surface brightness of the diffuse night sky originates largely within our own galaxy, and the extragalactic component has been shown over the last 30 years to be at most 5% of the background flux at optical wavelengths (see §1.3 and reviews by Mattila 1990, Bowyer 1991, and Henry 1991). Indeed, the expected level (as discussed in §1.1) is roughly 1–3% of the foregrounds. As is true of background measurements at all wavelengths, it is primarily the accuracy with which the foreground components can be determined that limits the accuracy with which the background can be measured. The work presented here is therefore concerned largely with the measurement of the foreground components, and also with absolute calibration at the same level of accuracy.

In this Chapter, we first discuss the scientific goals which motivate a measurement of the EBL in §1.1. The foreground contributions which complicate an optical background measurement are discussed in §1.2. Given that this work builds on a numerous previous attempts to measure the EBL over the last 30 years, we briefly discuss some of the more prominent of those experiments in §1.3. Finally, the details of the method employed in this work, an introduction to the data sets involved, and the primary technical difficulties are described in §1.4.

1.1 Models of the EBL and Motivation

The EBL includes the light from all extragalactic sources, both those which can be detected individually and those which are not detected due to low surface brightness, low total flux, or small angular size. While the limits of detection for individual galaxies are being extended to ever fainter levels with larger telescopes, better CCDs and space–based observations, an absolute measurement of the total flux from extragalactic objects remains an invaluable complement to the study of discrete objects by galaxy counts or redshift surveys. Populations of low surface brightness objects, as well as the majority of the luminosity function at high redshifts, are easily missed in both surface brightness limited galaxy counts and redshift surveys. Such objects will, however, contribute to the total diffuse background.

The EBL thus provides a means of quantifying the incompleteness of galaxy counts and redshift surveys, as it is immune to the surface brightness selection effects which inevitably bias the results of such magnitude–limited approaches. The EBL also avoids the "counting" ambiguities which arise from the non–uniform surface brightness distribution of individual galaxies in their rest–frame UV emission. This can cause counting errors even among the detected populations: single objects can be erroneously split into several and flux is lost from the regions in those objects where the surface brightness drops below the sky noise. Finally, both identification of faint galaxies and subsequent photometry becomes uncertain near detection limits. A measurement of the mean flux of the EBL avoids these inherent difficulties.

From the UV to the near–IR, the light of the EBL is dominated by the light of massive young stars, which emit most of their energy in the UV (1000–3000Å). The light seen in the optical originates from young stellar populations at moderate to high redshift ($\Delta\lambda/\lambda = z$), as well as older stellar populations at low redshift which have a redder spectral energy distributions. The massive young stars which produce the EBL are also responsible for the majority of metal production in the Universe, so that the metal mass density of the Universe and the EBL are also directly related. Thus, a measurement of the EBL is a very powerful constraint on many of the issues which galaxy counts and redshift surveys seek to address. Previous attempts to measure the EBL provide upper limits to the surface brightness we can expect (see Figure 1.5). Lower limits to the EBL can be derived from integrating the flux in detected sources, which, as discussed above and further in Chapter 7, is unavoidably incomplete. Predictions of the flux of the EBL are more generally models of the total star formation history of the Universe, as the EBL is the most inclusive observable consequence of that star formation history. Approaches to understanding the star formation history of the Universe fit into three general categories which then give predictions of the EBL.

The first category is models which are based on observations of the number of galaxies as a function of apparent magnitude (galaxy counts) or the number and intrinsic luminosity of galaxies as a function of redshift (redshift survey). Predictions about the nature of undetected objects based on extrapolating galaxy counts beyond the detection limit, or extrapolating luminosity functions more than several magnitudes beyond M^* can then be made in an attempt provide a more complete picture. This is the most common approach and is typified by models including dwarf populations, models invoking evolution in luminosity or number density, and models of starbursting populations with faded remnants (see Yoshii & Takahara 1988, Väisänen 1996, and references therein). Galaxy counts alone provide little information because they have uncertain completeness as a result of selection effects in surface brightness and morphology and provide only apparent magnitudes. The ability of redshift surveys to provide a lower limit to the luminosity density with redshift and wavelength makes them much more powerful as a tool for studying the evolutionary and formation history of galaxies. Redshift surveys are, however, even more prone to the selection biases than are galaxy counts. Redshift surveys are more likely to detect galaxies with high central surface brightness, emission lines, and small scale lengths. In addition, slight errors in characterization of the survey incompleteness can cause significant errors in the inferred results. It is interesting to note, however, that predicted flux level of the EBL which result from most extrapolated populations are relatively small (see Väisänen 1996 for a compilation of models which do not violate observed galaxy counts).

The second approach to modeling the star formation and metal enrichment history of the Universe is based on evolution in QSO absorption systems. The metal enrichment history of the Universe is linked directly to the star formation history as metals are produced by high–mass, rapidly evolving stars, the same hot young stars which emit the majority the UV light at high and low redshifts. The consumption of gas and evolution in metal density with redshift of the damped Lyman-α absorption systems seen in QSO spectra can be used to infer the star formation history required to produce that metal enrichment. This approach has been pioneered by Lanzetta et al. (1995) and by Pei & Fall (1995), who made significant improvements by considering the selection effects due to obscuration by dust which effect even the statistics of absorption systems. Even this approach, while very different from integrating the flux from detected sources, is still dependent on parameters based on observations of detected sources. Some of the more critical factors are the initial assumptions about the selection effects in QSO absorption line observations themselves, the properties of the IMF of the metal producing stellar populations (possibly as a function of redshift) and the optical properties, composition, and quantities of interstellar dust. It is precisely as a constraint to the parameters of such models the EBL is most useful.

And finally, theories which describe the formation of structure in the Universe such as those of Cole et al. (1994) and Kauffman et al. (1993) predict not only the properties of galaxy populations at all redshifts, but total luminosity density and, from it, the total integrated EBL. Observable characteristics of galaxies are used to constrain formation models. However some test, such as the observed mass–to–light ratio, will always be misleading if the total fluxes of galaxies are not detected and the measured luminosity density of the Universe is incomplete. To the degree that galaxy counts and redshift surveys can never completely constrain low surface brightness populations at all redshifts or the bulk of the luminosity function at high redshift, the EBL presents an invaluable observational test for such models.

It has often been suggested that the EBL can be used to differentiate between cosmological models (Olbers 1826, Whitrow & Yallop 1963, Partridge & Peebles 1967).

However, models of the EBL as a function of cosmological model have generally shown that when galaxy evolution is not considered, the change in the EBL flux is only 20–40% for values of q_0 between -1 and 2.5 (see Sandage & Tamman 1965, Yoshii & Takahara 1988). Evolution and the epoch of formation, on the other hand, can influence the EBL by factors of 2–3, as found by Yoshii & Takahara (1988; see also Tinsley 1973, 1977, 1978). The cosmological model has the greatest affect at longer wavelengths where the EBL includes contributions from hot, young stars at high redshift, and the total total volume of space at high redshift is therefore important. However these effects are dramatically overshadowed by our uncertainty in the formation epoch and evolution which describes the emitting populations. The dominant effect on the flux of the EBL, as argued by Harrison (1964, 1990), and Wesson (1991) is galaxy evolution.

As an integral flux over emitted wavelength and redshift, the EBL presents a result which does not translate directly into a luminosity density or star formation rate at any one epoch. However, absorption by neutral hydrogen produces a well defined high–redshift cut–off to the volume of space which contributes to a given band–pass as the Lyman limit shifts through observed wavelength range. At 3000Å, the EBL is dominated by the UV flux of galaxies at low z and can therefore be used to constrain the star formation rate at $z \lesssim 2.3$. At 8000Å, the EBL will include the light from stellar populations out to $z \lesssim 8$ (more than 80% of the age of the Universe in any cosmological model).

To give a general impression of the spectral ranges which contribute to our measurement as a function of redshift, we have plotted the contributing rest wavelengths as a function of redshift for each band–pass in Figure 1.1. The volume element as a function of redshift ($\Delta z = 0.1$) is plotted in Figure 1.2. It is difficult to determine what populations, or even what redshift ranges, will dominate the flux observed at 5500Å or 8000Å, because the age, IMF, and metallicity of the stellar populations have an enormous effect on the spectral energy distribution and total luminosity density with redshift. In addition, the star formation rate, which may be affected by merging and interactions, and the epoch of formation also influence the predicted flux and the redshift range which might dominate the EBL in a given band–pass. While the interpretation of the EBL is complicated by the integration of flux over a large range in redshift, it has a significant advantage over redshift surveys which isolate slices in redshift: as an absolute measurement of the total surface brightness from extragalactic sources, it is immune to the surface brightness selection effects which bias the galaxy population census obtained from the very limited range in apparent surface brightness which is accessible to redshift surveys (e.g., Lilly et al. 1996) and Lyman–limit selected surveys (e.g., Steidel et al. 1996, Madau et al. 1995).

1.2 Foreground Components

A firm detection of the EBL at optical wavelengths has remained elusive largely because of the difficulty of distinguishing the extragalactic background from the foreground contributions of terrestrial, zodiacal, and galactic sources. Upper limits from previous attempts to measure the EBL and lower limits from integrated galaxy counts give us an empirical estimate for EBL flux at 5500Å which is around 1×10^{-9} ergs $\mathrm{s^{-1}cm^{-2}sr^{-1}Å^{-1}}$ (hereafter, ergs $\mathrm{s^{-1}cm^{-2}sr^{-1}Å^{-1}}$ is abbreviated as I_λ), or roughly 28.2 AB mag arcsec^{-2}.[1] Relative to this expected EBL surface brightness, terrestrial airglow and zodiacal light are each roughly 100 times brighter, i.e., 100×10^{-9}, or 23.2 AB mag arcsec^{-2}. The contribution from diffuse galactic light can be relatively minor, with total surface brightness around that expected for the EBL. The relative fluxes of these foregrounds are illustrated in Figure 1.5.

In order to detect the EBL, we must measure not only the total surface brightness of the night sky to an accuracy of $1 \times 10^{-9} I_\lambda$, but each of the foreground components must be measured to that same accuracy. Inevitably, it is the accuracy with which the foreground contributions can be quantified which limits the accuracy with which the extragalactic background light can be measured.

To obtain the required sensitivity, we have addressed each of the foregrounds indi-

---

[1] AB mag is defined in the usual way as AB mag= $-2.5 \log F_\nu - 48.6$, with F_ν given in ergs $\mathrm{s^{-1}cm^{-2}Hz^{-1}}$.

vidually, either by measuring them directly, or by planning the observations to avoid or minimize their contributions. The characteristics of each foreground component and the approaches which we have adopted in dealing with them are described briefly in this section.

1.2.1 Terrestrial Airglow and Extinction

The Earth's atmosphere complicates the measurement of the surface brightness of the night sky in two ways. First, atmospheric emission ("airglow") dominates the flux of the night sky as seen from the Earth's surface. Airglow is the combination of molecular rotation–vibration bands, atomic line emission, and a continuum component which originate in distinct layers of the atmosphere, predominantly around an altitude of 90 km (Takano et al. 1990). Second, photons originating both above and within the atmosphere are affected by extinction (scattering and absorption) in the atmosphere as well, further complicating the removal of terrestrial emission. While airglow and extinction can both be modeled as functions of the line–of–sight path–length through the atmosphere, rapid temporal variations in the emission and extinction are observed, presumably caused by atmospheric motion, and also resulting from photo–chemical excitation and de–excitation even several hours after evening (or before morning) twilight. The high surface brightness of the airglow and the rapid temporal variations seen for both the airglow and the extinction have made these terrestrial effects the most difficult to remove in previous ground–based efforts to measure the EBL. Dube et al. (1977, 1979), for example, estimated that the uncertainty in their airglow removal for any given observation dominated their errors at the level almost six times the expected EBL.

The Hubble Space Telescope (*HST*) is in a high enough orbit to avoid terrestrial emission and extinction altogether. Thus, by using *HST* to measure the total surface brightness of the night sky, we avoid entirely one of the two dominant and most problematic foreground sources, the other being zodiacal light.

1.2.2 Zodiacal Light

Zodiacal light (ZL) is sunlight scattered off of dust grains in the solar system. The surface brightness of the ZL depends on the column density of the interplanetary dust (IPD) and on scattering geometry along a particular line–of–sight (see Figure 1.6 for definition of the angles which describe the ZL). The ZL is brightest in the ecliptic plane, where it goes from $200 \times 10^{-9} I_\lambda$ at large elongation angles ($\lambda - \lambda_\circ \approx 135°$) to over $1500 \times 10^{-9} I_\lambda$ at small angles from the Sun ($\lambda - \lambda_\circ < 30°$). Even at large angles from the Sun, however, the ZL varies by more than a factor of 3 from the ecliptic plane to the pole. The ZL reaches its faintest levels at viewing angles near $(\lambda - \lambda_\odot) \approx 135°$ and $|b| > 30°$, where it is $\sim 100 \times 10^{-9}\ I_\lambda$ at 5500Å. While the mean flux of the ZL can be predicted with roughly 10% accuracy based on scattering geometry and position out of the ecliptic plane, irregularity in the IPD cloud produces spatial variability of the ZL on scales smaller than 5–10° (Levasseur–Regourd & Dumont 1980, Richter et al. 1982). At the accuracies required here, a geometric model is inadequate for predicting the mean flux of the ZL. We can, however, measure the absolute flux of the ZL along a given line–of–sight by utilizing knowledge of its spectral features.

Neutral scattering would result in ZL with the same spectral energy distribution as the incident solar spectrum. If the ZL is reddened, the resulting spectrum is red with respect to color of the incident spectrum (rather than in an absolute sense). As this suggests, it is customary to define the broad–band color of the ZL as the ratio of the zodiacal to the solar spectrum as a function of wavelength,

$$C(\lambda, \lambda_0) = \frac{I_{ZL}(\lambda)/I_\odot(\lambda)}{I_{ZL}(\lambda_0)/I_\odot(\lambda_0)}. \tag{1.1}$$

We use this definition for the color of the ZL throughout this work.

Empirically, the ZL has a solar spectrum from λ =1500Å to 10μm with its broad–band color varying by only 5% per 1000Å from broad–band color of the Sun itself over that wavelength range. This is strong evidence that the scattering processes which produce the ZL are accurately described by Mie theory. Mie theory describes the interaction of photons of wavelength, λ, with solid particles, of diameter a. Mie theory has been shown to accurately produce the ZL spectrum over the full spectral range 0.15–10μm for scattering off of particles of the size and composition known to describe the IPD ($a \geq 10\mu$m and composed predominantly of astronomical silicate). The IPD grains are composed of layers of varying refractive index, have rough surfaces, include a small population of grains with $a \leq \lambda$, so that the Mie scattering which results is expected to be slightly wavelength dependent. Such wavelength dependence is empirically limited to levels less than 10%/1000Å even at widely varying orientations in the ecliptic plane by a number of ZL measurements (Leinert 1977, and references therein; Pitz et al. 1979; Murthy et al. 1990; Matsuura et al. 1995). For many reasons, however, it is very difficult to predict the exact color of the ZL with better than 5% accuracy. Among those reasons are the complexity of Mie scattering model when surface characteristics, size, shape and composition are taken into account. In addition, though a great deal has been learned from recent IR satellites concerning the composition and size of the IPD particles, the exact composition of the IPD grains and variations in size and composition along a particular lines of sight is not known.

We defer more detailed discussion of the IPD and the resulting color of the ZL to §6.2.1. The general understanding of the ZL as the result of Mie scattering off large particles has two main implications for our purposes. First, Mie scattering strength is slowly varying with wavelength and produces no spectral features for particles such as those which constitute the IPD (characterized by $a > \lambda$ and nearly constant albedo with wavelength). Thus, the width and depth of the features in the solar spectrum (e.g. Fraunhofer absorption lines) are reproduced in the ZL. Beggs et al. (1964) indeed showed that the Fraunhofer lines in the ZL show no measurable deviation from their solar equivalent widths to the accuracy of their measurements (2% calibration uncertainty). The second implication is that the exact color of the ZL from 2500 to 9500Å cannot be accurately predicted for our purposes, and measurement must be in the same scattering geometry and viewing direction with respect to the ecliptic plane in order to be relevant.

These two conclusions set the stage for the approach we have taken in measuring the ZL. We first use the known width and depth of the solar Fraunhofer lines which are seen in the spectrum of the night sky to determine the mean flux of the ZL at the wavelength of those spectral features. The technique is predicated on the definition of an equivalent width: if the equivalent width of a line in one contributing source is known ahead of time, then the measured depth and shape of the line uniquely determine the continuum level of that source at the wavelength of the feature. We then utilize empirical measurements of the observed color of the ZL to extrapolate from the mean flux of the ZL at the wavelength of the spectral features to other band–passes. The details of these techniques are further described in §4.3

1.2.3 Diffuse Galactic Light

The Galactic contribution to the optical flux of the night sky is a combination of the direct flux from discrete stars and a diffuse component from starlight scattered off of interstellar dust. In several previous attempts to measure the EBL, poor resolution made even the direct contribution from stars difficult to remove. With CCD images the contribution from stars can be easily removed, and any scattered light can be minimized to levels at which it is insignificant.

As we discuss in Chapter 5, work by Boulanger et al. (1988, 1996) and others has recently demonstrated that the 100μm emission at high Galactic latitudes is a good tracer of the dust, and a good predictor of the intensity of the optical scattering which will result from it. The diffuse Galactic light (DGL) at the wavelengths of interest to us can therefore be minimized by selecting fields which are at relative minima in the IRAS 100μm maps. In addition, we can estimate any contribution from the Galaxy using scaling relationships between the diffuse 100μm and near–UV or optical surface brightness. The results of previous investigations that have produced scaling relations between the diffuse IR emission and the scattered light in the near–UV and optical are discussed in Chapter 5, along with a simple scattering model which can reproduce the observed scaling relations to reasonable accuracy. The diffuse Galactic light is shown in Figure 1.5 at roughly the surface brightness appropriate to our observations.

1.3 Previous Measurements and Upper Limits

In the last 30 years, there have been many attempts to measure the EBL not only in the optical, but in the far–UV and IR as well. The foreground components which dominate the light of the night sky in each band are different; correspondingly practical methods and limitations in each band are different. We therefore limit our discussion of previous results to those measurements at optical wavelengths. The techniques we have adopted to deal with the foreground components in the range 2500-9000Å naturally build on methods which have been used in other attempts to measure the optical EBL. Our purpose in discussing previous experiments is to put both the techniques and results of this work in the context of previous efforts.

Previous attempts to measure the optical EBL have fallen into three general categories: (1) differential measurements, in which the foreground components are isolated from the background along different lines of sight, and thereby remove them without measuring them directly or distinguishing between them; (2) absolute measurements, in which foregrounds are directly measured and then subtract individually; and (3) escapist measurements, in which some subset of the foreground components are avoided by conducting the observations from a rocket or satellite. The experiment described here takes both an escapist and a direct approach to dealing with the foreground components. We avoid terrestrial airglow by using *HST*, while we directly measure the zodiacal and Galactic components.

To put this experiment in the context of those which have preceded it, we discuss below measurements which are representative of the general methods enumerated above. As mentioned above, foreground subtraction is the key to successful background measurements at optical wavelengths. In the last 30 years, enormous gains have been made in the communal knowledge regarding all of the foreground components in the optical (airglow, ZL, and DGL). The inherent difficulties and hazards of the techniques previously used to measure the EBL are now better understood, and several of the earlier efforts are now obsolete for that reason. We therefore limit our discussion to three experiments which indicate the general techniques listed above and illustrate the status of the field before the work we present here.

A more complete, although not exhaustive, list of previous results is show in Table 1.1. For a more complete discussion, see Mattila (1990) and references therein for optical EBL measurements, and Bowyer (1991) for UV. See Mattila (1990), Matsumoto et al. (1988), and Hauser (1996) for discussion of recent upper limits on the EBL at IR wavelengths (1.25–100μm).

Direct Foreground Subtraction: Dube et al.

In both spirit and general approach, the measurement which we have executed is most similar to that executed by Dube, Wickes, & Wilkinson (1977, 1979). Airglow, zodiacal light, and diffuse galactic light were each measured and removed individually in their work and our own. In detail, however, only their treatment of ZL is directly comparable to ours. Their measurement was conducted using the No. 1 36-inch telescope at Kitt Peak with a specially designed photometer as the detector. The field of view of the observations was 16 arcmin in diameter. The Palomar Sky Survey plates were used to select fields free of objects brighter than $m_V \sim 13$ mag and to identify and mask discrete sources in the field of view which were brighter than $m_V \sim 20$ mag. The discrete sources, both stars and galaxies, were masked in the focal plane of the telescope using spots of diameter 12 arcsec (for objects with $13 > m_V > 16$ mag) or 18 arcsec ($13 > m_V > 16$ mag).

They attempted to identify the airglow component by dependence of the total sky brightness on the zenith angle. One problem, which they discovered, is that the airglow is not stable with respect to the geometrical prediction. Fluctuations were observed at roughly a factor of 6 times the expected EBL. In addition, the geometrical "slab" model for the path–length through the atmosphere is not appropriate to an emission component which originates in a thin layer at an altitude of 90 km. Mattila has since discussed the fact that given the appropriate model for the airglow as a function of zenith angle, the upper limit quoted by Dube et al. (1979) is in fact a factor of 2 lower than their data support. Given the large random errors in their airglow solution, it is difficult to quantify this effect more precisely.

The ZL was measured, as in our own experiment, by the strength of the solar spectral features (Fraunhofer lines) which are present in the ZL. As photoelectric spectroscopy was not an option at that time, Dube et al. used narrow–band filters. The flux at the wavelength of a particular pair of Fraunhofer lines (the MgI doublet at 5172.7Å, and 5183.7Å) was measured using a filter centered at 5180Å, and $\Delta\lambda$ =15Å. For comparison with the strength on the absorption lines, and for the measurement of the total background flux, the "continuum level" level in the night sky was measured using a filter centered at 5115Å, $\Delta\lambda$=45Å.

Our own measurement does not use this portion of the spectrum because we found that a nearby airglow emission line at 5190Å was too strong and too variable through the night to allow a reliable measurement of the MgI lines (see Figure 1.4). While smoothly varying differences between the solar spectrum and the night sky spectrum (due to extinction and airglow continuum) do not present a difficulty for our purposes, the comparison between the night sky and the solar spectrum clearly indicates that airglow features will effect narrow–band measurements of the strength of the MgI lines.

The Dube et al. experiment was an original and careful execution of the general technique required to use the spectrum of the ZL to identify it's mean surface brightness. However, the use of a single Fraunhofer absorption feature made the measurement quite susceptible to the effects of airglow emission lines. The lunar and daytime sky spectra which were used to calibrate the narrow–band to continuum flux ratios were not effected by airglow to the same degree, and therefore gave systematically different calibration of the line strength than would be observed in the night sky. In addition to this systematic offset, they estimated that the *rms* error in their airglow removal for any given observation dominated their errors at the level almost six times the expected EBL ($6–10\times10^{-9}\ I_\lambda$).

Finally, the contribution from diffuse galactic light was modeled using a simple, "slab" model for the path–length through a uniform galactic disk. Great improvements in the current data on structure in the interstellar dust have shown that a slab model is too simplistic.

Differential Measurements: Mattila

One novel approach to the problem of removing foreground components was pioneered by Mattila in 1976. This method involved integrating on and off the line of sight to dark Galactic clouds in the hopes that the clouds would serve as opaque screens. Along the line of sight to the cloud, the foreground airglow, zodiacal light, and diffuse galactic light would be detected, in addition to any instrumental backgrounds. At an adjacent line of sight, airglow, ZL, diffuse galactic light, instrumental backgrounds and the EBL would be detected. The difference between the two measurements would then isolate the EBL from all instrumental and foreground emissions. The technique fails, however, because the clouds are luminous. Embedded stars, molecular fluorescence, and diffuse emission behind the cloud all contribute to the inconclusive results form this method. Spinrad & Stone (1978), Boughn & Kuhn (1986) both found similar difficulties, with the latter summarizing their efforts and constraining the EBL to have roughly the luminosity of the cloud (see Table 1.1).

Rocket based: Toller

A unique opportunity to conduct the ideal measurement of the EBL was afforded by the Pioneer 10 space–probe which traveled to a solar distance of 3 AU, outside the zodiacal dust cloud thereby escaping not one but both of the significant foreground components (airglow and zodiacal light). Unfortunately, components which can be dealt with effectively in most optical observations, integrated starlight, become quite difficult to remove when the spatial resolution of the observations is 2°, as for the Pioneer 10 data. The DGL, integrated starlight and calibration difficulties limit the result from Pioneer 10 data to an upper limit on the EBL. The upper–limits found by Toller (1983) at 4400Å from that data set are also shown in Table 1.1. For consistency, we quote the result in terms of a 3σ upper limit for comparison with the Dube et al. (1979).

Summary of Improvements

The current work takes advantage of significant gains in technology and also in the understanding of the foreground diffuse galactic light since the last attempts to measure the EBL. The primary technological improvement is the high resolution imaging from above the atmosphere which is afforded by HST. By observing from above the atmosphere, we avoid the airglow extinction and variable emission which dominated the errors of Dube et al. The high resolution imaging of HST also allows us to remove stars to $V \sim 28\,\mathrm{mag}$, which removes any doubt of significant stellar contamination, unlike the rocket–borne measurements of Toller.

Spectrophotometry using using CCDs is also a significant technological improvement over the narrow–band filter, photometer combination which was used by Dube et al. to measure the ZL. Spectra with resolution of a few angstroms over a 1000Å range in wavelength allow us to use many Fraunhofer lines to determine the surface brightness of the ZL as opposed to just one or two. In addition, as the airglow (emission line) spectrum and zodiacal (absorption line) spectrum make any continuum region difficult to identify, spectral resolution allows us to develop techniques which are insensitive to the continuum level (see §4.3).

We can also be far more confident of our removal of galactic light as a result of the data which was made available by the IRAS and DIRBE satellites of the 100μm emission from dust, and as a result of the work which has been done to correlate that thermal dust emission with the scattering of the incident stellar radiation field.

1.4 The *HST*/LCO Measurement of the EBL

Our strategy for measuring the EBL involves three simultaneously and independent data sets. Two of these sets are comprised of data from *HST*: images taken with Wide Field Planetary Camera 2 (WFPC2) through the F300W, F555W, and F814W filters; and low–resolution spectra at 3800–6800Å taken with the Faint Object Spectrograph (FOS) in parallel observing mode with the WFPC2 observations. We use both sets of *HST* data as independent measurements of the total surface brightness of the night sky from above the atmosphere. These measurements include the flux from the extragalactic background light and from zodiacal and galactic foreground components, but avoid terrestrial airglow and extinction altogether. Ideally, the entire experiment would be done from *HST*. However, the relatively low sensitivity of FOS requires the addition of a third data set to measure the ZL contribution.

The third data set is comprised of spectra taken at Las Campanas Observatory (LCO), covering 3800–5150Å with roughly 2.5Å resolution. We use these data to measure the mean flux of the ZL. As discussed in the previous section, this measurement utilizes the fact that solar spectral features are reproduced in the spectrum of the ZL, and the shape and depth of these features are well known. By measuring the apparent equivalent width of the Fraunhofer lines and blended features in the ZL, we can determine the continuum flux contributed by the ZL spectrum at the wavelength of the Fraunhofer lines. We found that ground–based spectra were necessary in order to obtain the high signal–to–noise ratio and resolution required to measure accurately the features of the ZL spectrum which have equivalent widths typically less than a few angstroms. Once measured in our ground–based spectra, the absolute flux of the ZL can then be subtracted from the mean flux observed by *HST*. Airglow complicates the measurement of ZL from the ground, however light pollution from cities would make the job harder still. The absence of light pollution at LCO makes this one of the few observatories in the world which can be used for this work.

Unfortunately, because of the strong features and surface brightness of the airglow, we can only make accurate measurements of the zodiacal Fraunhofer lines in the window from 3800–5150Å in ground–based spectra. In order to estimate the mean contribution from the ZL outside that wavelength range, we need to know how the flux of the ZL over the broader range 2500–8500Å relates to the flux in the 3800–5150Å range of our LCO observations. These details of the ZL subtraction are discussed in §6.2.

Finally, the diffuse Galactic contribution has been minimized by judicious field selection. The low–level contribution has been estimated by scaling relations between the 100μm thermal emission and the optical flux and from simple scattering models. As is clear from Figure 1.5, we must measure the ZL with an absolute error of order a few percent in order to detect the EBL. Because the contribution from DGL is so much smaller, estimates from scattering models and scaling relations are accurate enough to prevent the accuracy of DGL removal from contributing significantly to our errors.

1.4.1 Field Selection

The center of the *HST*/WFPC2 pointing is $\alpha = 3^{h}00^{m}20.''40$, δ= $-20^{\circ}10'45.''3$ (J2000). This corresponds to galactic coordinates $l \sim 206.^{\circ}6$, $b \sim -59.^{\circ}8$ and ecliptic coordinates $l \sim 35.^{\circ}5$, $b \sim -35.^{\circ}5$. We chose our target field to minimize the contributions from the following foreground sources: bright stars, diffuse galactic light (DGL) as traced in the IRAS 100μm maps, and ZL. We originally chose three target field, two within 10° of the galactic pole with ecliptic latitude $|b| \approx 30^{\circ}$, and one within 30° of the galactic pole with ecliptic latitude $|b| \approx 35^{\circ}$. All three fields are part of an ongoing program to measure the power spectrum of the EBL using the 2.5 m du Pont and 1 m Swope telescopes at LCO in Chile. Only the field near $|b| \approx 35^{\circ}$ was observable from *HST* because guide stars could not be found for the fields nearer the galactic pole. As we are concerned here only with the measurement of the mean flux of the EBL, the two fields near the pole are not discussed further.

To illustrate the characteristics of the field surrounding the *HST* pointing, we have overlaid the WFPC2 and FOS footprints on optical and IRAS 100μm maps (see Figures 1.7 and 1.8). The selected field clearly represents a compromise between avoidance of bright stars and galactic cirrus. Bright stars are actually a far greater problem for ground–based telescopes than for *HST* due to the large field of view and atmospheric far–field PSF: ground–based measurements of the power spectrum of the EBL (which were planned in conjunction with the mean–flux measurement from *HST*) required that bright stars be avoided as far as 1° from the field. This requirement is more stringent than necessary for the *HST* observations, as discussed below. Nonetheless, as is demonstrated in §5, the compromise achieved provides quite adequate avoidance of galactic cirrus as well.

1.4.2 Scattered Light

The sky level from *HST* is known to be affected by scattered light from the bright Earth limb. For roughly 50 minutes of every 90 minute orbit, the bright Earth limb produces negligible earthshine for most purposes. However, because the contribution of earthshine at even the 1% level would a concern for this work, we limited our observations to the 30–35 minutes during which the spacecraft is in the shadow of the Earth. During that portion of the orbit, no bright Earth is visible at all. While this is probably more restrictive than necessary, and reduces the usable exposure time per orbit, such scheduling was deemed far preferable to the risk of introducing unidentified stray light. With this restriction, the bright Earth limb is not a possible source of stray light.

Another possible off–axis source of scattered light is the moon. Scattered moonlight was avoided by requiring the observations to take place only with the moon at least 65° from the optical axis of the telescope, the angular separation at which the attenuation function becomes relatively flat with further increasing angles. The stray light characteristics of the telescope suggest that this will present roughly 10^{-5} fewer photons per second than the lower limit for the EBL count rate (STScI Technical Memo RSB–85–03). Finally, our observations of the field were separated into 3 visits staggered by one month each. For the first visit, the telescope was rotated by 90° with respect to the orientation during the other two visits. This has allowed us to check for scattered light, from on– or off–axis sources, as such effects should differ with a rotation about the optical axis of the telescope (see Chapter 2).

As discussed above, bright stars were also avoided. The nearest star brighter than $V = 7$ mag is more than 3° from the field. Based on the measured PSF of the telescope, the azimuthally averaged contribution to the WFPC2 count rate from stars closer than 5 arcmin from the field (of which there are three, each with AB mag

~ 13.5), is much less than 10^{-10} their total flux. The contribution from these stars completely insignificant, as their collective contribution to the total background flux is equivalent to that from one 39 mag star in the field of view. (ISR/OTA 06.1; STScI Technical Memos RSB–85–03 and RSB–85–02).

1.4.3 Scheduling

As mentioned above, we split the 18 orbits allocated to this project into three visits of six orbits each, with roughly a month between visits. The orbits were split in this way for three reasons. First, the surface brightness of the ZL can be predicted based on the elongation angle and ecliptic latitude of the line–of–sight at the time of observation. While this geometrical model cannot provide the ZL surface brightness to the accuracy we require, it does serve as a consistency check on the observations at the $\sim 5\%$ level. Second, we wanted to observe the field at different orientations so that scattered light which might be caused by bright stars in or around the WFPC2 field of view could be identified by variation in the pattern or intensity of the background with rotation of the telescope. Because the telescope orientation is dictated by the position of the field with respect to the Sun at a particular time of year, this required a lapse of at least 2 months between the first and last visits. Finally, by splitting the observations, random photometric anomalies which might affect one set of the observations might be identified by comparison with the other two visits.

The visits were scheduled for months during which the field could be observed at $(\lambda - \lambda_{\odot}) \approx 135°$ in order to minimize the zodiacal contribution. The field we chose is observable at the optimal orientation in December. However, the field is observable for the longest period of time while the satellite is in the shadow of the Earth when the field is in the anti–solar direction (late October). Unfortunately, the ZL increases slightly in the anti–solar direction due to the high efficiency of backscattering by the IPD (Levasseur–Regourd & Dumont 1980). We therefore scheduled visits for October, November and December so that we might hope to see some predictable modulation in the ZL, as a consistency check, and while having the most viewing time possible for the source. During all three months, a field at $|b| > 35°$ has a ZL surface brightness which is within 20% of the absolute minimum intensity of the ZL at any orientation. The exact date of the observations within those months was chosen to maximize the *HST* observing time in the shadow of the Earth and to avoid proximity to the Moon during the observations.

Another critical consideration for scheduling is the fact that spectroscopic observations to determine the ZL and the wide–band observations to determine the total night sky surface brightness must execute simultaneously in order to assure that the ZL contribution to both measurements is identical. The surface brightness of the ZL towards a particular extra–solar field may change rapidly as the line–of–sight through the IPD changes, because of uneven distribution of the near–Earth IPD or recent cometary or asteroidal in–fall to the IPD cloud along the field of view. For this reason, the spectroscopic observations from LCO and the November WFPC2 observations were arranged to occur on the same nights.

As a final note with regard to strategy, we point out that even if flux calibration is equally accurate in the WFPC2 images and the FOS spectra, the images are preferable for measuring the total diffuse sky surface brightness over the spectra for several reasons. First, the mean flux in a broad band can be measured more accurately with an 800 × 800 CCD detector than a narrow–band flux can be measured with the diode array of the FOS (in this case, 12 diodes per resolution element). This is true because the relative resolution and sensitivity of the two instruments result in far higher count rates for the WFPC2 than the FOS, especially relative to the count rate in the respective instrumental backgrounds. Second, the total field of view of the FOS is only a few square arcseconds, making that measurement difficult to justify as representative of the Universe in general. Indeed, the exact pointing of the *HST* was selected specifically to avoid galaxies in the FOS field of view down to a limiting surface brightness of 26 mag/arcsec^2. At the very least, we therefore avoid domination by foreground objects in the FOS measurement. Nevertheless, structure and field–to–field variations are, after all, expected and seen in the spatial distribution of faint galaxies. And finally, as a practical consideration, it is far easier to monitor the WFPC2 data for scattered light and photometric anomalies than the FOS data.

1.4.4 Flux Calibration

Our measurement of the EBL is differential. The absolute flux of the ZL, the dominant foreground component from space, is individually measured and subtracted from the *HST* measurement of the total background in order to obtain the residual flux of the EBL. Because the ZL is so much brighter than the EBL, both measurements must be calibrated to the same standard system with an accuracy of order a few percent in order to detect the EBL. The only other foreground component which contributes to the *HST* measurements is diffuse Galactic light, which is only of order 1% of the ZL. We can therefore tolerate a much larger error in the measurement of the DGL before it will contribute significantly to the total error in measuring the EBL.

Both the WFPC2 and FOS calibrations are based on the Oke (1990) secondary spectrophotometric system, which are in turn tied into the Hayes (1985, hereafter H85) absolute flux calibration of Vega. Because Vega cannot be observed from the southern hemisphere, the LCO spectra were calibrated relative to tertiary standards, which are calibrated with respect to secondary equatorial standards, which are in turn directly calibrated to the H85 spectrophotometry of Vega. The absolute accuracy of H85 Vega, the fiducial primary standard, is then nearly irrelevant for our purposes. What is crucial, however, is the accuracy with which the southern–hemisphere tertiary standards and the Oke (1990) secondary standards are tied into the same primary standard system. The accuracy of these standard systems relative to Vega is discussed in §2.2, §3.2, and §4.2.

It is also important to note the difference between the observations which are used for flux calibration and the observations we are doing in this experiment. The flux calibration of most astronomical instruments are based on observations of standard stars. Calibrations derived from standard star observations will automatically compensate for the light in the PSF which is lost outside the aperture when the observations being calibrated are also of point sources. For imaging, the extraction aperture for a point source observation is decided in the process of data reduction based on practical considerations, such as how the error due to background sky subtraction scales with aperture size, and how the PSF varies with position over the image and with time during the observations. For spectra, however, the aperture is a physical boundary in the focal plane of the telescope. The aperture size determines not only the spectral resolution but also, and more importantly for flux calibration purposes, the percentage of flux from a point source which passes through the focal plane of the instrument into the detector. The EBL is clearly not a point source. We want to measure the flux within a certain solid angle from a (nearly) uniform surface brightness source. To do so, we need to correct the flux calibration of each instrument to explicitly include the flux which is lost from the point sources used for calibration. For images, this means understanding the PSF of a point source in the image and correcting for the finite aperture within which flux from standard stars is extracted. For spectra, this means understanding the PSF both at the spectrograph aperture and at the detector plane. The aperture corrections and flux calibration of our observations are discussed explicitly for each instrument (see §2.2.4, §4.2.3, §3.2.2).

Table 1.1: Previous measurements and estimates of the EBL.

Collaboration	I^{a}_{EBL}	λ(Å)	Site,Method	M_{lim} (mag)
FUV[b]				
Hurwitz et al. (1991)	~ 0.6	1650	rocket,A	...
Martin et al. (1991)	< 3.5	1650	rocket,A	...
Optical				
Spinrad & Stone (1978)	< 14	4000	ground,E	... [e]
Toller (1983)	< 6.7	4400	space,B,C	$v \gtrsim 20$
Dube et al. (1979)	< 5.1	5115	ground,D	$v \gtrsim 23^{d}$
Boughn & Kuhn (1986)	$\sim 1.5^{c}$	6500	ground,E	... [e]
Galaxy Counts				
Milliard et al. (1992)	> 0.3	2000	balloon	$15.25 < UV < 18.25\,\mathrm{AB}$
Armand et al. (1994)[f]	0.38–1.2	2000	balloon	$UV > 15.25\,\mathrm{AB}$
Williams et al. (1996)	> 0.84	3000	*HST*	$U_{\mathrm{F300W}} > 23\,\mathrm{AB}$
Williams et al. (1996)	> 0.69	4500	*HST*	$B_{\mathrm{F450W}} > 23\,\mathrm{AB}$
Williams et al. (1996)	> 0.50	5900	*HST*	$V_{\mathrm{F606W}} > 23\,\mathrm{AB}$
Williams et al. (1996)	> 0.39	8000	*HST*	$I_{\mathrm{F814W}} > 23\,\mathrm{AB}$

a: I_{EBL} is in units of 10^{-9} ergs $\mathrm{s^{-1}cm^{-2}sr^{-1}\AA^{-1}}$.

b: The range $0.6–3.5\times10^{-9}$ is representative of the range of quoted detections and upper limits in the far–UV. See Bowyer (1991), Henry (1991), Sasseen et al. (1996) and references in each for a more detailed summary of results.

c: Minimum surface brightness of the nebulae.

d: The bright magnitude limit is quoted as "all stars and galaxies visible on the Palomar Sky Survey."

e: While no bright limit is given, the $\sim$10 arcmin^2 field of view implies that the bright–limit must be similar to $V < 23$ *AB mag* if "bright" galaxies that would be statistically rare in a field that size were avoided.

f: Extrapolated from galaxy counts of Milliard et al. (1992).

Method abbreviations:

(A) spectroscopic removal of DGL, and models of UV DGL from N(HI) (see Chapter 5);
(B) avoid airglow and ZL (outside IPD cloud, $R > 3\,\mathrm{AU}$);
(C) estimate of starlight from star counts $m_v \lesssim 11$;
(D) surface photometry of ZL, model dependent estimate of airglow and DGL;
(E) differential measurement using a galactic cloud as dark screen

The AB magnitude system is defined by the relation AB$= -2.5\log F_{\nu} - 48.6$, with F_{ν} given in ergs $\mathrm{s^{-1}cm^{-2}Hz^{-1}}$.

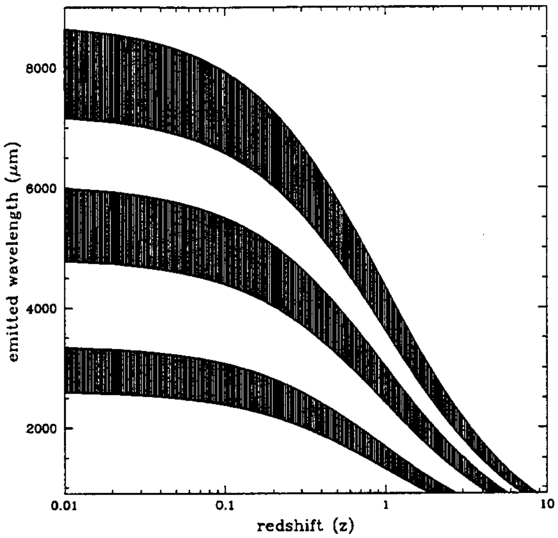

Fig. 1.1.— Bandpass as a function of redshift.

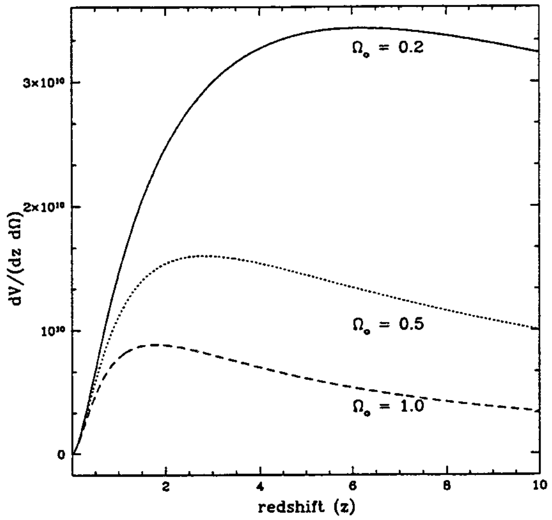

Fig. 1.2.— Volume element per steradian as function of redshift.

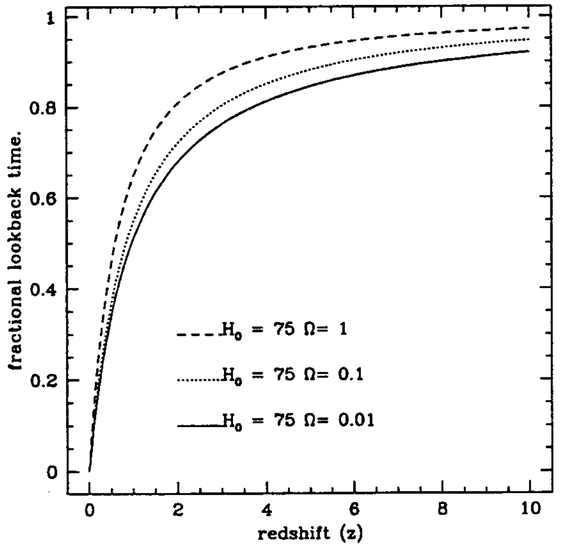

Fig. 1.3.— Fractional look-back time as a function of redshift.

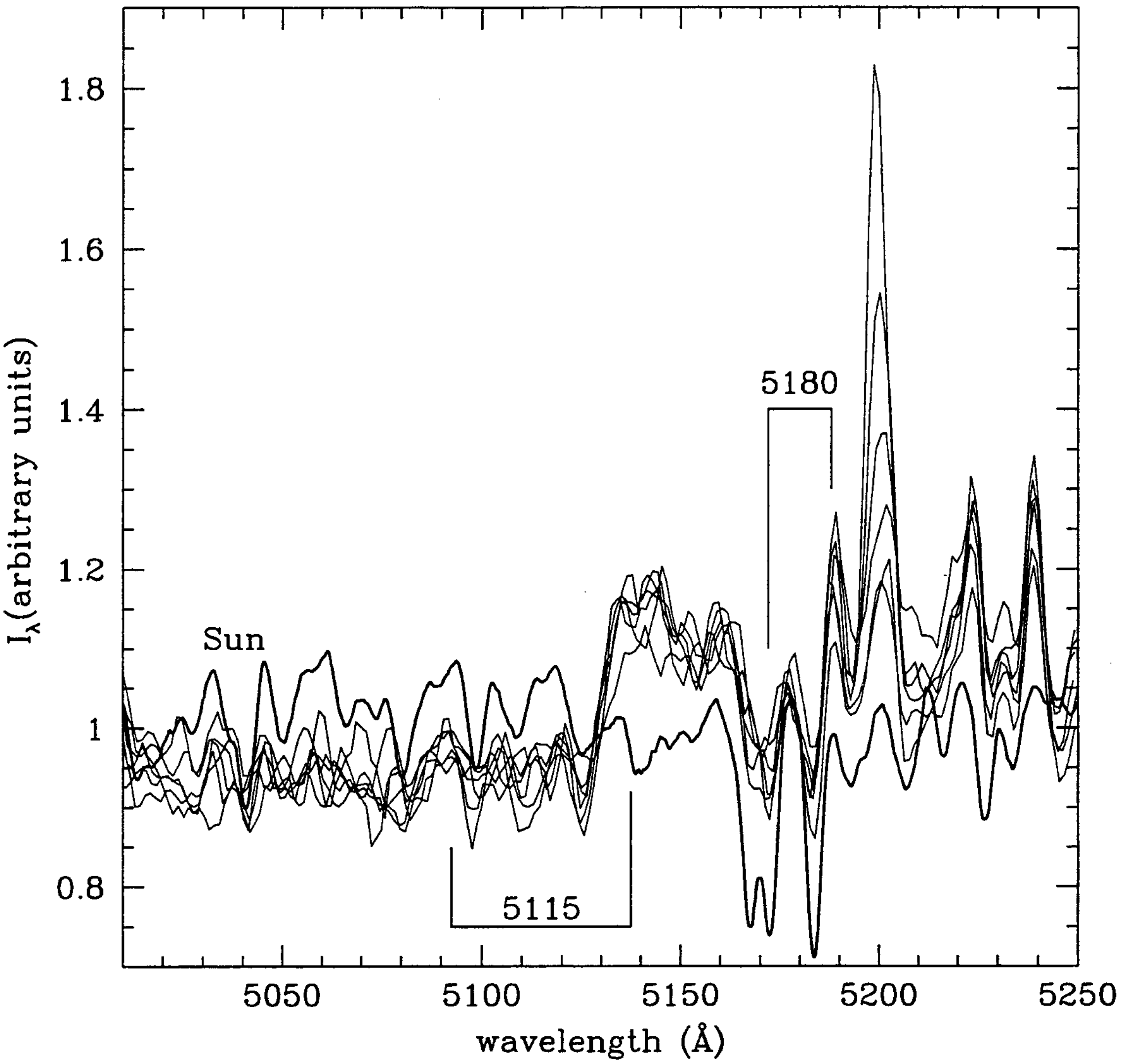

Fig. 1.4.— Several spectra of the night sky are compared to the solar spectrum (bold line) in the regions used by Dube et al. (1979) to measure the contribution of ZL to the uniform sky background. The spectra of the night sky shown here were taken during the same week as the LCO spectra presented in Chapter 4. A strong airglow feature near 5190Å is within the bandwidth which Dube et al. used to measure the flux in the MgI doublet in the ZL centered at 5180Å, I_{5180}. This feature is also variable, as can be seen from the spread of observed spectra shown. The calibration of line strength to continuum strength which would be expected from the ZL, $(I_{5180}/I_{5115})_{ZL}$, was made by observing the moon and the daytime sky, both of which would be unaffected by this feature. However the narrow-band observations of the night sky would be biased by the inclusion of a strong airglow feature in what is effectively a measurement of the equivalent width of the 5180Å MgI features. The band at 5150Å will also influence the "continuum" flux measured by the I_{5115}. These two bands seem to be significantly influenced by airglow features, and are therefore unlikely to give the correct ZL ratio.

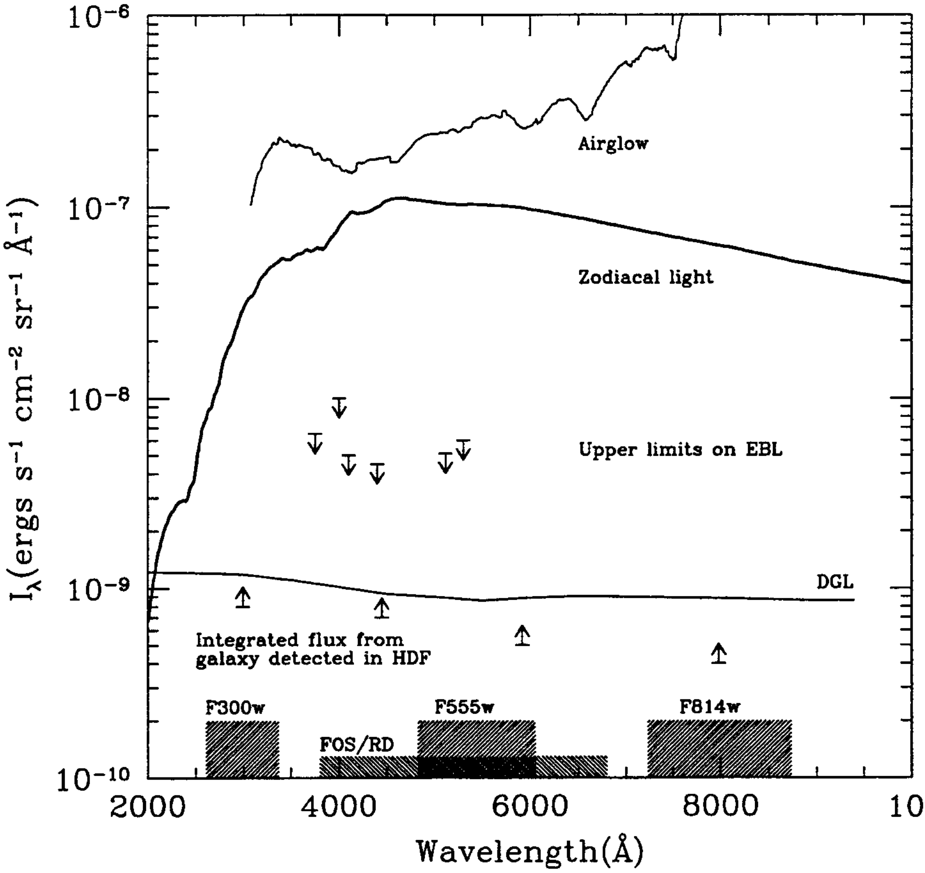

Fig. 1.5.— The surface brightness of foreground sources which contribute to the uniform surface brightness of the night sky are compared to upper limits on the EBL from other investigators (see Table 1.1) and also to the integrated flux from individually detected galaxies in the HDF with $V_{555} > 23$ AB mag. The latter provide an effective lower limit to the EBL by the observational definition we employ in this work. The ZL spectrum shown is representative of the contribution of ZL to our observations, which were designed to minimize this component (see §4.4 for discussion of the spectrum). The airglow spectrum shows the relative intensity over the range 0.31–1.0μm as observed by Broadfoot & Kendall (1968) scaled to match our own ground-based observations in the range 3800–5100Å. The hash-marked regions show the effective band-passes for our *HST*/WFPC2 and *HST*/FOS observations. The diffuse galactic component is also plotted at the level appropriate to this work, the estimation of which is discussed in Chapter 5.

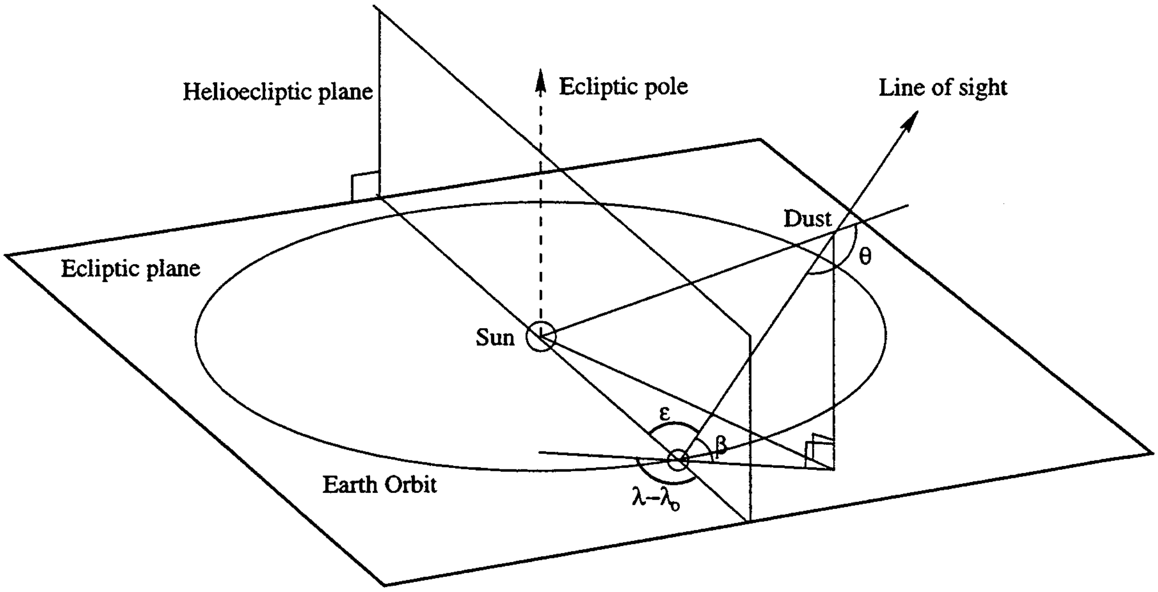

Fig. 1.6.— The basic geometry describing the zodiacal light (scattered sunlight off of the interplanetary dust). θ defines the scattering angle. The viewing line–of–sight is defined by ecliptic latitude, β, and geocentric ecliptic longitude, $\lambda - \lambda_{\odot}$, or alternatively, by β and the elongation angle, ϵ, defined by $\cos\epsilon = \cos(\lambda - \lambda_{\odot})\cos\beta$.

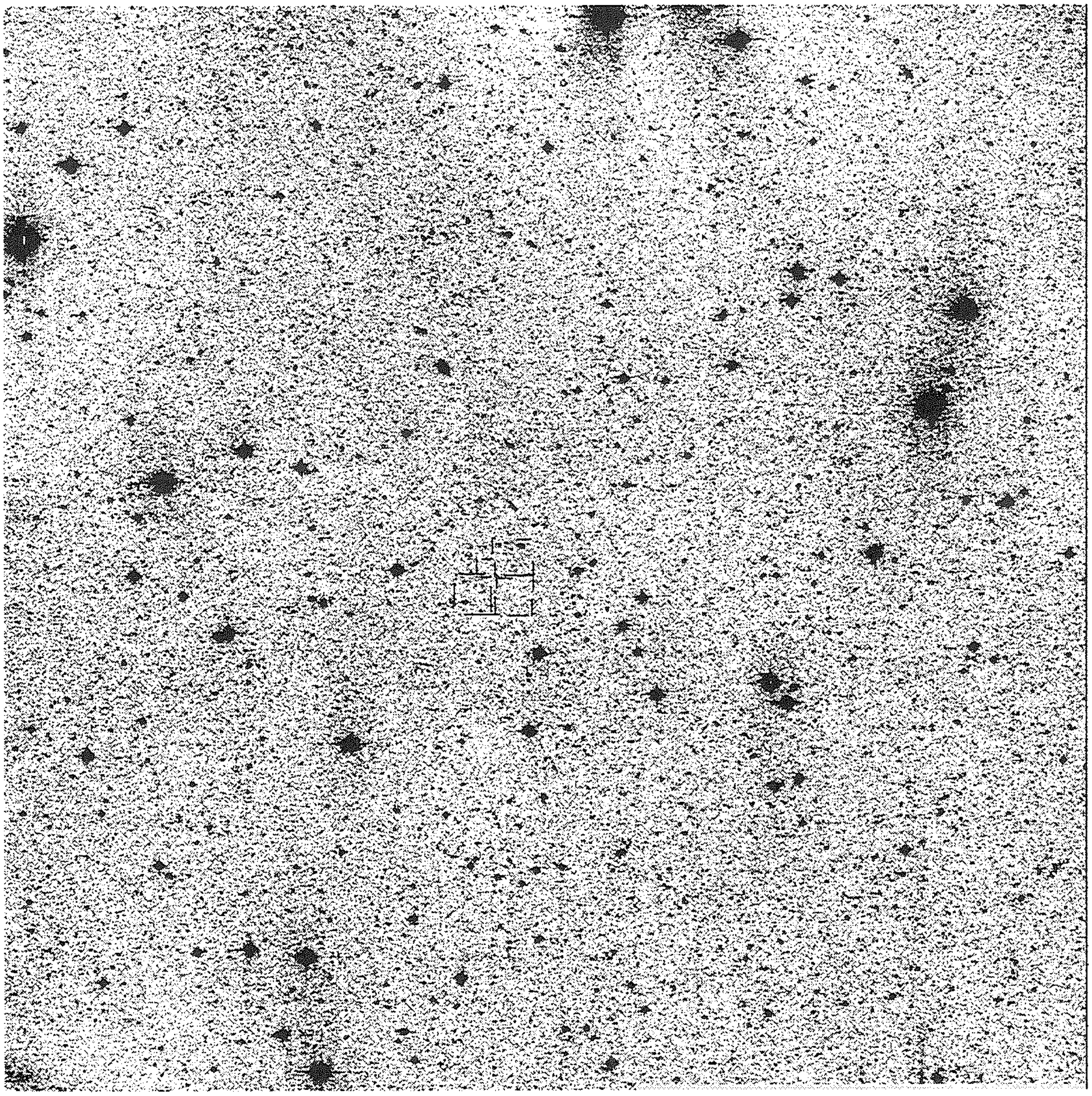

Fig. 1.7.— The *HST*/WFPC2 and FOS fields of view are shown overlaid on a Gunn-r 2×2 image mosaic taken with the 1 m Swope telescope at Las Campanas Observatory. The area shown is roughly $0.5^\circ \times 0.5^\circ$. The distribution and brightness of stars within 3° of the WFPC2 field are discussed in the §1.4.2 and are indicated in Figure 1.8.

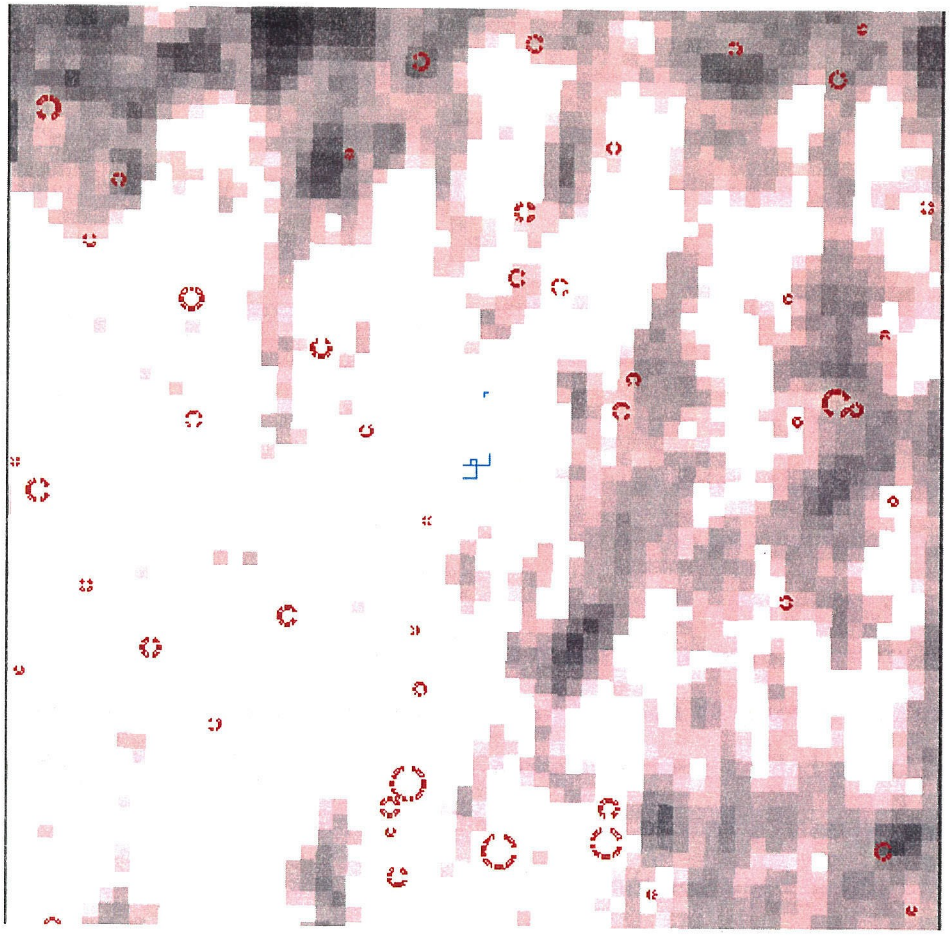

Fig. 1.8.— The *HST*/WFPC2 and FOS fields of view are shown overlaid on the IRAS $100\,\mu$m maps, $3\,\deg^2$. The dynamic range of the grey–scale is linear, with white indicating $100\,\mu$m fluxes of 0.6 MJy sr^{-1}(N(HI)$\sim 0.6\times10^{20}$, E($B-V$)$\sim$ 0.01), and black indicating 1.6 MJy sr^{-1}(N(HI)$\sim 1.6\times10^{20}$, E($B-V$)$\sim$ 0.03). The circles indicate the positions of bright stars. The radius of each circle is linearly proportional to the magnitude of the star it marks: the smallest circles indicate stars with $V\sim$ 12 mag; the largest indicate stars with $V\sim 7$ mag.

Chapter 2 *HST*/WFPC2 Measurement of the Diffuse Background

As described in §1.4, we use *HST*/WFPC2 to measure the total surface brightness of the night sky from above the atmosphere. This measurement includes the foreground contributions of the zodiacal light (ZL) and diffuse galactic light (DGL) as well as the component which is of direct interest to us, the extragalactic background light (EBL). The combined flux of the foreground components, dominated by ZL, is roughly 100 times brighter than the EBL, or $\sim 100\times10^{-9}\,I_\lambda$ (see Figure 1.5).[1] A 1% error in the WFPC2 measurement of the total sky flux translates to roughly $1\times10^{-9}\,I_\lambda$, which is of order the expected flux of the EBL. If we wish to detect the EBL, we must therefore obtain $\sim$ 1% accuracy in our measurement of the total surface brightness of the night sky with WFPC2.

To achieve this accuracy, unusual scheduling requirements were necessary to avoid contamination by stray starlight, as described in §1.4.3. In data reduction, methods beyond the normal pipeline data reduction procedures were needed to achieve the required zero–point and flux calibration. The WFPC2 observations, data reduction (§2.1), flux calibration (§2.2), and results (§2.3, §2.4) are described in this Chapter.

2.1 Observations and Data Reduction

Of the two available gain states for WFPC2, we used bay 4, which provides roughly $7\,e^-$/DN. The read noise is roughly $5.2\,e^-$ for each of the four CCDs. The field of view of each of the wide–field chip is roughly 1.7 arcmin^2, as each image contains 780×780 well–exposed pixels per image, and pixels are 0.1 arcsec square. The full field of view

---

[1] Surface brightness will be quoted in units of ergs $\mathrm{s}^{-1}\mathrm{cm}^{-2}\mathrm{sr}^{-1}\mathrm{\AA}^{-1}$, which we abbreviate as I_λ, as in Chapter 1.

of the WFPC2 wide–field chips is roughly 5 arcmin^2.

The 18 orbits allocated to this program were split into three visits of six orbits each. During each of the three visits, in October, November, and December 1995, observations were made using the F300W, F555W, and F814W filters. During each orbit, a single long integration (1800 sec) was taken while the satellite was in the Earth's shadow and one additional short integration (300–400 sec) was taken to fill the time between target acquisition and entry of the Earth's shadow. The short exposures were combined and used for cosmic ray rejection as well as limited photometry checks using the four stars which were imaged in the WF chips (see §2.3) The total detected signal in the 1800 sec (in–shadow) science exposures is roughly 12 DN ($85\,e^-$) per pixel above dark backgrounds and bias through the F555W and F814W filters, and roughly 0.3 DN ($2\,e^-$) per pixel above dark and bias through the F300W. Dark and bias frames were also taken while the satellite was on the bright side of the Earth: 5 darks of 1800 seconds each and 10 bias frames were taken per visit.

The basic calibration of our images was a mixture of standard pipeline and original calibration procedures. Among the pipeline procedures adopted were the corrections for analog–to–digital conversion errors, overscan subtraction, bias image subtraction, and flat–fielding. Any pixels which were indicated by the data quality files to be problematic for any reason were simply excluded from the subsequent analysis. The correction for dark backgrounds (by which we mean any signal which accumulates with time when the shutter is closed) was devised independently of the pipeline. Any additive errors, such as bias and dark, will contribute to the uniform surface brightness "detected" on the CCDs. Accurate subtraction of dark backgrounds is therefore crucial to this experiment. The subtraction of such backgrounds is usually of minor importance to typical astronomical measurements in which a "sky" background level is subtracted from measurements of individual objects to obtain the relative–to–sky photometry. The bias level of the WFPC2 CCDs has been both low and stable for several calibration cycles; the instantaneous dark level, however, can fluctuate by almost 50% with respect to the pipeline dark subtraction.

In the following sections, we discuss first the accuracy of the adopted pipeline calibration steps which we employ: analog–to–digital conversion corrections, overscan subtraction, bias subtraction, and flat–fielding. The information presented on these procedures is largely available from STScI documentation, but is repeated here for completeness and clarification. The dark current subtraction method which we have developed to meet the accuracy required for this measurement are discussed in §2.1.4. An additional concern for measuring a diffuse background is the effectiveness with which low energy cosmic rays can be identified and removed. We therefore discuss the detection of cosmic rays explicitly in the §2.1.5. The problem of varying charge transfer efficiency (CTE) in the WFPC2 chips has been identified in point source observations (see Holtzman et al. 1995a, 1995b). As variable CTE could cause significant calibration errors in this measurement, we have conducted laboratory tests to explicitly measure the effect of CTE variability on a low light–level, uniform source. CTE is discussed in §2.1.6. Other details of the flux calibration are discussed in §2.2. Finally, the objects and uniform background level detected in our WFPC2 observations are presented in §2.3 and §2.4, respectively.

2.1.1 Pipeline: Analog to Digital Conversion (ADC)

The signal chain for CCD data is rarely perfect, however the imperfections of the WFPC2 signal chain have been well explored. Errors accrued in the analog–to–digital conversion are corrected by the "A2DCORR" procedure in the pipeline calibration. This correction compensates for the problems described below.

In the process of reading the CCDs, the charge recorded in each pixel is converted to a digital value by comparing the levels read out to reference voltages. Each bit in the output value for a pixel reflects the binary outcome ("higher" or "lower") of input–to–reference voltage comparisons which successively approximate the incoming voltage level. Histograms of the WFPC2 data are structured in a way which indicates that DN values which correspond to all low–order bits will occur more frequently than will values one DN larger. This has been hypothesized to result from a slight mismatch in the reference voltage with respect to corresponding input voltages, caused by correlated noise in the input and reference voltages which arises from the use of switching power supplies in the WFPC2. When the reference voltage for the first bit is slightly too high, an input voltage which should correspond to exactly $(2^i * j)$ will be inappropriately set to $(2^i * j - 1)$. All bits downstream will be set high, as comparison voltages will be found to be lower than the input. The result is that the ADC produces $(2^i * j)$ for input signals which should have produced $(2^i * j - 1)$. The magnitude of the error is largest for larger signal values.

In this model for the digitization errors, the transfer function from input to output signals is monotonic but not linear. In order to correct for this effect, tests were conducted before flight to determine the DN values which resulted for a smooth distribution in input signal values. The ADC correction then involves replacing the output DN in an image with a value corresponding to the scaled average input signal at that output value. The average correction for DN values in the range of our data is 0.86 DN and changes smoothing. The same correction is used for each of the four CCDs in WFPC2.

The data to determine the correction were taken pre– and post–dynamic testing, with only 0.02 DN variation in the resulting ADC correction. The correction is therefore likely to be stable under normal usage, and was also found to be quite stable with changing temperature (STScI Technical Memo RSB–85–01). We therefore conclude that, at the signal levels of our data, the error resulting from the analog–to–digital conversion is of order 0.02 DN after the A2DCORR correction is applied.[2]

2.1.2 Pipeline: Overscan and Bias Subtraction

Bias subtraction was done using the "superbias" frames produced for the reduction of the Hubble Deep Field (HDF, see Williams et al. 1996). The HDF superbias is the average of 240 bias frames. The procedure used in making it is described in Williams

---

[2] As usual with calibration errors, any error in the A2DCORR correction will have minimal impact on observations of bright objects. This is true in the case of the ADC correction because it is a function of the signal level, and calibration of the instrument is based on large signal values (observations of bright stars with peak values near 1000 DN). As this is not the case for our data, it is fortuitous that the A2D correction appears to be stable.

et al. (1996). The 10 bias frames we took during each visit were used to test the accuracy resulting from the use of the HDF superbias frame for the reduction of our own images, however the bias frames from our program were not used for the bias subtraction directly because the noise level of the superbias frame was far better than could be obtained with our own 30 bias images. We found that the test–reduction of our own bias frames using the HDF superbias images resulted in a mean level statistically consistent with zero, with an *rms* variation of 0.002 DN. The estimated error in the dark subtraction will naturally include the error in the bias subtraction, and so it is not individually considered in the itemization of the errors contributing to our final EBL measurement.

2.1.3 Pipeline: Flat–Fielding Accuracy

Flat–fielding was performed using the images which were introduced to the pipeline calibration around May, 1996. The pixel–to–pixel error is reported in the WFPC2 Data Handbook (V3.0) to be roughly 0.3% for the WF chips, and 0.5% for the PC1. The errors over scales greater than 10 arcsec are less than 0.5% for all four chips. As we excluded data within 75 pixels of the edge of each chip from our analysis, issues of geometrical distortion and vignetting are largely avoided, and flat–fielding introduces a negligible error to our results. The calibration of the instrument is tied to the mean level of the flat–fielding images, and therefore no error is introduced in the mean over a frame due to flat–fielding.

2.1.4 Subtraction of Dark Backgrounds

The variable dark rate was suggested in the WFPC2 Instrument Handbook (V3.0) to result not from variation in the thermal dark current of the CCDs, but rather from variations in the glow contributed by MgF_2 field–flattening lenses which are positioned immediately in front of the individual WFPC2 chips. The details of the dark glow rate were not pursued until this work.

MgF_2 is known to exhibit broad–band fluorescence as a result of bombardment with even low–energy (200–2000 eV) ions and electrons (Qi et al. 1991). The transfer of electronic energy to the surface is by resonance or Auger neutralization, so that the time–scale for fluorescence is a fraction of a second. In further support of the suggestion that the face–plates contribute a dark glow, the strength of the glow drops by 50–75% towards the edges, in good agreement with predictions based on the geometry of the plano–concave lenses (B. Whitmore, personal communication).

Ions such as N_2^+ are plentiful in the upper atmosphere at orbiting altitudes, and are a likely cause of fluorescence from the MgF_2 face–plates. Another obvious source of charged particles is cosmic rays. Because the cosmic ray rate varies with orbital position, the instantaneous energy flux in cosmic rays will vary, and the dark glow will vary accordingly by up to $\sim 0.3\,\mathrm{DN}/1000\,\mathrm{sec}$. To some degree, the incidence rate of cosmic rays hitting the MgF_2 face plates can be monitored during the course of any given exposure by the total flux in cosmic rays events registered directly by the CCDs. Our first effort to determine the correlation between cosmic ray flux as measured from the DN in cosmic ray events on the CCDs and the dark glow rate is shown in the WFPC2 Instrument Handbook (V4.0).

In an effort to reduce the error in the dark subtraction in our data, we have isolated the dark glow component from the thermal dark component by determining the form of the correlation between the mean dark rate (thermal + glow) and total flux in cosmic rays hitting each of the individual CCDs. Once the two components are properly separated, a thermal dark image can be subtracted from every science exposure, scaled only for exposure time; a dark glow template image representing the correct shape of the dark glow component can then be scaled to the appropriate mean level (as predicted by the total energy in cosmic ray events in the exposure) and subtracted.

The dark glow component has a distinct shape over the image, peaking in the middle, and falling of by 25% at the edges. To quantify this shape, the following procedure was devised in collaboration with H. Ferguson (STScI, WFPC2 Instrument Team). We averaged together 1800 sec darks with a lower–than–average mean level to create an image with 1800 sec of thermal dark current, and a relatively low dark glow contribution. We also averaged 1800 sec darks with a higher–than–average mean level to create an image which also has 1800 sec of thermal dark current, but a larger–than–average glow component. By subtracting the two, the stable thermal components cancel, and we are left with an image which is purely a multiple of the dark glow component in two dimensions. This image was then fitted with a low order spline to produce a dark glow template, normalized to unity. This template can be scaled to any level to obtain the dark glow component appropriate for any single exposure, that level being inferred by the measured cosmic ray energy flux for that exposure.

The total dark can thus be parameterized in terms of a constant thermal dark rate, $T(x,y)$, and a normalized, two–dimensional dark glow component, G(x,y). The glow template can be scaled to a mean level appropriate for the glow in any image based on the total cosmic ray flux in the exposure, CR, and a constant scaling factor, A_i, in which the subscript indicates the CCD (1–4). The total dark background for a given pixel is then given by

$$D(x,y) = t\,T(x,y) \;+\; A_i\,CR\,G(x,y), \tag{2.1}$$

in which t is the dark–time of the image (total time elapsed since the CCDs were last read out). The glow template, $G(x,y)$, is normalized to a mean value of 1.0 over the central 400 × 400 pixels, so that the scaling determined by the cosmic ray flux in a each image can be used to scale the template directly. The glow has less than a few percent variation over the central 400 square pixels, so that it is adequate in practice to use the average over the center of an image as an estimate of D. Measurements of D and CR for 80 images were then used to fit for the slope, A_i, and intercept, T, of the correlation between dark glow and cosmic ray flux (see Figure 2.1).

Dark frames taken between October 1995 and January 1996 were used to fit for these constants. By using this sample of darks, taken within the time span of our observations, variations in the thermal dark rate with time are minimized. The thermal dark rates, T, found are listed in Table 2.1. Thermal dark ("superthermal") images for each CCD were created by subtracting off the dark glow from the dark images by the above prescription and averaging the remain thermal component. Hot pixels at the time of each visit were identified by comparing the 5 darks taken during each of our program visits o the superthermal.

A plot of the correlation between mean dark glow and cosmic ray flux is shown in Figure 2.1 for 15, 1700 sec exposures. These are the darks taken during our program, and were not used to produce the dark glow solution. Each point on the plot represents the mean dark glow and the measured cosmic ray rate for an individual chip during one exposure. The scatter around the linear fit for each chip is ~ 0.06 DN. The fact that good fits are found with a zero–valued y–intercept attests to the accuracy of the thermal dark level which was subtracted. It is also clear from this plot that the pipeline procedure of subtracting a single mean dark rate for all images can be wrong by as much as 0.35 DN for a 1700 sec exposure, which is a factor of 3–5 larger than the maximum error resulting from our method, with accuracy varying slightly between the 4 chips. As the F300W count rate from the total background is roughly 0.3 DN/1700 sec, this improvement in accuracy of dark subtraction is critical.

As a final test, three sets of 10 dark frames which were *not used* in determining the above solution were reduced in the identical manner to the program science images. After A–to–D conversion correction, overscan subtraction, bias subtraction, and dark subtraction by the prescription described above, the average mean level of 10 dark frames is consistent with zero, with an *rms* scatter of < 0.05 DN per 1800 sec exposure.

We attempted to further reduce the *rms* error in the predicted dark glow by including Julian date and time from the last DECON (days since the last time the chip was heated to remove contaminants) as parameters in the fit. This was done based on the rationale that the thermal dark current itself may drift on time–scales of years, or may be affected by the contaminants that the heating during DECON removes. A larger set of 120 darks was used for the purpose of these tests. No significant correlation was found in association with either time parameter. It is clear that any variation in the thermal dark level is much smaller than the random scatter in the dark glow resulting from the fluorescence of the MgF_2 field–flatteners. Finally, we also looked for a correlation between the scatter and the satellite position. This seems especially relevant as all of our darks were taken on the bright side of the orbit, in drastic contrast with the orbital position of the satellite during the science exposures. While the cosmic ray rate is correlated with the position of the satellite, we find no relationship between scale factor and the position of the satellite.

It is perhaps not entirely surprising that the correlation between dark glow and cosmic ray rate demonstrates some scatter. As is clear from the observed cut–off in the energy distribution of detected cosmic ray events (see Figure 2.3), the CCDs are either shielded from, or do not respond, to low–energy–level cosmic rays: the known energy distribution of cosmic rays increases with decreasing energy, however there is a sharp decline observed in the number of cosmic ray events with energy below approximately 50 DN/event (see §2.1.5). In addition, some other source of glow is possible, and is indeed indicated by the fact that a dark glow rate is higher for the PC chip than for the three WF chips. The PC chip only differs from the three WF chips in that it is contained within a longer CCD–lens housing. This may suggest that the paint lining the CCD–lens housing may also fluoresce in response to ion bombardment (J. Trauger, personal communication). In this case, fluorescence is again likely to be stimulated by ion bombardment, however the time–scale for fluorescence may not be instantaneous as it is with MgF_2.

In summary, we reduce the error in dark glow removal by a factor of 3–4 by using the method outlined above instead of the pipeline dark–subtraction. This method brings the error to levels acceptable for measuring the EBL in the near–UV (F300W) band–pass.

2.1.5 Cosmic Ray Detection

If low–energy–level cosmic rays were hard to detect, they would contribute the total background flux of an image. Figures 2.3 show histograms of the number of cosmic ray events as a function of the total flux per cosmic ray event, the peak flux per event, and the number of pixels affected per event. In each plot, it is clear that the number of cosmic ray events falls off sharply before it would become difficult to detect cosmic rays: the peak and total fluxes for cosmic ray events are significantly higher than the mean level of the background, and the total number of affected pixels only rarely drops below three. This gives us confidence that there is no difficulty in identifying and removing cosmic rays from our calculation of the mean, photon–induced flux detected in by the WFPC2 chips.

2.1.6 Charge Transfer Efficiency (CTE)

Another issue of great concern to this project is the efficiency with which charge is transferred from one pixel to the next while the chip is being read out, generically referred to as charge transfer efficiency (CTE). Accurate photometry requires that a *consistent percentage* of the electrons generated within a pixel can be read out and are correctly attributed to the pixel in which they originate. Be they a function of position on the chip, or a function of the number of electrons in a given pixel, variations in CTE are effectively non–linearities in detector response. Unfortunately, the WFPC2 chips are indeed known to have a "a small parallel CTE problem" (Holtzman et al. 1995b, henceforth H95b). That is, a *variable* percentage of the electrons in a given pixel are successfully transferred through the parallel gates (down columns). To date, the variations in the CTE have been attributed to differences in the mean light level of the exposure, the exposure time, and the row number of the object whose photometry is in question. For point sources, the observed errors in photometry can be as large as 4%.

Description of the Problem

General descriptions of these symptoms exist in WFPC2 documentation available from STScI and in H95b. However the information available to users concerning the physical explanation of the CTE problem or its solution are currently inadequate to consistently produce photometry accurate at the 1% level. This is especially true for surface photometry of a faint source, for which the effects of the CTE problem seen for point sources is not at all understood (S. Casertano, personal communication).

The CTE properties of the WFPC2 at the very low light–levels in our observations (2–85 e^-/pixel) cannot be addressed by tests on–board the spacecraft: it is nearly impossible to set up a controlled observation which would be relevant, as there is no light source, astronomical or on–board, which can supply such low light–levels in the repeatable or predictable manor required to measure CTE. In order to understand the effect that the CTE problem which is seen for point sources will have on a faint, uniform surface–brightness source, and on the calibration of the WFPC2 photometric system, we have conducted a series of linearity tests on a CCD which was cut from the same silicon wafer as the four WFPC2 chips. These tests were conducted with the help of John Trauger at the Jet Propulsion Laboratory using a set–up with which he has already reproduced the CTE seen for point sources.

Effect of Variable CTE on Point Sources

Photometry of point sources seems to be vary by $< 0.1\%$ with row number when the mean background level is greater than $\sim 200\,e^-$/pixel (J. Trauger, personal communication), implying that CTE is a non-issue for point sources when the mean count rate per pixel in the background reaches that level. The usual mode for standard stars, however, is short observations with very low background levels ($\sim$ 0.1 DN) and peak fluxes around a 1000 DN (7000 e^-) (S. Baggett, personal communication). Work by Trauger on "point source" data simulated in the lab, and on WFPC2 data taken in flight both show that 4% of the flux is lost from a point source when the point source is imaged at the top of the chip (4% loss per 800 rows). A CTE correction is thus crucial for the observations used to calibrate the WFPC2 photometric system. If the appropriate correction is applied, however, the error due to CTE is probably much less than 1%. This fact is well appreciated and the correction which is applied to the calibration observations is documented by STScI (Holtzman et al. 1995a), henceforth, H95a; H95b; WFPC2 Documentation http://www.stsci.edu). We therefore believe that the point source calibration of WFPC2 does properly account for variable CTE.

Effect of Variable CTE on a Uniform Source

The effect of this CTE problem on observations of a uniform surface–brightness source is not obvious from the preceding discussion. To understand the effect this problem will have in the case of a uniform source we must understand the cause of the problem, not just describe the symptoms in the case of point sources. Based on the laboratory tests done by Trauger on point source photometry, the CTE variation with row number can be explained as the result of electron traps which were created in the silicon before the pixel mask was etched into the wafer (J. Trauger, personal communication). Electrons in each pixel will populate a region which is well defined by the potential well. In this picture, more traps become accessible as the potential well fills with electrons because a greater area of the silicon, and hence more traps, become accessible to electrons. For example, when the uniform background level is 5 electrons per pixel, electrons will be confined to populate the bottom of the potential well and will sample a surface area of the chip such that only 1 trap (as we discover) is accessible per 5 pixels. When the full well is reached, a little more than 1 trap per pixel becomes accessible on average.

The most compelling evidence in favor of the trapped–electron explanation (as opposed to lose or displacement of electrons to other pixels during readout) is that the trapped electrons are entirely recovered from the traps with time delays from tens of seconds to twenty minutes. That is, if the chip is read out a second time, 20 min after the exposure was originally read–out, a residual ghost image appears. This is clear evidence that the electrons which were lost remained in their original location. The residual image indeed shows that the trapping occurs in the position of the original point source and in the pixels along the same column at row numbers below the point source. This shows that electrons become trapped in pixels through which the charge is transferred in the parallel direction, but not in pixels through which charge is transferred during horizontal readout. This is presumable due to the fact that clocking speed in the horizontal direction is roughly 800 times faster than the transfer speed through the parallel gates. The implication of the ghost image is that the minimum time required for electrons to “find” the traps is between 9×10^{-5} and 7×10^{-2} sec, the parallel and horizontal clocking speeds, respectively. The ghost image also suggest that electrons can escape from the traps in 10 and 1200 sec once the chip has been read–out and the potential wells are empty.

Evidence for the variable accessibility of traps with charge level is found in the fact that spurious charge is read out in bias frames. Spurious charge is generated on the chip during readout, so that the on–chip bias level is higher than the bias level indicated in the overscan region by a roughly $3\,e^-$/pixel. Because the $3\,e^-$/pixel *are* read out, there is clearly no difficulty in reading out single electrons sitting at the bottom of the potential well. Thus, trapping does not occur such that all of the first electrons in a pixel well are trapped. Some well depth must be obtained before trapping occurs. It could, of course, be the case that some of the electrons generated by spurious charge *are* trapped, and that, for example, only three of five electronically generated electrons are read out as spurious charge. In this case, those two electrons of spurious charge which are not read out will fill the first available traps. The fact that any spurious charge can be read out indicates that the lowest, photon–generated electrons can be read out uniformly. The sensitivity of the chip to low light levels and the ability to recover the first few photon–generated electrons should be no different for low backgrounds than for high background levels.

Laboratory Tests

The critical issue to determine for our purposes is the following: how many traps are available at what background levels? That is, if the background level generated in an image is $13\,e^-$/pixel, as in some of our images, how many electrons would we read out per pixel? To answer this question, we begin with the tests conducted by John Trauger on point source photometry. Figure 2.4 shows the percentage flux “lost” during read–out for varying peak fluxes (1×10^4 to 6×10^4 e^-) and varying background levels (0 to 600 e^-/pixel). The percentage lost during read out is determined for a peak flux level by comparing the total counts recovered from a simulated point source when the source is positioned near the bottom of the chip (few parallel transfers) and when the source is positioned near the top of the chip (almost 800 parallel transfers). This plot makes clear the fact that a high mean background level in all pixels will populate all of the available traps, so that fewer electrons will be lost from the point source as it is transferred along a column during readout. When the background level reaches 200 e^-/pixel, few traps remain to be filled and almost no electrons are lost from the point source during read out. When the background level is low, all traps are accessible at the time of read out, and electrons will be lost from the source. While better statistics would be desirable for more accurate determination, it is clear already that when the mean background level is negligible, roughly 1.1 e^-/pixel are trapped on average as a large signal is passed along a column, or total of 880 e^- lost for a point source which was imaged at the top of the chip. When the mean background is roughly 80 e^-/pixel, only 0.35 e^-/pixel are trapped on average during the readout of the source, or 280 e^- for a point source which was imaged at the top of the chip.

This emphasizes that it is the number of parallel transfers which causes the traps to be a significant problem for photometry. Even more important, it is the number of *unfilled* traps in every pixel through which charge is transferred during readout which causes the cumulative effect. For a uniform background source, accessible traps are filled in each pixel before read out in each pixel, but no further trapping occurs during the read out because the transferred charge reaches no new traps.

We can infer the number of traps which are filled in each pixel by the uniform background from the data shown in Figure 2.5. While 1.1 e^- were trapped per pixel for a near–zero background level, only 0.35 e^- were trapped when the background level was 60 e^-. Thus, one can infer that traps are available to roughly 0.75 e^-/pixel for a mean level of 60 e^-. This is the correction that should be applied to a uniform background of 60 e^-/pixel.

We can check this inference by performing a standard linearity test, which we have done with the help of John Trauger. Our linearity test was designed to expose the chip to a uniform source for a varying length of time, such that detected flux should vary linearly with exposure time. Any non–linearity in the resulting count–

rate indicates a non–linearity in the response or read–out of the CCD. In our case, the CCD was exposed to a bare diode light source, resulting in a nearly uniform illumination of the chip. The chip was first exposed to a single burst of light in a 10 sec exposure, then two burst of light over 20 sec, and so on. In this way, any dark background which would be expected to scale linearity with time would contribute linearly to the resulting count rates. A 20 min dark exposure was taken between each uniform background exposure and a series of five bias frames were taken before, at the mid–point, and after the sequence of uniform–source exposures. In order to prepare the chip before each run, a 30 min dark was taken, and the chip was "wiped" by taking several bias frames. The exact sequence of exposures taken during each run is listed in Table 2.2, along with resulting mean levels and count rates from one of the runs.

This test was run 4 times with identical results for two different gain settings and three different bias levels. The results of each run are plotted in Figure 2.6. If we assume that the lamp was not a significant source of error, which certainly seems reasonable given that the results reproduced exactly over 4 different runs, it seems that a slight nonlinearity is indeed evident from this experiment. If we assume that the trapping mechanism discussed above is responsible, then we may guess that roughly 1.1–1.3 electrons are lost per pixel from the mean background when the mean level reaches roughly 200 e^-/pixel. In that case, the lamp was producing roughly 0.468 e^-/sec. From that rate, one could predict the number of electrons which *should* have been detected per pixel as a function of exposure time. The difference between that expected and detected mean level is shown in Figure 2.7. For a mean level of roughly 80 e^-, roughly 0.75 e^- are trapped per pixel. For a mean level of 4 e^-, we find that $< 0.25\,e^-$ are trapped on average, in excellent agreement with the point source tests done by Trauger.

It is clear from the figures plotted that the number of traps accessible changes rapidly between 20 and 100 e^-/pixel. This is also seen with point sources superimposed on background levels between 20 and 100 e^-. It is difficult to say exactly how many traps are available at any particular level. To estimate the accuracy in our correction, we begin by noting that in 5 sequential exposures of 10 sec each, the mean level detected ranging from 4.61 to 4.52 e^-/pixel. While this looks like a moderate fluctuation on the figure, it is, in fact, amazingly constant, and underscores the fact that we are attempting to determine the presence or absence of 1 electron per 10 pixels. While Poisson statistics alone would imply that we should be able to measure means with accuracy of 0.008 e^-/pixel, in reality, there clearly are greater variations in the laboratory environment between exposures than in the statistical accuracy of the measured mean. The already–identified level of roughly 0.75 e^- trapped per 80 e^- then seems to be near the limit of achievable accuracy. We therefore apply the following corrections and estimate a generous error: 0.75 (± 0.25) e^-/pixel are assumed lost from a mean level of $\sim$ 80 e^-/pixel, and 0.1 (± 0.05) e^-/pixel are assumed lost from mean level of $\sim$ 2 e^-/pixel. It is clear that the maximum error in the inferred number of electrons lost per pixel is well within tolerable limits.

2.2 Flux Calibration

The flux calibration of WFPC2 is a problem which the WFPC2 Instrument Team is uniquely able to address. Many hours of observation of photometric standard stars are required to accurately determine the conversion from DN/sec to ergs $s^{-1}cm^{-2}Å^{-1}$. An excellent summary of the system calibration is found in H95a and H95b. Other groups have independently determined the PSF *interior* to the 0.5 arcsec aperture used by H95b and recalculated the color transformation from the WFPC2 standard system to the Kron/Cousins bands. All of these adjustments, however, have been augmentations to the H95b calibration of the ST mag photometric zero–points at 0.5 arcsec to meet the particular calibration requirements of specific programs (such as for very crowded fields), rather than redeterminations of the fundamental calibration. The filter and optical telescope assembly (OTA) transmission as a function of wavelength, the shape of the point spread function (PSF) at large angles (> 0.5 arcsec), and possible temporal variations in sensitivity all affect the calibration and have all been measured by the STScI teams alone. For completeness, we repeat here the results of the photometric calibration as reported by H95a and H95b, and also discuss the calibration provided by the most recently released response curves for the WFPC2 system.

As mentioned in the Introduction (§1.4.4), the accuracy of our surface brightness flux calibration is dependent on the accuracy with which the fiducial system is known, the accuracy of point source calibration, and the accuracy of the aperture correction. In the peculiar case of measuring the EBL, we are especially concerned with the accurate knowledge of the system throughput for each filter (effective filter bandwidth). While it is fine to measure the total background as defined by some random band-pass, that number cannot be turned in to an EBL measurement unless the band–pass is known well enough to determine the contribution of zodiacal light (ZL) through that same filters. Thus, we are extremely dependent on the accuracy of the WFPC2 synthetic photometry — photometry based on the convolution of spectrophotometric standards with the system bandpasses. All aspects of the WFPC2 calibration which are relevant to this experiment are discussed below.

2.2.1 Fiducial Spectrophotometric Standards

The standard stars used for WFPC2 calibration are the spectrophotometric secondary standards which were initially observed and calibrated to the Vega (Hayes 1985) system by Oke (1990). Slight grey–scale offsets were found to improve the internal agreement of the Oke (1990) observations, and the system was recalibrated to produce a secondary system which is "conservatively estimated" by to be within 1–2% of the optical calibration of Vega (Bohlin 1995; Colina & Bohlin 1994; Hayes 1985). Recall that Vega is the primary standard to which our ground–based observations are also tied, so that 1–2% error with respect to Hayes (1985) does represent the uncertainty in the fiducial spectrophotometry of these standard stars for our purposes.

2.2.2 Photometric Stability

Contrary to common lore, the photometric performance of WFPC2 is extremely stable. Monitoring of their regularly–used spectrophotometric standard, GRW +70 5824 (see Colina & Bohlin 1994; Bohlin, Colina, & Finley 1995; Bohlin 1995), between February 1995 and March 1997 shows variation of $\sigma < 1\%$ through the F555W, and $\sigma < 1.5\%$ through the F814W (STScI TIR/WFPC2 97–01). In fact, it seems likely that the majority of the variation could be attributed to the fact that the peak flux of star for a given observation can vary by factors of two due if the PSF is or is not well centered within a single pixel. As discussed above, variations in the percentage of trapped electrons could result from large differences in peak flux with different distributions of the stellar PSF across pixels. In that case, the photometric stability of the instrument would in fact be slightly better than the $\sim 1\%$ values listed above.

There has been concern that the UV sensitivity of the instrument is a linear function of the time from the last DECON (STScI, ISR/WFPC2 96–01).[3] More recent work, however, has shown that the decline in throughput appears to be due primarily to scattering rather than absorption, and thus due to a change in the PSF rather than the system throughput. This hypothesis is based on the observations of flat–field lamps before and after decontamination (STScI, ISR 96–01) as compared to observations of point sources during the same periods (STScI, ISR 96–02 & ISR 96–04). The variation in the F336W VISFLAT flux levels over the monthly DECON cycle is about 1.5%, while the variation in aperture measurements of stars is about 4.5%. Flux calibration is based on observations which are always taken shortly after a DECON, so that the UV calibration reflects the uncontaminated sensitivity of the instrument. While the F300W is not continually monitored in the standard calibration program, the nearest spectral equivalent, the F336W, shows variations of $\sigma < 1.5\%$ (STScI, TIR/WFPC2 97–01). Because we are making surface brightness measurements, the flat–fielding observations seem to indicate only a 1.5% correction would be needed for data taken 4 weeks after the last DECON. Our observations

---

[3] DECON refers to the once–monthly heating of the CCDs which is intended to remove the contaminants that are thought to affect the CCDs UV sensitivity (H95b).

took place within 1 week of a DECON and so require only at most one third of the maximum correction.

2.2.3 Point Source Calibration

It is clear that the internal consistency and stability of the calibration as provided by STScI is indeed excellent. The next issue to address is the absolute accuracy of the point source calibration. Because we are not interested in accurate point source photometry, we are not concerned with many of the issues which have plagued other programs. Such issues as the small–angle PSF, PSF variations around the field of view, and even conversion to a standard photometric system are all unimportant for this work. For our purposes, the only issue is the accuracy with which the total throughput is known. Accurate conversion from DN/sec to ergs $s^{-1}cm^{-2}Å^{-1}$ for a specific spectrum requires an accurate measurement of the throughput as a function of wavelength for each observing mode (F300W, F555W, and F814W).

The synthetic photometry system for WFPC2, as explained in H95b, was established by adjusting before–flight determinations of the *HST*–OTA reflectance, filter transmission, and CCD plus MgF_2 window response in order to match the observed count rates for a number of spectrophotometric standard stars. Built in to the calibration of point sources is the flat–fielding normalization, which corrects for vignetting in the optics around the field of view, the aperture size used for point source photometry, and the precise gain of each of the four CCDs. The response curves have been adjusted and improved since the Holtzman zero–points were published: errors in the data reduction of the standard star observations have been corrected, and also the strategy for incorporating the PSF and extraction aperture have changed. At present, the derived response curves (adjusted filter throughputs, OTA transmission, and detector response combined) are probably accurate to better than 1% for spectra which do not deviate greatly from those used for calibration (H95b). The accuracy of the *HST* fiducial standard system is discussed in §3.2.1.

2.2.4 Surface Brightness Calibration

CTE for a uniform surface brightness source was discussed in §2.1.6. As concluded there, a negligible error is accrued as a result CTE effects when they are properly treated: a correction with row number should be applied for the point source photometry used to calibrate the system, and a small correction per pixel should be applied for uniform sources as a function of mean detected flux.

The majority of error in calibrating a uniform surface brightness source comes from the accuracy with which the large–angle PSF is determined. The most accurate determination of the far–field PSF is in the H95a encircled energy curves (see H95a, Figures 5a & 5b, and Tables 2a & 2b). For the optical filters, the correction is nearly 10% from a 0.5 arcsec aperture to an infinite aperture.

The most recent system response curves for each filter (released in May, 1997) give the throughput appropriate to point–source photometry within a 0.5 arcsec aperture, with a flat 10% adjustment applied for light beyond that aperture. Thus, the most current system response curves are effectively the infinite–aperture throughput which is appropriate to a uniform surface brightness calibration. To compare the H95 calibration with the current version of SYNPHOT, we have corrected the H95 zero–points to an infinite aperture by including the same 10% aperture correction in all band–passes, as was done with the SYNPHOT calibration. It is clear from the values shown in Table 2.3 that the two calibrations are in good agreement. This is not surprising, since the SYNPHOT calibration was arranged to match the Holtzman zero–points after the July 1995 version. However, this does confirm that the effective aperture defined by the system throughput curves in the May 1997 version is indeed equivalent to the H95 calibration plus a flat 10% in all bands.

We can then estimate the error in the SYNPHOT calibration as a combination of the errors estimated by H95b (which should be similar to the errors quoted by the latest version of SYNPHOT) and the error in the aperture correction, which we can estimate from the encircled energy curve values published in H95a. H95b estimates roughly 1% error in the synthetic zero–point, based on accuracy of the synthetic photometry for standard stars covering a wide range of colors. The sensitivity of the instrument as measured by the standard star observations used to calibrate SYNPHOT has been stable to within roughly 1% over the last three years in the bands of interest (STScI, WFPC2/TIR 97–01). Slight adjustments to the total system throughputs were also made in the last SYNPHOT calibration, bringing those errors to the 1–1.5% level. Finally, the uncertainty in the aperture correction is estimated to be 1–2%, based on the encircled energy curves of H95. We therefore estimate the SYNPHOT system throughput curves and the zero–points and "PHOTFLAM" values which result to have an uncertainty of 1–2%.

2.3 *HST*/WFPC2 Resolved Objects

While the EBL can theoretically be defined as the integrated flux from all extragalactic sources, a finite field of view cannot contain a statistically representative sample of bright objects. The natural bright–magnitude cut–off for any measurement of the EBL is the magnitude at which the Poisson fluctuations in the number of galaxies per field is small, and therefore not a significant source of uncertainty. In the case of the $2 \times 2\,\mathrm{arcmin}^2$ *HST*/WFPC2 field of view, it happens that $V \approx 23\,\mathrm{ST\,mag}$ is a natural limit to adopt as the bright–magnitude cut–off.[4] Taking typical values for the number density of objects brighter than $V = 23\,\mathrm{ST\,mag}$, we can estimate that the contribution to the EBL from galaxies brighter than that cut–off is roughly 50%. This is a rough estimate only, as the field–to–field variation found by different groups at that magnitude is a factor of 2–3 (see Pozzetti et al. 1997 for recent results, and Koo & Kron 1992 for a review.) The integrated flux from such counts is discussed further in §6.3.

To illustrate that $V \sim 23\,\mathrm{ST\,mag}$ is a natural bright–magnitude cut-off for our observations, we show the differential number counts in our field in Figure 2.8. The

---

[4] At V_{555}, the ST mag zero–point is defined to be the same as for the AB system: V_{555} ST mag = V_{555} AB mag. At longer wavelengths, AB mag correspond to brighter fluxes than ST mag; the opposite at shorter wavelengths. We quote magnitudes for our own data in the ST mag system, which is an F_λ magnitude system (see H95b).

galaxy counts from the HDF are also plotted in that figure, however our purpose in doing so is purely to demonstrate that the field we have observed contains a typical field–galaxy population. The HDF is a convenient benchmark for this comparison simply because it has been so widely studied and compared to other results in the literature. As can be seen in Figure 2.8, the HDF has a factor of two more galaxies at magnitudes brighter than 23 ST mag in any of the three band, while the difference in number density below that magnitude is negligible. Such differences are well within the typical field–to–field fluctuations for galaxy counts.

Object identification and photometry for our images was done using the analysis package SExtractor (Bertin & Arnouts, 1996). The detection requirement was $1.5\sigma_{\rm sky}$ over 6 pixels, after smoothing with a 3×3 boxcar. The effect of different smoothing kernels and detection thresholds on the resulting source identification and photometry for objects brighter than $V_{555} \approx 27$ ST mag is entirely negligible, and therefore of no concern for the purpose of understanding the well–detected objects in the field. The total magnitude was defined as the flux within an area at least 2.5 times larger than the ellipse defined by the first moment radius (see Kron 1980) and isophotal elongation (MAG_ISOCOR as defined in SExtractor). For all practical purposes, the galaxy photometry we have employed is the same as that used for the HDF (see photometry discussion in Williams et al. 1996).

As is clear from the $\sqrt{N}$–error bars in Figure 2.8 (and Tables 2.4, 2.5, and 2.6), Poisson fluctuations in the number of galaxies per $2 \times 2\,\mathrm{arcmin}^2$ field of view become insignificant around $V_{555} \approx 23$. It is also clear by comparison with the HDF counts also shown in Figure 2.8 that the galaxies in our field represent a typical field population in colors and number density. Finally, we note that our detection limit in all three bands is as would be expected for the exposure time of these observations, which were more than 15 times shorter than HDF in near–V bands, corresponding to a difference in detection sensitivity of roughly 2 mag in the F555W and F814, and almost 2.5 mag in the F300W due to even longer HDF exposure times for that filter.

Four stars are detected in the WF chips, three in WF2 with V_{555} ~19.0, 20.5 and 20.8 ST mag, respectively, and one in WF4 with V_{555} ~22.0 ST mag. Star–galaxy separation poses no difficulty, stars brighter than V_{555} =23.0 ST mag are masked out regardless. No stars are expected at fainter magnitudes (Allen 1973).

2.3.1 On–axis Scattered Light

In estimating the possible error resulting from scattered light which is not removed by masking out (see §2.4) the detected isophotal extent of an object, it is interesting to note the percentage of flux contributed by the "bright" objects on the frame. Figure 2.9 shows the percentage flux detected from objects brighter than V_{555} =23.0 for each chip and each filter. It is clear from this plot that only ~ 5% of the flux in the F555W and F814W is contributed by bright objects in the WF2 or WF3. Several of the brightest galaxies are imaged the WF4, and ~ 15% of the flux in those images is from objects. In the F300W, the percentage contributed by bright objects is roughly 15–20%. The scatter in the F300W percentage is greater than in the other two bands for two reasons: (1) variations in the detected background level between chips are caused by errors in dark glow subtraction and dominate the errors in this band; and (2) real variations between the source flux and the background flux from chip to chip are much greater in this band because the ZL (the main component of the total background flux) is so much lower in this band than in the other two. As discussed in §4.5, the ZL contributes roughly 95% of the diffuse background at 5500–9000Å and only roughly 50% at 3500Å. Even assuming a large error of 2% in the removal of the objects due to light scattered outside the masked regions, the increase in the total measured background flux would increase by less than 0.1% at 5500Å, or equivalently, it would only raise our estimate of the EBL by $0.1\times10^{-9}\, I_\lambda$. Thus, the contribution to the diffuse background from on–axis scattered light is insignificant in our data.

2.4 *HST*/WFPC2 Total Measured Background Signal

After calibration, we measure the total background signal by simply taking the average of the detected flux in all pixels over the frame. This average naturally excludes pixels which fall into any of the three following categories: pixels which are flagged as bad data in the data quality file for any reason; pixels which are either associated with a cosmic ray event, or are within two pixels of a cosmic ray event; and pixels which are within the masked region around an objects brighter than $V_{555} = 23\,\mathrm{ST\,mag}$. The extent of the object masks are defined by ellipses with axial radii which are each a factor of three times the detected isophotal extent of the object. We show the masked regions in Figures 2.10, 2.11, and 2.12 for each of the WF chips. The masks were defined based on the F555W images only — identical masks were applied to images from all filters. Our detected EBL is thus defined by contributions from the same objects in all bands.

Each WF image from each 1800 sec exposure produces a measurement of the mean background. We have averaged together the six measurements from each visit to obtain the results shown in Figure 2.4 for the November and December 1995 data sets respectively. It is difficult to make the same limiting magnitude cuts in the PC chip as the WF chips, because of the very different detection limits. However, when only stars and the brightest galaxy (imaged in WF4) are masked out, the PC and WF chips all give the same mean to within ±2%, which is well within the range of the source variation over the 4 chips. We do not, however, include the PC chip in the measurements of the EBL beyond the detection limit of $V_{555} = 23\,\mathrm{ST\,mag}$ because the area sampled by the PC is a negligible increase over that sampled by the other three chips, and because it is difficult to be certain of the magnitude cut–off. The error bars plotted in Figure 2.4 show the *rms* variation between the six measurements (three WF chips, two exposures per filter) from each visit. This error is well matched to the predicted uncertainty due to random errors, as enumerated in Tables 2.7 and 2.8. Systematic errors are dominated by the flux calibration from DN to physical units and are, of course, identical for all points in each band. We do not show them here in the comparison between months (see §2.2).

Table 2.1: Comparison of thermal dark levels found in this work and during Thermal Vac. tests

chip	this work (DN/1000s)	Thermal Vac (DN/1000s)
PC	0.275 (±0.038)	0.23
WF2	0.224 (±0.034)	0.17
WF3	0.258 (±0.025)	0.21
WF4	0.228 (±0.036)	0.17

Table 2.2: Sequence of exposures for laboratory linearity test

#	exp time (s)	mean (e^-/pix)	e^-/pix/s	e^-/pix lost
1	0	0.011	···	···
2	0	0.041	···	···
3	0	0.018	···	···
4	1200	0.154	0.00013	···
5	10	4.560	0.456	0.296
6	1200	0.179	0.00014	···
7	20	9.240	0.462	0.474
8	1200	0.205	0.00017	···
9	40	18.714	0.468	0.714
10	1200	0.215	0.00018	···
11	60	28.536	0.476	0.606
12	1200	0.227	0.00019	···
13	80	38.325	0.479	0.531
14	1200	0.261	0.00022	···
15	100	48.015	0.480	0.555
16	1200	0.208	0.00017	···
17	200	95.945	0.480	1.195
18	1200	0.212	0.00018	···
19	300	144.517	0.482	1.192
20	1200	0.261	0.00022	···
21	400	193.170	0.483	1.110
22	1200	0.219	0.00018	···
23	0	0.045	···	···
24	0	0.020	···	···
25	0	-0.042	···	···
26	1200	0.278	0.00023	···
27	400	193.160	0.483	1.120
28	1200	0.240	0.00020	···
29	300	144.630	0.482	1.080
30	1200	0.219	0.00018	···
31	200	95.960	0.480	1.180
32	1200	0.222	0.00018	···
33	100	48.052	0.480	0.517
34	1200	0.282	0.00023	···
35	80	38.328	0.479	0.528
36	1200	0.236	0.00020	···
37	60	28.531	0.476	0.610
38	1200	0.262	0.00022	···
39	40	18.568	0.464	0.860
40	1200	0.245	0.00020	···
41	20	9.217	0.461	0.497
42	1200	0.215	0.00017	···
43	10	4.601	0.460	0.255
44	1200	0.282	0.00023	···
45	0	0.051	···	···
46	0	0.047	···	···
47	0	-0.01	···	···
48	10	4.553	0.455	0.304
49	10	4.569	0.457	0.288
50	10	4.618	0.462	0.239
51	10	4.652	0.465	0.205
52	10	4.616	0.462	0.241
53	10	4.611	0.461	0.246

Table 2.3: WFPC2 synthetic photometry zero–points.

Obs. Mode	Holtzman[a]		SYNPHOT[b]	
	PHOTFLAM[c]	$ZP_{\mathrm{ST\,mag}}$	PHOTFLAM[c]	$ZP_{\mathrm{ST\,mag}}$
WFPC2,3,F300W,a2d7	5.825e-17	19.487	5.985e-17	19.457
WFPC2,3,F555W,a2d7	3.439e-18	22.559	3.439e-18	22.559
WFPC2,3,F814W,a2d7	2.464e-18	22.921	2.449e-18	22.927

a: Synthetic photometry from Holtzman et al. (1995b) with a 10% aperture correction in all bands to approximate an infinite extraction aperture.

b: SYNPHOT calibration, version released in May 1997. 0.5 arcsec apertures were used with a 10% correction in all bands to approximate the throughput appropriate to an infinite extraction aperture.

c: WFPC2 Data Handbooks calls the conversion factor from DN to physical units is PHOTFLAM, which is given in units of (ergs $s^{-1}cm^{-2}Å^{-1}$)/DN. The correspondence between PHOTFLAM the zero–point of the magnitude system is given by $m_{\mathrm{ST\,mag}} = 0 = -2.5\log(\mathrm{PHOTFLAM}) - ZP_{\mathrm{ST\,mag}}$.

Table 2.4: Differential galaxy counts in the F300W

	EBL field, U_{300}	
ST mag	N detected	$\log(N)(\mathrm{mag}^{-1}\,\mathrm{deg}^{-2})$
22.25	2	3.551
22.75	3	3.727
23.25	4	3.852
23.75	10	4.250
24.25	31	4.741
24.75	52	4.966
25.25	63	5.049
25.75	28	4.697
26.25	3	3.727

Table 2.5: Differential galaxy counts in the F555W

EBL field, V_{555}		
ST mag	N detected	$\log(N)(\mathrm{mag}^{-1}\,\mathrm{deg}^{-2})$
22.25	1	3.218
22.75	3	3.696
23.25	3	3.696
23.75	9	4.174
24.25	22	4.562
24.75	40	4.821
25.25	60	4.997
25.75	82	5.133
26.25	100	5.219
26.75	118	5.291
27.25	155	5.410
27.75	140	5.365
28.25	48	4.901
28.75	8	4.122
29.25	3	3.696

Table 2.6: Differential galaxy counts in the F814W

EBL field, I_{814}		
ST mag	N detected	$\log(N)(\mathrm{mag}^{-1}\,\mathrm{deg}^{-2})$
22.25	4	3.821
22.75	4	3.821
23.25	6	3.997
23.75	9	4.174
24.25	21	4.542
24.75	27	4.651
25.25	50	4.918
25.75	83	5.138
26.25	85	5.149
26.75	99	5.215
27.25	110	5.261
27.75	137	5.356
28.25	70	5.064
28.75	23	4.581
29.25	11	4.261

Table 2.7: WFPC2 error budget for background flux: random error per image

	F555W, F814W	F300W
Off–axis scattered light (§1.4.2)	< 0.001 DN	< 0.001 DN
Dark and bias subtraction (§§2.1.4, 2.1.2)	±0.05 DN	±0.05 DN
Flat–fielding (§2.1.3)	...	...
CTE (§2.1.6)	±0.03 DN	±0.007 DN
Cumulative	0.06 DN or 0.5%	0.05 DN or 18%

Table 2.8: WFPC2 error budget for background flux: systematic uncertainty

	F555W, F814W	F300W
A–to–D conversion[a] (§2.1.1)	±0.02 DN (0.2%)	±0.02 DN (6%)
Point source flux cal.(§§2.2.2, 2.2.3)	1%	1.5%
Aperture correction (§2.2.4)	1%	1%
Solid angle (pixel scale)(§2.2.4)	0.1%	0.1%
Cumulative	1-2%	6-8%

a: The A–to–D conversion is an additive correction, the error resulting from an incorrect A–to–D conversion is therefore the ratio of the A–to–D error and the mean level in the frame. All other entries in the table are multiplicative.

Table 2.9: Results of total background measurement with WFPC2

filter	λ_0(FWHM) Å	mean	($\pm$ *rms*)[a]	[$\pm$ sys][b]
November				
F300W	3000 (770)	3.58×10^{-8}	($\pm$ 9%)	[$\pm$ 6–8%]
F555W	5500 (1230)	1.06×10^{-7}	($\pm$ 0.3%)	[$\pm$ 1–2%]
F814W	8000 (1540)	7.24×10^{-8}	($\pm$ 0.2%)	[$\pm$ 1–2%]
December				
F300W	3000 (770)	3.36×10^{-8}	($\pm$ 7%)	[$\pm$ 6–8%]
F555W	5500 (1230)	1.04×10^{-7}	($\pm$ 0.4%)	[$\pm$ 1–2%]
F814W	8000 (1540)	7.11×10^{-8}	($\pm$ 0.2%)	[$\pm$ 1–2%]

a: *rms* errors quoted here reflect the scatter found from the results of the six measurements per visit (three images per exposure, two exposures). Compare to estimated errors in Tables 2.7.

b: Systematic errors are those tabulated in Table 2.8.

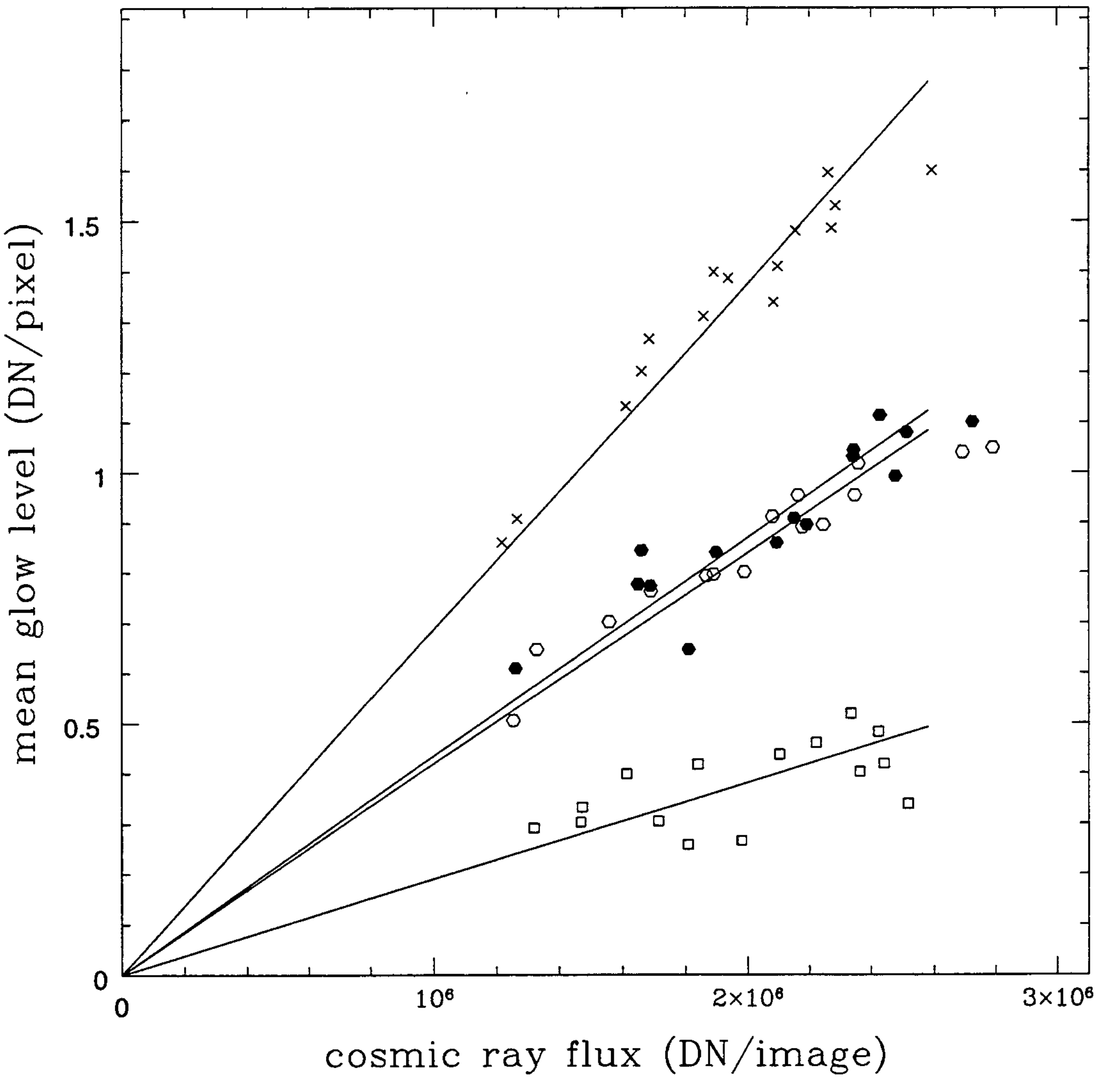

Fig. 2.1.— Correlation between total cosmic ray flux and mean dark glow from the MgF_2. The different symbols show the relations for the 4 chips: ×'s for PC1, boxes for WF2, open circles for WF3, and filled circles for WF4. The points have negligible errors in both axis; the cosmic ray flux is merely the sum of detected cosmic rays, and the glow level is statistically determined using $\sim 10^6$ pixels.

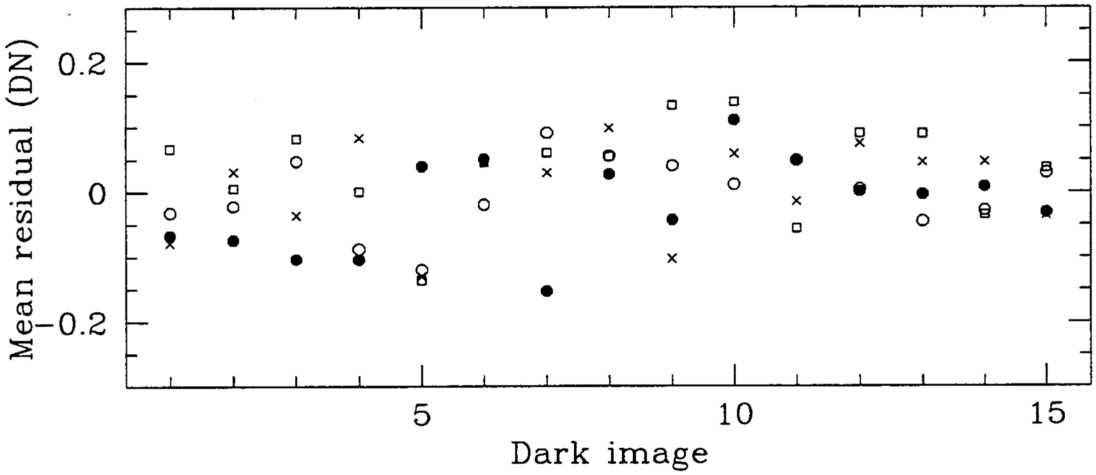

Fig. 2.2.— The residual mean level in test-reduced dark frames after A-to-D correction, bias subtraction, and dark subtraction by the methods described in §2.1.4. The dark frames shown in this test are those taken during the bright portion of 15 orbits during the execution of our program. The integration time for each dark was 1800 seconds. The residual mean levels for the PC chip are marked by open squares, WF2 by ×'s, WF3 by open circles, and WF4 by solid circles.

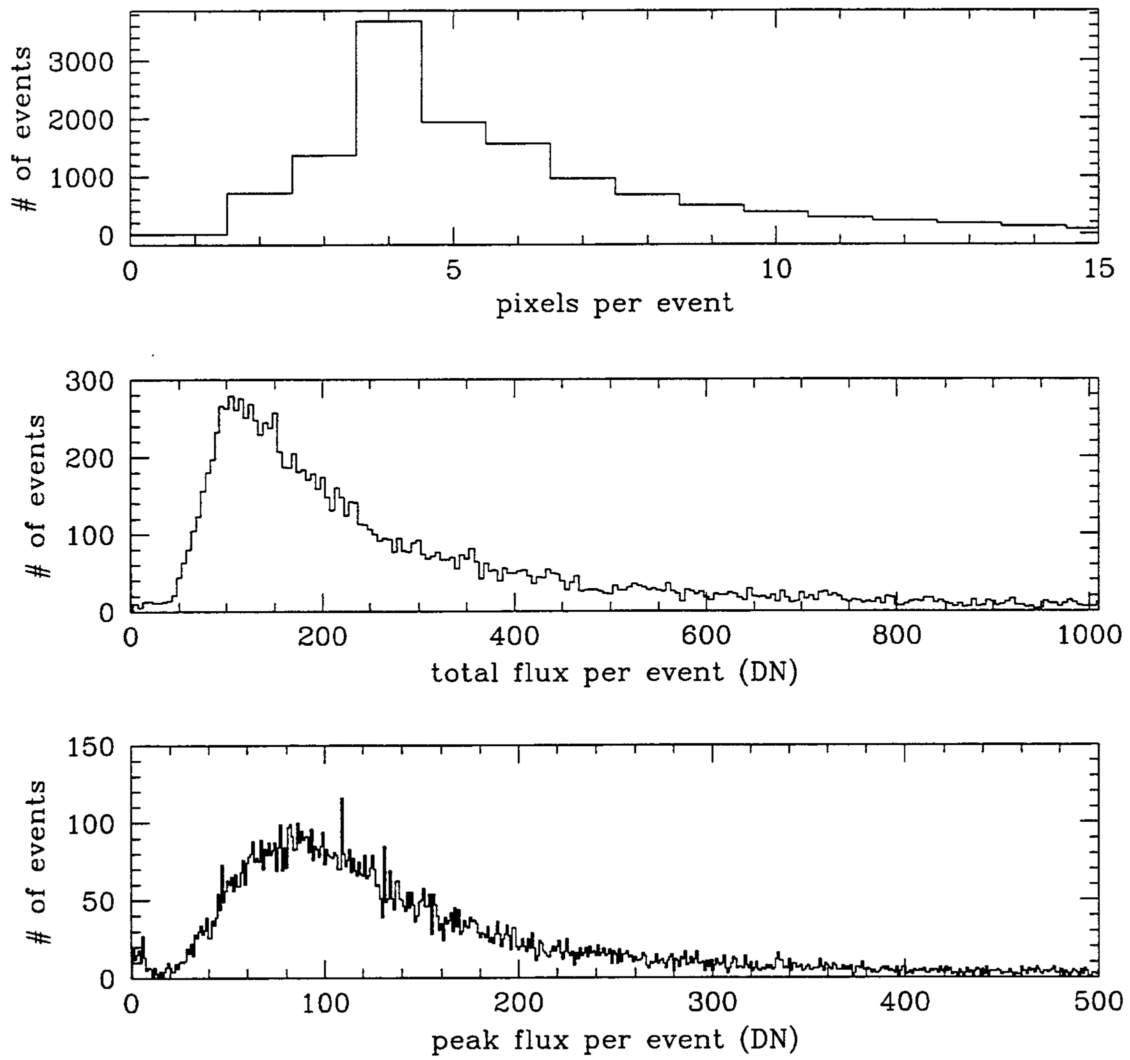

Fig. 2.3.— Histogram of cosmic ray events as a function of peak flux, total flux, and affected pixels. Clearly, the distribution of cosmic rays drops off well before cosmic rays would become difficult to detect: there are no cosmic ray events with flux levels near the mean of the data (roughly 0.3 DN for the F3000W exposures and 12 DN for the F555W and F814W), and cosmic ray events involve at least 2 pixels.

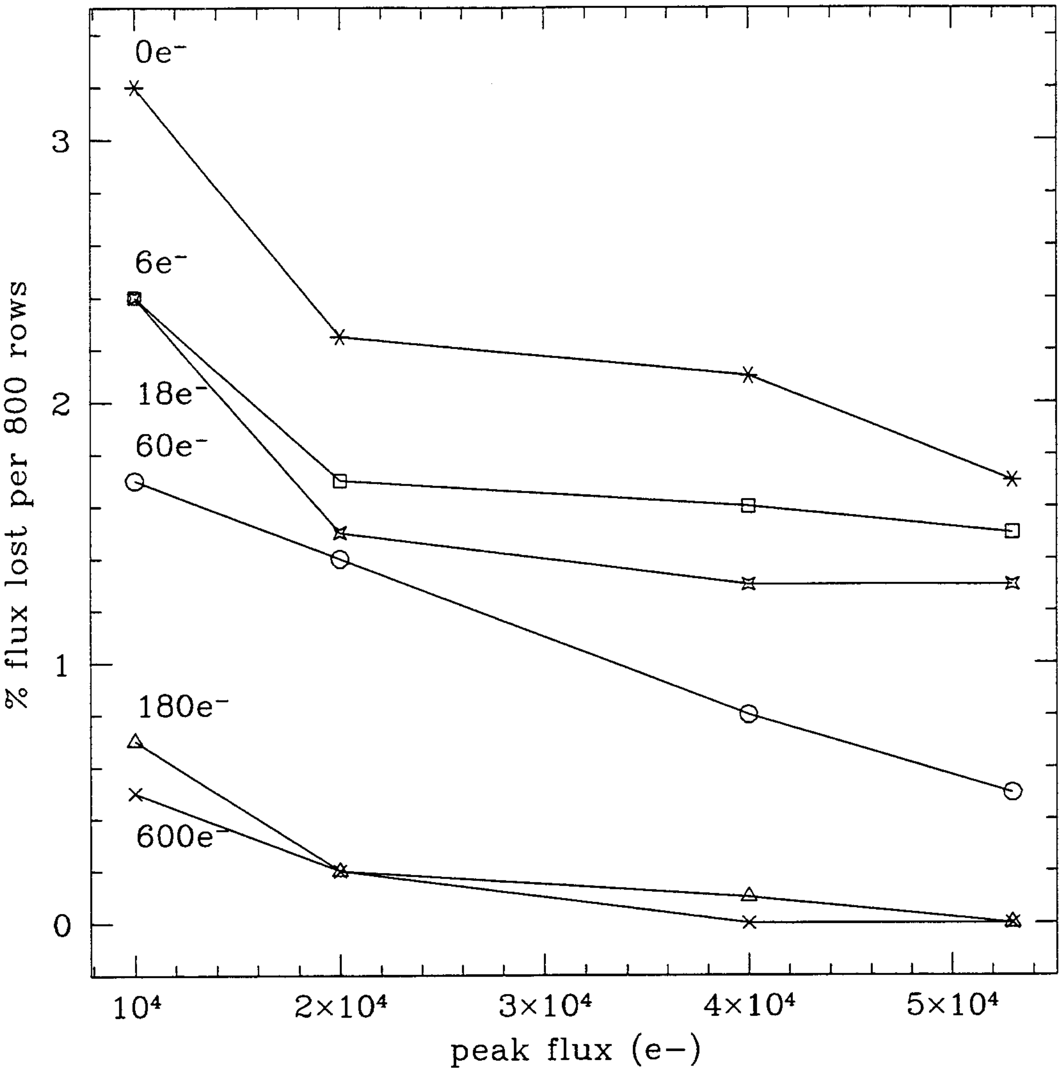

Fig. 2.4.— Percentage flux lost from point sources due to CTE (electron trapping) as a function of the peak flux of the point source and the mean background level. The lines connect measurements in images with the same mean background level. This plot indicates the phenomenon which is commonly described by WFPC2 documentation, namely that the percentage flux lost from a point sources is a function of the background level in the image. The statistical error in detected flux decreases with the peak flux. With the exception of the measurements for a 60 e^- background level, the peak flux of the star has a relatively minor effect on the flux lost. The strongest variation is due to differences in background level. These data were obtained from J. Trauger (personal communication).

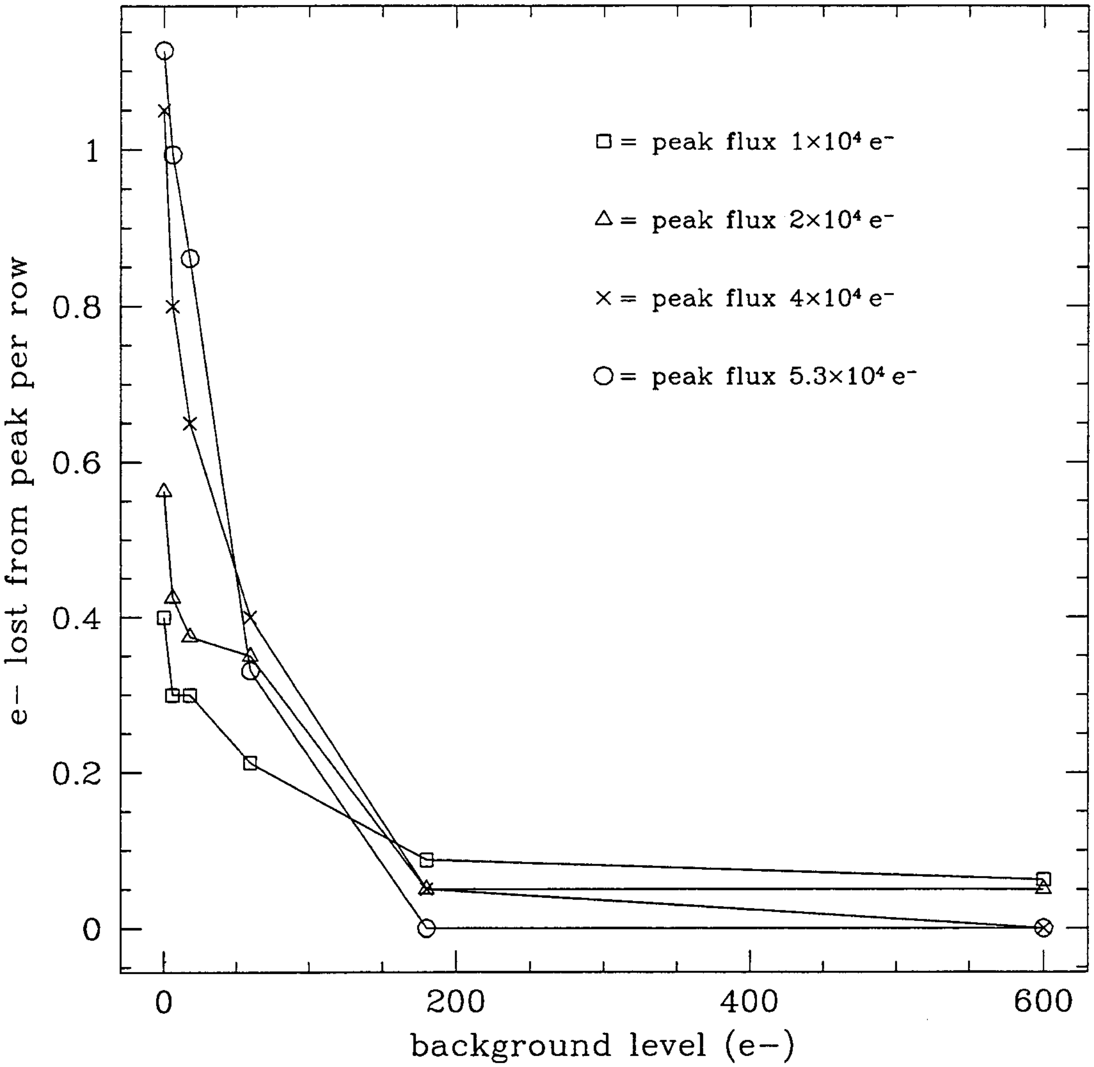

Fig. 2.5.— The number of electrons trapped per pixel as a function of background level as measured from the point source photometry tests shown in Figure 2.4. The lines connect data for point sources with the same peak flux. Like Figure 2.4, this plot clearly indicates that the percentage flux lost from a point sources is a function of the background level in the image. The variation in the number of electrons lost from point sources when the background level is 600 e^-/pixel is indicative of the measurement errors.

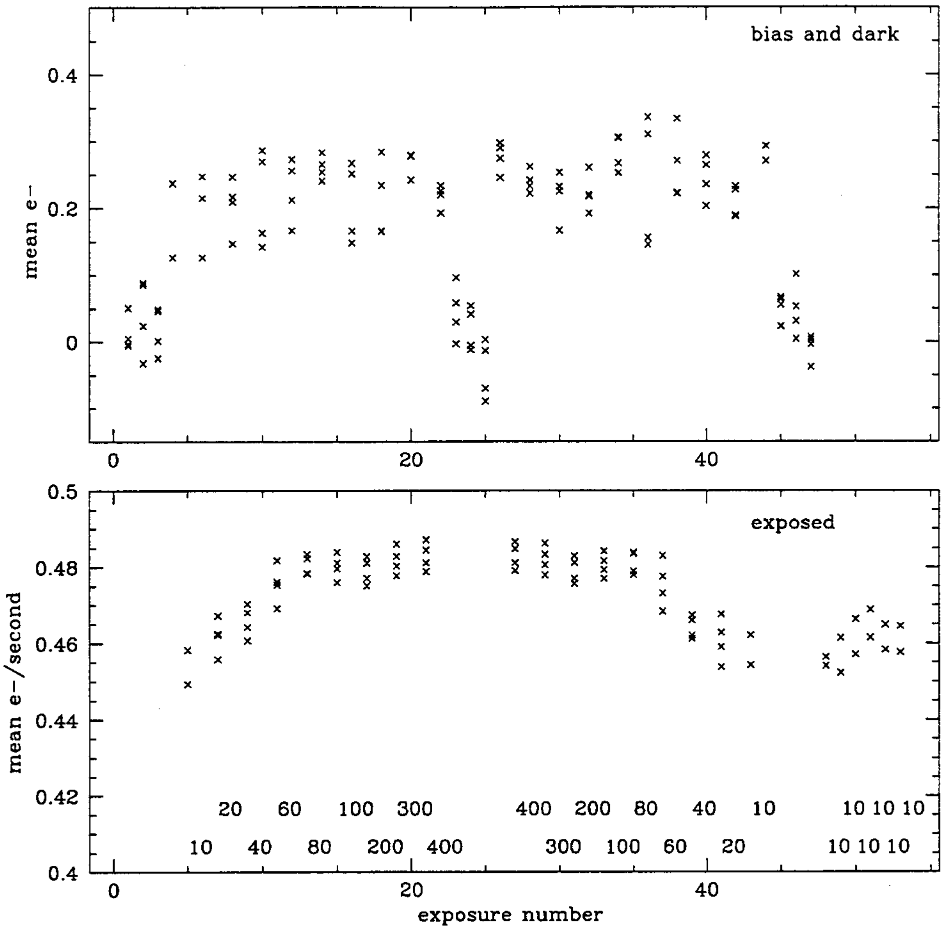

Fig. 2.6.— The results of four separate tests to measure the linearity of the WFPC2 chips at low surface brightness are plotted. The X-axis of both plots indicates the exposure number of the image. See Table 2.2 for a complete listing of the sequence of images taken during each run. The upper plot shows mean levels in bias and dark images. Bias frames monitor the stability of the CCD during the run. The variation in the bias level (frames 1-3, 23-25, and 45-47) indicates the stability of the CCD and signal chain in addition to the accuracy with which the mean level in a frame might be measured. These effects are indistinguishable. The dark frames should show increasing mean if trapped electrons are released from the traps on time scales of 1200 seconds. Only a slight trend, albeit consistent, is seen. The lower plot shows the count rate in e^-/s/pixel for the exposed images. The results reveal a slight non-linearity in the number of electrons read out for a uniform surface brightness sources between 10 e^-/pixel and 200 e^-/pixel. The results are obviously extremely repeatable both during and between runs, indicating the lamp was not responsible for the variations seen. These data were obtained with the help of John Trauger.

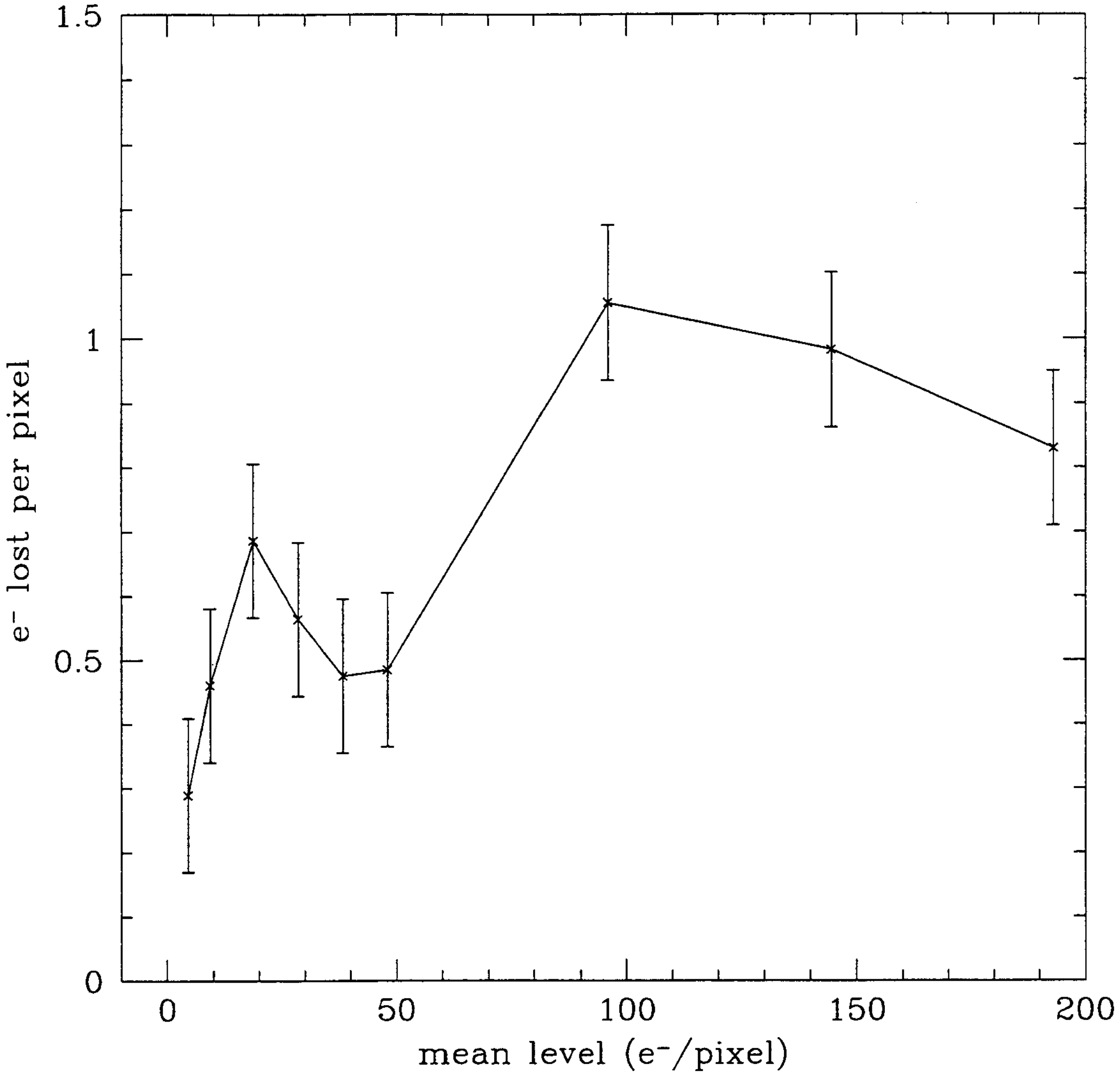

Fig. 2.7.— The number of e$^-$/pixel which are lost as a function of mean background level. These numbers are obtained by assuming the true rate (e$^-$/s/pixel) is such that the loss at 200 e$^-$/pixel is the loss seen per pixel for point sources on a 200e$^-$/pixel background. This plot shows that, based on that assumption, the number of electrons trapped per pixel as a function of background level scales the same way for a uniform source as for point sources. The losses being measured here range from 1 e$^-$ per 5 pixels to 1 e$^-$ per pixel. The line drawn through the points is merely to guide the eye; the number of electrons trapped is a quantized value, and trap accessibility is unlikely to be a smooth function of the mean e^- level. The increase in the number of trapped electrons between mean background levels of 50 and 100 e^-/pixel could occur gradually or suddenly over that range. Note that the mean is reliably determined to roughly 1 e$^-$ per 7 pixels in this test.

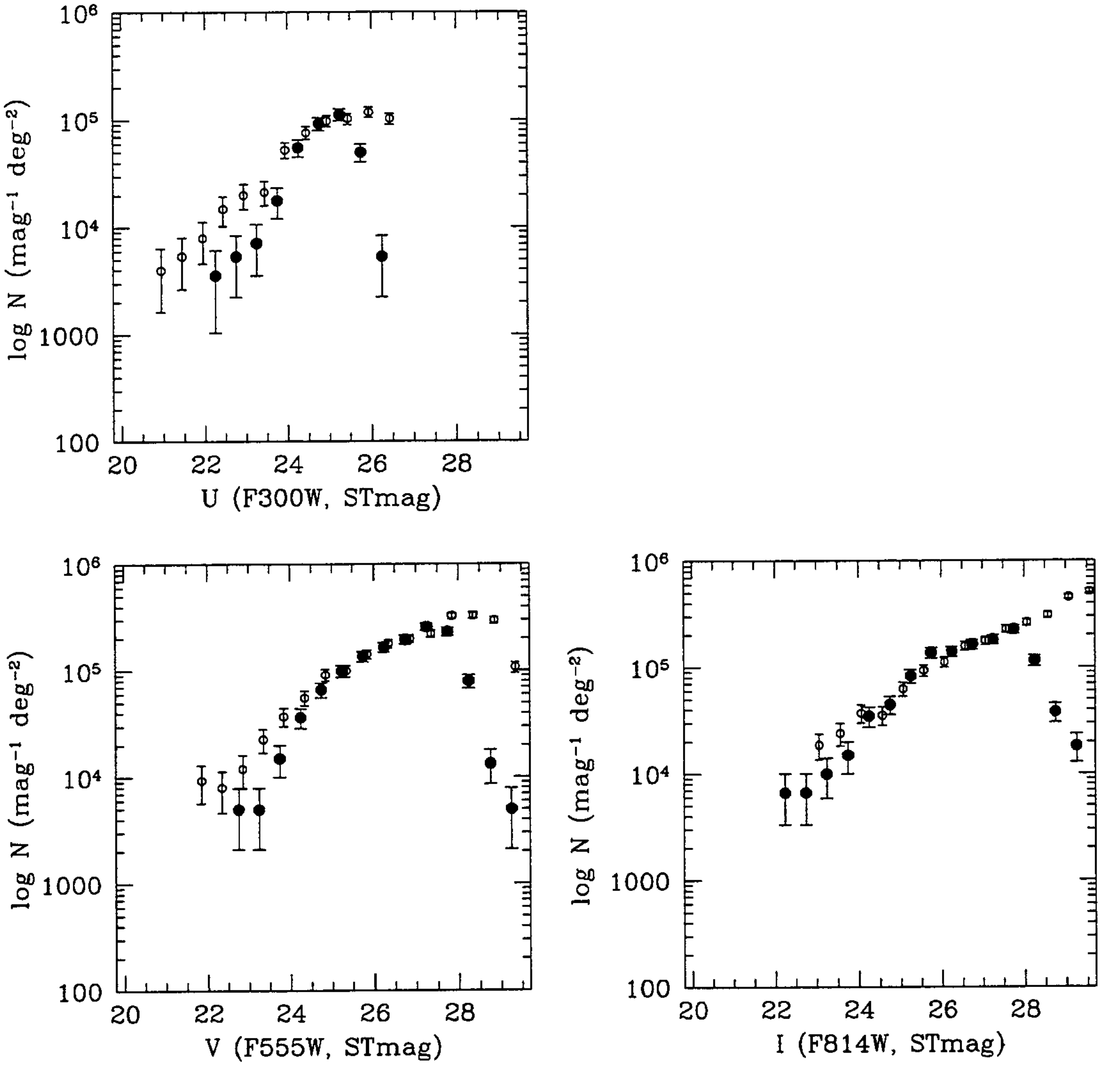

Fig. 2.8.— Differential galaxy counts in the EBL field compared with the HDF. The open circles show the HDF counts; the filled circles show the counts from our own data. The galaxy populations in the two data sets are clearly very similar both in density and in color. It is clear from the turn–over in our counts that our completeness limit in V_{555} is roughly 1.5 magnitudes below that of the HDF, which is expected from the factor of 15 difference in exposure time between the two data sets. The turn–over in the other bands is likewise in keeping with the incompleteness expected relative to the HDF counts due to differences in exposure time.

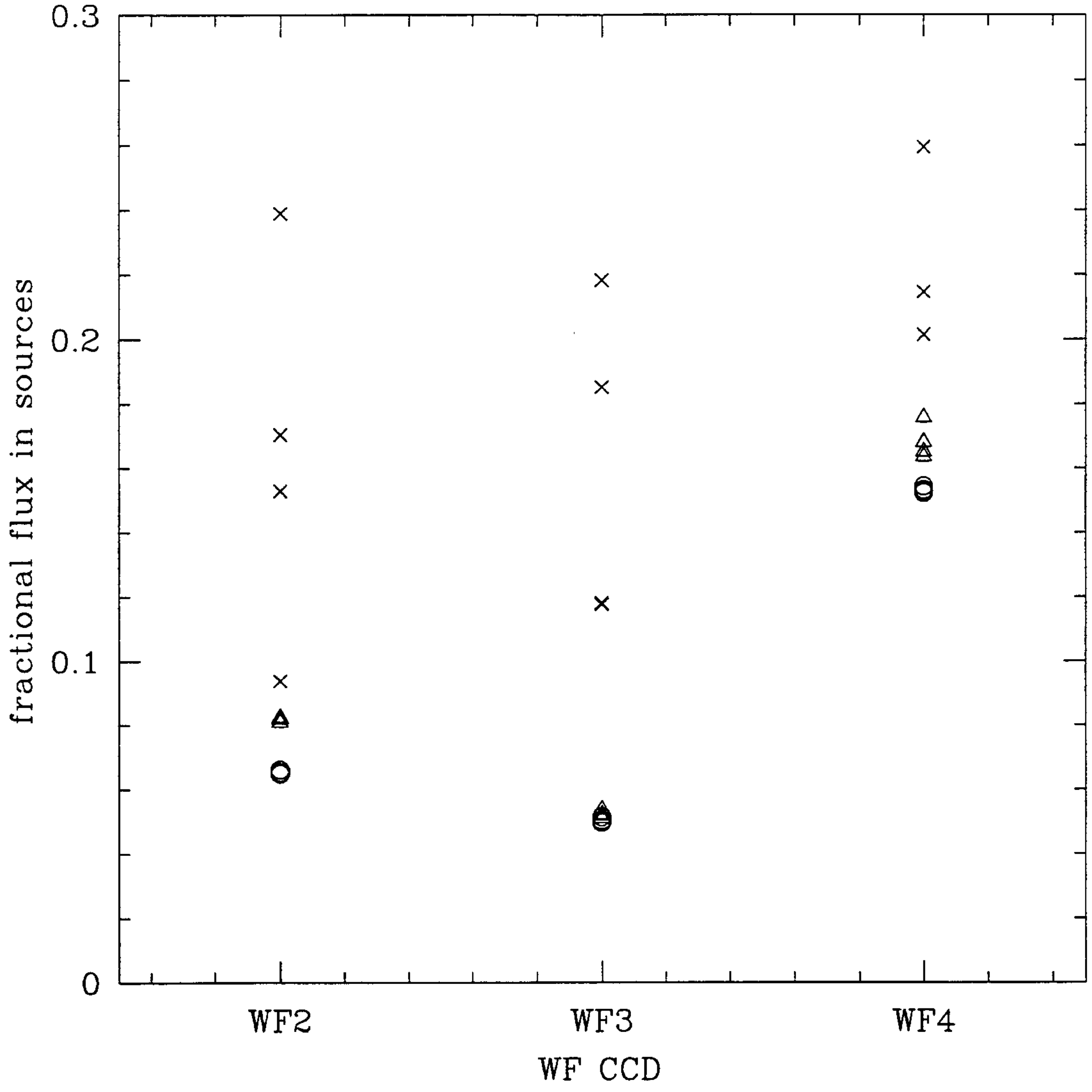

Fig. 2.9.— The fractional flux in the 3 WF chips contributed by all objects (galaxies, save 4 stars) with V_{555} brighter than 25 STmag. The circles show the fractional flux in objects in the F555W data; triangles show F814W; X's show F300W. One point is plotted for each of the four November and December 1800 sec exposures. The greater scatter in the F300W flux is a result of both *rms* error in dark background removal, and real variation in the number of bright objects between the chips. Because the ZL in the F300W is so much fainter than in the other two band, it does not dominate the total flux and the Poisson variation in the number of bright objects is more apparent from chip to chip.

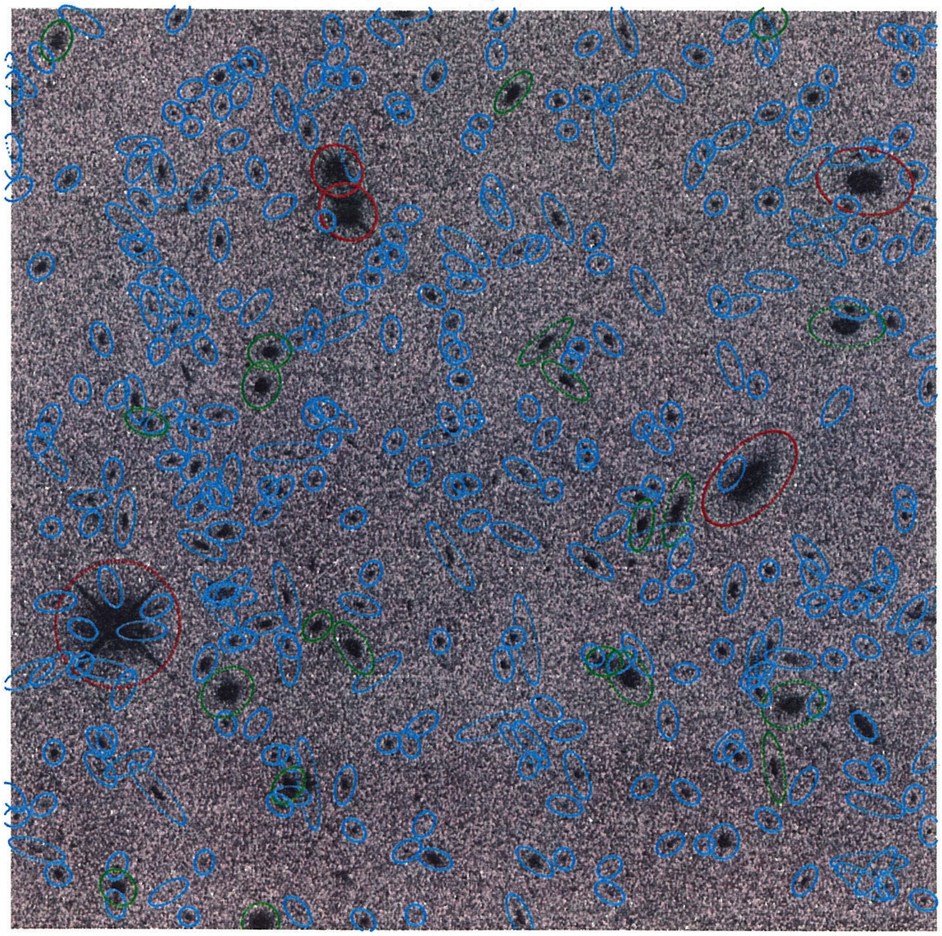

Fig. 2.10.— Combined F555W images, WF2 chip. The ellipses indicate the regions around each object which would be masked out in order to exclude that object from the measurement of the diffuse background. Mask–regions for objects with $V_{555} \leq 23$ mag are shown in red, $23 < V_{555} \leq 25$ are shown in green, and $25 < V_{555} \leq 28$ are shown in

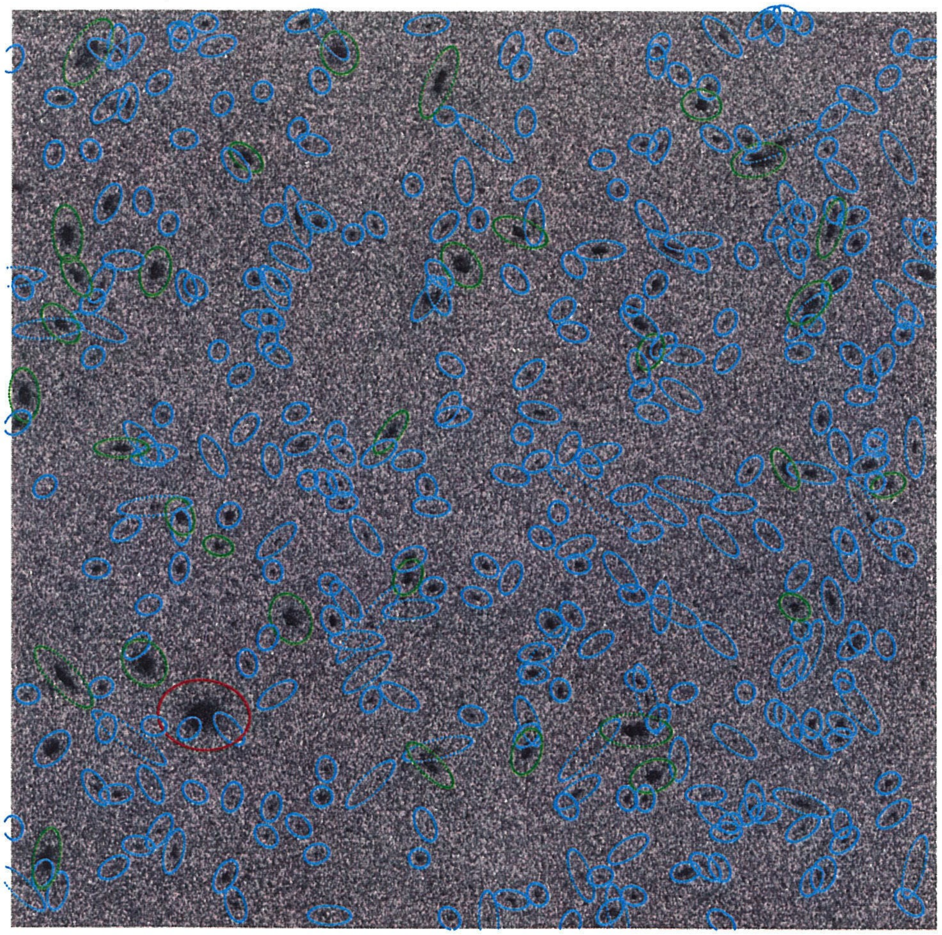

Fig. 2.11.— Combined F555W images, WF3 chip. Ellipses are as described in the caption of Figure

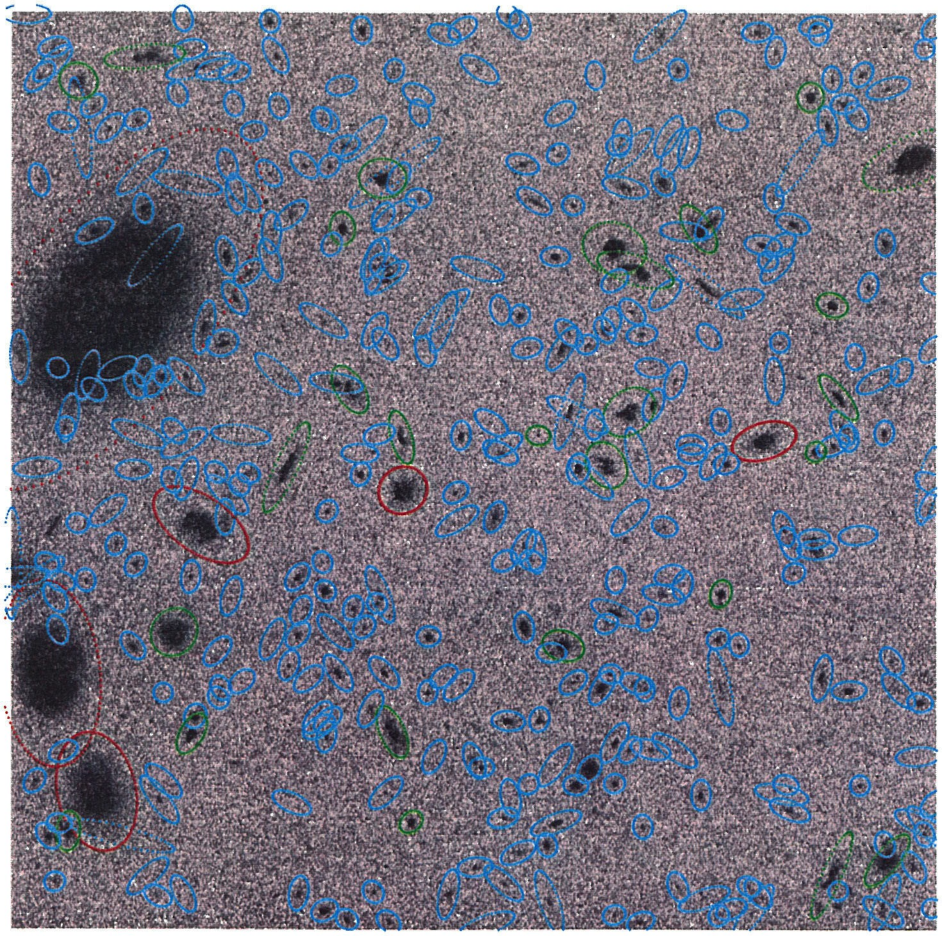

Fig. 2.12.— Combined F555W images, WF4 chip. Ellipses are as described in the caption of Figure

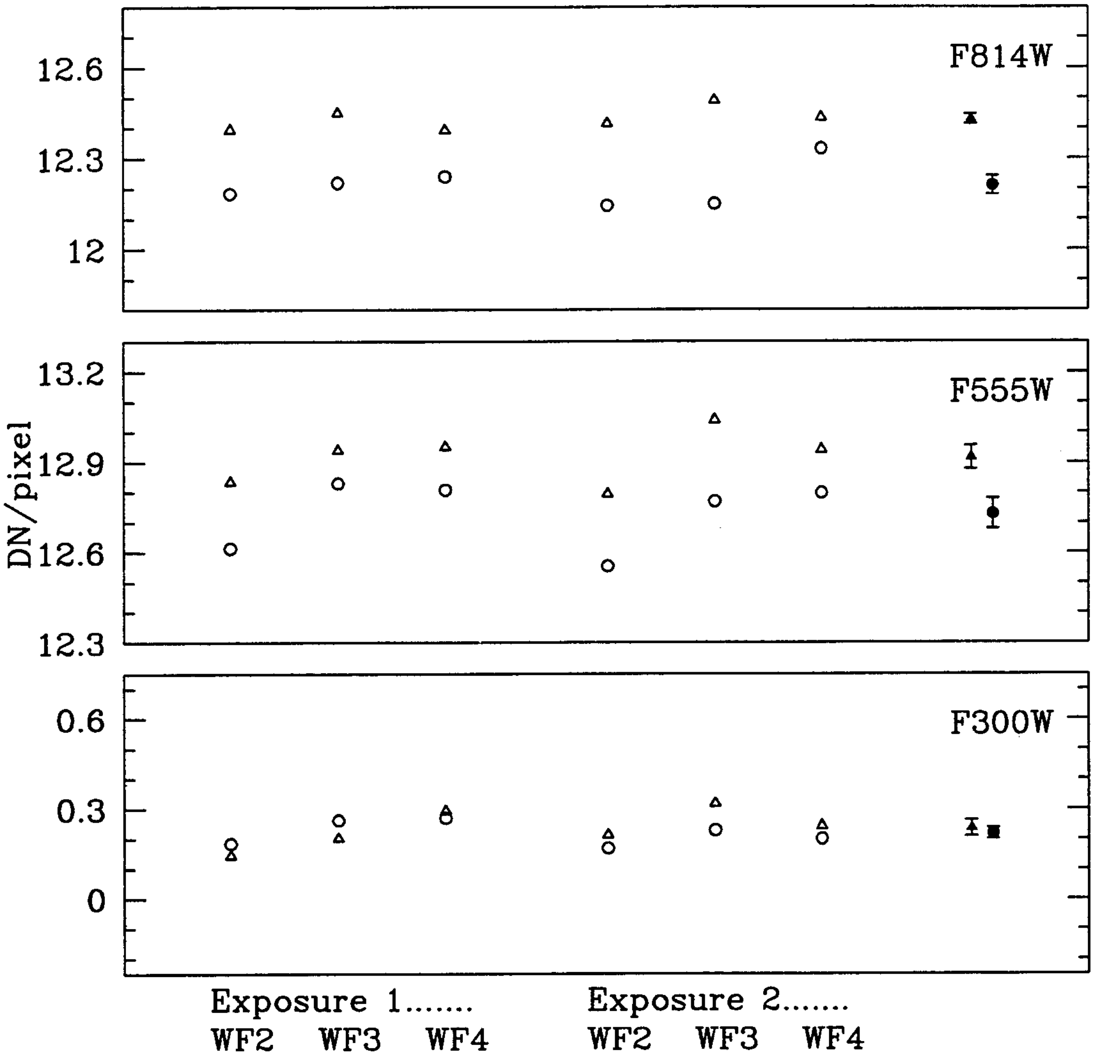

Fig. 2.13.— Total background detected in each of the 3 WF chips (DN/pixel) from each of 2 exposures (1800 seconds long) taken in the November and December visits. Objects brighter than $V_{555} = 23\,\mathrm{mag}$ are masked out for this calculation. The November data are marked by open triangles, the December data by open circles. The average of the total background flux found from each month's results is shown with filled symbols. The error bar on the averaged result indicates the *rms* scatter in the 6 measurements. Note that the 1 σ errors in the mean level of the diffuse background for each month is very well predicted by the sum of the *rms* errors listed in Table 2.7. Variation between the November and December results is consistent with the expected temporal change in the ZL contribution between the two months. For this comparison, the mean levels for each chip have been adjusted by the ratio of the gain for each chip to that for WF3 (see H95b).

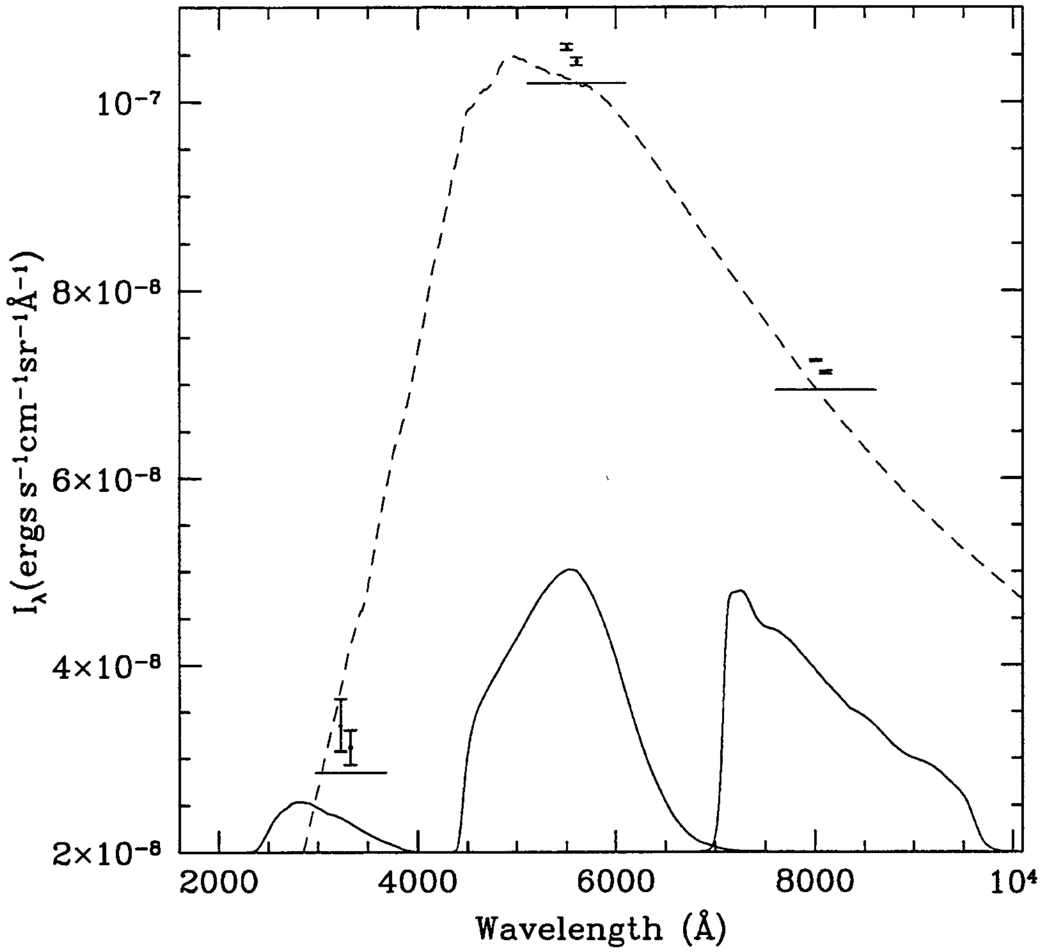

Fig. 2.14.— The total background flux detected in I_λ from the WFPC2 Nov. and Dec. data. As discussed in the text, the total background is the average surface brightness of the images after galaxies brighter than $V_{555} = 23$ ST mag are removed, $I_{\rm Tot}(V > 23)$. The dashed line shows the solar spectrum scaled to the level we detect for the ZL (see §4.5). It is clear even from this plot that more than 95% of the flux redward of 4000Å is from ZL. The results from the November data are plotted centered on the effective wavelength of each passband. The marks indicating the results from the December data are plotted slightly offset toward longer wavelengths for clarity. The error bars indicate the *rms* errors indicated in Table 2.7. The solid curves show the shapes and relative throughputs of the filters used in this work. From blue to red they are the F300W, F555W, and F814W. These results are combined with our measurement of the ZL and DGL to obtain the EBL in Chapter 6.

Chapter 3 *HST*/FOS Measurement of the Total Background

The Faint Object Spectrograph (FOS) on *HST* was used in parallel mode during all of the WFPC2 observations, and provides data which turn out to be crucial to the measurement of the EBL. As discussed below, the FOS data are not as valuable for absolute surface photometry of the total background as the WFPC2 data; however, the spectral resolution of the FOS data makes it extremely useful for separating the zodiacal (ZL) from the extragalactic signal. The accuracy of the FOS surface photometry, the total background flux, and, most importantly, the color of the total background as measured by FOS are discussed in this Chapter.

3.1 Observations and Data Reduction

Observations with the FOS (red side) were scheduled in parallel mode during each of the three visits with the WFPC2. The original intent of these observations was to provide high signal–to–noise, high resolution spectra of the total background flux contemporaneously with the WFPC2 images and without airglow. From such data, we could then measure the absolute surface brightness of the ZL as a function of wavelength in the range 4000–7000Å using the method outlined in §1.2.2 and §4.3. The absence of airglow lines and simultaneity with all three of the WFPC2 visits would be significant advantages over the ground–based data from Las Campanas Observatory (LCO): airglow lines preclude measuring the absolute flux of the ZL with LCO data beyond the range 4100–5100Å, and LCO time only overlapped with the November *HST* observations.

Unfortunately, early versions of the FOS exposure time calculator had a bug which set a invisible lower limit to the input flux at 21 mag/arcsec^2. Calculated count rates for fainter input fluxes were thus appropriate to the lowest allowed magnitude, which is a factor of 6 brighter than the ZL. As a result, the original configuration (FOS/RD, G570H dispersion element, 1.0–PAIR aperture) was intended to produce a 4.5Å spectrum, 4500–6800Å, with a moderate signal–to–noise ratio. Unfortunately, this configuration produced count rates comparable to the dark rate (~ 0.01 counts/sec/diode). High resolution spectra of the ZL are clearly not attainable with the FOS. Accordingly, we changed our strategy for the second two *HST* visits to obtain very low resolution spectra, with good signal to noise. For obvious reasons, we limit our discussion to the data obtained during the second and third visits, in November and December 1995, respectively. Six spectra were obtained during each visit, one per orbit. The integrations were all 1300 sec long limited by the requirement that the exposures execute entirely within the 1800 second WFPC2 exposures in order to avoid conflicts in writing the data to storage.

The FOS configuration during the November and December visits included the G650L dispersion element and the A–1 science aperture, which has the largest solid angle of the available apertures ($3.66 \times 3.71\,\mathrm{arcsec}^2$). The G650L produces 25Å per diode over the range 3800–7000Å, however a uniform surface brightness source viewed through the A–1 aperture will have approximately 12 diodes (300Å) per resolution element. Narrow–band imaging as such is not useful for determining the mean ZL flux by the strength of its spectral features. These data are, however, useful as a second, independent measurement of the surface brightness of the total background and do provide better wavelength resolution than wide–band photometry from the WFPC2. In the G650L/A–1 configuration, the signal–to–noise ratio of the resulting spectra is almost 20 per resolution element. With a statistical error of 2% per 1000Å band, the FOS provides good narrow–band photometry in this configuration.

3.1.1 Instrument Overview and Pipeline Calibration

The FOS is comprised of two Digicon detectors with independent optical paths. Our data were obtained with the red side of the FOS, which is sensitive to light from

1620–8500Å. Light entering the FOS passes through the aperture wheel and a filter grating wheel before it is focused onto a two dimensional, transmissive photocathode. Each dispersion element produces a focused spectrum on a different portion of the photocathode, from which photoelectrons are magnetically directed to a linear array of 512 diodes. The available dispersion elements each illuminate a subset of the diode array. In the case of the G650L, only 144 diodes are illuminated. The diodes are read out continuously and have no read–noise. The diode array is 1.29 arcsec tall in the spatial direction, y, and each diode is 0.30 arcsec wide in the dispersion direction, x. With the A–1 aperture (roughly $3.6 \times 3.6\,\mathrm{arcsec}^2$), the diode height sets the limit on the solid angle in the spatial direction.

It is difficult to improve on the excellent results of the data reduction pipeline procedures, or even to contribute significantly to the data set from which calibration is obtained. The pipeline calibration procedure for FOS observations regularly produce photometric repeatability of 1–2% for point sources. The wavelength calibration has relative errors of only 0.01–0.08 diodes, and zero–point errors as small as 0.1 ± 0.1 diodes on the red side. Nonetheless, because of the absolute calibration required for this measurement and because the target object is a uniform surface brightness source, some improvements on the pipeline calibration were required. Specifically, we have performed a zero–level correction (subtraction of dark backgrounds) which we derived independently from the pipeline procedures. Also, we have recalculated the aperture correction needed for the calibration of a uniform brightness source.

The majority of the standard pipeline calibration which is applicable to these data was used. In order, the pipeline procedures employed were the conversion from counts to count–rate (CNT_CORR), flat fielding (FLT_CORR), wavelength calibration (WAV_CORR), and flux calibration (AIS_CORR, APR_CORR, and TIM_CORR). The flux calibration for the A–1 is the most accurate of that for any of the apertures and is used to define the throughput relative to which other aperture throughputs are defined. Consequently, the relative correction (APR_CORR) for the A–1 aperture is unity. Also, the G650L has no observed time variation, so that the corrective factor applied by the TIM_CORR procedure is also unity. Pipeline flux calibration for A–1 aperture observations is therefore unaffected by the last two corrections. A complete description of these steps can be found in the *HST* Data Handbook V3.0.

The pipeline steps which were not applied are generally self–explanatory. The sky subtraction task (SKY_CORR) is clearly not needed for observation of the background itself; the paired pulse correction (PPC_CORR) compensates for saturation in the detector electronics and is needed for count rates higher than 10 counts per second, well above those seen in our observations; the geomagnetic motion corrections (OFF_CORR) are used only for data taken before April 1993; and finally, the background subtraction routines (BAC_CORR, GMF_CORR, and SCT_CORR) which remove dark backgrounds and scattered light were replaced by our own procedures, as described below.

3.1.2 Dark Subtraction

The dark background for this instrument is not thermal dark current in the typical sense, but is rather the result of Cherenkov radiation from cosmic rays striking the photocathode. As is clearly evident from both the FOS and the WFPC2 data, the cosmic ray flux and the backgrounds which result from it will vary rapidly with time and orbital position. The pipeline calibration does not adequately deal with the fluctuating absolute level of this background source. The relative intensity of the dark signal from diode–to–diode is a function of the instrument geometry and is quite stable. In the case of the G650L, only 144 diodes are illuminated by the spectrum, conveniently leaving a large fraction of the diodes unexposed and ideal for instantaneous measurement of the effective dark rate during any given exposure. We used dark spectra from the HDF parallel observations (Program 6342, Freedman; Program 6339, Larry Petro) to produce a template of the dark rate per diode.

The HDF dark was then scaled to the level indicated by the unexposed region of each of our FOS observations and subtracted. The only structure visible in the HDF dark is that resulting from the diodes which have been turned off due to poor performance (dead diodes). The appropriate dark level to which the HDF dark was scaled was determined from the average flux in pixels 900–1100. A scaled version of the averaged, HDF dark as appropriate for typical 1300 second exposure from our program is shown in Figure 3.1. Approximately 25 dark frames went into this averaged dark, resulting in Poisson noise of 0.3 counts per pixel, or 0.15 counts per diode.[1] After dark subtraction the mean level in the unexposed regions of the array showed no residual features and was consistent with zero. The statistical variation between pixels in the unexposed region of a 1300sec science exposure is the shot noise on 5 counts, or $\sim$ 2.2 counts. The statistical error in the dark signal subtraction is a negligible contributor to the final error in the surface brightness measurement, as the dark rate is more than 6 times smaller than the sky signal.

3.2 Flux Calibration

The pipeline calibration procedure for FOS observations regularly produces internal photometric repeatability of 1–2% for point sources. Nevertheless, there are a number of factors which are known to diminish this accuracy even for point sources. These factors include granularities in the transmission efficiency of the photocathode; the accuracy with which electrons are directed at the diode array from the photocathode; the finite size of the diodes relative to the energy distribution of a point source. Finally, we discuss the issues peculiar to surface brightness calibration: the aperture correction and solid angle of the instrument. The fiducial spectrophotometric system is the same as is used for all of the *HST* instruments and was discussed in §2.2.1.

3.2.1 Point Source Calibration

While pipeline calibration for FOS observations regularly produce internal photometric repeatability of 1–2% for point sources, the situations in which such excellent photometry is obtained are tightly constrained. The situations which produce less–

---

[1] FOS spectra have four pixels per diode due to sub–stepping in the x–direction. This provides spectra with continuous wavelength coverage even though some of the 512 diodes in the array have been turned off due to malfunction.

accurate photometry are instructive for our surface brightness measurement.

The transmission efficiency of the photocathode is not uniform across the two dimensional extent of the detector. This granularity affects the flat-fielding, and thus the calibration of the instrument. Flat-fields are made from observations of well-centered targets, and therefore sample well specified regions of the photocathode. Spatial displacements as small as 0.2 arcsec can produce sharp features of up to 20% variation in count rates over small (10 diode) regions of the spectrum (Keyes, Calibrating *HST*: Post Servicing Mission, FOS Post-Costar Flats, page 41). In this program, we have the advantage that an aperture-filling source may average out such variations, as the spatial extent of the photocathode which is sampled by the spectrum will be much larger than for a point source. However, flat-fielding errors are likely to account for some of the non-solar features in our spectra (see Figure 3.5). We can estimate the error due to such sharp calibration features by considering the factor by which such a feature will be diluted for an aperture-filling source as opposed to a point source. The increase in the area on the photocathode is roughly a factor of nine — a factor of 3 in the spatial direction and a factor of 3 greater than the 10-diode extent of sharp features. We estimate that random errors should then be roughly less than 2.5%. This is roughly the size of the non-solar spectral "features" which can be seen in our FOS data (see Figure 3.6).

Another concern for point source calibration is the accuracy with which the photoelectrons are directed at the diode array. It has been seen that slight errors in centering can cause significant variation in detected flux. For example, a point source must be centered to with an accuracy of 0.08 arcsec in the A-1 aperture in order to guarantee 5% accuracy in the resulting spectrophotometry. For a aperture filling source, the accuracy of this deflection is less important because the aperture is larger than the diode array in the spatial (y) direction, and the source will not "miss" the diodes. There is, however, one very important implication of this effect for our purposes: the observed, 5% loss in the flux detected for a badly centered source indicates that the radius which encircles 95% of the flux from a point source is not significantly smaller than the diode height. This is not surprising given that the encircled energy at ~1 arcsec for the WFPC2 is also around 95%, however it clearly indicates that the aperture correction should take into account both the light lost from a point source in the aperture plane, and the light lost in the diode plane. The determination of the aperture correction is discussed in the next section.

3.2.2 Aperture Correction

The flux calibration of the FOS naturally compensates for light in the wings of the PSF which is not detected during observations of a point source because the standard stars are also point sources with the same observed PSF. Light can be lost in the wings of the PSF at the aperture plane if some percentage of the PSF falls outside the physical aperture, or in the diode plane if the PSF extends beyond the diode array in the spatial direction (in the spectral direct, the spectrum is smoothed by the shape of the PSF). For observations of a uniform background, however, no light is lost. A point source calibration will therefore underestimate the true throughput and the estimated surface brightness will be too high. Consequently, an aperture correction needs to be applied to correct for this over–compensation when the source has uniform flux over the extent of the aperture. The value of the aperture correction is simply the fractional flux from a point source which is detected in a standard star observation.

Flux calibration of a uniform source begins with the pipeline calibration for point sources. The integrated flux from a uniform background is a function of the pipeline calibrated spectrum in ergs $\mathrm{s}^{-1}\mathrm{cm}^{-2}\text{Å}^{-1}$, $F(\lambda)$, the solid angle of the detector in steradians, Ω, the percentage flux from a point source which gets through the A–1 science aperture in the focal plane of the FOS, $T(\mathrm{A}\text{–}1)$, and the percentage of flux which makes it to the diodes once through the science aperture, D. The total surface brightness of a diffuse source can be expressed as a function of these terms as

$$I(\lambda) = \frac{F(\lambda)\, T(\mathrm{A}-1)\, D}{\Omega}. \tag{3.1}$$

Modeled PSF

The total aperture dilution factor $T(\mathrm{ap}) \times D$ which is quoted in all versions of the FOS Instrument Handbook is the result of modeling based on the OTA with post–Costar configuration; it is not a measurement. The modeling software, called TIM, is based on polynomial representations of the shape of the wavefront produced by the OTA. No official Instrument Science Report exists to document the throughput of the FOS apertures, however George Hartig produced an unofficial estimate of 97% for the monochromatic transmission with the A–1, post-COSTAR configuration at 6500Å. The Data Handbook V3.0 contains the value 95%. TIM models were independently produced by several other members of the FOS science instrument team (Don Linder, Ralph Bohlin and Ian Evans) and agree to within $\sim 3\%$. These variations in TIM results are likely due to variations in the choice of maximum aperture radius.

Measurement of the PSF

The PSF can be measured directly from data taken in an observing mode called ACQ/IMAGE. No dispersing element is used in this mode; instead, the mode produces two–dimensional images by stepping the deflection of electrons from photocathode to diodes through a range in y–positions, effectively adding a second dimension to the one–dimensional diode array. ACQ/IMAGE observations of point sources are therefore ideal for determining the energy which falls within the diodes array during point source observations in spectroscopic mode. A calibration program (Proposal 5262, Koratkar et al.) took the data necessary to determine the PSF in the spatial and spectral directions; however, a measurement of the PSF has not yet been made available by STScI. [2] Those data are now available in the archive. In order to be more confident of this crucial factor in the flux calibration of our data, we have used the data from Proposal 5626 to recalculate the PSF ourselves. The stepping pattern used in the observations was kindly provided to us by E. Smith at STScI.

We have re-reduced the 5626 data using the usual pipeline, ACQ/IMAGE reduc-

---

[2] The report which presented the results of that Proposal 5626 (FOS/ISR-148) was withdrawn due to an error in the data reduction. A new report has not yet been released.

tion to produce the image shown in Figure 3.2. The image shown in that figure maps the distribution in the detector plane of whatever light passed through the aperture. If light is blocked out in the aperture plane, then 100% of the flux in this image would still only represent some fraction of the total flux from the source. It is important, therefore, to estimate what fraction of light might have been lost in the aperture plane. To this end, consider the encircled energy curve for the light within a region defined by the physical extent of the A–1 science aperture ($3.63 \times 3.71\,\mathrm{arcsec}^2$). This region is illustrated in Figure 3.2. The shape of the PSF within this region will be, if anything, less centrally concentrated than it was before passing through the spectroscope optics and is thus a worst case scenario for the PSF in the aperture plane.

In Figure 3.3 we have plotted the growth curve of the PSF as seen in the diode plane. Only the area within the $3.86 \times 3.86\,\mathrm{arcsec}^2$ extent of the aperture shows the true PSF. Outside of that region, the PSF is artificially flat due to (intentional) obscuration of the field of view by the A–1 aperture. To estimate the flux that came through the A–1 aperture, we fit the outer PSF and extrapolate to recover the growth curve which was obscured in the aperture plane. We deduce from the curve plotted in Figure 3.3 that roughly 98% of the total flux in a point source is contained within the extent of the A–1 aperture in the aperture plane, or $T(\text{A–1})=0.98$.

Once through the aperture, the smooth PSF outside of the physical extent of the A–1 aperture demonstrates that some defocusing and scattering does occur in the spectrograph. However, the PSF is very symmetric in the wings and the flux level at the edges of the image is down by more than eight orders of magnitude relative to the peak. It is therefore unlikely that any significant portion of the PSF in the diode plane is not mapped by this image. Correspondingly, we can define an aperture within this image which can reasonably be assumed to enclose 100% of the light which falls in the diode plane. This 100%-flux aperture is marked in Figure 3.2 and encompasses $8.0 \times 8.0\,\mathrm{arcsec}^2$ in the diode plane.

In calculating an exact percentage flux contained within the diode array, it is important to understand the resolution of ACQ/IMAGE data. In imaging mode, sub–stepping in the $x-$ and y–directions provides measurements of the flux every

0.076 arcsec in x and every 0.081 arcsec in y. The resolution of the image, however, is still set by the x and y size of the individual diodes. The diodes essentially produce an image which is boxcar smoothed by the diode width in x and the diode height in y (4 pixels by 16 pixels), making it impossible to accurately determine the fraction of light within the y–extent of the diode array, causing the PSF to appear elongated on small scales. Aside from the diode–shaped elongation on small scales, the only visible asymmetry in the PSF appears as a nearly vertically bright bar which is caused by the secondary mirror supports. The otherwise symmetric appearance of the PSF at radii greater than the size of the diodes makes it reasonable to assume that PSF is radially symmetric on all scales. Assuming that the PSF is symmetric, we can measure the percentage of the light within 1.29 arcsec in the x–direction, where we are not hampered by smoothing on the scale of interest. We argue that this measurement is representative of a well sampled growth curve in the y–direction as well.

We can test this argument by boxcar smoothing the image in the x–space to match the y–space sampling, and examining the resulting flux as a function of radius. The result of this test is shown in Figure 3.4, in which we plot the distribution of light in the x–direction before and after boxcar smoothing, and the flux distribution in the y–direction. While the flux within 1.29 arcsec is easily calculated from the high-resolution PSF, it is clearly impossible to obtain from the low-resolution PSF. In addition, the flux distribution in y does indeed seem well represented by the boxcar smoothed distribution in x. The flux contained within 1.29 arcsec in the x–direction is 96.5% of the total flux on the image. We take this value as accurate for the y–direction as well, in good agreement with the results of the TIM modeling for the flux falling within the diode array.

Finally, the TIM software show only a 0.3% change in the T(A–1) as a function of wavelength between 3500Å and 6300Å. Nonetheless, the white–light image of the PSF has a pivotal wavelength of 3500Å, while our spectra are centered around 5500Å. We therefore adjust our measurement by 0.2% to reflect the appropriate value for our central wavelength, giving us an aperture correction at 5500Å of

$$T(\mathrm{A}-1) \times D + 0.002 \approx 0.95. \tag{3.2}$$

The statistical error in this estimation is much less than 1%, however the systematic errors might be as large as 1% based on the discussion above.

3.2.3 Solid Angle of the A–1 Aperture

The effective solid angle of the detector is a function of both the diode height and the aperture width. The A–1 science aperture measures $3.63 \times 3.71\,\mathrm{arcsec}^2$, with 1% errors in both dimensions. The spatial height of the aperture is only relevant for determining the throughput at the aperture plane, as the diode height is a factor of 3 smaller and therefore limits the relevant y–dimension of the instrument. Each diode in the array is $0.301 \times 1.289\,\mathrm{arcsec}^2$, in width (spectral direction) and height (spatial direction) respectively. Again, the error in both dimensions is approximately 1%.[3] Thus, the solid angle of the detector is $3.63 \times 1.29\,\mathrm{arcsec}^2$, or $4.67\,\mathrm{arcsec}^2$ with a 1σ error of ±1.5%.

3.3 *HST*/FOS: Results

With roughly 80 counts/diode, and twelve diodes per resolution element, the statistical error per resolution element for one spectrum is roughly 4%. The average of the six spectra taken during the November 1995 visit and the average from the December 1995 visit are both shown in Figure 3.5, smoothed to the appropriate resolution of roughly 300Å. These statistical errors in the averaged spectra (roughly 1.5–2%) are indicated by the error bars at intervals of 300Å, the size of the resolution elements. The dark subtraction contributes an error of less than 0.5% per resolution element.

Systematic errors in the flux calibration will affect the absolute calibration of

---

[3] These dimension were measured originally in the lab (Instrument Science Report ISR CAL/FOS–019), and were scaled by the measured change in the FOS plate scale before and after COSTAR was installed (ISR CAL/FOS–123,141).

both the November and December data in the same way. Comparisons between the two data sets are subject only to statistical errors in the two results. Therefore, it is interesting to compare the two spectra, irrespective of their absolute accuracy. Observations of the zodiacal light (ZL) from the ground and from space indicate that the total intensity of the ZL reaches a minimum at $(\lambda - \lambda_\odot) = 130°$ (the position angle of our field at the time of the December visit) and should be several percent brighter at $(\lambda - \lambda_\odot) = 150°$. Indeed, we find that the total integrated background was brighter by roughly 2% in November than in December 1995.

The reddening of the zodiacal spectrum with respect to the solar spectrum is also known to be a function of the field position at the time of observation. Again, the trend we observe is the same as that seen by other experiments, most notably the Helios Space Probe observations (Leinert et al. 1981). Employing the definition of color with respect to the solar spectrum as defined in §1.2.2, we find $C(6500, 5500) = 1.04$ for the November visit, and a factor of 1.07 in the December data, as shown in Figure 3.6. We stress, however, that the FOS spectrum includes both the EBL and the ZL, and therefore we must be careful not to assume the color of the ZL has been measured explicitly from these observations. It is not possible to determine the color of the ZL separate from extragalactic components except by explicit measurement of the ZL spectral features. All published colors of the ZL rely on broad-band observations, and therefore always include possible EBL and DGL components. At orientations closer to the ecliptic plane, were the ZL is at least a factor of two brighter, the ZL is much less likely to be significantly affected by possible extragalactic contributions. The color of the ZL is discussed further in §6.2.1.

An error budget for the absolute flux calibration of these data is shown in Table 3.1. For comparison with the WFPC2 observations, we can integrate the FOS spectrum through the F555W bandpass. The error in that comparison includes both the error in flux calibration of the FOS results, and the error in conversion to WFPC2 band-passes which results from uncertainties in the WFPC2 calibration. The comparison with WFPC2 and LCO results are discussed in §6.

Table 3.1: FOS error budget for background flux (per resolution element)

	rms Error	Systematic Uncertainty
Poisson noise (§3.1)	2%	···
Dark subtraction (§3.1.2)	$< 0.25\%$	$< 0.5\%$
Fiducial standards (§2.2.1)	···	$\sim$1%
Point source flux cal. (§3.2.1)	···	$\lesssim$2.5%
Aperture correction (§3.2.2)	···	$\sim$1%
Solid angle (§3.2.3)	···	2.5%
Cumulative	(±2.0%)	[± 4-7%]

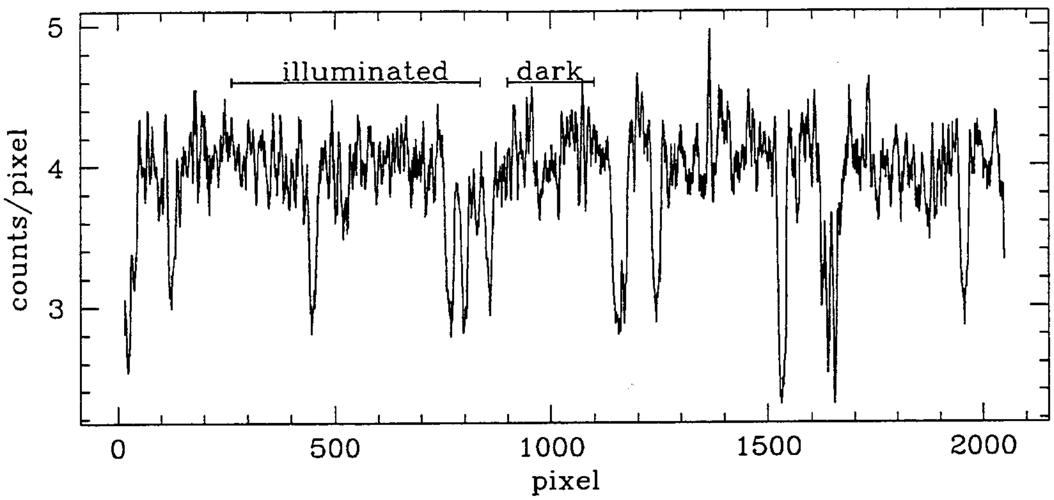

Fig. 3.1.— Typical dark signal in a 1300 sec FOS exposure. The mean level varies with orbital position and orientation during integration, but the shape of the dark background over the spectrum is unvarying. Sub–stepping in the spatial direction causes each pixel to contain data from 5 diodes. Where diodes have been turned off due to poor performance, the pixel has a fraction of the total integration time and sharp features occur. Apart from features caused by dead diodes, the dark has no structure.

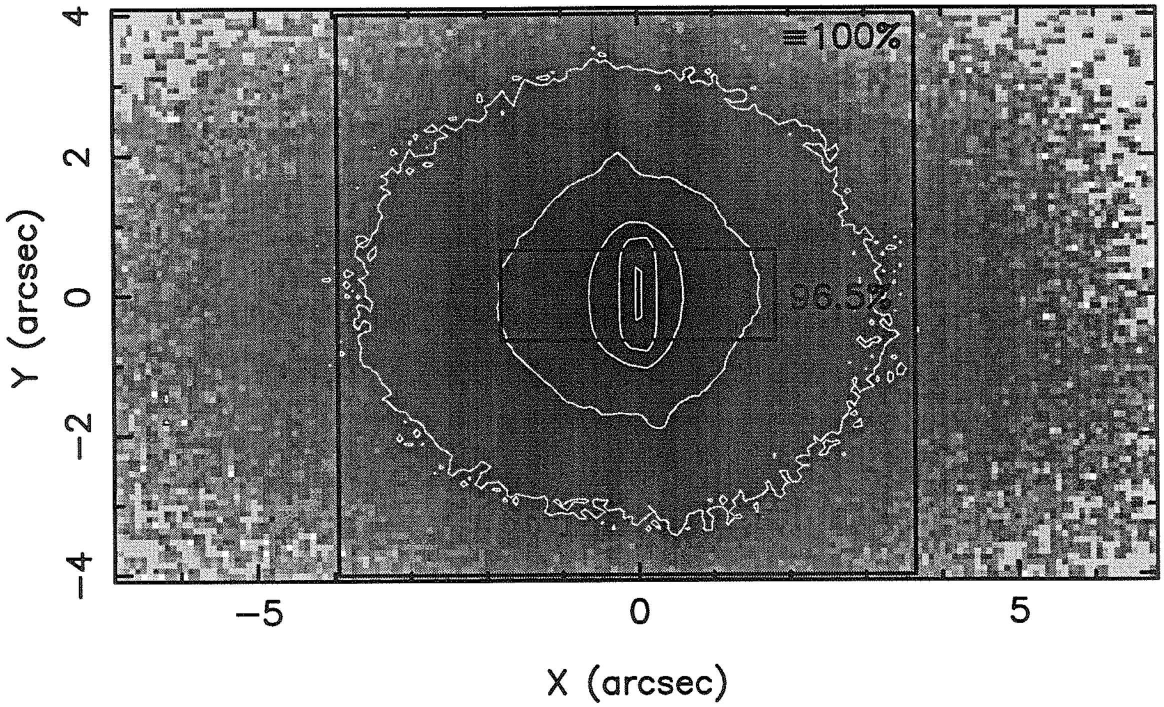

Fig. 3.2.— FOS imaging mode data showing PSF in the diode plane. The logarithmic grey-scale covers eight orders of magnitude in flux. The contours indicate flux levels at intervals of a factor of 10 between 1 and 10^{-5} times the peak flux. The large square aperture is that which we have defined to contain 100% of the flux *which passes through the aperture* from a point source. The rectangular aperture indicates the diode array within one resolution element, and contains 96.5% of the flux which falls in the diode plane. This percentage was calculated based on the PSF in the x–direction, rather than the y–direction, to avoid the boxcar smoothing caused by the rectangular diodes in the y–direction. This effect causes the PSF to appear elongated in the y–direction (see §3.2.2).

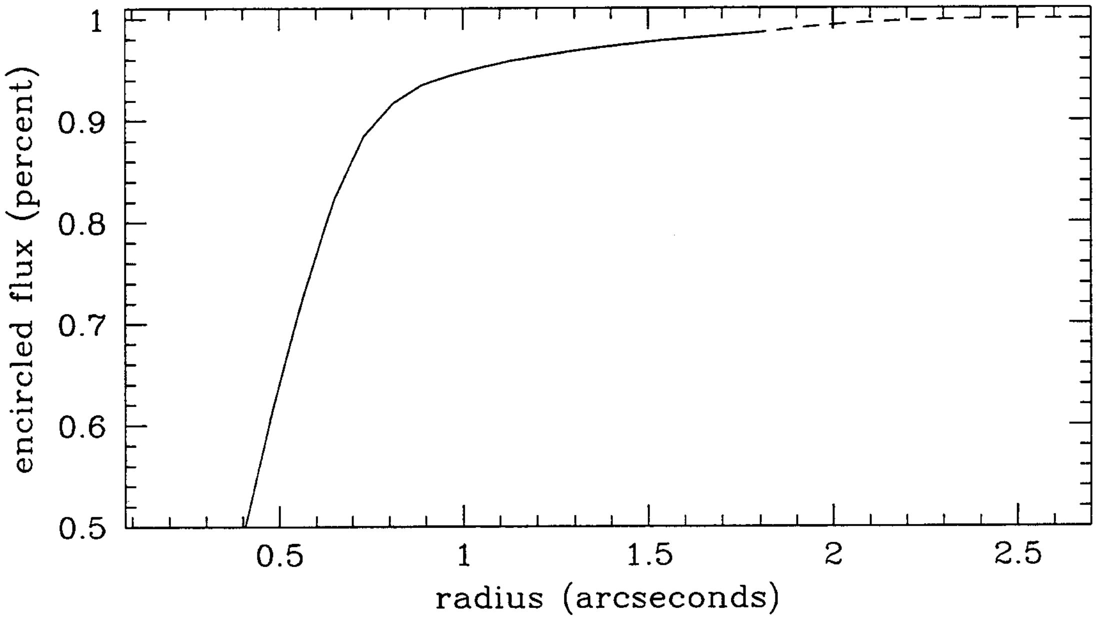

Fig. 3.3.— Encircled energy within the FOS A-1 aperture. The aperture half width is 1.83 arcsec. Beyond that radius we extrapolate based on the derivative of the growth curve within 0.2 arcsec of the edge of the aperture to estimate the point at which all of the flux is contained. Based on that extrapolation, 98.5% of the light passes into the spectrograph through the A-1 aperture.

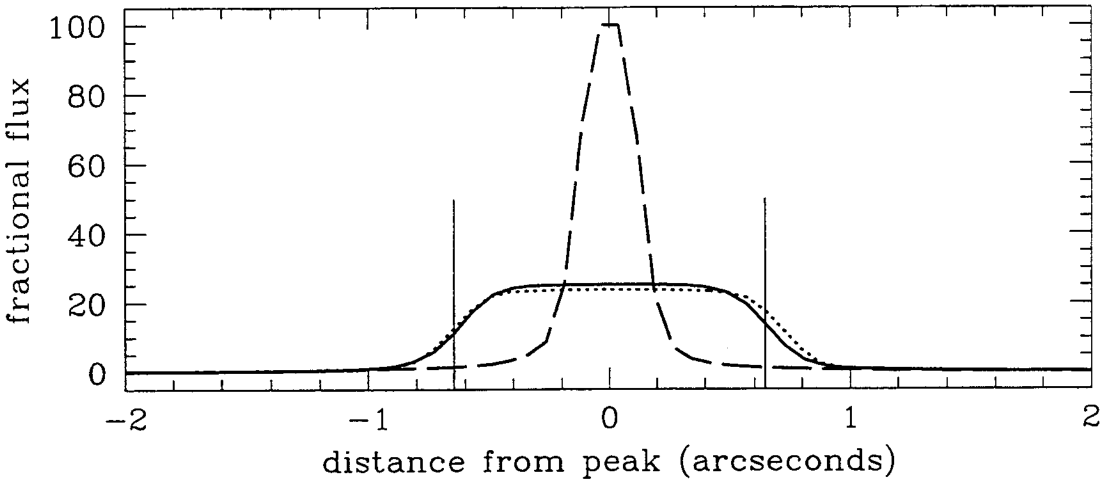

Fig. 3.4.— Resolution of the FOS image in x and y. The dashed line show the PSF in the x-direction at the detected resolution (0.076 arcsec sampling, boxcar smoothed by the diode width to 0.31 arcsec). The dotted line shows the same x-direction PSF after boxcar smoothing by the diode height of 1.29 arcsec to match the detected resolution in the y direction The solid line shows the PSF in the y-direction at the detected resolution (0.081 arcsec sampling, boxcar smoothed by the diode height to 1.29 arcsec), which is clearly well approximated by the x-direction PSF.

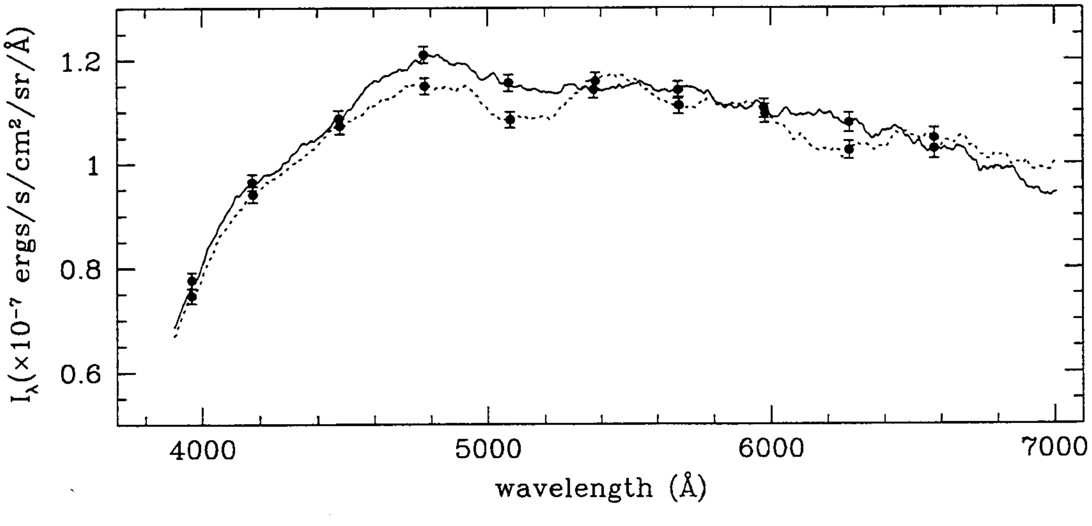

Fig. 3.5.— Surface brightness of the total background from FOS. The solid and dashed lines show the average of all six spectra taken during the November and December 1995 visits, respectively. The error bars show the statistical error of roughly 1.5-2% per 300Å resolution element.

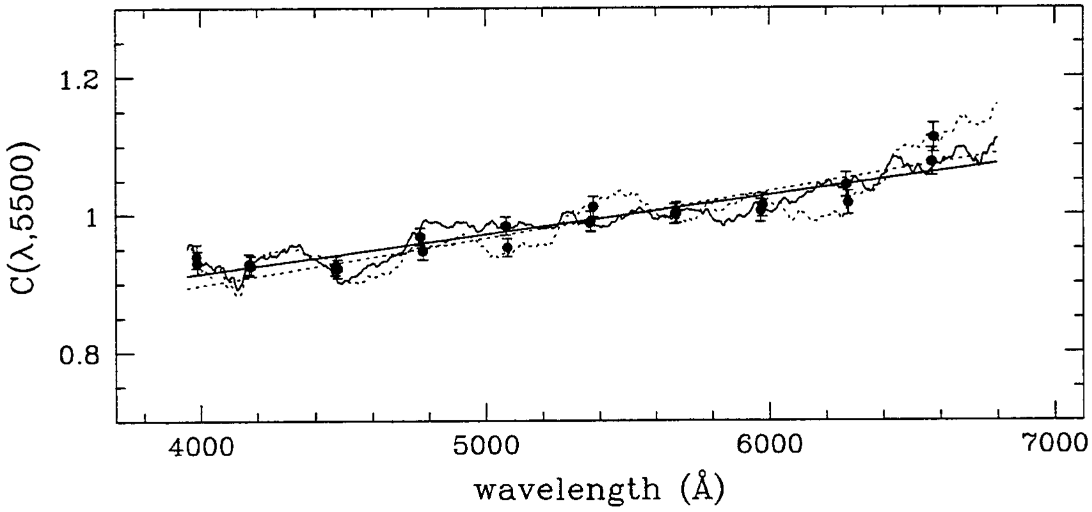

Fig. 3.6.— Color of the total detected background with respect to solar. The solid and dashed lines show the detected background (November and December, respective) as shown in Figure 3.5 divided by the Neckel & Labs (1984) solar spectrum at matched resolution. Straight lines show the linear fits to both color spectra. The error bars are the statistical errors in the FOS spectra per resolution element. Errors in the solar spectrum used are negligible, as discussed in §4.4.

Chapter 4 LCO Spectrophotometry: Measurement of the Zodiacal Light

The second HST visit for our program took place on November 29, 1995. On November 26–29, 1995, we also used the Boller and Chivens Spectrograph on the 2.5 m du Pont telescope at Las Campanas Observatory (LCO) to obtain long–slit spectra of the night sky in the HST/WFPC2 field. We use those spectra to measure the absolute flux of the zodiacal light (ZL) which contributes to the total background flux seen from HST. The first night of the LCO run was lost to clouds, and data from the third night was discarded due to a detector malfunction (see §4.1.1). The data from November 27 and 29, however, are excellently suited to measuring the absolute flux of the ZL in the direction of the HST field at the end of November 1995.

The ground–based spectrum of the night sky is dominated by an absorption line spectrum (zodiacal light) and an emission line spectrum (airglow) which contribute in almost equal parts. Our goal is to measure the strength of the absorption features of the ZL, which necessitates unusual data reduction and analysis. Both are described in detail below.

4.1 Observations and Data Reduction

The exact coordinates of the spectroscopic observations were selected from ground–based imaging to avoid objects brighter than r=26 mag/arcsec^2 (see Figure 4.1). We used a 600 l/mm grating to obtain spectra over the wavelength range 3860–5150Å with $\sim$ 1.27Å per pixel. A slit–width of $\sim$ 1.5 arcsec (see §4.2.4) produced roughly 2.7Å resolution in the program observations. Spectrophotometric standards were observed through a slit 10.8 arcsec wide.

To minimize read–noise, the data were on–chip binned by four pixels in the spatial direction. With a slit–width of 1.5 arcsec, the solid angle per binned pixel is 3.59 arcsec^2. The slit is approximately 3.5 arcmin long, illuminating roughly 85 binned columns, the central 80 of which were used in the analyses. The total integrating area is thus roughly 215 arcsec^2. From a a single image, spectra with a signal–to–noise ratio near 40 can be obtained for the ZL, which has a V–band flux near 23 mag/arcsec^2.

The general data quality is demonstrated by Figure 4.2, in which we show a wavelength calibrated spectrum obtained from just one column of an 80 column image. We detect approximately 45 DN/pixel from the sky at the red end, and 20 DN/pixel around 4100Å. Above 4100Å, the count rate is more than twice that of the dark current, which is 7 DN/1800 sec with 4×1 on–chip binning. The spectrum obtained from a full, 80 column image is also shown in Figure 4.2. The maximum error at the blue end (3900Å) is 10% per resolution element. Above 4100Å, the error per resolution element from a single image is roughly 1%.

As described in §1.2.2, we determine the contribution of the ZL to the total background by the strength of the solar Fraunhofer lines in the spectrum of the night sky. While the ZL is a uniform source spatially, our measurement of the features of the ZL is actually a *differential* measurement as a function of wavelength. Unlike the measurement of the uniform surface brightness in the HST images, bias and dark current are not significant problems for measuring the ZL, as long as both are spatially uniform over the two dimensional extent of the chip; an error in the mean level of the bias or dark subtraction merely adds to the pedestal of the background. Flux calibration, however, is obviously as crucial for these observations as for the WFPC2 and FOS data. The point source calibration, aperture corrections and tertiary standard system used for calibration are all discussed in detail below.

4.1.1 CCD Characteristics and Data Quality

The detector used is a thinned Tektronics/SITe 1024^2 CCD with 24μm pixels. The gain setting was roughly 1.15e$^-$/DN and read–noise was roughly 8.6e$^-$ in the 4×1 binned configuration. The quantum efficiency of the CCD is near 50% over the spectral range of these observations, however then transmission of the spectrograph optics drop by a factor of two between 5000Å and 3800Å (see sensitivity curve in Figure §4.3).

Charge Transfer Efficiency (CTE)

The chip sensitivity and dark current were extremely stable on three out of four nights. In the middle of the run, however, temperature regulation of the chip became erratic and a drop in CCD temperature caused an increase in the spurious charge and a drop in the charge transfer efficiency (CTE) to unacceptable levels ($\sim 99.995\%$).[1] The data taken on November 28 was therefore dropped from further analysis. Even during that night, however, the two–dimensional pattern of the dark current over the chip showed no change. Before this problem occurred, and after it was resolved, the dark and bias levels were stable to within 0.4 DN. In addition, the sensitivity of the chip varied by less than 1% between the first and last nights of the run, as determined by our standard star calibrations.

There are several ways we can monitor an individual frame for CTE difficulties. A strong and easily–identified symptom of low CTE is trails on cosmic rays in the read direction. However, for this data set, the bias row provides a more easily quantified diagnostic for CTE. Only one third of the chip in the spatial direction is illuminated by the slit, and the bias row on each image is the average of 16 rows read immediately after the final data row is read off. A sharp change in the level of the bias row at the boundary of the exposed and unexposed portions of the chip contains the charge lost from the data rows. On the nights during which the temperature of the CCD remained stable, the bias level was found to be negligible higher in columns illuminated by the slit even in the dome flats (with mean level of 7000 DN^{-}/pixel). Thus, the loss of charge in even the last row of the chip was found to be less than 0.5% in the data

---

[1] In contrast to the CTE discussed with respect to WFPC2, we here mean CTE in the usual sense implied by the term: when charge in moved down the column during read–out, only some fraction of the charge is successfully transfered at each parallel gate. If that fraction is 99.9995%, then after 1024 transfers, 99.5% of the charge which originated in pixel 1024 is read–out in each column. If that fraction drops to 99.995%, however, 5% of the charge is lost from row 1024 and is smoothly distributed to subsequent rows in an exponential manner.

which we used in our analysis. For reasons described in the §4.3, no data beyond row 700 was used in the final analysis anyway, so that the most charge lost due to CTE in the data we used was negligible (0.3%) even in the highest numbered rows.

Deferred charge

Another possible cause of non–linearity at low count levels is deferred charge. Deferred charge refers to electron trapping similar to that described for WFPC2, such that D electrons are deferred if N electrons are read out when $D + N$ electrons are generated in a pixel. As we have seen with WFPC2, traps can be uniformly distributed, in which case typical tests for linearity at low–light levels should reveal the problem, or can be particular to some fraction of the pixels. We performed the standard tests for deferred charge as described in Gilliland (1992). Only 0.3% of the pixels showed deviations from linearity greater than four times the read–noise in their response to low and high light levels. These pixels were flagged as bad in all images and excluded from analysis.

We also performed a standard linearity test by taking flats with exposure times between 0.5 and 200 seconds. Slight instability in the dome-flat lamp was averaged out by running up and down the time–series four times. We found no deviation from linearity between 20 and 20,000 DN, with an *rms* scatter in the detected rate of roughly 1%, which we attribute mostly to the lamp. We therefore conclude that no significant error is accrued as a result of non–linearity between the flux level of the standard star observations (peaking at roughly 5,000 DN) and the program observations (20–50 DN on average).

4.1.2 Bias Subtraction

Bias level and dark backgrounds can only affect the accuracy of this measurement if sharp features are present in the dispersion direction of the spectra, which happens to be the read direction of the chip. Variation in the spatial direction will contribute random errors to the mean flux measured at a particular wavelength. Periodic fluctuations and occasional jumps on the order of $\sim 1\,\mathrm{DN}$ are seen in the read–direction of the bias. These features do not appear in the same row from image to image. Slow drifts along rows and columns are also common to both the bias and dark current. Both can have quite measurable effects on the apparent strength of spectral features in any one image.

Every image contains two diagnostics for the bias level during the read–out of that image. The first is the overscan region, which is obtained by reading 150 pixels at the end of every physical row on the chip. This results in 150 columns of overscan, which are useful for monitoring the variations in bias level between rows during a single CCD read. This overscan region has a mean level which is 60 DN lower than the mean bias level over the physical extent of the chip. The last row of each image (row 1024) is the average of 16 rows which are read after the last physical row of the data is read out. The level of this row is representative of the level on the chip. Our bias subtraction method utilized both of these diagnostics.

First, the overscan columns were averaged and fitted with an Savitsky–Golay routine (Press et al. 1992), which follows rapid jumps in the mean level while smoothing over the noise from pixel to pixel. This fit was subtracted from each column of data, which did an excellent job of removing row–to–row variations in the bias level. The mean level in the bias row, which varied by less than $\pm 2\ e^-$ over the run, was then removed by subtracting the mean value of that row. Finally, there is some two–dimensional structure over the chip due to consistently hot pixels and characteristic amplifier behavior at the start of each row. These were removed using a "superbias" frame, which was made using 250 bias frames from which the overscan and bias row had first been subtracted.

To verify the accuracy of our bias subtraction procedure, we tested our procedure on 50 bias frames which were taken at the end of the run and which had not been included in the superbias. After reduction, these bias frames had an average value of $0.005 \pm 0.03\,\mathrm{DN}$, and showed no systematic trend in the residuals and no identifiable patterns or jumps in the residual level of individual frames.

4.1.3 Dark Current Subtraction

The mean level of the dark current was found to be constant to better than 1 e^- peak–to–peak over the course of the first two days of the run, and the last two days of the run. Even when the apparent dark level (spurious charge) increased when the CCD became too cold in the middle of the run, the pattern of the dark current over the chip showed no measurable change. Dark frames were taken immediately before and after observations on each night, making the mean level of the dark current during each set of observations well determined.

A superdark was made by combining 20 darks taken at the beginning and end of the run. The noise in the resulting dark was read–noise dominated, and too large to provide any pixel–to–pixel information. To avoid adding noise to the program frames, and to make possible the removal of the mean level (which drifted by 1.0 DN over the extent of the frame), the superdark was smoothed using sliding 3×3 boxcar median filter. Dark frames taken in the middle of the run were not used in making the superdark. Test–reduction of these frames verify that the dark subtraction was good to ±0.25 DN on the November 27 and 29, with no residual pattern.

4.1.4 Flat Fielding and Illumination Correction

Flat–field and slit–illumination corrections were created from dome and twilight sky flats, respectively, using the tasks RESPONSE and ILLUMINATION in the IRAF SPECRED package. Program observations of the ZL were taken through a 1.5 arcsec slit to preserve resolution, while the standards were taken through a 10 arcsec slit to maximize detected flux. Different sets of flat–field and illumination corrections were required for the two different slit–widths for two reasons. First, microscopic roughness on the edges of the slit jaws caused shadowing which changed as a function of slit–width. Second, the slit–jaw mechanism on this spectrograph is such that the jaws are parallel for separations up to $\sim$ 5.4 arcsec (500 μm), but are not parallel when the jaws are set to 10.8 arcsec in the center. Variation in slit–width is almost 10% from end to end when the width at the center is 10.8 arcsec in the middle. To compensate for the variable slit–width for standards, the illumination corrections for both slit–widths were normalized to the spatial center of the slit. Standard stars were all observed within two pixels of the central column used for normalization, which places them within 99.98% of the nominal value for the wide–slit illumination correction.

4.2 Flux Calibration

The accurate calibration of our ground–based spectra is dependent on the usual three factors which contribute to accurate spectrophotometry: the accuracy of the fiducial standard star fluxes; the accuracy of our point source calibration (sensitivity function and extinction correction); and the accuracy of the conversion from point source calibration to surface brightness calibration. The solid angle of the field of view and the aperture correction are crucial for the last point. These issues are all discussed in the following section. The conversion from a flux calibrated spectrum of the ZL to the mean flux of the ZL through the WFPC2 band–passes is discussed in §6.3.

4.2.1 Accuracy of Tertiary Standards

Calibration to Vega

Hamuy et al. (1992, henceforth H92) quote the internal precision of their tertiary spectrophotometric system to be better than 0.01 mag at all wavelengths, a claim which is well corroborated by the small *rms* errors we find in our own spectrophotometric flux calibration (see below). An additional concern for our purposes, however, is the agreement between the H92 system and the primary calibration for Vega, especially in the wavelength range spanned by our spectra (approximately the extent of the Cousins B–band, 4200–5100Å).

The tertiary system of H92 is calibrated based on the equatorial secondary standards of Taylor (1984), which were in turn calibrated to the Hayes & Latham (1975) absolute flux measurements of Vega. In an attempt to adhere to the widely accepted

Hayes (1985, hereafter H85) calibration of Vega, H92 recalibrate the Taylor (1984) secondary standards in two steps. First, they apply small corrections as a function of wavelength to improve the agreement between Taylor's Vega spectrum and the H85 Vega spectrum. Second, they integrate Taylor's secondary spectra over the Kron–Cousins photometric bands (producing "synthetic" photometry) and applying slight grey–shifts to bring each spectrum into agreement with published broad–band photometry. The photometry for nine of the ten grey-shifted secondary standards is from Cousins (1971, 1980, 1984), the remaining one is from Johnson et al. (1966). For the details of this method, the reader is referred to the careful discussion in H92.

H92 estimate that their internal consistency in converting Taylor's results to the Hayes (1985) Vega system is 0.009 mag in the wavelength range of the Cousins B. As a check on this conversion, they compare synthetic photometry of the adjusted Vega spectrum with the broad–band photometry of Vega by Johnson (1954), and find offset of -0.016 (± 0.009) mag in B (in the sense of Taylor minus Johnson). This is, in fact, very nearly the B–band flux (-0.016 mag) that Hayes himself finds for the H85 Vega spectrum, indicating that regardless of the agreement (or lack their of) with the 30 year old Johnson measurement, H92 is quite solidly on the Vega H85 system. In addition, the slight discrepancy between H92 and Johnson can be explained by the fact that there is some difference between the Cousins UBV systems to which nine of the ten secondary standards are calibrated, and the original Johnson system, to which Vega is compared (Menzies et al. 1989).

H92 have also checked their agreement with other secondary standard systems in a number of ways. First, they find good agreement between Baldwin & Stone (1983) monochromatic fluxes and their own, with most deviations between the two systems resulting from the fact that the Stone and Baldwin fluxes are on the Hayes & Latham (1975) Vega calibration. Second, the H92 calibration included photometric observations, calibrated to Graham (1982) and Menzies et al. (1989) with careful attention to the color solutions. They find their own photometry of the tertiary standards agrees very well with their integrated spectra (0.006 ± 0.011 mag in Cousins B). And finally, three stars in the northern hemisphere were included in the program.

They find less than 0.03 mag deviation between their monochromatic fluxes for these stars and the monochromatic fluxes of Massey et al. (1988). Again, Massey et al. are calibrated to the HL75 system, and deviations are in the direction expected given the conversion to H85.

Comparison with the HST Spectrophotometric System

Given that the calibration of HST involves grey–shifts to match an average of B and V photometry of Landolt (1992), the comparison between the H92 and Landolt (1992) photometry of the southern tertiary standards is especially relevant to the issues at hand. H92 find a differences of $+0.013 \pm 0.009$ mag in B between the synthetic magnitudes derived from their spectrophotometry and the Landolt (1992) results (in the sense Hamuy minus Landolt). The Landolt UBV system is well known to be quite different in B from the Cousins UBV system, with a strong color dependence in the range $0 < (B - V) < 1$ (see Figure 2 of Menzies et al. 1989). However, the expected difference between Johnson–B and Landolt-B magnitudes for a star with the average color ($B - V \approx 0.24$ mag) of the tertiary standards used here is $B_{\mathrm{Cous}} - B_{\mathrm{Land}} = 0.0 \pm 0.01$ mag. If there is any discrepancy between the Landolt (1992) calibration and the H92 tertiary systems in the B–band, it is evidently of order 1%, and it cannot be explained by a difference between the filter systems. For ease of interpretation, possible future adjustments to the calibration, and because the offset is within the 1σ errors of both systems, we do not adopt an offset but rather use both calibrations without adjustments.

4.2.2 Point Source Calibration

We observed tertiary spectrophotometric standards roughly 15 times each night. Nine different standards were used throughout the run, with colors $0.0 < (B - V) < 0.6$ mag. Fiducial spectra for these tertiary standards were from H92. The color distribution of the standards we observed is as broad a distribution as is available from the H92 standards, and is in fact well distributed around the color of the night sky (zodiacal light plus airglow in nearly equal proportions). All standards were observed with the slit aligned with the parallactic angle as tabulated by Filippenko (1982) to minimize flux lost due to atmospheric refraction. To center the star in the slit we followed the procedure outlined in H92: we first centered the star in a narrow slit (~ 2 arcsec), and opened the slit to the width used for observations only after guiding was established.

Extinction curves were calculated from these data for each night individually in 50Å bins with typical *rms* residuals of 0.01 mag on November 27 and 29. As no difference was found between the two nights, the final extinction curve was constructed using data from both nights together (see Figure 4.4). We used sixth–order Legendre polynomials fit to these data to obtain the extinction curve as a function of wavelength. The extinction solution obtained from these spectra is in excellent agreement with the $r-$ and $g-$band extinction terms which we obtained from imaging data the previous year (November 1994). Due to the unusual nature of the program spectra — spatially uniform and not dominated by a component originating outside the atmosphere — the method adopted for extinction correction of the program data involves an equally unusual technique and is discussed in the §4.3.

After the extinction corrections were applied, the sensitivity curve for each night was determined using the task SENSFUNC in the IRAF, SPECRED package. The agreement between the sensitivity curves for the two nights is excellent: the variations between the sensitivity curves found for November 27 and 29 are 3% at the 4100Å, and 2% redward of 4500Å (see Figure 4.3). Variations in the QE on this level could result from slight temperature fluctuations in the CCD (M. Blouk, personal communication), and so we do not force the sensitivity function to be identical on different nights. We estimate that the error in the shape of the sensitivity curve is roughly the internal *rms* error of the SENSFUNC solutions (0.011 mag) from either night individually.

Even with the slit open to near its maximum width (10.8 arcsec), a significant portion of the PSF for standard star observations falls outside of the slit. An aperture correction is therefore required to determine the appropriate system throughput for a uniform surface brightness source.

4.2.3 Aperture Correction

The aperture correction is calculated in two stages to compensate for lost flux from the optical path in two places. The first stage of the aperture correction compensates for the flux lost from the PSF in the focal plane of the telescope (at the slit). The PSF in the focal plane is circular, with 95% encircled energy at a radius of 5 arcsec. The slit used for standard star observations had a 5 arcsec half–width, thus allowing only $\sim$ 95% of the flux from a point source into the spectrograph. This holds generally true for modern telescopes equipped with standard CCD detectors mounted behind glass windows (Racine 1996). The second part of the aperture correction compensates for further degradation of the PSF due to scattering in the spectrograph. The spectrum of a star can only be extracted so far out into the wings of the PSF in the spatial direction before the signal–to–noise ratio is too low to be useful. Unfortunately, of the flux which gets into the spectrograph, several percent is located as far out as 1 arcmin from the peak of the spectrum in the spatial direction.

To measure flux lost in the aperture plane, we measured the PSF from images taken on the last night of the run (November 30, 1995). We plot the growth curve for five different stars in Figure 4.2.3. To be certain that focus does not effect the PSF at a 5 arcsec radius, the stars used for this plot were taken with widely varying focus. As 5 arcsec in the focal plane of the du Pont 2.5m telescope corresponds to 0.45 mm (almost 19 pixels for a 24μm/pixels CCD), it is difficult to have the telescope out of focus enough to effect the enclosed flux at a radius of 5 arcsec, as is clear from the lack of variation in the shape of the growth curves shown in the figure. The flux enclosed at the half-width of the slit is 97.88 ($\pm$ 0.2)%.

We measure the growth curve of the standard stars along the spatial extent of the slit in order to determine the percentage of flux which is included in the extracted spectra. We have mapped the growth curves along the spatial extent of the two dimensional spectra for all 45 standards taken during the run. The sky level for this test was taken from pixels further than 80 arcsec from the peak of the star. In order to get adequate signal in the sky, we averaged 400 rows near the peak sensitivity of the spectrograph. As the PSF is not strongly wavelength dependent over the narrow range of wavelengths used here, averaging in this way does not affect our results. In order to confirm that no wavelength dependence is in fact seen over the $\sim$ 1000Å range which we use in our final analysis of the ZL, we calculated the aperture correction at both the blue and red ends of the spectral range and found no variation in the growth curve. The growth curve along the slit for the 18 highest signal–to–noise spectra are shown in Figure 4.5. The differences in the encircled energy at the inner–most radius plotted are a result of differences in sub-pixel centering for spectra observed with 4×1 binning, and is irrelevant if a ± 4–pixel extraction aperture is used.

Standards were extracted with APSUM, out to a 10.6 arcsec radius (central pixel ± 4 pixels), which is well within the region of good signal–to–noise in the star. This includes 98.4 (± 0.1)% of the flux which passed into the spectrograph. Sky background was measured outside an annulus of 25 pixels (60 arcsec) from the peak of the star. This aperture is small enough to ensure adequate signal–to–noise in the extracted stellar spectrum, and also ensures minimal error due to sky subtraction, as the stellar signal is much brighter than the sky background in the inner 11 arcsec. Because we are explicitly correcting for lost flux outside that extraction aperture, we do not attempt to include "all of the light" in the extraction aperture.

The total aperture correction to be applied to the sensitivity function in order to calibrate a uniform source is then the multiple of the fractional encircled energy at the aperture plane and the fractional extracted flux from the spectrum, or 96.8 (± 0.2)%.

4.2.4 Solid Angle of the Program Observations

The accuracy with which we can measure surface brightness is limited not only by the accuracy of our flux calibration, but additionally by the accuracy with which the solid angle is known. The solid angle is a function of both the angular pixel scale (spatial direction) and the angular slit–width (dispersion direction). We therefore take great care to determine both explicitly.

The pixel scale was measured empirically by taking spectra of two stars with known angular separation while they were simultaneously aligned in the slit. The measured separation in pixels was then calibrated to the known angular separation of the stars. Four pairs of stars were observed in this way with angular separations in the range 44–82 arcsec. With a 1.5 arcsec slit, the apparent angular separation of pairs of stars which are of order 1 arcmin apart is relatively insensitive to the exact alignment of the slit. Nonetheless, each pair of stars was observed with the slit at 3 positions differing by less than 1 degree, in an attempt to obtain truly parallel slit alignment. The stars used for this purpose are in the field of M67, for which the relative astrometry of members is known to better than 0.3 mas (Girard et al. 1989). The pixel scale was found to be 0.5843 ± 0.0035 arcsec/pixel (1σ error).

The slit–width of the spectrograph is adjusted by a manual micrometer while the instrument is on the telescope. After observations were completed, the calibration and repeatability of the micrometer was verified using a microscope. As used in our program observations, the slit width was measured to be 1.536 ± 0.002 arcsec (1σ error) at the center of the jaws. The repeatability of the width setting was tested by opening the jaws to their maximum extent between each of several sets of measurements. That accuracy is included in the 1σ error quoted above. The total solid angle of each pixel is therefore 0.8975 ± 0.0054 arcsec^2(1σ error).

4.3 Analysis

To motivate the technique we use in measuring the mean ZL surface brightness present in the LCO spectra, we first briefly review the general characteristics of the spectroscopic night sky and the components which contribute to it.

We can describe the observed spectrum of the night sky, $I_{\rm Total}$, as a combination of airglow and extraterrestrial components,

$$I_{\mathrm{Total}}(\lambda, t, \chi) = I_{\mathrm{air}}(\lambda, t, \chi) + [I_{\mathrm{ZL}}(\lambda) + I_{\mathrm{EBL}}(\lambda) + I_{\mathrm{DGL}}(\lambda)] \exp(-\epsilon\chi). \tag{4.1}$$

The contribution from airglow, I_{air}, is a rapidly varying function of time and increases as a complex function of airmass (van Rhijn 1924, 1925; Roach & Meinel 1955), the specific dependence of that function being of no particular importance for our purposes. Of the extra–terrestrial components, only the ZL has significant spectral features. Any spectral features in the EBL are suppressed due to contributions over a wide range of redshifts. The DGL which results from scattering will have the spectral features of the ambient interstellar radiation field, which is also likely to be fairly smooth and is unlikely to have emission lines in the range of interest, as we discussed in Chapter 5 (see Martin et al. 1991, Dube et al. 1976, Reynolds 1990). Moreover, the EBL and DGL are roughly two orders of magnitude fainter than ZL and airglow, and would not contribute consistently to all of the solar features in the 1000Å range used in this measurement. Thus, they could only add noise to the measured ZL flux. Any diffuse stellar contribution from the galaxy which contributes consistently to the strength of the solar features, however, will contribute to our estimate of the ZL, and be conveniently removed along with it. This is clearly not a problem either.

We can thus consider the observed spectrum to be comprised of a time and airmass dependent component (airglow), a stable and featureless component (EBL+DGL), and the ZL. Because the reddening of the ZL is only a few percent per 1000Å (see §6.2.1), we can consider the ZL as a constant multiple of the solar spectrum over 100Å bands. Thus, we can express the featured portion of the night sky spectrum as

$$\begin{aligned} I_{\mathrm{obs}}(\lambda, t, \chi) &= I_{\mathrm{air}}(\lambda, t, \chi) + I_{\mathrm{ZL}}(\lambda) \exp(-\epsilon\chi) \\ &= I_{\mathrm{air}}(\lambda, t, \chi) + c_i(t) I_{\odot}(\lambda) \exp(-\epsilon\chi). \end{aligned} \tag{4.2}$$

In which $I_{\odot}(\lambda)$ is the total solar flux and $c_i(t)$ is the scaling which relates the mean surface brightness of the ZL to the mean flux of the Sun. We assume that this value is independent of wavelength in $\sim$ 100Å-wide band-passes labeled by the subscript i, and allow $c_i(t)$ to vary with time over the three days of the observations. The trick, then, is to find an accurate way to measure $c_i(t)$.

This problem is complicated by several practical considerations:

(1) The airglow spectrum is one of emission with an effective continuum due to O+NO (NO_2) recombination, broad rotation–vibrational transition bands, scattered light, and blended lines. The ZL is a pure absorption spectrum with a continuum surface brightness which is, anticipating our results, nearly equal to that of the airglow component. The combination of the two makes continuum identification nearly impossible.

(2) There is no digital airglow spectrum which one might consider fiducial for our purposes. Published airglow spectra are often continuum subtracted; fail to cover bluer wavelengths where airglow emission features are relatively low intensity compared to the spectrum redward of 5577Å; are low–resolution; and include a zodiacal component by default. Furthermore, airglow is variable with time, location, and geological events. During the course of this LCO program (1992 to 1996), volcanic activity in the southern hemisphere caused noticeable variation in the spectral features and flux of the night sky.

(3) The two components of the spectrum have roughly inverse dependence on airmass. The ZL spectrum has the usual wavelength dependent extinction with airmass, while airglow increases as a complex function of airmass.

(4) Finally, the emission from the atmosphere and the absorption features in the ZL do occasionally overlap. For example, Figure 4.7 demonstrates the variability of the Hβ Fraunhofer line due to time–varying emission from the atmosphere. The CaI feature at 4227Å is also clearly affected by O_2 emission and an unidentified line at 4207Å. We observed in the range 3800–5100Å because the strong MgI lines at $\sim$ 5170Å were found to be frequently affected by variable airglow features. For lack of stronger Fraunhofer line candidates above 5100Å, Ca H & K were included in our observations.

As a result of these four complications, measuring the equivalent width of the individual Fraunhofer lines is extremely difficult. In addition, there are only 10 Fraunhofer lines with equivalent width less than 1Å at optical wavelengths $\lambda \lesssim 5577$Å. Redward of that wavelength, the airglow emission line spectrum becomes prohibitively dense. The entire spectral range from 3800–5100Å does, however, contains identifiable *blended* solar absorption lines. To take advantage of the whole spectrum and to avoid ambiguous continuum identification, we have developed a conceptually simple approach to the problem of determining the scalings $c_i(t)$.

Identification of Scaling Factors

We begin by guessing at a reasonable range of $c_i(t)$, and subtracting the scaled solar spectrum from the observed spectra. When we have used a scaling which produces the correct surface brightness of the ZL as it is observed in these spectra, what remains is a pure airglow spectrum:

$$I_{\mathrm{air}}(\lambda, t, \chi) = I_{\mathrm{obs}}(\lambda, t, \chi) - c_i(t) I_{\odot}(\lambda) \exp(-\epsilon\chi). \tag{4.3}$$

While $I_{\mathrm{air}}(\lambda)$ will vary with time and airmass, it should be free of solar features. As a quantitative diagnostic with which to determine the presence of residual solar features in what we think is a "pure airglow" spectrum, we use a linear correlation. When the correlation between the residual airglow and solar spectrum is minimized, the ZL surface brightness has been appropriately subtracted.

In practice, some details complicate the execution of this method. Namely, the appropriate extinction correction varies with wavelength and with time; the spectral resolution varies slightly as a function of wavelength due to varying focus; and, most importantly, the respective color of the airglow and solar spectra will dominate the strength of the diagnostic correlation if the continuum shape is not properly removed. These problems were addressed as follows.

In order to obtain a solar spectrum which was well matched in resolution to our observed spectra, we convolved an ultra–high–resolution spectrum (see §4.4) with a gaussian of variable FWHM. The appropriate width as a function of wavelength was determined from the shape of the lines in the arc lamp spectra which were used for wavelength calibration.

As is implied by equation 4.1, we can compensate for extinction by applying the extinction directly to the scaled solar spectrum. Thus, we effectively simulate the appearance of the ZL in our spectra at each airmass by applying the extinction curves measured from the standards stars. Any error in this correction will show up as a trend in the inferred ZL surface brightness with airmass.

Finally, in order for the strength of the linear correlation of $I_{\text{air}}(\lambda)$ and $I_{\odot}(\lambda)$ to reflect the strength of coincident spectral features, both spectra must have stationary mean values as a function of wavelength. The continuum must therefore be subtracted from both spectra. Unlike the requirements for measuring equivalent widths of features in typical object spectra, the absolute flux level of the continuum is irrelevant in our case: it is only important to correctly remove the color of both spectra on scales much larger than the features we are trying to match. This can be seen clearly in the generic expression for a linear correlation:

$$R_i(x,y) = \frac{\sum_n (x_n - \overline{x})(y_n - \overline{y})}{\sqrt{\sum_n (x_n - \overline{x})^2}\sqrt{\sum_n (y_n - \overline{y})^2}}. \tag{4.4}$$

In this case, x and y are $I_{\text{air}}(\lambda)$ and $I_{\odot}(\lambda)$ respective, the subscript n runs over wavelength, and the subscript i designates individual band-passes. It is clear from this expression that the mean flux drops out of the correlation, while difference from the mean are crucial.

In practice, we have found that consistent results cannot be obtained in regions where the airglow contains strong rotation-vibration bands: broad features cause rapid fluctuations in the mean value of the spectra over a broad spectral region, making it difficult to define the level on which the solar features are superimposed. We therefore limit our efforts to the regions where the airglow continuum is fairly smooth and can be well approximated by a first or second order polynomial fit. Within those regions, indicated in Figures 4.6 and 4.7, we find that our results do not vary significantly with the method of continuum removal. Among the methods we used for continuum estimation were boxcar smoothing with scales between 75Å and 199Å, first and second order polynomial fitting, and Savitsky–Golay smoothing (Press et al. 1992). Consistent results were obtained from all of these continuum-subtraction methods within the indicated regions, which do not include regions with rapidly varying mean levels. The ZL indicated by each spectrum is taken to be the average of the result in the three bands.

Note that the solution is not sensitive to Doppler broadening at the level which it might affect the ZL (see §6.2.1). This is true because Doppler broadening will not alter the total flux across a feature. The correlation is unaffected by the saw-tooth effect of subtracting features with mismatched widths at the level of the 0.3Å Doppler broadening we might expect. In addition, we allowed for a shift in the central wavelength when calculating the correlation, and found none. Figure 4.8 shows a pure airglow spectrum (the night sky spectrum after zodiacal light is subtracted) with some of the identified features labeled.

4.4 Fiducial Solar Spectrum

The requirements for the accuracy of our fiducial solar spectrum are not as stringent as one might think. Recall that our method for determining the ZL in the WFPC2 band–passes relies on a measurement of the ZL flux at 4200–5100Å, which is independent of the absolute flux of the fiducial solar spectrum. The flux at 3000 and 8000Å is then found by scaling the same fiducial solar spectrum to the appropriate flux at 4650Å, and applying a reddening which is defined with respect to that fiducial solar spectrum. Any error in the absolute broad–band color of the Sun is subsumed in the reddening correction, and the total flux of the zodiacal light at 4650Å is based solely on the flux calibration of our own spectra. We do, however, need a high–resolution solar spectrum which represents the width and depth of the absorption line features to high accuracy in the range 4200–5100Å. Outside of that range, a low–resolution spectrum will suffice.

There are several flux calibrated reference spectra of the Sun available in the wavelength range 0.2–1μm. A comprehensive review of the virtues and accuracy of each can be found in Colina, Bohlin & Castelli (1996), to which we refer the reader for a more complete discussion. For the reasons just discussed, we adopt the NL84 spectrum, both because it is the most accurate at blue wavelengths, and because it is the standard for defining the ZL color.

The only available, high–resolution spectrum of the Sun is the National Solar Observatory spectrum at 0.01Å resolution (Kurucz et al. 1984). The individual pieces of the spectrum are normalized to the local apparent continuum as described in the published Atlas. Quoted errors are of order 0.1% in the residual spectrum, and as is shown in the Atlas, agreement in the overlapping regions of the normalized scans is generally much better than 0.25%. In addition, atmospheric absorption due to H_2O or O_2 is thought to be negligible below 6500Å. In the optical, the normalized spectrum is converted to absolute solar irradiance using the NL84 absolute calibration. We therefore have confidence that the accuracy of the high–resolution spectrum does not contribute any significant error to our results.

The broad band–pass colors of various measurements of the solar spectrum vary by as much as 5–10% in the 3000–9000Å range. However, we need only be consistent in using the same solar reference spectrum with respect to which the ZL has been calibrated. Indeed, the standard solar spectrum against which the color of the ZL has typically been defined is the Neckel and Labs (1984) spectrum (Leinert 1977, Leinert et al. 1981). In addition, our own determination of the color of the ZL is by comparison of our FOS spectra with the Neckel and Labs spectrum. The color of the NL84 spectrum over the range 4000–9000Å is thus built into our definition of the color of the ZL, and its absolute accuracy is therefore irrelevant. Beyond the wavelengths observed by NL84, we have used the solar spectrum of Arvesen et al. (1969) in the near–IR (8700-9600Å), and Woods et al (1996) in the near–UV as recommended by Colina, Bohlin & Castelli (1996). These data were obtained from the STScI World Wide Web site (http://www.stsci.edu).

4.5 Results

The absolute flux of the ZL as measured from each of the 18 spectra taken on November 27 and November 29 are shown in Figure 4.9. The measurements plotted for each spectrum reflect the combined solution for the three wavelength regions indicated in Figure 4.6. Since we only expect roughly 4% variation in the color of the ZL with respect to the Sun over a 1000Å range, the *rms* scatter in our results is not small enough to detect the change in color over the 500Å range of our measurements. We therefore average results from the three wavelength bands together and estimate the error from the *rms* scatter.

There are several points to note about the results. First, while airglow features change continually throughout the night, our ZL measurement shows no temporal trends over the 18 spectra taken from twilight to twilight on two different nights, despite monotonic variations in the strength of airglow features (see Figures 4.9 and 4.7). Variations in the strength of Hg lines near 4130Å and 4915Å, for example, are clearly visible in Figure 4.7. In addition, the fact that our ZL measurements show no trend with airmass demonstrate the accuracy of our extinction solution, which we derived from our own standard stars observations. Finally, the same solution is obtained from data sets taken on two different nights, which were treated as completely independent data sets. These results are excellent agreement with typical values for the same viewing geometry quoted in the literature (see the geometrically smoothed averages given by Levasseur–Regourd & Dumont 1980).

Table 4.1: LCO error budget for zodiacal light flux

Step	Random Error	Systematic Uncertainty
Bias level removal (§4.1.2)	$< 0.01\%$	⋯
Dark current removal (§4.1.3)	$< 0.01\%$	⋯
Pixel–to–pixel flat–fielding (§4.1.4)	$< 0.01\%$	⋯
Slit illumination (§4.1.4)	⋯	$< 0.1\%$
Point source flux cal. (*rms* error)(§4.2.2)	0.5%	⋯
Extinction correction (*rms* error)(§4.2.2)	0.1%	⋯
Aperture correction (§4.2.3)	⋯	0.4%
Solid angle (§4.2.4)	⋯	0.5%
rms in correlation (§4.3)	0.8%	⋯
Total	0.9%	0.5-0.9%

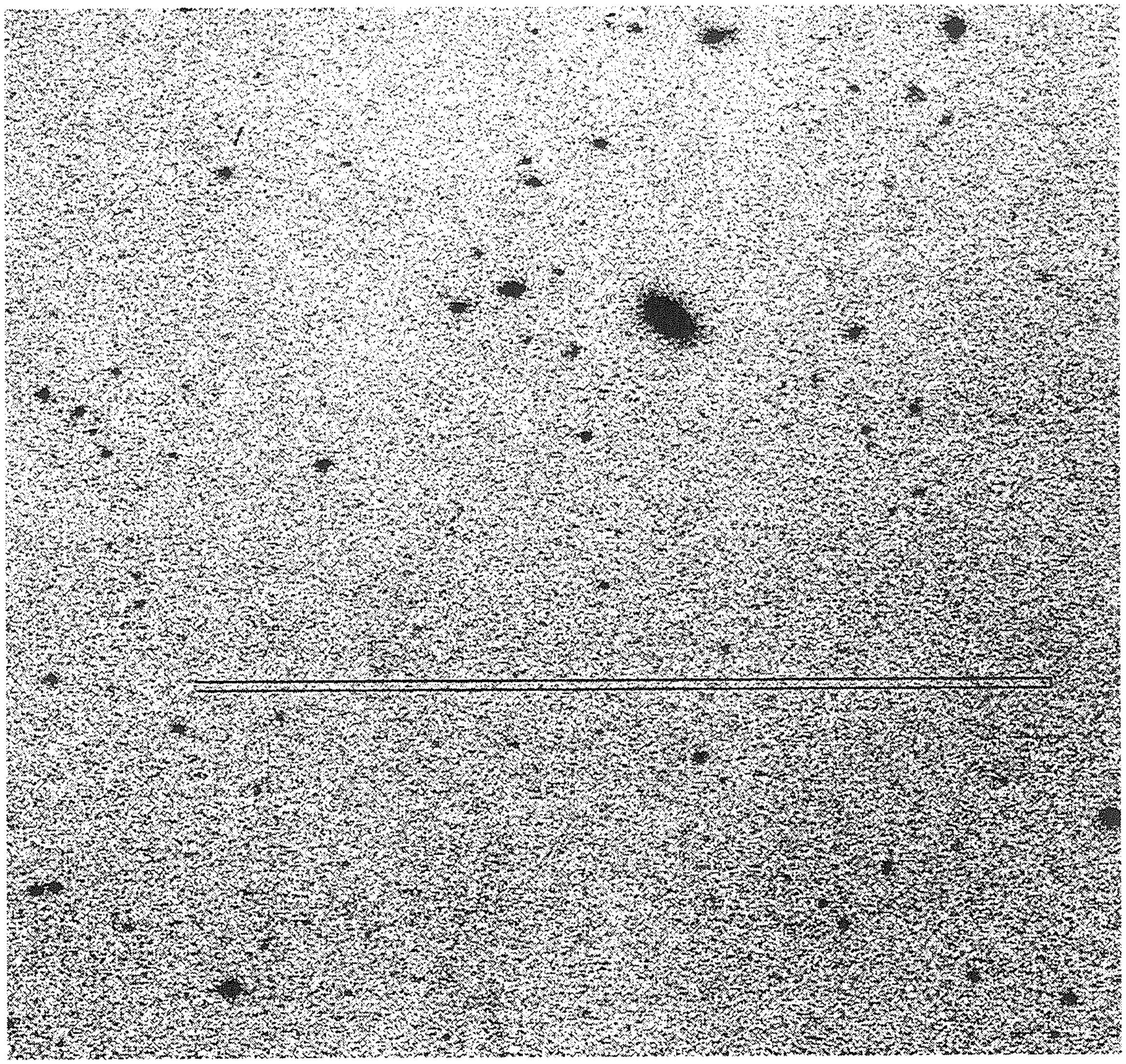

Fig. 4.1.— The slit position for the LCO observations is shown overlaid on an r-band image of the field taken with the 2.5m du Pont telescope at LCO. The pointing was selected to avoid galaxies to a limiting magnitude of 26mag/arcsec^2. The bright galaxy in the field is that imaged in the fourth WFPC2 chip (WF4). North is up. East is left.

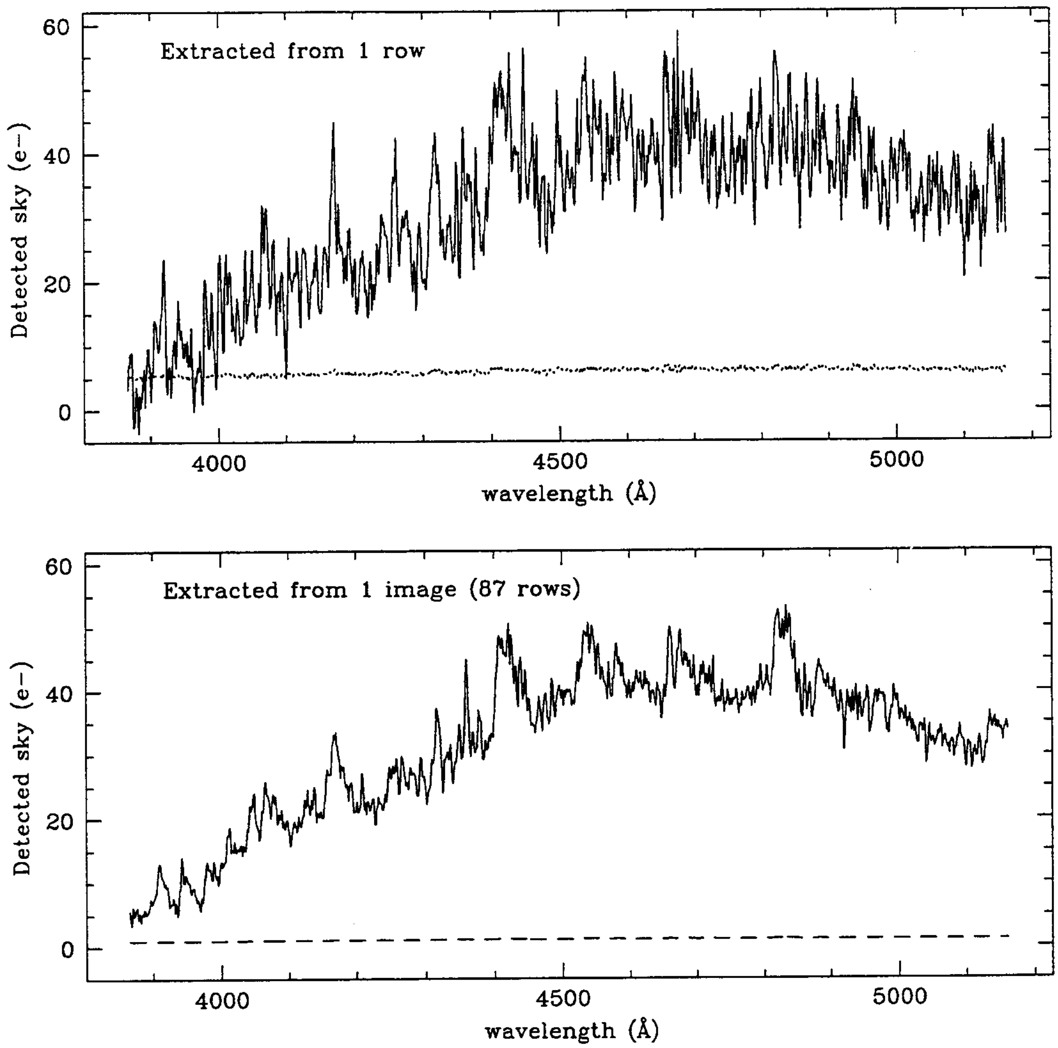

Fig. 4.2.— The upper plot shows the raw, wavelength calibrated spectrum obtained from a single row an 1800 second LCO observations of the night sky. The spectrum has been smoothed to the resolution of the observations. The dotted line shows the noise spectrum, which is read-noise dominated and therefore roughly constant across spectrum. The lower plot shows the spectrum produced by averaging together the data from 87 rows (a full image).

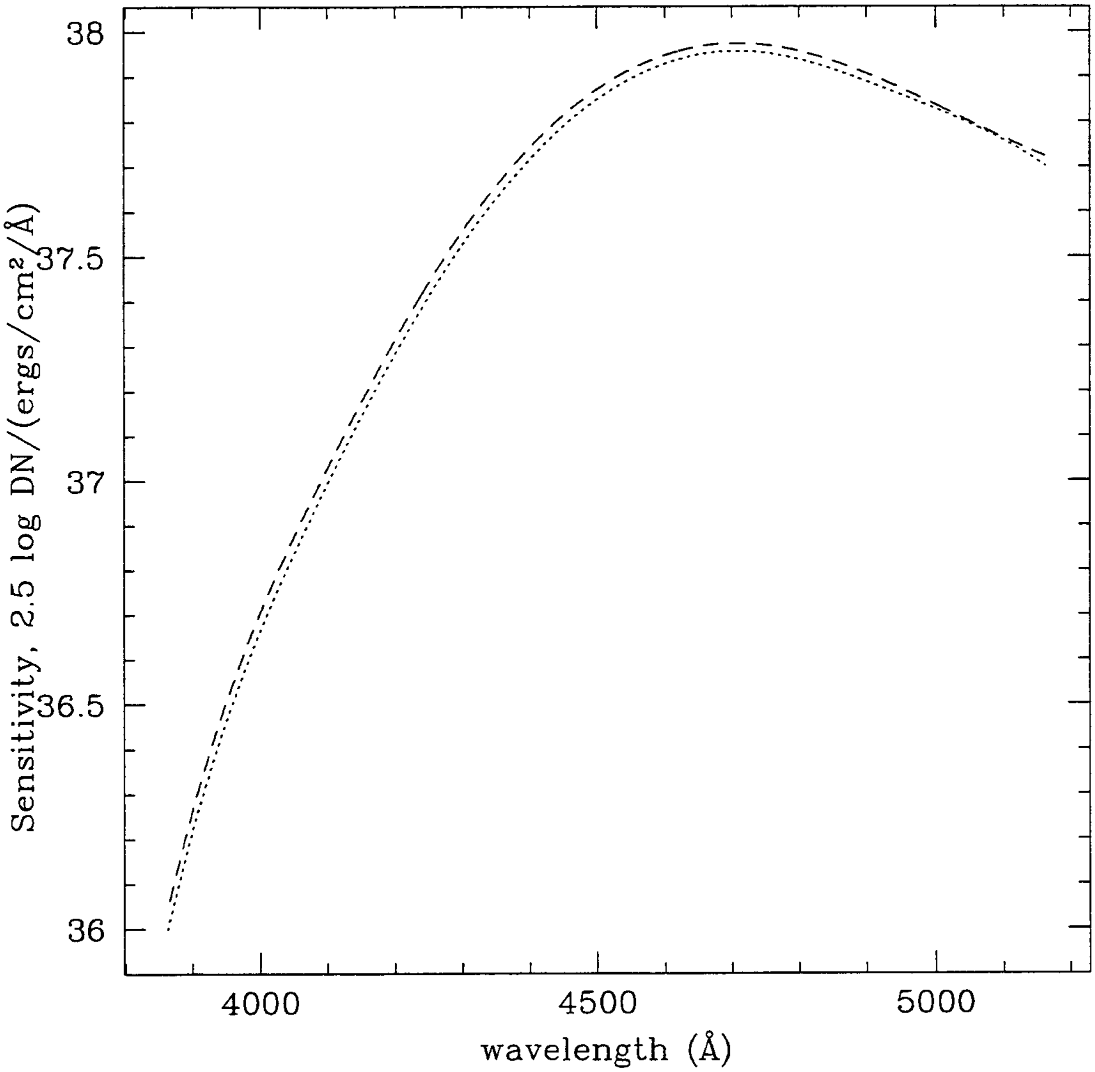

Fig. 4.3.— The plot shows the sensitivity functions obtained from observations of tertiary standards on 2 different nights. The solutions differ by 1-2%, well within the fluctuations which are expected due to slight variations in chip temperature.

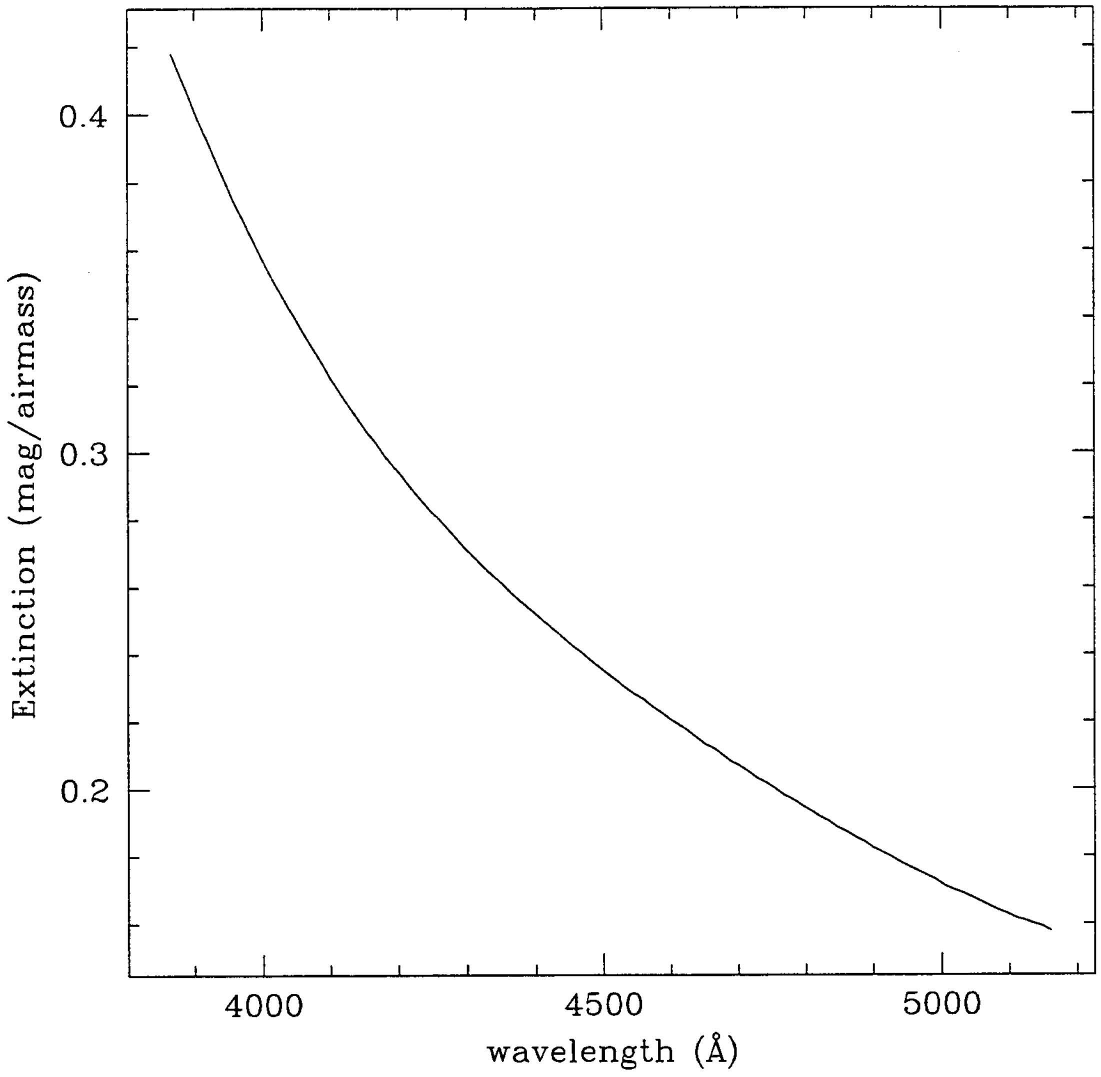

Fig. 4.4.— The plot shows the extinction function derived from standard star observations taken on two different nights. The extinction solutions on the two nights were found to be identical to within the errors (*rms* variations of less than 0.01 mag), so that the final extinction solution was determined from both nights together.

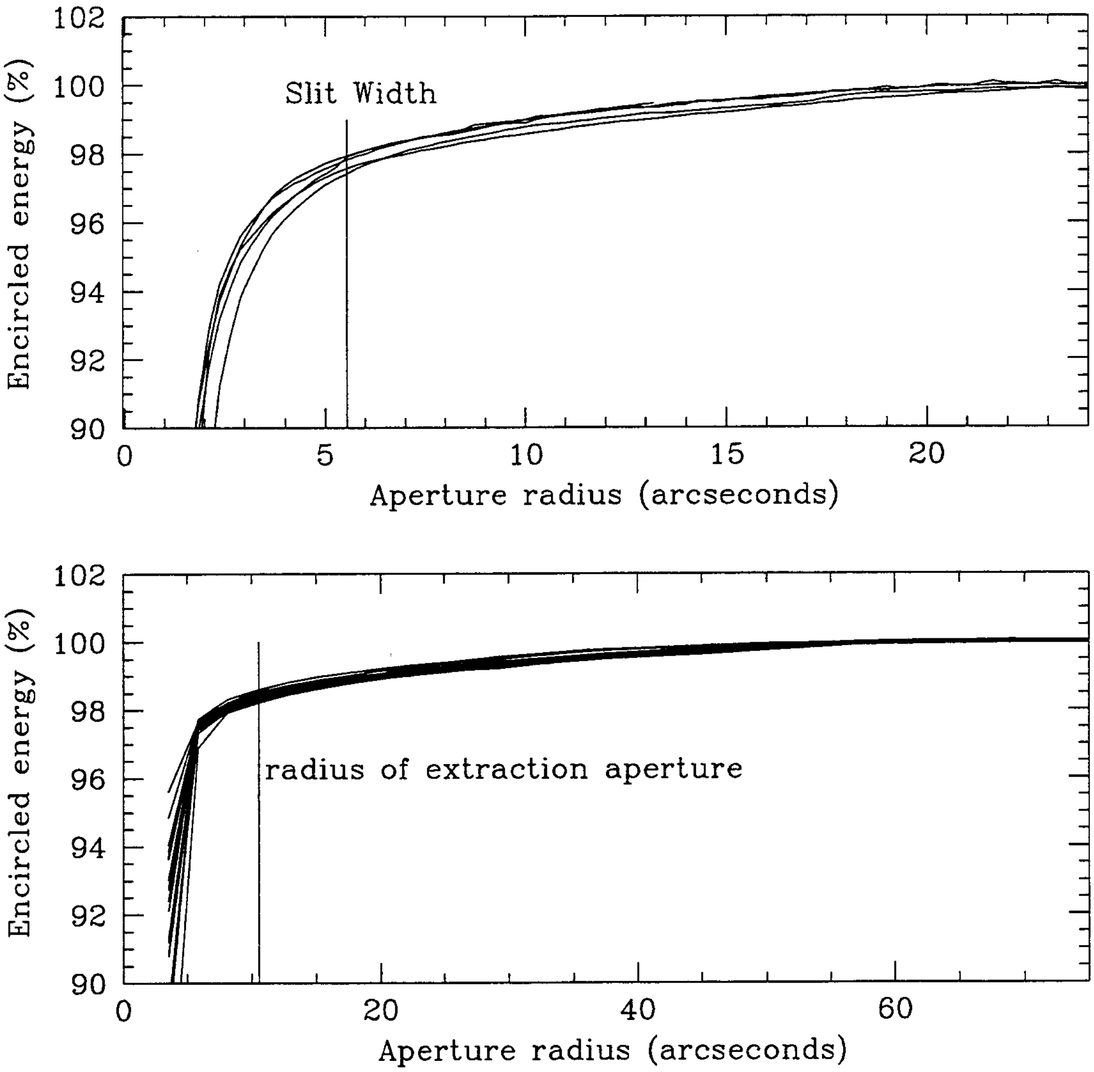

Fig. 4.5.— The upper plot shows the encircled energy curves in imaging data. Images are taken in the focal plane of the telescope and therefore can be used to determine the flux which will enter a 5.8 arcsec slit during spectroscopic observations. The lower plot shows the encircled energy curve along the spatial direction of a spectroscopic image. This plot shows that resolution is lost due scattering in the spectrograph: 98.4% of the light which passes through the aperture will be included in a 10 arcsec extraction aperture.

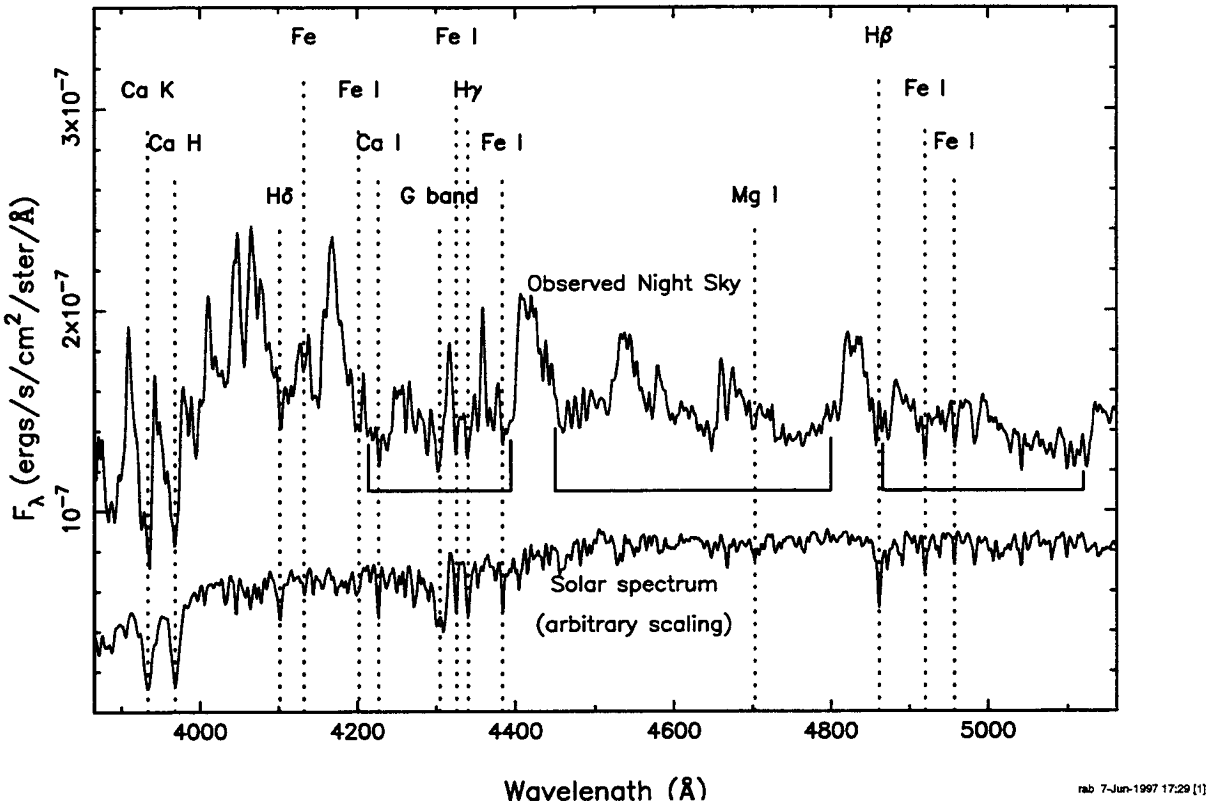

Fig. 4.6.— The plot shows both a spectrum of the night sky and a solar spectrum scaled to roughly the mean flux of the zodiacal light. The ZL contributes roughly two thirds of the total flux of the night sky from LCO. The solar absorptions features which are reproduced in the spectrum of the ZL are clearly visible in the spectrum of the night sky. The strongest Fraunhofer lines are marked. Note, however, that many of the solar features that appear at this resolution are blended, and therefore not marked. Most of these are also clearly visible in the spectrum of the night sky. The square brackets indicate the bands in which we measure the ZL.

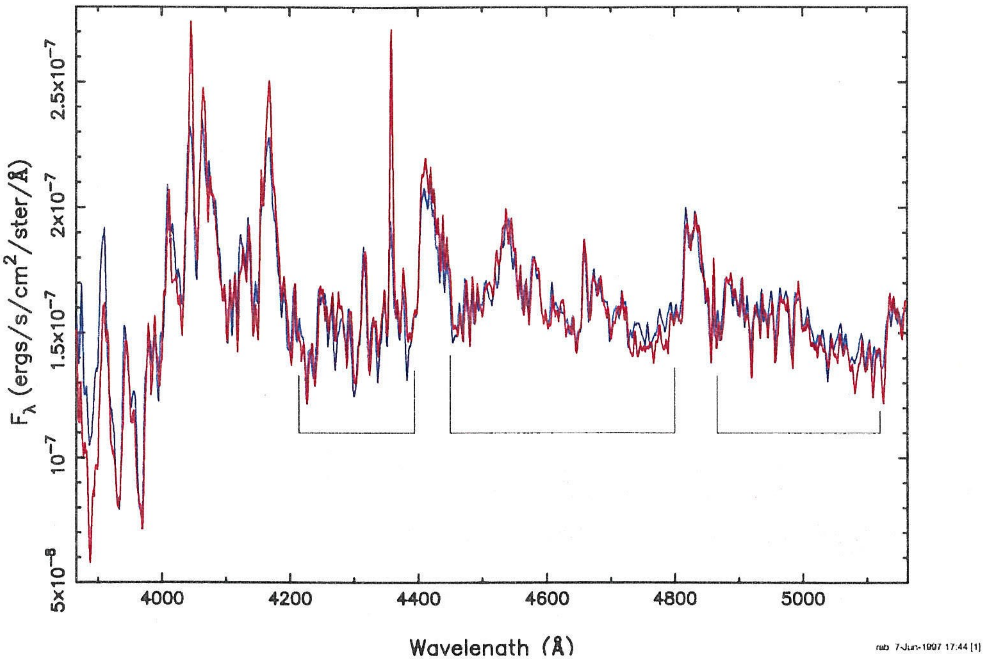

Fig. 4.7.— The plot shows two spectra of the night sky, both taken several hours from morning or evening twilight. Rapid fluctuations are evident in the strength of many of the airglow features.

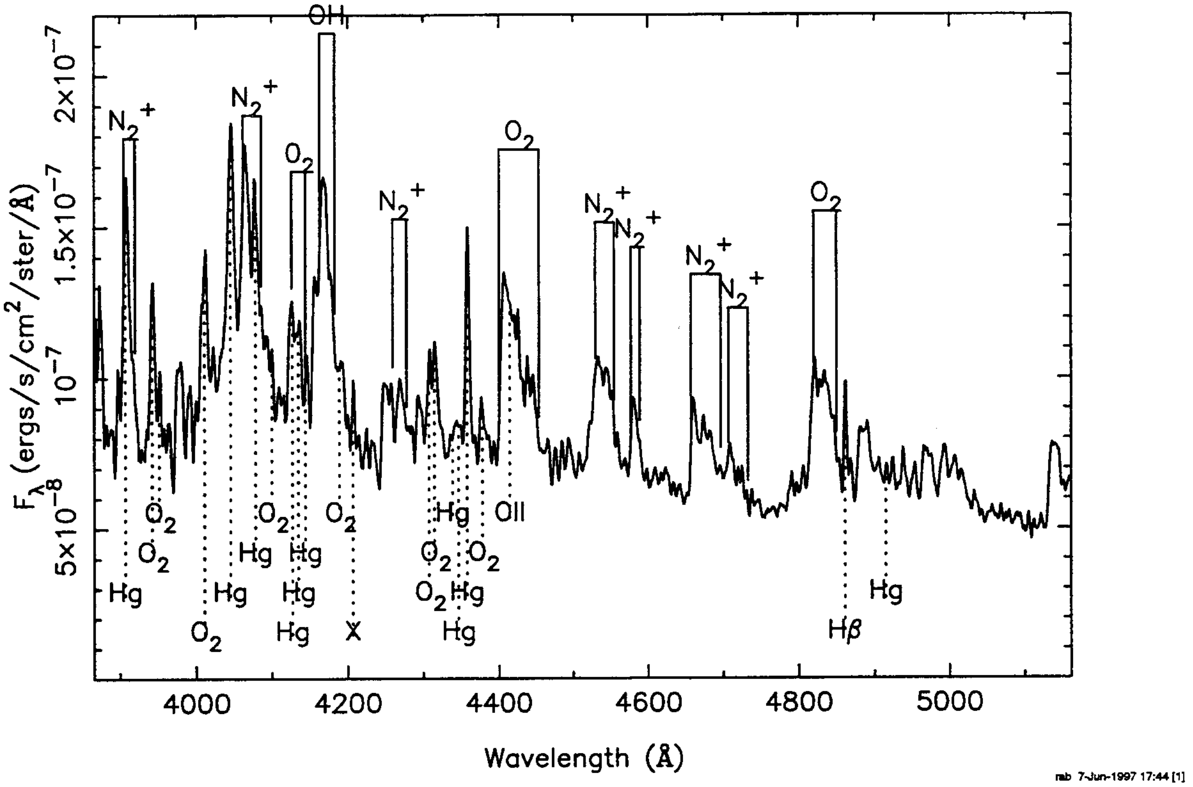

Fig. 4.8.— We label here some the prominent airglow features. The wide features are primarily molecular rotation–vibration bands of O_2, N_2, H_2, OH, and NO_2. Collisional de-excitation of these molecules contributes a continuum as well. Some emission lines from atomic transitions (photoionized O and Hg) are also present in this wavelength range.

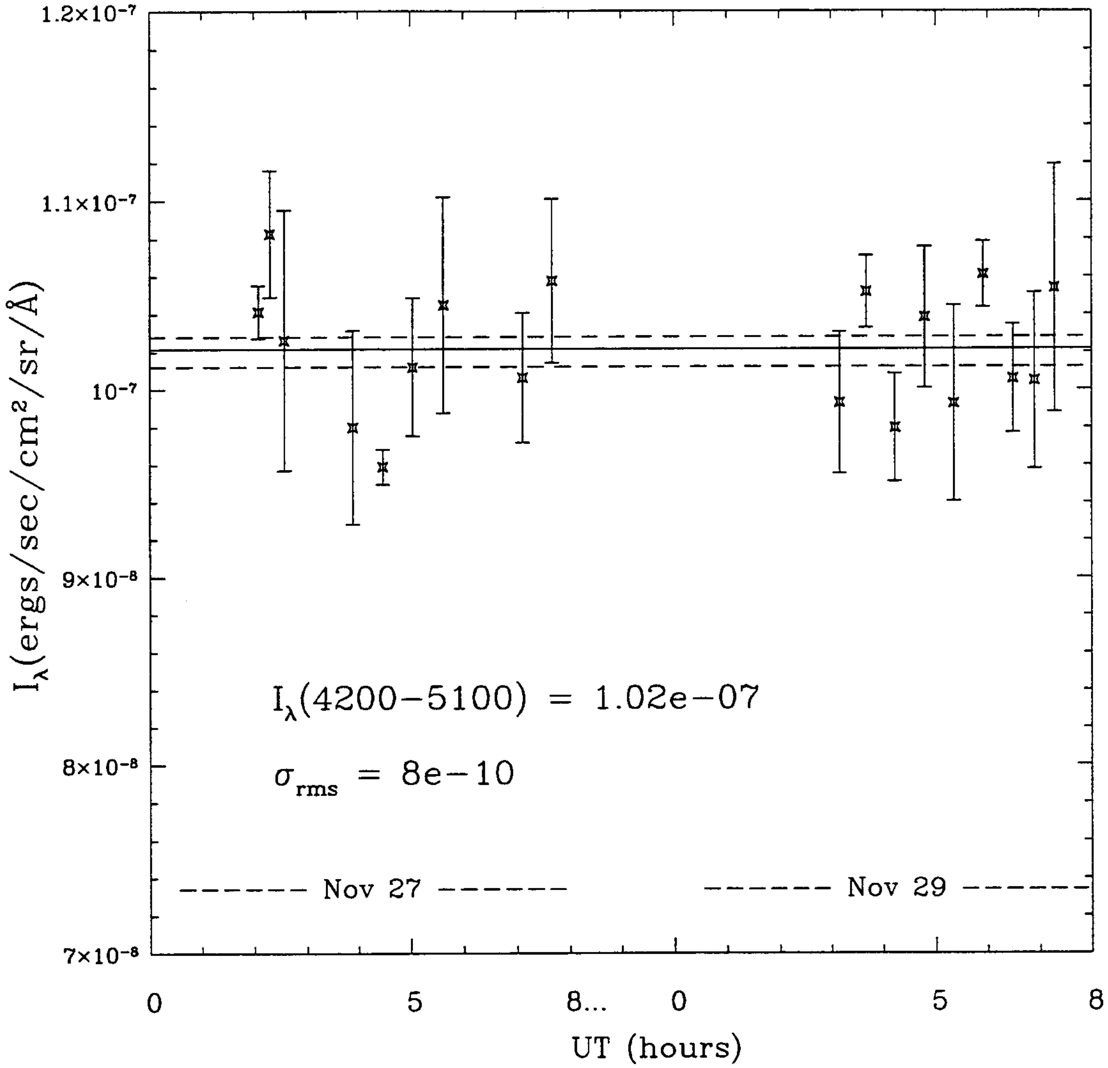

Fig. 4.9.— The points plotted show the mean flux of the zodiacal light as measured from 18 spectra taken on November 27 and 19. The error bar on each points indicates the scatter in the solution obtained from different regions of the spectrum. The solid line marks the level of the mean in our usual I_λ units, ergs $s^{-1}cm^{-2}sr^{-1}\AA^{-1}$. The dotted line shows the 1σ *rms* error in the mean level.

Chapter 5 Diffuse Galactic Light (DGL)

The diffuse Galactic contribution to the optical (3500 Å–1μm) surface brightness of the night sky is predominantly ambient starlight scattered off of interstellar dust. The distribution of dust in the Galaxy is highly structured and well correlated with the distribution of hydrogen nuclei. Both the optical scattering and thermal emission from interstellar dust are therefore non–isotropic and strongly correlated with observed HI column densities. Even where the surface brightness of the optical scattering is very low, it can therefore be predicted by the brightness of thermal emission from the dust, and also by the 21–cm emission line brightness which identifies the HI column density along the line of sight. In the near–UV (2500–3500 Å), the diffuse Galactic light consists of non–isotropic, dust–scattered starlight as well, but also includes an isotropic component resulting from free–free, bound–free, and two–photon emission.

In the following chapter, we discuss both the non–isotropic and isotropic components of the DGL. We begin with a discussion of the non–isotropic component caused by scattering of the interstellar radiation field (ISRF) off of dust, as this component dominates the DGL over the full range of our observations. We use a simple scattering model to predict the surface brightness of the optical and UV scattered light based on the observed thermal emission at 100μm. We compare the results of the model with observed ratios of UV and optical scattering to the thermal emission (I_{UV}/I_{100} and I_R/I_{100}, respectively). The isotropic contribution to the wavelength range of our observations is discussed in §5.2.

The reference frame of interest for discussing of the Galactic foreground contribution to our field is, of course, Galactic. Recall that in Galactic coordinates, the field center is at $l \sim 206.^\circ6$, $b \sim -59.^\circ8$ — well out of the plane and 154° from the Galactic center in longitude. The thermal emission at 100 μm in this field is given by the IRAS SkyFlux maps as roughly 0.4 MJy sr^{-1}. The absolute calibration of the SkyFlux images at 100μm is 20% with a sensitivity of $\pm$0.5 MJy sr^{-1}and 2 arcmin resolution (IRAS Explanatory Supplement, 1986). The extinction in the direction of this field can be estimated from the Burstein & Heiles (1978) HI observations, and is roughly $E(B-V)\sim 0.009$, or $A_V \sim 0.03$ mag.

5.1 DGL Due to Scattering (Non–isotropic)

Large scale optical structures associated with dust even at high Galactic latitudes have been noted in Schmidt plates by several observers over the last 30 years (de Vaucouleurs 1955; de Vaucouleurs & Freeman 1972; Sandage 1976; Danziger et al. 1974; King et al. 1979; Impey et al. 1996). The significance and prevalence of interstellar dust at high Galactic latitude, however, was not widely appreciated until the mid–1980's, when IRAS 100 μm maps showed thermal emission from dust streaking the sky at all Galactic latitudes. The dust which produces these cloudy structures is now commonly referred to as "Galactic cirrus."

Multiple–wavelength observations by both IRAS (12, 25, 60 and 100 μm) and DIRBE (100, 140, and 240 μm) have produced blackbody emission spectra for the dust which is characterized by temperatures $\sim 17°$K at high Galactic latitudes ($|b| > 50$) (Boulanger et al. 1996). While the dust is therefore not hot enough to radiate in the 2500–8500 Å range of our observations, it does scatter the ISRF efficiently and produces a non–isotropic, diffuse optical background which is correlated both with the dust column density and with the intensity of the ambient ISRF along the line of sight. As the surface brightness of the 100 μm flux is also a function of the dust column density and the strength of the ISRF which heats the dust, the easily–detected 100 μm emission is a good predictor of the optical surface brightness of the diffuse Galactic light.

The sensitivity of the IRAS 100 μm SkyFlux maps is roughly 0.5 MJy sr^{-1}(IRAS Explanatory Supplement). Poor calibration causes negative valued fluxes in some high latitude fields after the zodiacal light has been subtracted. HI atlases of the Galaxy show, however, that the N(HI) does not drop below a $\sim 3\times10^{19}\,\mathrm{cm}^{-2}$ at any orientation (Burstein & Heiles 1978; Stark et al. 1992). Burstein & Heiles (1978) estimates of the average E($B-V$) at the North and South Galactic poles are 0.01 and 0.02 mag, respectively. Based on scaling factors between I_{100} and N(HI) or E($B-V$), which are discussed below, one can infer that even at high Galactic latitudes, dust radiates with flux levels $> 0.1\,\mathrm{MJy\ sr^{-1}}$.

5.1.1 Empirical I_{UV}/I_{100} and I_R/I_{100} Correlations

Several groups have investigated and identified correlations between the IR surface brightness of the Galactic cirrus and its UV and optical surface brightness. In Tables 5.1 and 5.2, we list correlations found between measurements of the DGL at wavelengths between 1600Å and 7000Å at a range of Galactic orientations and low to moderate 100 μm flux levels (N(HI)$< 5 \times 10^{20}\,\mathrm{cm^{-2}}$, $I_{100} < 5\,\mathrm{MJy\ sr^{-1}}$). In general, while strong correlations between IR fluxes and optical or UV fluxes are found by all groups, poor agreement is found between the exact flux ratios. A technical cause of this disagreement is the low surface brightness and difficulty of the measurements, especially in the UV where detector backgrounds have been difficult to remove (Henry 1991, and references therein; Murthy & Henry 1995). A physical cause is asymmetric scattering from the dust.The intensity of the radiation scattered at an angle θ with respect to the direction of the incident light is described by the intensity weighted asymmetry factor,

$$g = \frac{\int_0^\pi I(\theta)\cos\theta\sin\theta d\theta}{\int_0^\pi I(\theta)\sin\theta d\theta} = \langle\cos\theta\rangle. \tag{5.1}$$

A value near 1 indicates strong forward scattering, a value near 0 indicates isotropic scattering. Evidence for large asymmetry factors ($g \gtrsim 0.6$) at near–UV to near–IR wavelengths comes from laboratory measurements of g for the components of astronomical dust and from observations of stellar outflows (Draine & Lee 1984, and references therein; Onaka & Kadaira 1991; Witt et al. 1997). Large asymmetry factors for interstellar dust imply that the light scattered to the observer is also a function of the direction from the scattering angle along the line of sight and the direction from which the ISRF illuminates the dust. Strong forward scattering causes the optical and UV fluxes to be weaker at high latitudes ($|b| > 50$) and at longitudes away from the Galactic center ($130 < l < 230$), where the scattering angle towards the observer would be large (i.e., backward scattering). This trend in I_{UV}/I_{100} and I_R/I_{100} can be seen in general from the data in Table 5.1 and 5.2. The entries in both tables are arranged from large (backward) to small (forward) scattering angles.

The data shown in Table 5.2 is a partial list of investigations of the optical/IR correlation for cirrus clouds at high Galactic latitudes. The correlations found for different clouds vary strongly, but also considerable variation is evident within the clouds (see, for example, Figures 5 & 6 in Guhathakurta & Tyson (1989), Table 1 in Laureijs et al. 1987). Measurement errors in both IR and optical or UV intensities are $\gtrsim 10\%$ in most cases. Note that the IR flux levels and N(HI) column densities for the fields list in Table 5.2 are roughly a factor of 10 higher than the values for our observed field ($I_{100} \sim 0.4$ MJy sr^{-1}, N(HI)$\sim 0.47\times10^{20}$ cm^{-2}, or E($B-V$)$\sim$ 0.009 mag).

5.1.2 Simple Scattering Model for I_λ/I_{100}

The near–UV is not a popular band for studying scattering off of Galactic cirrus. Empirical relations have been published in the far–UV and at optical B– and R–bands, but the expected surface brightness from scattering at 3000Å is not clear from these results: neither the optical depth of interstellar dust nor the ISRF is a monotonic function of wavelength between 1600Å and 4500Å (see Savage & Mathis 1979 and Mathis, Mezger, & Panagia 1983). To better understand contribution of non–isotropic DGL over the full range of our observations, we have used a basic radiative transfer model to predict the scattered light from dust. We compare the results of this model to the observations UV and optical dust–scattered DGL.

Assuming the Galactic cirrus along the line of sight in question is optically thin ($A_\lambda < 1.08$ mag), the surface brightness of scattered light off of interstellar dust can be expressed as a function of the scattering cross–section of the dust, $Q_\lambda^{\rm scat}$, and the surface brightness of the radiation field, j_λ, in ergs s^{-1}cm^{-2}sr^{-1}Å^{-1}. The effective scattering cross–section of the grains along the line of sight can be expressed as a function of the effective albedo of the dust population, ω_λ, and the total extinction along the line of sight, $Q_\lambda^{\rm scat} = \omega_\lambda \tau_\lambda$. The surface brightness of scattered light from the dust which scatters uniformly ($g = \langle \cos\theta \rangle = 0$) is simply $I_\lambda = j_\lambda\, \omega_\lambda\, \tau_\lambda$. Allowing for non–uniform scattering, the back–scattered intensity is given by Jura (1979) as

$$I_\lambda = j_\lambda\, \omega_\lambda\, \tau_\lambda\, S(g,b), \tag{5.2}$$

in which $S(g,b)$ is the Henyey–Greenstein phase function as expressed by Jura (1979) in terms of Galactic latitude, b, and average phase function of the dust, g:

$$S(g,b) = 1 - 1.1g\sqrt{\sin b}. \tag{5.3}$$

For $b \geq 50°$ and $g \approx 0.6$ (Draine & Lee 1984, hereafter DL84), $S \approx 0.4$. Note that this assumes no dependence on the scattering angle between the line of sight and the Galactic center (i.e., Galactic longitude). Such a dependence would merely imply that a significant fraction of the incident ISRF is from the direction of the Galactic center, which is indicated by the ratios I_λ/I_{100} listed in Tables 5.1 and 5.2.

To estimate the optical and UV scattered light, we then need estimates of τ_λ, ω_λ, and j_λ for a particular line of sight. Measurements of the optical depth, τ, or equivalently, the optical extinction in magnitudes, $A_\lambda = -2.5 \log e^{\tau_\lambda}$, have long been known to correlate well with the hydrogen column density. We can therefore use the scaling between τ and N(HI) to estimate τ. Although the relationship between total hydrogen nuclei column density, N(HI + H_2), and E($B-V$) has less scatter than the N(HI)–E($B-V$) relation, measurements of N(H_2) are much more difficult than for N(HI) alone.[1] This relation can be expressed as

$$\tau_\lambda = 0.921 \frac{R_\lambda}{N(\textrm{HI})/\textrm{E(B}-\textrm{V)}}\, N(\textrm{HI}), \tag{5.4}$$

---

[1] 21 cm line emission comes from the forbidden transition between the two hyperfine levels of the ground state of HI. The populations of the two levels is 3:1 for kinetic temperatures (close to the excitation temperature for interstellar gas) more than a few degrees Kelvin. Because probability distribution of states is known, the emission line strength is directly proportional to the number of atoms within the beam. The observed brightness temperature is therefore directly proportional to the column density of HI.

in which $R_\lambda = A_\lambda/\mathrm{E}(B-V)$ is the usual expression of the normalized extinction. Several groups find N(HI)/E($B-V$) between 48×10^{20} and $50\times10^{20}\,\mathrm{cm}^{-2}\,\mathrm{mag}^{-1}$ from measurements of the HI densities from 21 cm line emission strength and the reddening to globular clusters and star counts (Bohlin, Savage & Drake 1978, Burstein & Heiles 1982, Knapp & Kerr 1974). N(HI) can then be measured from in 21 cm emission maps to get the extinction along any line of sight when reddening studies or star counts are not practical.

The extinction can also be obtained by measuring the intensity of $100\,\mu$m thermal emission from the dust along a line of sight. The correlation between thermal emission and extinction is another consequence of the association between dust and hydrogen nuclei which produces the τ–N(HI) relation. I_{100}/N(HI) has been calibrated by Boulanger et al. (1988) using the IRAS $100\,\mu$m maps and a collection of N(HI) measurements around the sky from 21 cm observations. The correlation was corroborated using the better–calibrated COBE data (DIRBE and FIRAS instruments) and the Leiden/Dwingeloo N(HI) atlas of the Galaxy (Hartmann & Burton 1995). In both data sets, however, the simple linear relation between I_{100} and N(HI) breaks down for N(HI)$> 5 \times 10^{20}\,\mathrm{cm}^{-2}$, or $I_{100} > 5\,\mathrm{MJy\ sr}^{-1}$. Not surprisingly the τ/N(HI) correlation breaks down at that same point, as a direct result of the fact that the molecular gas fraction shows a sudden increase at N(HI)$= 5 \times 10^{20}\,\mathrm{cm}^{-2}$, corresponding to E($B-V$)$\sim 0.1$, or $\mathrm{A}_V \sim 0.3$ (Savage et al. 1977).

N(HI) rarely reaches such high levels at galactic latitudes of $|b| > 50$. The correlation between I_{100} and N(HI) which we use in our model for scattering should therefore be taken from high latitude N(HI) data. The fluxes in our field (roughly $0.4\,\mathrm{MJy\ sr}^{-1}$, or $0.47\times10^{20}\,\mathrm{cm}^{-2}$ are well within the range N(HI) $<5\times10^{20}\,\mathrm{cm}^{-2}$ found by Boulanger et al. (1996) to be described by I_{100}/N(HI)$\propto 0.85\,\mathrm{MJy\ sr}^{-1}/(\times10^{20}\,\mathrm{cm}^{-2})$.[2]

We take our estimate of the albedo of the dust from the models produced by DL84, which give both the albedo and asymmetry factor of interstellar dust based on an exponential distribution in grain sizes suggested by Mathis, Rumpl & Nordsieck

---

[2] A slightly different scaling, I_{100}/N(HI) $\propto 0.53\,\mathrm{MJy\ sr}^{-1}/(10^{20}\,\mathrm{cm}^{-2})$, is seen in from the DIRBE results (Boulanger et al. 1996). The difference is attributed to a well known calibration offset in the IRAS maps. Since we are using IRAS fluxes, we use the IRAS correlation.

(1977). The grains population consists of graphite and astronomical silicate[3] grains, the relative and overall abundances of which were determined by fitting synthetic extinction curves for the two populations to the observed extinction curves as summarized in Savage & Mathis (1979). The observed extinction curves are reproduced extremely well by the two–component model. Even more impressive is that they very accurately predict the thermal emission seen by DIRBE, which has better calibration than the IRAS 100 μm observations. This agreement implies that the τ–N(HI) estimate to which they calibrate the dust abundance and the ω–τ relation which results are well matched to the empirical evidence and produce an accurate, self–consistent picture.

Finally, the ISRF used here is that found by Mathis et al. (1983) for the solar neighborhood, taken as 10 kpc from the Galactic center. The spectrum Mathis et al. give is a combination of four stellar components which are combined to fit the observed radiation fields. The four components include a combination of early type stars, which dominate the UV emission, disk stars, which are described by diluted blackbody radiation with $T \sim 7500\,^\circ$K and $4500\,^\circ$K, and red giants, described by blackbody radiation with $T \sim 3000\,^\circ$K. Their estimates of the ISRF show the intensity dropping by a factor of 2 by 13 kpc. As our observations are 60 degrees out of the Galactic plane and away from the Galactic center ($l = 206\overset{\circ}{.}6$), this estimate of the ISRF is appropriate for our purposes, if not slightly high.

In summary, we use the values quoted in DL84 for the dust albedos, which are nearly constant at 0.6 over the wavelength range of our observations. The phase function from their models are high enough to imply that the scattering will be strongly forward, evidence for which is also seen in the lack of agreement between scattering strengths around the sky (see Table 5.1 and Witt et al. 1997). We take the energy density of the interstellar radiation field at 10 Kpc from Mathis et al. (1983). And we estimate the optical depth of the dust by the correlation $\mathrm{E}(B-V)/\mathrm{N(HI)} \propto 0.02\,\mathrm{mag}/(10^{20}\,\mathrm{cm}^{-2})$, which can then be expressed in terms of 100μm intensity as

---

[3] Astronomical silicate is a variation on olivine. Its scattering and emission properties are taken from laboratory measurements of olivine at high photon energies, and astronomical observations of stellar outflows in the infrared.

$E(B-V)/I_{100} \propto 0.024\,\mathrm{mag}/(\mathrm{MJy\ sr}^{-1})$, as found by Boulanger & Perault (1988). This allows us to calculate the intensity of optical and UV scattered light along the line of sight for a given I_{100}. The predicted scattered fluxes from our model are shown in Table 5.3.

5.1.3 Comparison Between Model and Observations

For ease of comparison with the quoted UV and optical correlations to IR fluxes, the results are expressed in units common to UV, optical and IR observations. The results demonstrate that the majority of scattering seen is well explained by a simple scattering model, which reproduces the observed mean fluxes and optical/UV colors of the scattered light with reasonable accuracy between the in 1600 and 4500Å, as is clear from comparison with the values listed in Tables 5.2 and 5.1 at $b > 45$. The phase function changes by less than 10% at latitudes $|b| > 50°$, so the values shown in Table 5.3, for which $|b| = 50$ was used, are generally representative for high latitude fields.

However, as noted by Guhathakurta & Tyson (1989, hereafter GT89), the observed optical colors, $B-R$ and $R-I$, are redder than predicted. GT89 find ratios of $I_\nu(R)/I_\nu(B) = 3.2$, 2, and 1.7 for fields ir1, ir2, and ir3, respectively, and $I_\nu(I)/I_\nu(R)$ 2.3, 2.1, and < 1.5 for ir3, ir4, and ir2. The predicted rations are $I_\nu(R)/I_\nu(B)$=1.4 and $I_\nu(I)/I_\nu(R) = 0.95$. One possible explanation for the discrepancy is that the scattering is more symmetric at longer wavelengths (see ω and g values from DL84 in Table 5.3), hence backscattered flux becomes stronger. The solution for ω and g from observed temperature and intensity relations is degenerate, so that larger g and smaller ω are possible (Witt et al. 1997, Onaka & Kodaira 1991, Laureijs et al. 1987), however strong wavelength dependence in the range 4500–9000Å has not been found from laboratory or space observations.

One obvious explanation for the red observed optical colors of cirrus is a contribution from something other than dust scattering. One possibility is structured Hα emission. Optical studies of cirrus are differential, and would only be sensitive to a structured contribution. GT89 have, however, looked for structured Hα emission using narrow–band observations in their fields and have failed to identify a dust–correlated contribution. Diffuse ionized gas at high Galactic latitudes does produce Hα emission (see discussion in §5.2), but a uniform contribution would not be identified in relative flux measurements on and off of the clouds being studied.

Another possible explanation is suggested by observations of reflection nebulae, which also show excess red emission over predictions of scattered fluxes. In reflection nebulae, the emission is thought to be associated with fluorescence from molecular hydrogen, and hydrogenated amorphous hydrocarbons (HAC) and polycyclic aromatic hydrocarbons (PAH) excited by ultraviolet radiation. Such emission would be expected to correlate with CO, and in fact, strong correlations between the small scale structure in CO and I_B have been observed by Stark (1995) in clouds with high peak I_{100} fluxes (5–7 MJy sr^{-1}), large A$_V$ (0.4–1.0 mag). As mentioned above, the relevance of this contribution to fields with 10 times less I_{100} and N(HI) is not clear, however, as the density of molecular gas is correlated with column densities of N(HI) $> 5\times10^{20}$ cm^{-2}. Strong variations in the correlation between color and molecular gas density both in and between fields indicate that the emission may be very sensitive to self–shielding effects, optical depth and local ISRF. Indeed, the results of GT89 show that the degree of reddening is well correlated to the average I_{100} emission, even if it does not correlate well with the structure within the cloud. Stark (1995) has demonstrated that variations within the cloud can be a complicated function of the CO distribution. It seems conservative, therefore, to adopt optical colors found for the fields with the lowest IR flux in the GT89 sample, listed in Table 5.2. Note that the IR flux in the 2 lower flux fields (ir2 and ir3) is more than a factor of 10 higher than in our own.

We therefore estimate the optical flux in our field from using our scattering model for $\lambda < 4500$, and adjust the predicted scattering model at redder wavelengths to match the average colors observed by GT89: $I_\nu(R)/I_\nu(B) \sim 1.8$ and $I_\nu(I)/I_\nu(R) \sim 2.0$. The resulting spectrum is flat in I_λ, with a value of roughly 0.9–1.0$\times10^{-9}$ ergs s^{-1}cm^{-2}sr^{-1}Å^{-1}from 3000–9000Å. Finally, we note that our scattering model was not dependent on Galactic longitude, although observations do show some dependence on the scattering angle of interstellar radiation from the Galactic center. This, again, makes our predicted values conservatively large for the field of our WFPC2 observations.

5.2 Isotropic Contributions to the DGL

Isotropic components at wavelengths < 3700 Å have taken longer to identify and appreciate than the scattering component for the obvious reason that faint, isotropic components are only seen in absolute measurements of surface brightness. In the far–UV ($\lambda < 2000$ Å), the zodiacal light makes a negligible contribution to the background light. Contributors to the isotropic or slowly varying background flux as seen from rocket-borne observations in the far–UV are therefore either Galactic or extragalactic. In the last 10 years significant progress been made in differentiating the two (Reynolds 1985; Henry 1991; Martin, Hurwitz, & Bowyer 1991; Wright 1992).

The presence of warm ionized gas well beyond the plane of the Galaxy ($|b| > 15$) is demonstrated by pulsar dispersion measures and also by the faint optical emission lines of Hα, [NII]λ6584Å, [SII]λ6716Å. Fabry–Perot observations of the diffuse Galactic Hα emission find significant levels at all orientations. For $|b| > 5°$, Reynolds (1984) finds the average intensity to be consistent with that predicted by the path–length through a slab model for the galaxy, with significant flux even at the poles: $I(\mathrm{H}\alpha) \approx 2.9 \times 10^{-7} \csc|b|$ ergs $\mathrm{s}^{-1}\mathrm{cm}^{-2}\mathrm{sr}^{-1}$(Reynolds 1992). Note, however, that line emission of this strength would contribute roughly 0.1% to the background we have detected with the WFPC2 through the F555W filter even if the line were at the point of peak sensitivity in the band–pass. Hα, however, is only at the edge of the F555W band–passes, where the sensitivity is roughly 10% of peak, so that Hα of the strength found by Reynolds will contribute at most 0.01×10^{-9}ergs $\mathrm{s}^{-1}\mathrm{cm}^{-2}\mathrm{sr}^{-1}$Å^{-1}to our measurement. [OII] at 5007Å, which is near the peak of our band–pass, is predicted (and detected) to be lower in intensity than Hα by a factor of 20 (Reynolds 1985, Shields et al. 1981).

More important than the total flux contributed by Hα, however, is the hydrogen two–photon, free–free and bound–free continua associated with the ionized gas densities that are implied by the detected Hα line strengths.[4] The spectrum of continuum emission is flat in I_λ with a few notable exceptions. Bound–free emission arises from the recombination of free electrons to bound states. The recombination coefficient changes abruptly at the onset of recombination to each level, causing a sharp drop in emission at Balmer (λ = 3648Å) and Paschen (λ = 8208Å) limits, corresponding to electron capture to levels $n = 2$ and $n = 3$ in hydrogen. The other exception occurs in the far–UV and is the result of two–photon emission during the transition of electrons from the 2s–1s bound states. The probability distribution of emitted photons is peaked at equal energy ($\nu(\mathrm{Ly}\alpha)/2$, λ=2421Å), so that the energy emitted as a function of wavelength is skewed, peaking on the low-wavelength side of the distribution, at 1620Å. While two–photon emission is significant for far-UV observations, it therefore does not significantly contribute to our observations: it peaks in the far–UV at roughly 0.6×10^{-9}ergs s^{-1}cm^{-2}sr^{-1}Å^{-1}, and falls roughly as $\lambda^{-1.4}$ at longer wavelengths.

The combined spectrum of free–free, bound–free, and two–photon emission was calculated by Aller (1987) as a function of electron and ion densities, and has been expressed by Reynolds (1992) as a function of the observed Hα emission. The total continuum spectrum which is emitted as a function of the Hα observed at the Galactic poles is a function of the temperature of the warm ionized medium. For our purposes, a conservative estimates of the total isotropic, continuum for gas temperatures $T \sim 10^4$ is given by Aller (1987) and Reynolds (1992) as $I_\lambda(\lesssim 3700\mathring{A}) < 0.3\times10^{-9}$ergs s^{-1}cm^{-2}sr^{-1}Å^{-1}and $I_\lambda(\gtrsim 3700\mathring{A}) < 0.01\times10^{-9}$ergs s^{-1}cm^{-2}sr^{-1}Å^{-1}.

---

[4] Several forbidden lines in the far–UV and near-IR ([NII]λ1220 and λ2050Å, [CII]λ158Å, and [CII]λ7μm) are also associated with the observed Hα, but are not relevant at the wavelengths of this work.

5.3 Summary

The DGL predicted by our scattering model gives us an upper limit to the non-isotropic Galactic contribution to our field. It includes dust properties from the DL84 model, which are very well matched to observed thermal, scattering, and extinction properties of the interstellar dust at high Galactic latitudes. Our model includes a scattering phase function which accounts for Galactic latitude, but not for Galactic longitude. In this respect, the results are an upper limit, as larger scattering angles for light from the Galactic center will produce smaller scattered fluxes. The model is in good agreement with the observed ratios of scattering to thermal emission, but is slightly bluer at long wavelengths than some observations have seen. As all of these observations are in clouds with higher N(HI) (and higher 100 μm fluxes) than our own field by a factor 10, it is not clear that the molecular effects which are thought to cause this reddening are relevant to our field. Nonetheless, as a conservative estimate of the DGL contributing to our observations, we have corrected our model to have redder colors between 4500 and 9000Å.

The isotropic contribution to our field from continuum emission (two–photon emission) is negligible. The flux from line emission also makes a negligible contribution to our band–passes, both because most of the atomic transition lines miss our band–passes, and also because our bands are 1000Å wide, and line emission is therefore strongly diluted.

We take the DGL contribution to each of WFPC2 fields to be $I_\lambda(DGL) = 1.0\times10^{-9}$ (ergs $s^{-1}cm^{-2}sr^{-1}Å^{-1}$) at F300W, 0.8×10^{-9}at F555W, and 0.8×10^{-9} at F814W.

Table 5.1: Observed correlation: $I_{0.16\mu\mathrm{m}}/I_{100}$

Reference	l^a	$\|b\|^a$	$I_{0.16}/I_{100}$		I_{100}
	(°)	(°)	$\mathrm{CU}^b/(\mathrm{MJy\,sr^{-1}})$	$I_\lambda{}^c/(\mathrm{MJy\,sr^{-1}})$	$\mathrm{MJy\,sr^{-1}}$
Witt et al. (1997)[e]	$\langle 145\rangle$	$\langle 30\rangle$	72	0.86×10^{-9}	$2-8$
Hurwitz et al. (1991)[d]	$135-220$	> 40	$80(\pm10)$	0.96×10^{-9}	$1-5$
Sasseen et al. (1995)[e]	$\langle 270\rangle$	$\langle 45\rangle$	< 233	$< 2.8\times10^{-9}$	$2-8$
Jacobsen et al. (1987)	$\langle 70\rangle$	$\langle 50\rangle$	$65(\pm25)$	0.78×10^{-9}	$1-2.2$
Witt et al. (1997)	$\langle 290\rangle$	$\langle 45\rangle$	258	3.10×10^{-9}	$2-8$

a: Bracketed values represents an average for the data used in the calculation.

b: CU = photons $\mathrm{s^{-1}\ cm^{-2}\ sr^{-1}\AA^{-1}}$.

c: I_λ = ergs $\mathrm{s^{-1}cm^{-2}sr^{-1}\AA^{-1}}$.

d: We calculate $I_{0.16}/I_{100}$ for Hurwitz et al. (1991) from the points plotted in their Figures 2a,b.

e: Witt et al. use a model which includes the average scattering angle and phase function along the line of sight. Based on their observations, this entry shows their predict value for $I_{0.16}/I_{100}$ at the Galactic position indicated.

Table 5.2: Observed correlations: $I_{B,R,I}/I_{100\mu\mathrm{m}}$

Reference	$l°$	$b°$	$I_{0.45}/I^a_{100}$	$I_{0.65}/I^b_{100}$	$I_{0.90}/I^c_{100}$	I_{100}
GT89 - ir1[d]	174	-42	0.36×10^{-3}	1.1×10^{-3}	...	11.4
Laureijs et al. 1987[e]	211	-37	0.48×10^{-3}	...	...	6.3
GT89 - ir2	235	37	1.1×10^{-3}	2.2×10^{-3}	$< 1.6\times10^{-3}$	3.6
Paley et al. 1991	104	-32	4.8×10^{-3}	8.0×10^{-3}	11.0×10^{-3}	2.5
GT89 - ir3	38	45	2.6×10^{-3}	4.4×10^{-3}	6.0×10^{-3}	5.9

All intensity units in this table are I_ν expressed in MJy sr^{-1}.

a: At 0.45 μm, I_ν (MJy sr^{-1}) = 1.5×10^{-6} I_λ(ergs s^{-1}cm^{-2}sr^{-1}Å^{-1}).

b: At 0.65 μm, I_ν (MJy sr^{-1}) = 7.1×10^{-7} I_λ(ergs s^{-1}cm^{-2}sr^{-1}Å^{-1}).

c: At 0.90 μm, I_ν (MJy sr^{-1}) = 3.7×10^{-7} I_λ(ergs s^{-1}cm^{-2}sr^{-1}Å^{-1}).

d: Guhathakurta & Tyson 1989 – field designation

e: From the data in Laureijs et al. 1987, Table 1

Table 5.3: Model correlations: I_λ/I_{100}

λ	τ_λ/N(HI) [a]	ω^b_λ	$S(g,b)^c$	I_λ/I_{100}		
Å	$(10^{20}\,\mathrm{cm}^{-2})^{-1}$			CU[d]/(MJy sr^{-1})	(MJy sr^{-1}/(MJy sr^{-1})	I_λ[e]/(MJy sr^{-1})
1600	0.120	0.410	0.42	181.96	1.86×10^{-4}	2.18×10^{-9}
2500	0.130	0.550	0.50	94.54	3.69×10^{-4}	1.77×10^{-9}
3000	0.105	0.581	0.54	118.09	7.97×10^{-4}	2.66×10^{-9}
4500	0.068	0.600	0.56	68.75	1.57×10^{-3}	2.32×10^{-9}
5500	0.047	0.600	0.59	42.85	1.78×10^{-3}	1.77×10^{-9}
6500	0.042	0.600	0.61	32.66	2.24×10^{-3}	1.59×10^{-9}
8000	0.032	0.540	0.68	18.82	2.41×10^{-3}	1.13×10^{-9}
9000	0.025	0.500	0.71	11.76	2.14×10^{-3}	7.94×10^{-10}

a: Optical depth as a function of HI column density. The values used are given by Savage & Mathis (1979) and match the standard value of A_V/N(HI)=0.06 mag/ ($10^{20}\,\mathrm{cm}^{-2}$) (Bohlin, Savage & Drake 1978).

b: Albedo, taken from model by Draine & Lee (1984).

c: Scattering phase function in terms of asymmetry parameter, g, as calculated by Draine & Lee (1984).

d: CU = photons $\mathrm{s}^{-1}\mathrm{cm}^{-2}\mathrm{sr}^{-1}\mathrm{Å}^{-1}$.

e: I_λ = ergs $\mathrm{s}^{-1}\mathrm{cm}^{-2}\mathrm{sr}^{-1}\mathrm{Å}^{-1}$.

Chapter 6 Combining HST & LCO Measurements to Detect the EBL

In the previous chapters we have described two measurements of the absolute flux of the night sky from *HST* using WFPC2 and FOS. These measurements include the extragalactic component from galaxies fainter than our adopted bright magnitude cut–off of $V_{555} = 23$ as well as zodiacal and galactic foreground emission. We have also described a ground–based measurement of the zodiacal light (ZL) using spectra from Las Campanas Observatory. This measurement of the ZL is in the field of view of the WFPC2 images and was made at precisely the same time as the WFPC2 and FOS observations. Finally, we have used both empirical results in the literature and a simple scattering model to estimate the contribution of diffuse galactic light (DGL) due to dust–scattered starlight.

As in Chapter 2, we use the notation $I_{\rm EBL}(V > 23)$ to indicate the extragalactic flux from all galaxies fainter than $V_{555} = 23$. This reflects the fact that we use the V_{555}–band to define the bright magnitude cut–off and also to define the masking regions used for all three of the WFPC2 bands. This ensures that we are consistent in our definition of the EBL as a function of wavelength, and that the contribution as a function of wavelength is not varying due to the detection limits or spectral energy distributions of the detectable objects. The flux from extragalactic sources, $I_{\rm EBL}(V > 23)$, is the difference between the total background measured from *HST*, $I_{\rm Tot}(V > 23)$, and the foreground components of ZL and DGL. The accuracy with which we can determine $I_{\rm EBL}(V > 23)$ depends upon the accuracy of the individual measurements, and the assumptions we must make in synthesizing the results. We therefore begin this chapter by reminding the reader of the accuracy and limitations of each of the measurements, and the methods we employ to incorporated the foreground and background results. The confluence of Chapters 2–5 is measurement of the EBL which is presented in §6.3.

6.1 Summary of Foreground and Background Measurements

The total integrated background has been measured from above the Earth's atmosphere using data from *HST*/WFPC2 and *HST*/FOS. The WFPC2 images provide measurements of the total background $I_{\rm Tot}(V > 23)$ through wide–band filters centered at 3000, 5500, and 8000Å. These are the F300W, F555W, and F814W filters, respectively, and each is roughly 1000Å wide. We have excluded galaxies brighter than $V_{555} = 23$ from this measurement by masking them out, and hence we refer to a total flux from objects with $V > 23$ as $I_{\rm Tot}(V > 23)$. The measurements which result from these observations have random errors of $< 1\%$ of the total background flux (Table 2.7) and systematic uncertainties of roughly 1–2% of the total background flux (Table 2.8). The mean levels of $I_{\rm Tot}(V > 23)$ shown in Figure 2.14. Recall that $I_{\rm ZL}$ is between 20 times the predicted minimum for $I_{\rm EBL}$ from galaxy counts at 3000Å, and as much as 90–100 times the predicted minimum at 5500Å and 8000Å (see Figure 1.5). An uncertainty of 1% in $I_{\rm Tot}$ therefore translates into 20% and as much as 50–100% uncertainty for our measurement of the $I_{\rm EBL}$ in the near–UV (3000Å) and optical (5500 and 8000Å) band–passes, respectively.

The FOS spectra also provide a measurement of total flux in the range 4000–7000Å with spectral resolution of roughly 300Å. The precision per resolution element is around 2.5%, and the systematic uncertainty over the full range is roughly 4%. Again, these percentage errors are fractions of the total background flux, $I_{\rm Tot}$, in the FOS observations, and therefore several times the expected EBL. The FOS has too small a field of view (see discussion in Chapter 3) and these errors are too large to make the FOS useful for measuring the absolute flux level of the EBL. However, the majority of the systematic uncertainty in the FOS observations results from wavelength independent effects. The FOS spectra therefore provide a measurement of the color of the total background flux which has a statistical error of $\lesssim 1\%$ in the slope.

Anticipating our results, the total background from *HST* is $\sim 97\%$ zodiacal light. The color of the spectra taken with the FOS is therefore clearly dominated by the color of the ZL. The color of the ZL is relevant to this measurement because the absolute flux of the ZL can only been determined using high resolution spectra (~ 2Å) with excellent flux calibration ($\pm 1\%$). At present, these criteria can only be met using ground–based observations, and airglow lines preclude the measurement of the ZL outside of the range 4000–5100Å. Accordingly, we have measured the absolute flux of the ZL in a band centered at 4650Å using spectra taken at Las Campanas Observatory; the resulting measurement has a precision of 0.8%, and a systematic uncertainty of $< 1\%$. This absolute flux must be extrapolated from 4650Å down to 3000Å and up to 8000Å in order to remove the ZL contribution from the *HST* measurements of $I_{\rm Tot}$. This requires knowledge about the color of the ZL. As discussed in §§1.2.2, and 4.5, the broad–band spectrum of the ZL is redder than the spectrum of the Sun by roughly 5%/1000Å.[1] Our FOS measurement is the most accurate measurement of the ZL color available; but like most measurements of the color of the ZL, it includes the color of the EBL which we are trying to isolate. This limitation is not insurmountable, but it does figure prominently in our uncertainties.

In this chapter, we briefly discuss the observations and calculations of the color of the ZL. As mentioned above, most measurements of the ZL color in the literature include the color of the EBL which we seek to measure. Our measurement with the FOS is no exception, however the WFPC2 observations can be used in conjunction with the FOS and LCO data to place much stronger limits on the color of the ZL than has previously been possible.

---

[1] As discussed in §1.2.2, it is common to describe the broad–band color of the ZL as a function of the solar spectrum: $C(\lambda, \lambda_0) = \frac{I_{ZL}(\lambda)/I_\odot(\lambda)}{I_{ZL}(\lambda_0)/I_\odot(\lambda_0)}$. If $\lambda > \lambda_0$, then $C(\lambda, \lambda_0)$ is greater than 1 for a spectrum which is red with respect to the solar spectrum.

6.2 The ZL Through the WFPC2 Band–passes

We can create a spectrum of the ZL with absolute flux calibration by scaling a solar reference spectrum to match our measurement of the absolute flux of the ZL at 4650Å. At this stage in the analysis, we use as our solar reference spectrum a composite of the UV solar spectrum of Woods et al. (1997), the optical spectrum from NL84, and the infrared spectrum produced by Arveson (1969), as recommended by Colina, Bohlin & Castelli (1996). We obtained this spectrum from the STScI World Wide Web site (http://www.stsci.edu), where it was made available by that collaboration.

In addition to scaling the solar spectrum to the mean level which we measure for the ZL at 4650Å, we must also redden our scaled solar spectrum slightly to obtain the correct color in the flux calibrated ZL spectrum over the full range 2500–8500Å. Our FOS spectra provide the most accurate measurements of the combined $I_{\rm ZL}+I_{\rm EBL}$ color available from 4000–7000Å, and are clearly the most relevant to our observations as they pertain exactly to the scatting angles and zodiacal dust column densities at issue here. Before we discuss the degree to which the color of $I_{\rm ZL}$ and $I_{\rm EBL}$ can be separated, it is interesting to compare our results to other observations of the ZL in the literature. We begin with a brief explanation of the scattering which produces the ZL spectrum and the color which is predicted by scattering theory.

6.2.1 Evidence for the Color of the Zodiacal Light

Röser & Staude (1978) showed that Mie scattering of sunlight by large ($r > 10\mu$m) grains could explain the solar–like spectrum of the ZL over the full wavelength range from the UV to the near–IR (1500Å to 10μm). While near–neutral colors for the ZL were long claimed, slight color deviations are now well documented (Leinert et al 1981; Murthy et al. 1990; Matsuura et al. 1995). At the 10% level, the color of the ZL results from several competing effects, with the dominant effect varying as a function of wavelength. Mie scattering from smooth grains is wavelength independent for wavelengths (λ) and grain sizes (a) such that $a \gtrsim \lambda$. For $a < \lambda$, however, longer wavelengths will be less efficiently scattered, causing bluing of the spectrum. Surface roughness, on the other hand, causes less efficient scattering at wavelengths shorter than the characteristic roughness scale, and therefore results in reddening of the incident spectrum. The exact color of the spectrum produced by Mie scattering was shown by Weiss–Wrana (1983) to depend strongly on the exact composition of the scattering particles, and by Schiffer (1985) to depend strongly on the exact scale of the characteristic roughness. A great deal is known about the composition of the IPD and the size distribution of the particles from far–IR observations (Reach et al. 1996, using ISO; Reach 1988, using IRAS; Berriman et al. 1994, using DIRBE), laboratory scattering studies of particles captured in the upper atmosphere (Brownlee 1978), studies of lunar microcraters (Fechtig et al. 1974), and basic dynamical considerations (Dermott et al. 1996). Nonetheless, the composition and size distribution of the IPD is not uniform, and both models and laboratory results show that the spectra are extremely sensitive to size distributions, compositions, and surface properties. The color of the zodiacal light cannot, therefore, be predicted with the accuracy we require. We turn then to the empirical observations.

The Helios space probe measured the ZL at visual wavelengths to be reddened by of order 5% per 1000Å with respect to solar spectrum (Leinert et al. 1981), with reddening decreasing at larger elongation angles (ϵ) and greater ecliptic latitudes ($|b|$). Specifically, Leinert et al. find $C(5500, 4400) = 1.05$ and $C(3650, 4400) = 1.03$ (quoted accuracy ± 0.04) for orientations similar to those of our own observations ($\epsilon \approx 130°$, $|b| \approx 31°$). Models for the Galactic background were used to isolate the color of the ZL, however the EBL was not considered in their measurement.

In a program designed to measure the EBL in the UV, Murthy et al. (1990) found that the color of the ZL in the UV is almost linearly related to $|b|$, and actually becomes bluer than the Sun at high enough viewing angles out of the ecliptic plane ($|b| \gtrsim 50°$). At the ecliptic latitude of our measurement ($|b| \sim 35\overset{\circ}{.}5$), they find $C(5500, 2500) = 1.17$ (redder than solar), with a total calibration uncertainty of at least 0.1. The correlation between color and latitude is likely to indicate that smaller grains ($< 0.5\mu$m) are more uniformly distributed out of the plane than larger grains (due to Poynting-Robertson forces), so that while the redder wavelengths are less efficiently scattered at $|b| \gtrsim 30°$, scattering efficiency at shorter wavelengths does not drop off as quickly. Murthy et al. (1990) do not find a strong change in the color of the ZL over the spectral range of their observations, 1650–3100Å, which makes it seem unlikely that the color of the ZL is very much farther from unity than the value they quote. Their measurement results from spectral observations, which allows them to isolate the ZL from the EBL. While this is encouraging in terms of a consistent picture for the ZL and interplanetary dust (IPD) characteristics, the limited accuracy of this measurement is not particularly helpful for our purposes (see Figure 6.1).

Finally, the results of recent rocket experiments (Japanese rocket programs S-520-11/15) at 1.4–4μm find the near-IR color of the ZL to be $C(5500, 1.25\mu\mathrm{m}) = 1.3 \pm 0.2$ around $b = 45°$ (Matsuura et al. 1995). While the poor absolute calibration of this result makes it of limited use for us in pin-pointing the ZL color, this value is in excellent agreement with the $\sim$ 5%/1000Å at optical wavelengths, which would predict $C(5500, 1.25\mu\mathrm{m}) = 1.35$ if the color remains linear over the full near-UV to near-IR wavelength range.

6.2.2 Implications

Two important conclusions may be drawn from the empirical and theoretical evidence concerning the broad-band color of the ZL. First, the color of the zodiacal light at all wavelengths is seen to change not only with scattering angle but also with ecliptic latitude. This is evidence for a gradual change in the characteristics of the IPD as a function of position in the ecliptic. Such changes are not particularly surprising, as distinct structures have also been observed in the IPD. The near-Earth ring and low-latitude dust bands are good examples of the dramatic segregation of particles which can result from dynamical effects (Dermott et al. 1996; also see Reach et al. 1996 for ISO results; Reach 1988, from IRAS; and Berriman et al. 1994, using DIRBE/COBE).[2] Thus we conclude that for observations of the ZL color to

---

[2] Gravity and Poynting-Robertson drag dominate the forces on larger particles, so that they tend to spiral in towards the Sun. Smaller particles ($\lesssim 0.5\mu$m are more affected by Lorentz forces, and thus tend towards increasing inclinations and orbital radii. Such grains would thus have a much more uniform distribution with latitude, while the large grains which scatter visible light would

be relevant to an observation, they must be taken along very similar lines of sight to the observations in question. With this limitation, the results of other groups from observations along similar viewing angles (discussed above and plotted in Figure 6.1) are clearly in good agreement with the color we find from our ZL measurements. Given the low accuracies of the results plotted for other groups, and the necessary inclusion of the EBL in those measurements, this is not particularly enlightening for our purposes, although it does represent the sum total of knowledge on the issue.

The second conclusion to be drawn is far more helpful to us, and concerns the rate at which the color of the ZL varies with wavelength. The observed broad-band spectrum of the ZL is well explained by Mie theory and only weak wavelength dependence is observed. Between 2000Å and a few microns, the color of the zodiacal light is seen to be roughly linear with wavelength — the total intensity of the zodiacal light changes by 5% with respect to intensity of the Sun over every 1000Å interval from 2500Å–1.4μm. If variations in this linear slope exist, they have not been observed. If any higher order dependence on wavelength does exist between the scales of moderate resolution spectroscopy and broad-band photometry, measurements would clearly need to have accuracies on order 1% to detect them. Our FOS observations border on this accuracy, and we note that no significant deviations from a linear color are apparent in our data.

6.2.3 Adopted Color

For the reasons enumerated above, we use our own FOS and WFPC2 data to determine the color, $C(\lambda)$, of the ZL under the assumption that the color of the ZL is a linear function of wavelength and that any slight deviations from linear will be averaged out over the 1000Å band-widths of the WFPC2 filters. By subtracting the spectrum of the DGL from the total background spectrum measured by FOS, we

---

concentrate in the plane. The UV bluing trend at large $|b|$ can thus be interpreted as the result of a drop in visible surface brightness with increasing ecliptic latitude, while the UV surface brightness resulting from small ($a \sim \lambda$) grains does not change as quickly with latitude. In addition, cometary contribution to the IPD will have high orbital inclinations and will therefore remain out of the plane while the low-latitude IPD will be predominantly asteroidal in origin.

obtain a color for the remaining flux ($I_{\rm EBL} + I_{\rm ZL}$) which is roughly 4.4%/1000Å.

Based on the results in the literature, we can assume that the color of the ZL does not vary by more than a few percent from this value over the range 2000Å–1μm. We can identify more stringent limits for the color of both the ZL and the EBL, however, if we consider the mutual constraints which are set by the WFPC2, FOS, and LCO data. For clarity, we describe below the calculation of the ZL through the WFPC2 band–passes before we return to the discussion of separating the EBL from the ZL in the next section (6.3).

The spectrum of the zodiacal light is uniquely defined by our measurement of the mean flux of the ZL at 4650Å, the solar spectrum, and the color of the ZL:

$$I_{\rm ZL}(\lambda) = I_{\odot}(\lambda)\, C(\lambda)\, \frac{I_{\rm ZL}(4650)}{I_{\odot}(4650)}. \tag{6.1}$$

Explicitly, for reddening of 4.4%/1000Å with respect to solar, normalized at 4650Å, the color of the ZL is given by $C(\lambda) = 0.044 \times (\lambda/1000\text{Å}) + 0.795$.

The spectrum $I_{\rm ZL}(\lambda)$ as expressed above is then an absolute flux-calibrated spectrum of the ZL, which we can convolve with the SYNPHOT throughput tables (using the version released in May 1997) in the usual way to obtain the absolute flux of the ZL through each of the filters. The flux through the WFPC2 band is given by

$$I_{\rm WF}(\lambda) = \frac{\int T(\lambda)\, I_{\lambda}(\lambda)\, \lambda\, d\lambda}{\int T(\lambda)\, \lambda\, d\lambda}, \tag{6.2}$$

in which $T(\lambda)$ is the throughput of a WFPC2 filter, $I(\lambda)$ is the spectrum of the zodiacal light, and all spectra are in units of of ergs $\rm s^{-1}cm^{-2}sr^{-1}Å^{-1}$, as usual. No addition error results from convolving the flux calibrated ZL with the band–passes that define the WFPC2 system, as any error in the SYNPHOT synthetic photometry is incorporated in our estimate of the WFPC2 systematic errors. As discussed in §§2.2.1 and 4.2.1, the agreement between the two fiducial systems is well within the quoted uncertainties of point source calibrations.

6.3 The Extragalactic Background Light

The EBL in each of the three WFPC2 bands is the difference between the total mean background measured in the WFPC2 images, I_{Tot}, and the foreground contributions of ZL and DGL:

$$I_{\mathrm{EBL}}(\lambda) = I_{\mathrm{Tot}}(\lambda) - \left[I_{\odot}(\lambda)\, C(\lambda)\, \frac{I_{\mathrm{ZL}}(4650)}{I_{\odot}(4650)} \right] - I_{\mathrm{DGL}}(\lambda). \qquad (6.3)$$

As we have noted, the color indicated by the FOS must include a contribution from the EBL and the DGL. The DGL is relatively flat in I_λ, and that contribution can easily be removed using the results of Chapter 5. After the DGL is subtracted, the FOS spectrum is composed of ZL and EBL. Only if the EBL is flat in I_λ would the color of ($I_{\mathrm{EBL}} + I_{\mathrm{ZL}}$) be the appropriate color to adopt for the ZL. If, on the other hand, the EBL is blue, then the ZL is slightly redder than the color measured by the FOS spectra. If the EBL is red, the ZL is slightly bluer.

At both 3000Å and 8000Å, we infer the maximum ZL flux if we assume the minimum possible flux for the EBL. By considering the maximum possible I_{ZL} at 3000 and 8000Å, and comparing those maxima to the absolute flux which we have measured at 4650Å, we can identify the extrema possible for the color of the ZL. The WFPC2 data can be used to define a maximum value for the ZL independent of the LCO and FOS data if we can identify a minimum possible EBL. We can do so by making the very conservative assumption that all of the flux in the EBL is associated with objects brighter than our completeness limit of $V_{555} = 28$ ST mag. This is a conservative assumption in the sense that even if all extragalactic light is associated with galaxies, our detection limit is quite bright: objects are detected down to $V_{555} \sim 30$ ST mag in the deeper exposures (e.g., the HDF). We then need to identify the flux associated with detected galaxies in order to determine the maximum ZL at 3000 and 8000Å.

The simplest method for measuring the flux from detected objects fainter than $V_{555} = 23$ ST mag, without using our absolute ZL measurement, is the following. After the initial detection of the objects, we can simply measure the total sky flux, including foregrounds, by masking out a generous region around every object brighter than $V_{555} = 23\,\mathrm{ST\,mag}$ and taking the average of the remaining pixels in the image.[3] As discussed in §2.4, this gives us the the total background sky flux including all objects fainter than 23 ST mag, $I_{\mathrm{Tot}}(V > 23)$. If the goal were an absolute measurement of the EBL, then we would need to subtract exactly the flux of the foreground contributions, $(I_{\mathrm{ZL}} + I_{\mathrm{DGL}})$. As our goal in the current exercise is to determine a *lower limit* to the EBL, we can simply mask out *all* detected objects to our detection limit ($V_{555} > 28\,\mathrm{ST\,mag}$) and take the average flux per pixel over the remaining pixels, $I_{\mathrm{Tot}}(V > 28)$, as an estimate of the foreground flux. This approach avoids the process of local sky estimation and individual object photometry. In other words, we measure the total flux in the frame including objects and the total flux in the same frame excluding objects. The difference of the two is obviously the flux contributed by objects. This measurement has no systematic flux calibration errors and none of the typical photometry errors which result from local sky estimation or detection–limit–defined isophotal, total, or corrected magnitudes. This method of measuring flux from objects is simply the equivalent of using a *very* generous aperture magnitude and with a single estimate of the sky value taken from the whole frame.

To mask objects in the range $23 < V < 28\,\mathrm{ST\,mag}$, we use the same basic mask definition (an elliptical region 3 times the isophotal detection radius) which was used for the $V < 23\,\mathrm{ST\,mag}$ galaxies discussed in §2.4, with the additionally stipulation that the minor radial axis must be at least three pixels. In other words, if the detection isophote had a minor axial radius of less than three pixels, then the radius was set to three, the major axial radius scaled accordingly, and then both dimensions were grown by a factor of three. This produces masks which are never smaller than $\sim 10\,\mathrm{kpc}$ in the rest frame of the object.[4] Note that we have masked out regions which are a factor of three times larger than maximum area used for the smallest

---

[3] $V_{555} = 23\,\mathrm{ST\,mag}$ is the magnitude at which galaxies become numerous enough in a $2\,\mathrm{arcmin} \times 2\,\mathrm{arcmin}$ WFPC2 field that the Poisson fluctuations in their number density become an insignificant source of error.

[4] The minimum apparent angular size corresponding to 1 kpc is 0.14 arcsec, for $\Omega = 0.2$, $H_0 = 75$ km/s/Mpc, or 0.17 arcsec for $\Omega = 1.0$.

objects in the HDF object catalog, in which objects are allowed to have two pixel (0.2 arcsec) radii, and are grown by a factor of two in area, or $\sqrt{2}$ in radius.

Any "uniform" extragalactic component will be included in this estimate of the sky level, so that the method we are describing here does not provide a true measurement of the EBL, but rather a strict lower limit. Not only will inter-galactic components be included in this sky estimate, but any contribution from objects with central surface brightness faint enough to escape detection will also be included. This is quite different from measuring the EBL by identifying the absolute fluxes of the foreground sky (ZL and DGL) explicitly. At the very least, roughly 1000 galaxies are seen in the HDF with V_{606} or B_{450} magnitudes in the range 28—30 ST mag (see Figure 2.8). We can therefore be certain of overestimating the foregrounds by using $I_{\rm Tot}(V > 28)$ as an estimate of the sky level.

In the remaining work, we abbreviate this method for determining the flux from detected objects (a minimum value for the EBL) as $I_{23<V<28}$. Note that we can calculate this quantity for all three of the bands F300W, F555W, or F814W using the masks made from the detection of objects through the F555W. The minimum EBL estimated in this way is shown in Figure 6.3. Note that this minimum EBL measurement is immune to all systematic calibration problems which have been mentioned in the Chapters 2–4, because only one instrument and one calibration system is involved. All of the systematic errors discussed in Chapters 2–4 which affect absolute surface brightness calibrations are irrelevant here. Only *rms* errors contribute to this measurement of the minimum EBL flux. This lower limit therefore has error bars which are less than 1% of 1×10^{-9}, not 1% of 100×10^{-9}. This limit is also immune to possible errors in galaxy photometry, as we have not assigned individual fluxes to the galaxies. The minimum EBL in the V_{814}–band is then 0.5×10^{-9}, which tells us precisely the maximum flux of the ZL at 8009Å (the effective wavelength of the ZL through the V_{814}–band). One extreme for color of the ZL then follows by comparing the $I_{\rm ZL}(8009\AA)$ with the absolute flux which we measured for the EBL at 4650Å. The change in the relative strength of the ZL to the solar spectrum, $C(\lambda)$, is constrained in this way to be $\lesssim$5.5%/1000Å.

Similarly, the minimum flux of the EBL at 3230Å (the effective wavelength of the ZL through the V_{300}–band) indicates that the ZL can be no bluer than 3.5%/1000Å. The possible colors of the EBL are then constrained to the hatch–marked region in Figure 6.3. The maximum uncertainty in the EBL in the F300W and F5555W measurements is then less than 1×10^{-9} due to uncertainty in the ZL, while the flux in the F814W is dominated by uncertainty in the ZL. This is difficult to avoid as the ZL must be extrapolated over 3000Å to obtain an estimate at the F814W based on our measurement at 4650Å.

The WFPC2 and LCO observations therefore show that the total range of possible colors for the ZL in our field as $C(\lambda)$=3.5–5.5%. This is completely independent of the FOS measurement, but does, in fact symmetrically bound the 4.4% color found for the total background as measured by FOS. Beyond demonstrating merely that all three instruments were looking at the same sources, as one would certainly hope, this also shows that the calibration of all three instruments is in excellent agreement.

We can summarize our detection of the surface brightness of the EBL from galaxies fainter than V_{555} = 23 ST mag as follows (units of ergs $\mathrm{s^{-1}cm^{-2}sr^{-1}Å^{-1}}$):

I_λ(F300W): 4.0×10^{-9} $(\pm1.9\times10^{-9})_{rms}$ $[\pm2.0\times10^{-9}]_{sys}$ $[\pm0.4\times10^{-9}]_{C(\lambda)}$,
I_λ(F555W): 2.8×10^{-9} $(\pm0.8\times10^{-9})_{rms}$ $[\pm1.6\times10^{-9}]_{sys}$ $[\pm0.7\times10^{-9}]_{C(\lambda)}$, and
I_λ(F814W): 2.3×10^{-9} $(\pm0.6\times10^{-9})_{rms}$ $[\pm1.1\times10^{-9}]_{sys}$ $[\pm1.7\times10^{-9}]_{C(\lambda)}$.

The systematic uncertainty in each measurement, indicated by the subscript *sys*, is given separately from the uncertainty caused by the possible range in the color of the ZL, which is indicated by the subscript $C(\lambda)$.

We can define strict lower limits to the EBL, with errors less than 0.001×10^{-9}, by computing the flux from all detected objects using the method which we have abbreviated as $I_{23<V<28}$. The lower limits to the EBL are:

$I_{23<V<28}$(F300W): $\geq 2.9\times10^{-9}$ $(\pm\ 0.2\times10^{-9})_{rms}$ $[\pm\ 0.14\times10^{-9}]_{sys}$,
$I_{23<V<28}$(F555W): $\geq 0.6\times10^{-9}$ $(\pm\ 0.01\times10^{-9})_{rms}$ $[\pm\ 0.01\times10^{-9}]_{sys}$, and
$I_{23<V<28}$(F814W): $\geq 0.5\times10^{-9}$ $(\pm\ 0.01\times10^{-9})_{rms}$ $[\pm\ 0.01\times10^{-9}]_{sys}$.

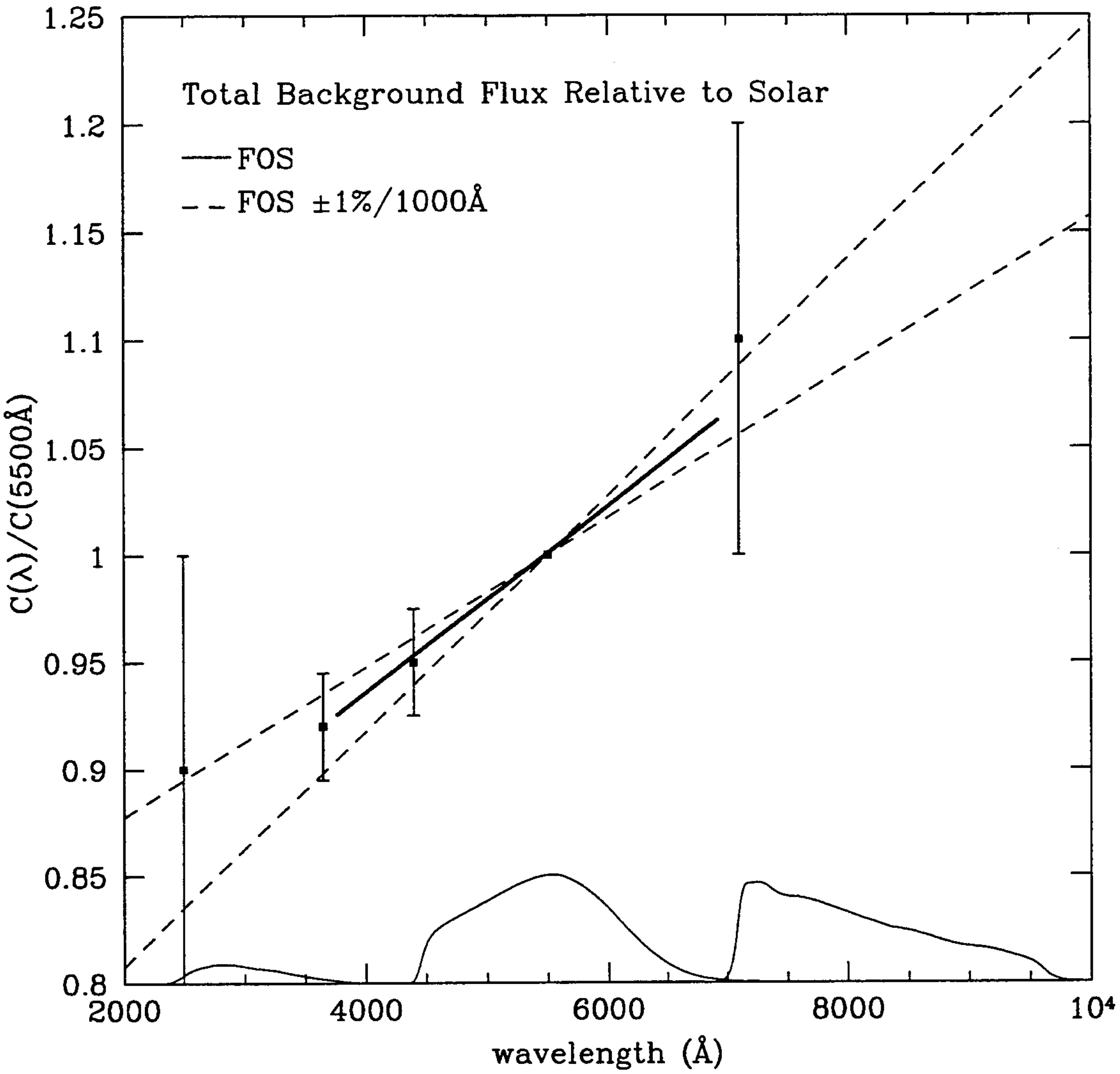

Fig. 6.1.— Observed colors of the zodiacal light relative to the solar spectrum. The solid line shows the color we obtain for the total background flux, ZL+EBL+DGL, with the FOS relative to the solar spectrum. The slope of the FOS data is 4.25%/1000Å redder than the solar spectrum. The points at *U* (3650Å) and *B* (4400Å) show the results of the Helios space probe at $|b| \sim 35°$ and elongation angle $\epsilon \sim 135°$ (Leinert et al. 1981). These measurements also include any diffuse galactic component and the EBL. The point at 2500Å shows the results of Murthy et al. (1990) at pointings near $|b| \sim 35°$, $\epsilon \sim 135°$. The Murthy et al. work isolates the ZL color from other backgrounds spectroscopically, so that the point plotted represents the color of the ZL alone. The point at 7100Å shows the data of Frey et al. (1974), also at $|b| \sim 35°$, $\epsilon \sim 135°$, and it includes other backgrounds. The dashed lines show the bluest and reddest ZL colors which our WFPC2 data allow, 3.0%/1000Å and 5.5%/1000Å, respectively.

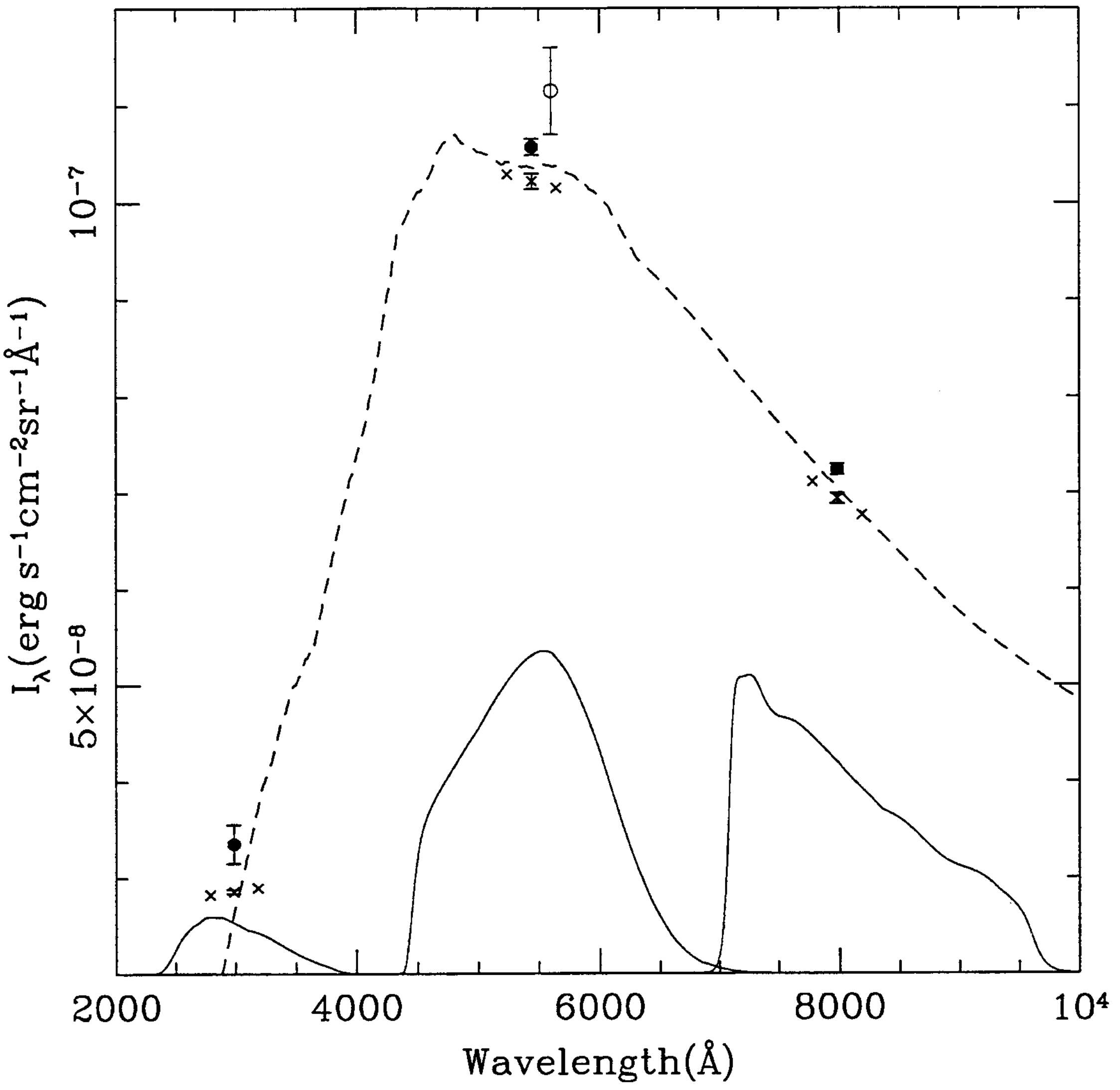

Fig. 6.2.— The total background fluxes in each WFPC2 band are plotted as filled circles, with the error bars indicating the random error in each measurement as tabulated in Table 2.7. The open circle shows the flux measured by FOS integrated over the WFPC2 F555W band-pass (see equation 6.2). The ×'s show the absolute flux of the ZL in each band as defined by equation 6.3 with three different assumptions for the color of ZL with respect to the solar spectrum. The ZL in each band-pass which is obtained by adopting a nominal value for the color of the ZL (4.25%/1000Å) is marked with error bars which show the *rms* error in the LCO measurement of the absolute ZL flux at 4650Å. The reddest possible color for the ZL (5.5%/1000Å) produces fluxes in each band-pass which are offset by +100Å from the central wavelength each WFPC2 band. The bluest possible color or the ZL (3.0%/1000Å) produces the results which are offset by -100Å. The relative throughput of the effect band-passes are shown at arbitrary scale at the bottom of the plot.

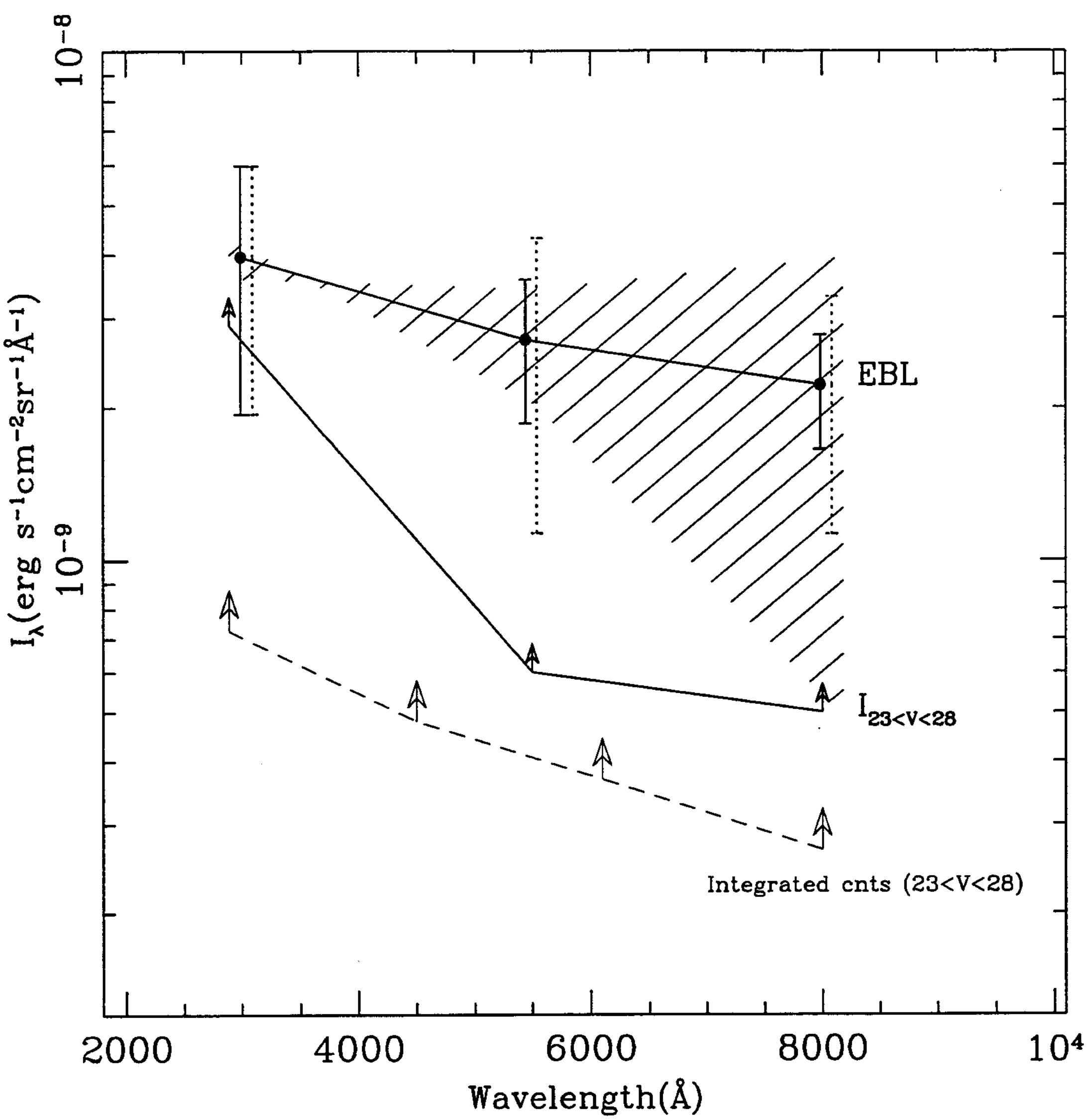

Fig. 6.3.— The points plotted show the EBL which results for a nominal color for the ZL with a constant slope of 4.25%/1000Å, normalized at the wavelength where we have measured the ZL (4650Å), i.e., $C(\lambda) = 0.0425 \times (\lambda/1000\text{Å}) + 0.798$. The hatch-marked region indicates the full extent of the range which results from assuming the bluest and reddest possible ZL colors. These limits for the ZL result merely from the fact that the EBL contributed by galaxies fainter than $V_{555} > 28$ ST mag cannot be negative (see text). The dashed line indicates the sum of the flux in objects detected with $23 < V_{555} > 28$ ST mag. The sum in detected objects in our own field is identical to that in the HDF. The line above that represents the difference in the EBL we detect in our own data from objects fainter than $V_{555} = 23$ ST mag, and that from objects fainter than $V_{555} = 23$ ST mag. For the latter, we mask out objects brighter than 23; for the former, we mask all objects brighter than 28 ST mag.

Chapter 7 Discussion

The EBL which we detect by absolute surface photometry is roughly a factor of 3 brighter than the integrated flux in individually detected galaxies (see Figure 6.3). In the most general sense, the EBL which we have detected could be explained in two ways: it is either associated with the galaxies we detect, or it is not. If it is coming from the galaxies we detect, why is the number we get from absolute surface photometry greater than the integrated flux in photometry of individual galaxies? If it is not coming from galaxies detect, but rather from regions of the sky which we do not identify with individual galaxies, then what is the source of the light?

The difference between the minimum EBL at 5500Å as determined by the method $I_{23<V<28}$ (see §6.3) and the total EBL ($I_{\rm EBL}$) as determined by absolute surface photometry of the night sky and foregrounds suggests that there is a contribution which is *not* associated with galaxies we can detect. In some sense, this is not particularly surprising. The HDF demonstrates that there are galaxies fainter than $V = 28$ ST mag which we have not detected with our comparatively short exposures. The flux we have identified from detected galaxies, $I_{23<V<28}$, therefore excludes a known, faint population. As these faintest galaxies are included in our measurement of the EBL by absolute surface photometry, we naturally expect $I_{\rm EBL}$ to be greater than $I_{23<V<28}$. It is commonly argued, however, that the faintest magnitude bins do not contribute significantly to the EBL based on the fact that the integrated flux as a function of magnitude is flattening out at the faintest magnitudes (see Figure 7.2). While this argument becomes significantly less convincing in light of the discrepancy between $I_{23<V<28}$ and the integrated galaxy counts for objects $23 < V < 28$ mag, it is still surprising that the majority (1/2 – 2/3) of the EBL is not associated with (i.e., within 1 arcsec of) galaxies at $23 < V < 28$. Even with our detection limit of $V < 28$, the discrepancy between the minimum EBL, $I_{23<V<28}$, and $I_{\rm EBL}$ from subtracting the foreground ZL and DGL suggests that a significant fraction of the EBL is not associated with detected galaxies.

It is also true, however, that the flux we find associated with objects by the method $I_{23<V<28}$ is roughly a factor of 2 brighter than the integrated flux from galaxy counts in all three bands. This suggest that the difference between the $I_{\rm EBL}$ we have detected and the integrated flux in galaxy counts can be associated in part with the detected galaxies, and that their individual fluxes are systematically underestimated by photometry methods typified by the HDF. While the two methods for finding the flux contributed by detected objects — $I_{23<V<28}$ and integrating the flux in galaxy counts — are clearly similar, the $I_{23<V<28}$ method of masking objects and summing the flux in the remaining pixels has the important distinction of avoiding the photometry errors which (as shown below) do appear to have a significant impact on the integrated flux in differential galaxy counts.

In this chapter, we attempt to put this detection in the context of simple limiting cases for the source of the EBL flux. We explore the possible sources for the EBL which we have detected in two general ways. First, we consider the difference between the minimum EBL from the method $I_{23<V<28}$ and the minimum EBL from integrated galaxy counts. This difference does not address the issue of undetected objects, as both of these methods assume a sky level which will clearly include any unresolved extragalactic contribution. It does, however, help to identify errors which may result from loss of flux in the outer isophotes of detected galaxies. Second, we discuss the level to which the extragalactic flux may include a significant contribution from objects which are below the detection limit of the deepest data. This falls under the general description of a "uniform" background in that it cannot be identified except by absolute surface photometry. For this discussion, we use the HDF as an example of deep imaging data: it has the advantages that it is among the deepest imaging data ever taken, it is well calibrated, and it is publicly available. In addition, it is very similar to our own data, albeit with the notable distinction that the exposure times for the HDF were longer by a factor of 15 for the F555W data, 17 for the F814W, and 21 for the F300W.

7.1 Missed Flux from the Outer Isophotes of Detected Galaxies

Standard galaxy photometry packages, such as SExtractor (Bertin & Arnouts 1996) and FOCAS (Valdes 1982, Jarvis & Tyson 1981), determine the flux of an object by measuring the flux within some detection isophote in excess of a locally determined sky level. Various corrections are sometimes made to this isophotal magnitude (see, for example, Smail et al. 1995) to compensate for the light outside the isophotal limit which is not detected. Often, the total magnitude for an object is measured within some "grown" area which is a constant multiple of either the radius of the limiting isophote or an intensity weighted radius. In the case of the HDF object catalog (Williams et al. 1996), the total magnitude is measured within an aperture which is twice the isophotal area, or $\sqrt{2}$ times the isophotal radius. When we adopt the same method for photometry in our own data, we find a difference between the integrated galaxy counts ($23 < V < 28\,\mathrm{ST\,mag}$) and $I_{23<V<28}$ to be roughly a factor of two. For the purposes of comparison, our discussion of galaxy photometry refers to the photometric methods employed in the HDF, however the conclusions we draw are not strongly dependent on the use of aperture, isophotal, Kron, or "total" magnitudes, as we discuss below.

The inferred flux from detected galaxies could be underestimated as a result of two distinct effects. The first has to do with sky estimation and is deferred to the next section. The second likely effect is that the photometric methods we discuss fail to recover flux from the outer isophotes of a galaxy. This will become significant for isophotal surface brightness levels near the noise level of the local "background" sky. This second effect clearly occurs to some degree, as it is difficult to recover flux below the surface brightness level of the sky noise unless one can average over enough pixels to improve the statistical determination of the mean. One could hope to recover the flux lost in the outer isophotes if one could integrate over enough pixels. However the fact that $I_{23<V<28}$ is roughly a factor of two larger than the integrated flux from galaxy counts implies that the total area in the outer isophotes of one object is not large enough to recover the flux in an object near the sky–noise level.

An estimate of the magnitude of this effect could be obtained by concentrically combining all galaxies in a given faint magnitude bin ($V \sim 28\,\mathrm{ST\,mag}$, for example), thus creating an average profile of galaxies from which one could measure the cumulative flux in the outer isophotes with significantly improved signal–to–noise. For our purposes, however, a more direct estimate of the flux lost in the outer isophotes can be obtained by exploiting the fact that we do indeed average over more than one object when we measure $I_{23<V<28}$. If flux is indeed lost from the outer isophotes of faint galaxies, then we should be able to lower the total background flux contributed by galaxies in any magnitude bin if we increase the size of the masks. That is, if a significant fraction of the EBL we detect is spatially associated with detected galaxies, then we should be able to decrease the detected EBL by masking out larger regions around those galaxies.

To test this, we have made masks of two different sizes. The size of the small masks is defined by ellipses which enclose twice the area of the limiting detection isophote (a factor of $\sqrt{2}$ in radius). This is the same definition used to calculate the "total magnitude" of an object in the HDF catalog, and is typical of galaxy photometry packages such as FOCAS (Valdes 1982, Williams et al. 1996). The size of the large masks is defined by ellipses which enclose at least nine times the area of the limiting detection isophote (a factor of three in radius) with the additional requirement that the minor axis which defines the ellipse be no smaller than 9 pixels, or 0.9 arcsec. The large masks are those which we have used to block the flux from galaxies in our measurement of the total background (described in §2.4 and §6.3). If we assume that a typical scale length of a disk is roughly 3.5 kpc (de Jong 1996), then the large masks enclose regions out to at least three scale lengths for objects at all redshifts. As the scale lengths of the faintest detected galaxies are observed to get smaller with fainter magnitudes (see Abraham et al. 1997), our "large" masks should be significantly larger than three scale lengths for the galaxies fainter than $V \sim 26\,\mathrm{ST\,mag}$.

We present the results of this test as a function of magnitude bin in Figure 7.1, which shows the normalized, differential contribution from objects in magnitude bins V = 23–24, 24–25, 25–26, 26–27, and 27–28, define as $(I_{\rm Tot}(V > 23) - I_{\rm Tot}(V > 24))$, $(I_{\rm Tot}(V > 24) - I_{\rm Tot}(V > 25))$, and so on. The solid line shows the differential contribution from objects when large masks are used; the dashed line shows results from small masks. The two numbers printed in each plot show the total flux from detected objects, $I_{23<V<28}$, found using the large masks and small masks (upper and lower numbers, respectively). The differential contributions per magnitude bin resulting from both sized masks are normalized to the total flux detected using the large masks.

Two important effects are demonstrated by Figure 7.1. The first is evident from a comparison of the numbers printed in each plot: roughly 20% of the EBL flux which is contributed by detected galaxies ($23 < V < 28$ ST mag) is located between $\sqrt{2}r$ and $3r$, in which r is defined by the isophotal detection limit of the image. This can also be seen as a function of magnitude by comparing the histograms marked with the solid and the dotted lines, which indicate the results for large and small masks, respectively. Further, the histograms show that while only a ~5% change is found in the total flux identified by small and large masks for bright objects, 50% of the light is lost at the isophotal limit for objects in the faintest bins (near the detection limit of the data). Regardless of the surface brightness of the limiting isophote for any particular data set, this test indicates that an error of 50% will result in the detected flux for objects at the faint limit of the data. Because galaxy photometry uses *local* sky estimation, part of the flux from the faintest objects is very likely included in the sky value for faint objects. As galaxy photometry is really a measure of the excess flux over the sky level for any object, the flux in outer isophotes is not only being excluded from the sum but may even be subtracted from the flux of small galaxies if the radius of local sky annulus was too small. The total effect is large enough to move a $V = 30$ ST mag object into the $V = 29$ ST mag galaxy counts bin for the HDF. Clearly, the EBL as determined from HDF–style photometry of individual galaxies is an underestimate. It should be noted that the flux which we estimate is excluded by the "total" magnitudes of the HDF catalog is similar in magnitude to the correction factor which has been identified for isophotal magnitudes of galaxies near the detection limit in other published galaxy counts (see, for example, Smail et al. 1995). The flux lost to the outer isophotes of galaxies is thus a measurable effect, but cannot fully explain the difference between integrated galaxy counts and $I_{\rm EBL}$.

The second important conclusion to be drawn from these histograms is that the majority of the EBL which comes from the cores of galaxies is associated with the galaxies at $V = 24 - 26\,\rm ST\,mag$. The photometry errors for individual objects are small in terms of absolute flux, and the total flux associated with the faintest bins is getting smaller. This implies that the difference between the $I_{\rm EBL}$ (from absolute surface photometry and subtraction of the ZL and DGL) and the minimum EBL we infer from $I_{23<V<28}$ cannot be entirely associated with regions we have masked out around the cores of detectable galaxies. In other words, it seems that when we use $I_{\rm Tot}(> 28)$ as an estimate of the sky level, we include a significant extragalactic component which is not being removed by masking out detected galaxies, even with the larger masks. When the local sky is measured for galaxy photometry, therefore, the result is evidently not a good estimate of the foregrounds (ZL+DGL, from *HST*); it includes an extragalactic contribution. While the flux lost in the outer isophotes is apparently relatively small, the local sky estimates are too high, making the estimated fluxes too small. The integrated flux from those individually measured galaxies will therefore never be a complete measurement of the EBL, because the sky levels subtracted in galaxy photometry include an extragalactic component. We explore the nature of this extragalactic component in the next section.

7.2 The Contribution of Detected Objects to the "Uniform" EBL

One possible explanation for extragalactic component implied by the difference between $I_{23<V<28}$ and $I_{\rm EBL}$ is that it comes from overlapping wings of objects we can detect. The total number of detected objects in the HDF is roughly 2100 over the three WF chips, which corresponds to roughly 1 object per 9 arcsec^2. We can calculate the contribution from the wings of detected galaxies to the mean sky level by estimating the contribution to any given point on the sky by the objects around it. We use for this simulation the detection limits of the HDF, and, for consistency, the HDF galaxy counts. Locally, galaxies typically have scale lengths of ~ 3.5 kpc, corresponding to ~ 1 arcsec (~ 0.7 arcsec) at $0.5 < z < 3.5$ for $\Omega_0 = 1.0$ ($\Omega_0 = 0.2$). Fainter galaxies, however, are observed to have smaller scale lengths. We therefore take 3.5 kpc as a typical scale length for galaxies brighter than $V = 26$ mag, 1.5 kpc as a typical scale length for fainter galaxies.

We estimate the contribution of the total galaxy population to any given point on the sky by integrating the contribution from galaxies that fall at distances between 1 and 30 arcsec. Contributions from any given galaxy were only considered outside of what would be the detection limit for that galaxy. While the total magnitudes quoted in the HDF catalog for an individual galaxy at $V \sim 28$ mag can be low by as much as 50%, as discussed above, for simplicity we take these to be the correct total magnitudes. Note that our results from this simulation are therefore a lower limit to the flux from the wings of galaxies. This minimum radius guarantees the "sky pixel" would not be within the detection masks we use for a typical galaxy. The maximum radius is empirically the limit at which galaxies cease to contribute significantly due to entirely negligible surface brightness (~ 30 arcsec). Based on a Monte Carlo simulation with 10,000 trials, we find the average contribution to the background sky level from the wings of detected galaxies to be ~ 28.8 AB mag/arcsec^{-2} or 3×10^{-10} I_λ. The distribution in the sky level is plotted in Figure 7.5. We remark on the average of the distribution, as opposed to the mean or mode, because it is the average flux level within a certain solid angle (an image) which defines the sky level.[1]

The asymmetry of the histogram is an indication of how much of the signal comes from brighter galaxies, which have less uniform distribution. As mentioned above, the total region within which galaxies were considered to contribute to the sky was $4\pi r^2$,

---

[1] The histogram we calculated is the average contribution to 10,000 different points on the sky. Neighboring points on the sky will obviously be correlated, because they will contain contributions from the same galaxies' wings.

with $r = 30\,\mathrm{arcsec}$. Over the magnitude range we considered ($22 < V < 29.5\,\mathrm{mag}$), at least one galaxy in every magnitude bin would appear in a region that size, so that the histogram we have produced is not unreasonable. To gain some intuition regarding the severity of the asymmetry of the sky histogram in Figure 7.5, we can imagine smoothing an image which had such a histogram. If we smooth on spatial scales of a few arc seconds, we would find that the sky level would drift around the average level, rarely below the mode. The fluctuations in the sky level are of order a few $\times 10^{-10}$. The foregrounds from ZL and DGL are at least $\sim 1 \times 10^{-7}$ at 5000–6000Å, so that fluctuations would be $< 0.5\%$ of sky. Such fluctuations are certainly seen, and are part of the reason that the sky is determined locally for photometry of individual galaxies. In fact, the standard deviation of local sky measurements in the HDF catalog is 1.4 DN per dithered pixel or 28.37 AB mag/arcsec^2, 0.5 mag brighter than our estimated variations (see Williams et al. 1996 and http://www.stsci.edu for catalog).

The faintest galaxies in the HDF are likely to actually be fragments of galaxies (as discussed in Colley et al. 1996 and 1997, for example). By treating them as individual galaxies we distribute their flux more uniformly over the sky than is appropriate. We can correct for this in an approximate way by combining the flux of the associated fragments into one object at the center of the fragmented groups. Doing so changes the average sky level by less than 0.01×10^{-10}, a negligible amount even in this context. This result is not surprising, because treating them individually does conserve flux. Also, the fragments are likely to be within one scale length of the "parent" galaxy, so that the flux was distributed only marginally beyond the scale of the parent galaxy when the fragments were treated separately.

Based on this exercise, the "uniform" extragalactic contribution from *detected* galaxies over a WFPC2 observation is at least 3×10^{-10}ergs s^{-1}cm^{-2}sr^{-1}Å^{-1}(10–20% of our detected I_{EBL}). Undetected sources will, of course, contribute to the estimated sky levels as well, as we discuss in the next section.

7.3 Undetected Objects

Several recent surveys have demonstrated the existence of significant number densities of galaxies with central surface brightness (μ_0) fainter than the canonical Freeman limit, which was long thought to define the typical μ_0 (Freeman 1970). These populations are faint enough to have been excluded from most estimates of the local luminosity function, such as those from the APM, CfA and LCRS redshift surveys. The results of Sprayberry et al. (1997) and Dalcanton et al. (1997) collectively show that "low surface brightness" (LSB) galaxies with central surface brightnesses in the range $23 < \mu_0 < 25$ $V\,\mathrm{mag/arcsec^2}$ are at least as numerous as "normal" ($\mu_0 = 20.5$ $V\,\mathrm{mag/arcsec^2}$) galaxies. They further have shown that these galaxies contribute at least an additional 30% to the known luminosity density in galaxies with $M_V^* \gtrsim -15$.

Our EBL measurement was made in a very small surface area, which corresponds to a very small volume at low redshift. In addition, it is defined by a bright–magnitude cut–off of $V = 23\,\mathrm{AB\,mag}$. Together, these restrictions guarantee that the EBL we have measured is not strongly affected by local ($z < 0.05$) galaxy populations. However the existence of LSB galaxies at low redshift implies the possibility of their existence at high redshift, where they would certainly be included in our measurement. To estimate the possible contribution of a population which would escape individual detection in the HDF data, we can simply calculate the surface brightness limit which is beyond detection in those data and consider the likelihood that such a population might exist at high redshift, based on the distribution in surface brightness of galaxies at low–redshift.

We may estimate the HDF detection limit in the F606W data from the information presented in Williams et al. (1996). The average noise level in a "drizzled" pixel ($0.002\,\mathrm{arcsec^2}$, or 6.25 drizzled pixels per standard WFPC2 pixel) is 2.8 DN for the final combined image (exposure time 109,050 sec).[2] The detection limit as quoted in

---

[2] Drizzling is a technique which was developed to recover sub–pixel resolution taking images with sub–pixel relative offsets and combining images onto a sub–pixel grid. See Williams et al. (1996) and references therein.

Williams et al. (1996) is $4\sigma_{\rm sky}$ over 25 drizzled pixels, which corresponds to roughly 26.0 AB mag/arcsec^2 (25.8 ST mag) in the central 0.04 arcsec^2 of an object.[3] It is impossible to fit a profile to objects near this detection limit. However, as this is the required flux level over the entire 25 pixels in the core, it is reasonable to take this level as an estimate of the limiting central surface brightness for detection.

The obvious question, then, is whether or not a population of galaxies with $\mu_0 \gtrsim$ 26.0 AB mag/arcsec^2 might exist at high redshift. To answer this question, we can ask how a passively evolving galaxy which had $\mu_0 \gtrsim 26.0$ AB mag/arcsec^2 at high redshift would appear at $z \sim 0$. In Figure 7.3, we have plotted the central surface brightness at $z = 0$ of a galaxy which had $\mu_0 \sim 26.0$ AB mag/arcsec^2 at redshifts $0 < z < 3$. For this calculation, we have used the K and evolutionary corrections of Poggianti (1997) for galaxies of Hubble types E, Sa and Sc. From this plot, it is clear that galaxies at $z \sim 0$ with central surface brightness between $22 < \mu_0 < 24$ V ST mag could easily be undetectable in the HDF by redshifts of $z \gtrsim 0.5$. As shown by McGaugh et al. (1995, 1996), Sprayberry et al. (1996), and Dalcanton et al. (1997), there are populations locally which could easily be identified with such galaxies at higher redshifts.

If the luminosity density contributed by these galaxies does *not* increase with redshift, then the contribution of such galaxies to the luminosity density of the Universe will contribute an additional 30% ($\sim 3 \times 10^{-9}$ based on the integrated local luminosity density, Sprayberry et al. 1997) over the integrated flux from galaxies with central surface brightnesses high enough to be detected in the HDF. [4] Based on this estimate, galaxy counts would underpredict the EBL by at least 30% due to undetected galaxies.

---

[3] These numbers were calculated based on information in Williams et al. (1996). Note, however, that 2.8 DN is a much lower value than the average measured $\sigma_{\rm sky}$ values quoted for the objects in the HDF catalog, which is available at http://www.stsci.edu. A histogram of the sky level in the F606W, WF2 image shows that sigma in the sky is roughly 3.9 DN per drizzled pixel. The level 26 AB,mag/arcsec^2 is therefore a generous detection limit by the definition used in the Williams et al. (1996).

[4] It is also possible that dust obscuration at high redshift would cause galaxies with normal intrinsic surface brightness to have low apparent surface brightness in the observed optical (rest–frame UV), as discussed further in Chapter 8.

7.4 Summary

We have suggested three effects which could explain the disagreement between the EBL flux we detect and the EBL flux implied by the integrated galaxy counts. The first is that individual galaxy photometry does not fully recover the flux near the isophotal detection limit of detected galaxies. Taking the HDF as an exemplary case for the deepest imaging data in general, "detected" means that the core surface brightness is higher than μ_0=26 AB mag/arcsec^2 $\sim$25.8 ST mag/arcsec^2 in V_{606}. Our estimate of the magnitude of this effect shows that roughly 20% of the total flux from galaxies at all magnitudes is recovered between the radius $1.4r_{\rm iso}$ and $3r_{\rm iso}$, where $r_{\rm iso}$ is the radius of isophotal detect. The loss from individual galaxies is as great as 50% for the faintest galaxies. The lost flux is likely mistakenly included in the sky estimates in standard photometry, which would largely explain why the integrated flux from galaxy photometry is 40% lower than what we find by our method $I_{23<V<28}$ (see §7.1). This also implies that galaxies in the faintest bins should be brighter by roughly 1 magnitude, making it less clear that the counts are turning over.

We have also suggested two reasons why the sky level may be underestimated. The first is that objects are likely to exist which have core surface brightnesses below the detection limit. Such lurking galaxies need not have dramatically low intrinsic surface brightness at high redshifts ($z \gtrsim 3$). Even at lower redshifts, standard evolutionary corrections and K–corrections indicate that galaxies which are observed in significant numbers in the local universe today could be faint enough to evade detection in the HDF at redshifts $z \gtrsim 0.5$. The second reason for underestimating the sky is that the galaxies which we do detect have high enough surface density to contribute significantly to the *uniform* sky level. The crucial point to be gained from these three tests is that the EBL can be explained by known galaxy populations without suggesting that the photometry of individual galaxies in those known populations is wrong by large factors. For the faintest galaxies, HDF–style photometry is indeed wrong by roughly 50%, but that does not explain the entire difference between the detected EBL and the EBL inferred by the counts. The real distinction to be made is between the sky levels which are determined by absolute photometry of the foreground components, ZL and DGL, and the sky levels which one finds by standard methods of averaging over the area surrounding detected objects. Our analysis shows that roughly 20% of the flux is lost from the outer isophotes of galaxies when standard methods of photometry are employed, and that the missed flux may be included in sky estimates, further compounding the error to 40%. In addition, it is possible 40–50% of the difference between galaxy counts and the EBL we detect is contributed by objects with low apparent surface brightness. Finally, our simulations show that 30% of the light we detect is contributed by the wings of detected objects. These effects together explain much of the difference between the EBL we detect and the flux in resolved objects.

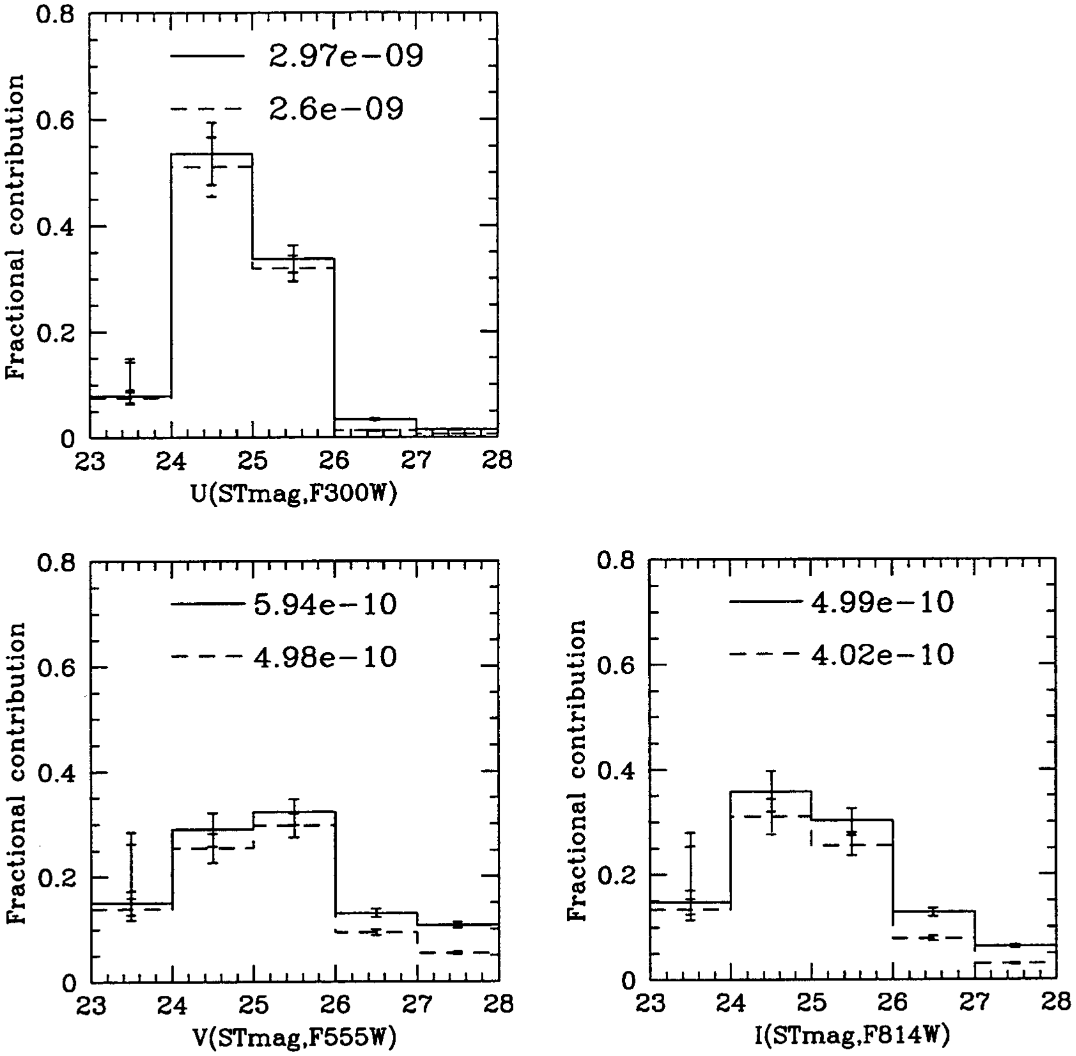

Fig. 7.1.— Differential contribution to the EBL from objects with V_{555} = 23–24, 24–25, 25–26, 26–27, and 27–28 ST mag. The solid line shows the result using large masks; the dashed line shows the results using small masks of the size typically defined as the total "grown" area for galaxy photometry (see text for details). The upper numbers (in our standard units of ergs $s^{-1}cm^{-2}sr^{-1}Å^{-1}$) printed in each plot shows flux contributed by objects over the full range. EBL($23 > V_{555} < 28$ ST mag) using the large masks. The lower number shows the total flux determined using small masks. The fractional flux in each bin was normalized by the total flux found using the large masks. The total flux from the large masks represents an absolute minimum on the EBL at 5500Å from galaxies fainter than V_{555} = 23 ST mag. The error bars in the center of each bin represent the 1σ error in the mean value plotted for each bin, based on the $\sqrt{N}$ variation in the number of galaxies per bin and chip to chip. The drop–off in contribution from galaxies brighter than $V_{555} = 23$ is probably statistically relevant, as it is merely indicative of the fact that the number density of 23 mag objects varies by at least factors of two around the sky and are poorly sampled in any 4 arcsec^2 region due to random fluctuations in their number density.

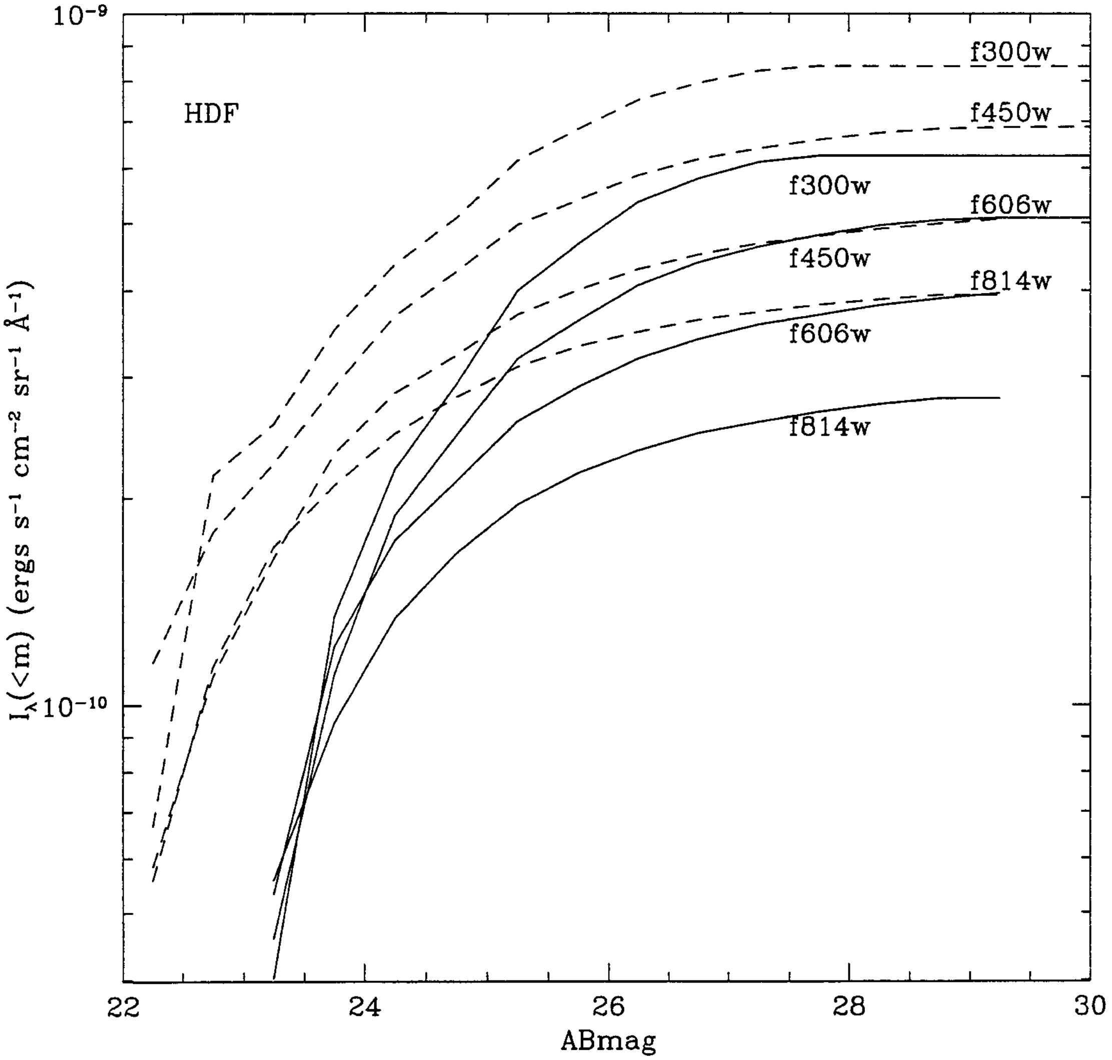

Fig. 7.2.— Integrated light from galaxies detected in the HDF as a function the magnitude cut–off at the faint end. The dashed lines include the flux of 22 AB mag objects, while the solid lines show the integrated flux with magnitude starting at the cut–off of 23 AB mag which we use in our EBL measurement. The curves gives a general idea of the contribution from each bin.

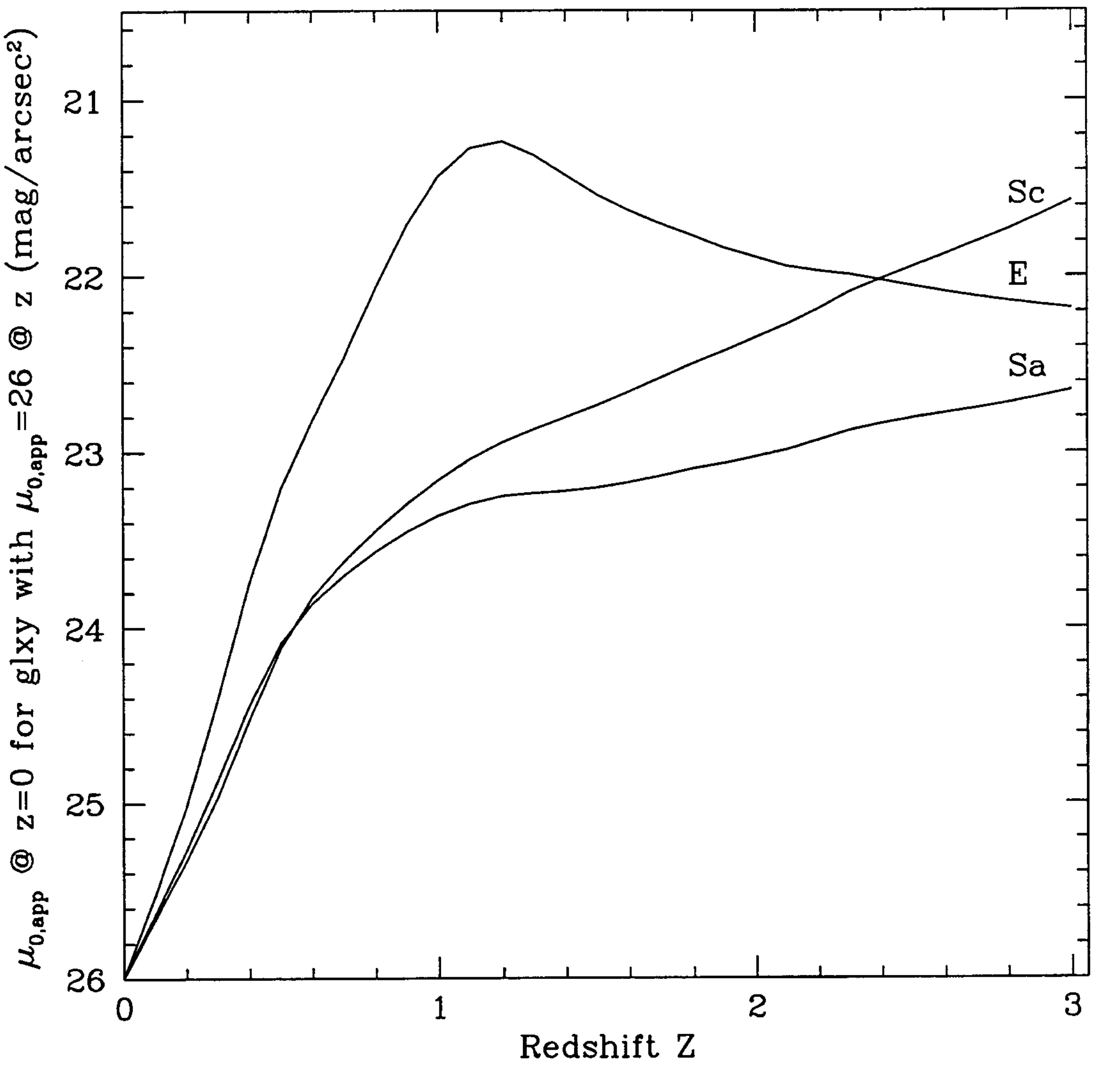

Fig. 7.3.— The curves show the apparent surface brightness at $z = 0$ of galaxies which could have escaped detection at a redshift of z. As discussed in the text, the limiting core surface brightness for detection in the HDF is 26 mag/arcsec^2. For example, a galaxy of Hubble type E which has the requisite surface brightness of 26 mag/arcsec^2 to escape detection at a redshift of $z = 1.1$ would have a surface brightness of 21.3 mag/arcsec^2 at $z = 0$. The plot demonstrates that galaxies with surface brightness of 21.5–24 mag/arcsec^2 could have counterparts at redshifts $0.5 < z < 3$ which would go undetected. The K-corrections and evolutionary–corrections used in this calculation are shown in Figure 7.4.

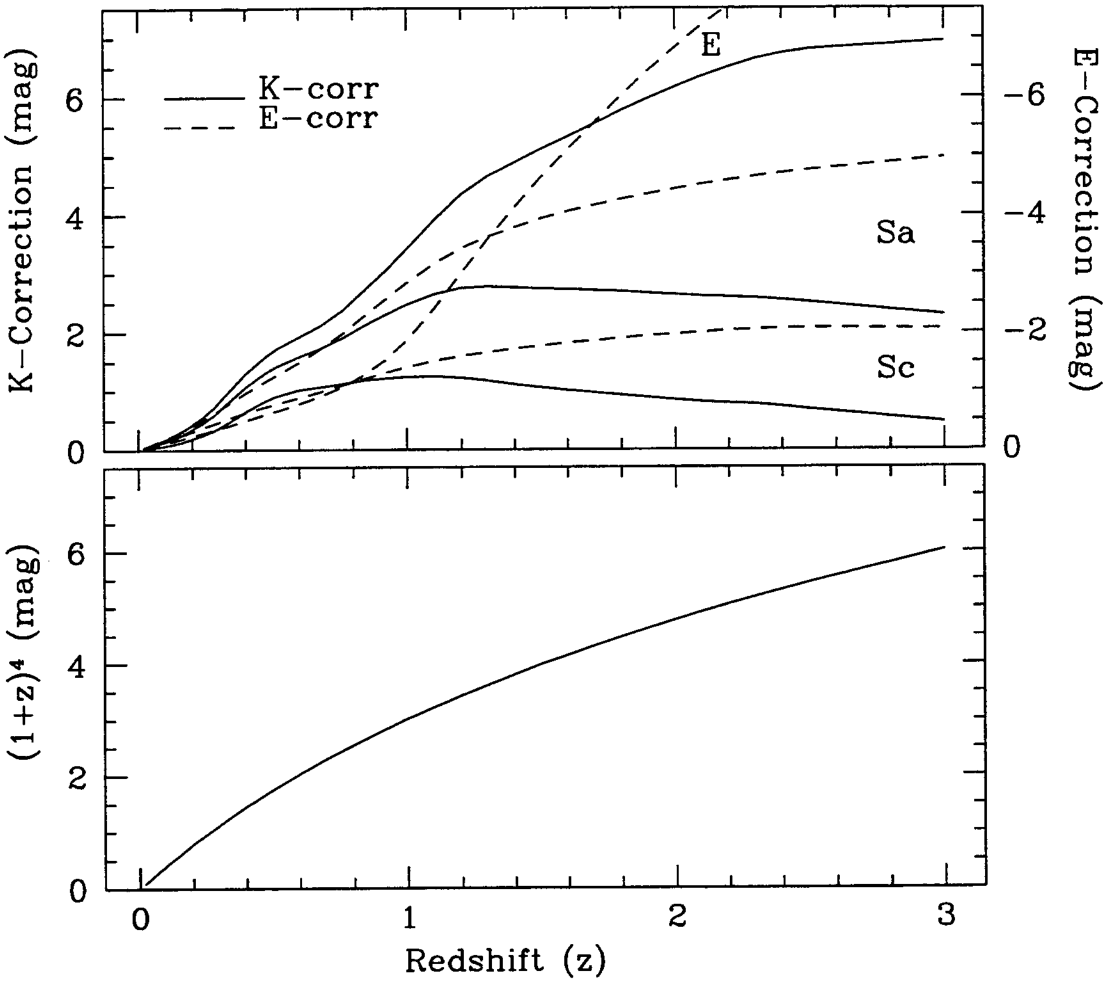

Fig. 7.4.— The upper plot shows the evolutionary and k–corrections for galaxies of E, Sa, and Sc Hubble types. The Hubble types labeling the lines pertain to the two closest lines, and the right and left axis indicate the scale for the k-corrections and evolutionary corrections respectively. The lower plot shows the surface brightness dimming which results from change in angular size and luminosity distance as a function of redshift. The central surface of an object which had central surface brightness mu_{app} at a redshift, z, will have a central surface brightness μ_0 at the present epoch, $z = 0$, which is given by $\mu_0 = \mu_{\mathrm{app}} - 10 * log(1 + z) - \mathrm{K}_{\mathrm{corr}} - \mathrm{E}_{\mathrm{corr}}$. Corrections taken from Poggianti (1997).

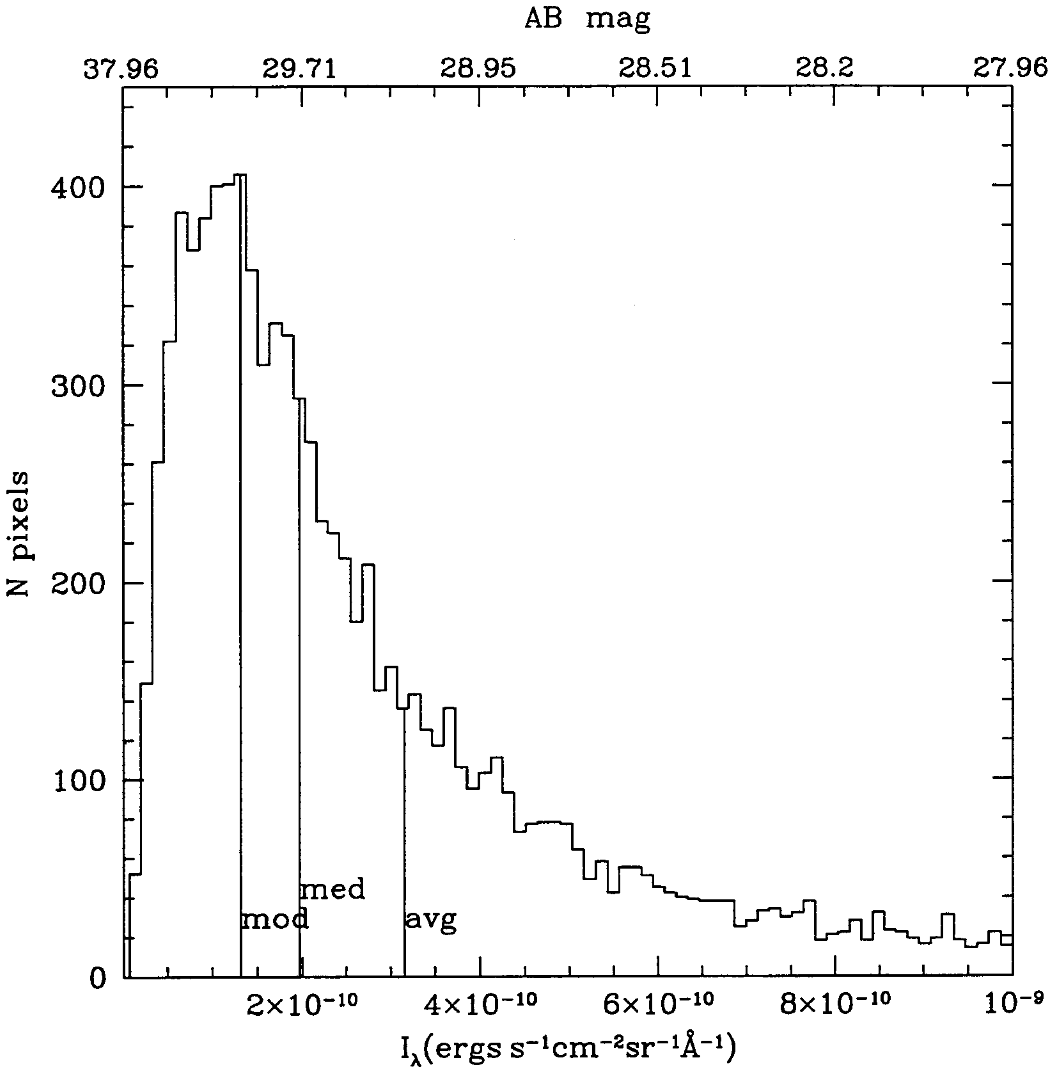

Fig. 7.5.— The results of a Monte Carlo simulation of 10,000 trials which shows the contribution to any point on the sky from the wings of detected galaxies. The HDF surface densities as a function of magnitude were used, and only galaxies which were statistically well represented within a region of radius 30 arcsec, were considered to contribute to a given point. See text for details. The simulation indicates that the uniform contribution from detected galaxies to the diffuse flux at any point on the sky is roughly 3×10^{-10}. It also indicates that slow fluctuations from the wings of galaxies will cause the locally determined sky level to vary on scales of 10's of arcseconds around the sky by roughly a $1\text{–}2\times10^{-10}$.

Chapter 8 Implications and Future Prospects

In Figure 8.1, our results are compared to the integrate flux from the deepest available galaxy counts (HDF) and to the results from previous efforts to measure the EBL at optical, UV and near–IR wavelengths. The upper limits to the optical and UV measurements plotted are given in Table 1.1. As discussed in the Introduction, a meaningful observational definition of the extragalactic background light includes a bright–limit cut–off to the sources which are considered to contribute. In our case, that limit is $V \gtrsim 23\,\mathrm{ST\,mag}$. Similar bright magnitude cut–offs were used in the other optical experiments plotted (see §1.3).

The detection of the EBL presented in this work provides a constraint for models which attempt to explain the nature of galaxy evolution and formation. The observed EBL is an integration over redshift of the emission from all stellar population and rest–frame wavelengths. Any inferences of star formation rate or luminosity density as a function of redshift are strongly dependent on the assumed initial mass function (IMF) and its high–mass cut–off, the metallicity of stellar populations, and the effective optical depth both internal and external to the originating galaxy. All of these effects no doubt vary with redshift. It is therefore not possible to go backwards from a measurement of the EBL in a single passband to a detailed picture of the star formation history of the Universe. The utility of this measurement is as a constraint to models which consider these effects and predict the EBL, and as a completeness check on the light detected in resolved sources (galaxy counts and redshift surveys).

8.1 Comparison with Galaxy Counts

The EBL which we have detected is a factor of 2–3 greater than the flux detected in galaxy counts. While it is common to consider the integrated flux of detected sources as the total integrated background light (e.g., Cowie 1996), this is clearly not the case. As was illustrated by several tests in Chapter 7, it would in fact be very surprising if a measurement of the surface brightness of the EBL from absolute surface photometry of foregrounds and backgrounds *did* produce the same result as the integrated flux of individually detected galaxies and standard, relative–to–sky photometry. We have demonstrated in Chapter 7 that a substantial fraction (40–60%) of the difference between our measured EBL and the flux in galaxy counts could in fact be contributed by the very galaxies that are identified in the counts. Flux from detected galaxies could be incorrectly assessed due to errors in sky–estimation which results from the overlapping wings of even *detected* galaxies, let alone from the lower surface brightness populations. Errors in measured flux could also result from lost light in the outer isophotes of galaxies.

In addition, LSBs which are excluded from measurements of the local luminosity function (from which come local luminosity density estimates) contribute an additional 30–50% to the luminosity density at low redshift; at high redshift, only the bright end of the luminosity function has been directly observed, and surface brightness limits there will cause even greater incompleteness in LSBs.

Obscuration of UV light by dust in the parent galaxy is not an explanation for the disagreement between the EBL we detect and the integrated light from sources. If a galaxy were completely obscured by dust, its UV light would not contribute to either the diffuse background or the counts at UV or optical wavelengths. However galaxies will certainly be removed from resolved–object detection before they are completely obscured, and in that sense, the EBL may contain light from dust–enshrouded galaxies which are not included in galaxy counts. In other words, a galaxy which drops out of galaxy count surveys at moderate to high redshifts because it has low *apparent* surface brightness need not be an LSB in the sense of low intrinsic mass surface density, as is typically meant when LSBs are discussed in the local universe.

The most important conclusion from this work is that the EBL which we detect does not require exotic populations in order to be explained. It does, however, indicate that the photon census from resolved–source methods is currently incomplete even for the resolved sources which are detected.

8.2 General Comparison with Models

The most common method used to predict the EBL is from detected sources: galaxy counts and redshift surveys. It is important to appreciate that these two approaches are far from independent. To address star formation, redshift surveys are used to construct absolute luminosity functions, which can then be integrated to get the luminosity density in a given redshift range. The best example of such an approach is the CFRS work (see Lilly et al. 1996 and references to the earlier papers in that series). Luminosity functions are typically normalized to galaxy counts, so that an agreement between the EBL calculated from integrating the luminosity density and the EBL calculated by integrating galaxy counts is a consistency check, not a confirmation of the completeness of either result. It is nonetheless interesting to compare our detection with the detected flux in resolved sources and the current picture of galaxy evolution and formation in general. To do so, we take the differential galaxy counts as a function of magnitude from the HDF, and the CFRS redshift survey (see Lilly et al. 1996) as representative of what can currently be achieved in the case of either observational approach.

If complete, the luminosity density as a function of redshift and wavelength, $J_\lambda(z)$ from surveys like the CFRS is precisely the information one would need to study the evolution of the SFR with redshift. At low redshift ($z < 0.2$), the CFRS data was augmented by the luminosity function results from large–area local surveys (Marzke et al. 1994, Loveday et al. 1992, da Costa et al. 1994, and Lin 1996), which are in agreement in the resulting luminosity density only to within roughly a factor of two (see, also, discussion of the low–surface brightness incompleteness of local surveys in

§7.3, Impey et al. 1996, and Impey & Bothun 1997). At high redshift ($0.75 < z < 1.0$) the CFRS includes only galaxies at most 1 AB mag fainter than M^*. While this is an impressive sample for such high redshifts, the luminosity function is extrapolated to more than 4 AB mag below M^*. Soberingly, the correction for incompleteness at $0.75 < z < 1.0$ is a factor of 2 in the computed J_ν. The integrated flux at observed wavelength, λ, can then be calculated from the Lilly et al. luminosity density ($J\nu(z)$) as

$$I_\lambda = \frac{1}{4\pi}\int_{z_1}^{z_2} dz \frac{dl}{dz} J_{\lambda'}(z) \tag{8.1}$$

in which $\lambda' = \lambda/(1+z)$. This value, as shown by Fall, Charlot & Pei (1996) and by Madau (1997), is roughly a factor of two smaller than our detected EBL, $I_\lambda(V > 23)$.

As was mentioned in the Introduction, extrapolations beyond the detection limits in either counts or luminosity functions can be attempted to complete this picture, however the points raised in Chapter 7 suggest that the counts themselves may well be in error at the faint end. Extrapolations which are constrained by the counts are then additionally uncertain. A convenient compilation of models which meet the observational criteria imposed by galaxy counts is given in Väisänen (1996). As noted in §1.1 the results actually show little variation, all producing roughly 1×10^{-9}ergs s^{-1}cm^{-2}sr^{-1}Å^{-1}at optical wavelengths.

The problem with such approaches is that it is inherently circular to predict the optical EBL based on detected optical sources, especially if the information in detected sources is inherently incomplete and systematically biased. An intriguing method for predicting the EBL which is not circular is that of predicting the emission from stars from the consumption of gas and production of metals as a function of redshift. This approach was pioneered by Lanzetta et al. (1995) and further developed by Pei & Fall (1995) and Fall et al. (1996). As discussed in §1.1, the hot young stars which produce the EBL are also responsible for the majority of metal production. The rates of metal production and gas mass conversion to stars both can be used to predict the emitted light from young stellar populations, however the result is strongly dependent on the IMF (especially high–mass cut–off), starting metallicity, and dust obscuration of the emitted light.

An added concern is that the absorption line systems which are studied may themselves present a biased sample due to dust obscuration of QSOs. The most recent incarnations of these models by Pei & Fall (1995) and Fall et al. (1996) take into account the effects of dust in obscuring QSOs (and thus absorbers and their contribution to the comoving HI and metal density), intergalactic absorption, and absorption in the emitting galaxy. The last of these corrections is based on local observations of starbursting galaxies, which may over–compensate for the loss of UV light in the parent galaxy (see Hurwitz et al. 1997). The predicted luminosity density with redshift and the EBL can be brought into good agreement with the results of Lilly et al. (1996), and consequently, with the results of most galaxy counts. The EBL which we have detected can also, however, be easily explained by the published models of Fall et al. (1996) when slightly different input parameters for the effects of dust and the stellar IMF are used. The current results of that work do not so much demonstrate that the star formation and metal production history of the Universe *are* completely understood as that they *can* be understood and explained in agreement with all of the observable constraints currently available: emission of galaxies, absorption seen in QSO spectra, and the EBL which we have detected.

The effect of dust is a recurring uncertainty in the inferred SFR from both the method used by Pei & Fall (1995) and from the luminosity density with redshift from Lilly et al. (1996) (see Madau et al. 1996, 1997). Even relatively small quantities of dust in the ISM (a few percent of that found in our own Galaxy) can absorb and be heated by UV radiation, and subsequently re–radiate that energy in the far–IR. This significantly complicates efforts to identify the star formation rates at all redshifts, and even making it difficult to detect galaxies at moderate to high redshifts. As we mention above, the EBL will include more of the UV light from obscured galaxies than galaxy counts will, but both will be effected.

The importance of IR observations in addressing this issue has recently been underscored by deep IR and sub–mm source detections which seem to indicate that the conversion of UV and optical light to thermal emission from dust may be considerable.

Rowan–Robinson et al. (1997) and Smail, Ivison, & Blain (1997) have published results which would indicate roughly 2 orders of magnitude more star formation at high redshifts than is currently identified by Madau et al. (1996) based on the IMF– and dust–dependent interpretation of Lyman–limit surveys of galaxies at $z \sim 3$. Results from Pettini et al. (1997a,b) suggest a much smaller correction of a factor of 3 to the SFR at $z \gtrsim 1$ which Madau et al. (1995) infer. The Pettini et al. correction is based on the rest–frame UV colors of the Lyman–dropouts, and also the comparison of the star–formation rate inferred from the rest–frame UV continuum compared to the rate inferred from the strength of H_β. UV flux that goes to heating dust will be re–radiated into the IR, thus a measurement of the EBL at IR wavelengths in addition to the optical would provide very interesting constraints on the total UV and optical light emitted by young stars. The IR EBL completes the detected–source studies in the IR just as it does in the optical.

8.3 Metal Production and the EBL

As there is a correlation between the background UV–optical light from hot, massive stars and the total production of metals, it is interesting to note whether the observed metal mass density seems to match the observed total background flux. While Songaila et al. (1990) have noted that the resolved sources appear to account for the metals observed in the luminous portions of galaxies, there are a number of indications that as much as 90% of the metals in the universe may be located in the intergalactic medium (IGM). Mushotsky & Loewenstein (1997) find that the total mass density of metals in clusters at redshifts $0.14 < z < 0.3$ is consistently 2–10 times the metal mass in stars, making the intercluster medium (ICM) the primary location of iron mass in clusters. The gas and metals ejected by cluster galaxies are trapped in the cluster potential where they can be studied with relative ease. In the absence of a cluster environment, metals produced by field galaxies may be ejected into the IGM and would be more difficult to identify. The constancy of the measured metallicity with redshift indicates that the metals produced at high redshift were largely expelled from the parent galaxies, and that a great deal of metal production and inferred star formation at high redshift may be overlooked by the DLA systems used in models by Pei & Fall (1995) and Fall et al. (1996). The inferred UV and optical light would be significantly higher, as the metallicity found in clusters is roughly 10 times that used by Songaila et al. (1990). If the EBL is identified with this early star formation, the conclusion would be that the star formation occurred in either sub–luminous regions, and is only included in a measurement of the diffuse background, or in dust–enshrouded regions, in which case the IR EBL would be high as a result. It is interesting to note that the metal enrichment history of the Milky Way also indicates that much of the enrichment might have occurred before $z \sim 1$. Also, studies of nearby starbursting galaxies have shown that outflows of hot, metal–enriched gas are triggered by periods of rapid star formation, and that metals need not be identified with the parent galaxy, but could be "hiding" in the intergalactic medium.

8.4 Future Prospects

The work presented here is a significant improvement over previous efforts to measure the total flux of the diffuse EBL in several respects. The measurement of the absolute flux of the ZL presented here is a new and very accurate technique which builds on long–standing knowledge of the spectral features of the ZL. In addition, ours is the first measurement of the mean level of the EBL to make use of the vast increase in knowledge of the DGL that came about as a result of the IRAS mission and as a result of a number of N(HI), optical, and UV studies of the Galactic, interstellar dust. Finally, the use of a high resolution, well calibrated, spectrophotometric detector *above the atmosphere* has made possible the removal of starlight and eliminated the unpredictable airglow contribution.

Two factors have been principally responsible for the errors in this measurement: the use of different instruments for measurement of foreground and background components, and the lack of a direct measurement of the ZL at all wavelengths. As discussed in Chapters 1 and 3, we originally proposed to measure the absolute flux of the ZL by the strength of its spectra features over the full range 3000–8000Å using the FOS. This would have allowed us to elliminate the color of the ZL as a source of uncertainty in our results. To succeed in directly measuring the color of the ZL with 1% accuracy is the single most important improvement to be made in any future attempts to measure the EBL. The ZL color cannot be measured from the ground for reasons we discuss in Chapter 4, but may be measured from space if a high resolution ($\sim$ 1Å) spectrograph with good absolute calibration becomes available in the future. Second, if the foreground ZL and total background are both measured with the same instrument, then the calibration requirements for the experiment practically disappear: it is only because we subtract two, very large, independently calibrated numbers from each other that we require $\sim$ 1% accuracy in absolute calibration.

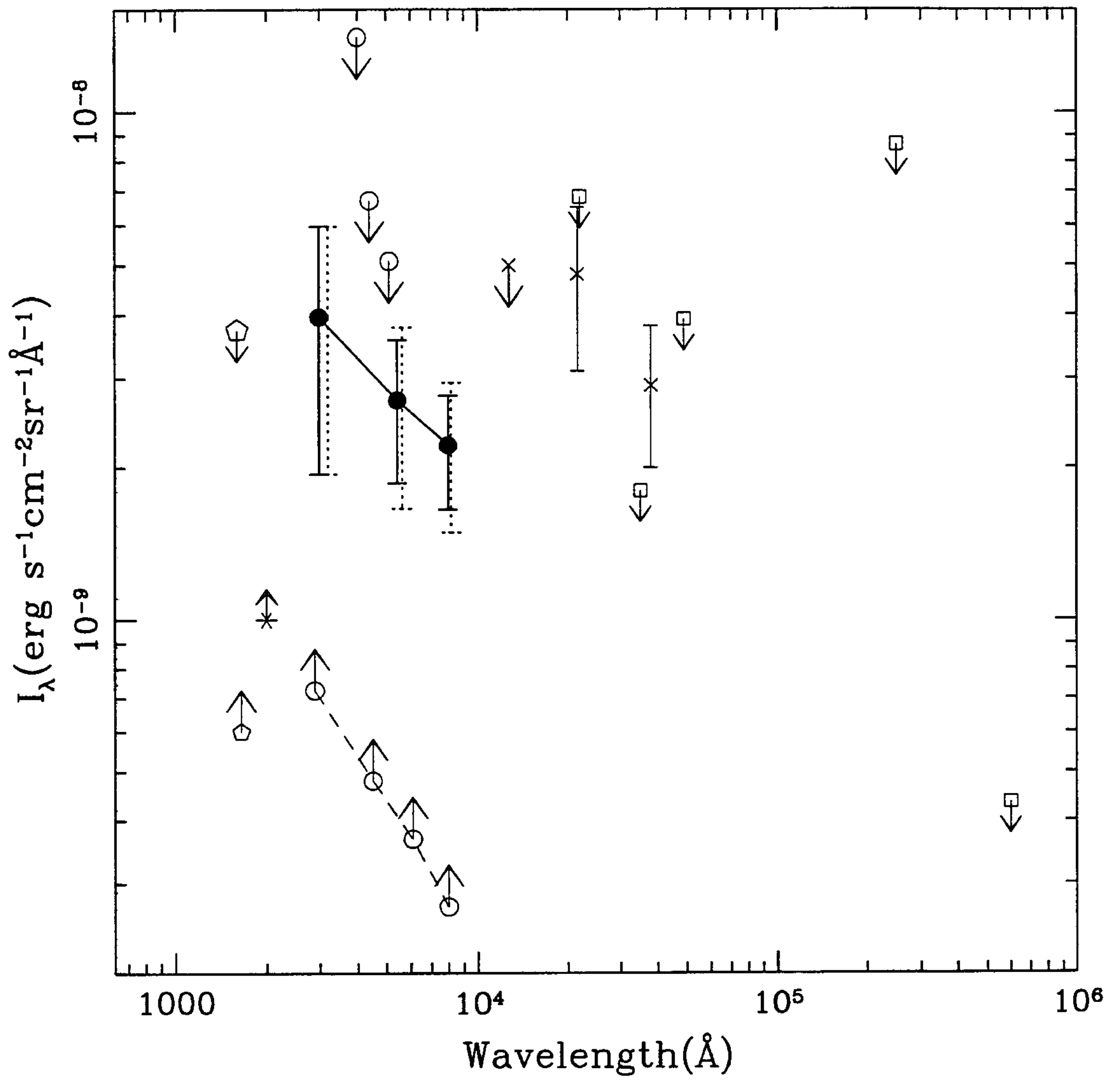

Fig. 8.1.— Our detections of the EBL at 3000, 5500, and 8000Å (marked in filled circles) are compared to the results results form previous efforts to measure the EBL at optical, UV and near–IR wavelengths. Systematic errors for our results are shown by the dashed error bars; random errors are shown by the solid error bars. The lower limits in the optical (open circles with upward arrows) are integrated flux from the HDF galaxy counts. Only galaxies with $V > 23$ ST mag were included in this sum, which is the bright–limit we use in defining our EBL measurement. The lower limit at 2000Å is the integrated galaxy counts of Armand et al. (1992). The upper and lower limits at 1600Å are from Hurwitz et al. (1991) and Martin et al. (1991), respectively. The upper limits at optical and UV wavelengths are given in Table 1.1. The open squares show the results of DIRBE (see Hauser 1996). The ×'s show the results of Matsumoto et al. (1988). See text for further discussion.

Bibliography

Allen, C.W. 1973, *Astrophysical Quantities (3rd Edition)*, (London: Athlone Press)

Aller, L.H. 1987, in *Physics of Thermal Gaseous Nebulae (Physical Processes in Gaseous Nebulae)*, (Dordercht: Reidel), Vol. 112, p.101

Arvesen, J.C., Griffin, Jr., R.N. & Douglas Persson, Jr., B. 1969, Appl. Opt., 8, 2215

Beggs, D.W., Blackwell, D.E., Dewhirst, D.W. & Wolstencroft, R.D. 1964, MN, 127, 329

Berriman, G.B., Boggess, N.W., Hauser, M.G., Kelsall, T., Lisse, C.M., Moseley, S.H., Reach, W.T. & Silverberg, R.F. 1994, ApJ, L63

Bertin, E. & Arnouts, S. 1996, AAS, 117, 393

Bohlin, R.C., Colina, L., & Finley, D.S. 1995, AJ, 110, 1316

Bohlin, R.C., Savage, B.D. & Drake, J.F. 1978 ApJ, 224, 132

Bohlin, R.C. 1995, Calibrating HST: Post Servicing Mision, STScI

Boughn, S.P. & Kuhn, J.R. 1986, ApJ, 309,33

Boulanger, F. & Pérault, M. 1988, ApJ, 330, 964

Boulanger, F., Abergel, A., Bernard, J.-P., Burton, W.B., Désert, F.—X., Hartmann, D., Lagache, G., Puget, J.-L. 1996, AA, 312, 256

Bowyer, S. 1991, ARAA, 29, 59

Brownlee, D.E. 1978, in *Cosmic Dust*, ed. A.M. McDonnell (New York: Wiley and Sons), 295

Burstein, D. & Heiles, C. 1978, ApJ, 225, 40

Burstein, D. & Heiles, C. 1982, AA, 87, 1165

Calzetti, D. 1997, AJ, 113, 162

Casertano, S. 1997, personal communication

Cole, S., Aragon-Salamanca, A., Frenk, C.S., Navarro, J.F. & Zepf, S.E. 1994, MN, 271, 781

Colina, L. & Bohlin, R.C. 1994, AJ, 108, 1931

Colina, L., Bohlin, R.C. & Castelli, F. 1996, AJ, 112, 307

Colley, W.N., Gnedin, O.Y., Ostriker, J.P., & Rhoads, J.E. 1997, astro–ph/9702030

Colley, W.N., Rhoads, J.E., Ostriker, J.P. & Spergel, D.N. 1996, ApJ, 473, L63

da Costa, L. et al. 1994, ApJ, 424, 1

Cousins, A.W.J. 1971, R. Obs. Ann. No. 7

Cousins, A.W.J. 1980, SAAO Circ., 1, No. 5, 234

Cousins, A.W.J. 1984, SAO Circ., 1, No. 8, 69

Cowie, L.L., Gardner, J.P., Lilly, S.J. & McLean, I. 1990, 360, L1

Cowie, L.L., Hu, E.M. & Songaila, A. 1995, Nature, 377, 603

Cowie, L.L., Songaila, A., Hu, E.M., & Cohen, J.G. 1996, AJ, 112, 839

Cowie, L.L. 1996, *Procedings of the 36th Herstmonceux Conference: HST and the High Redshift Universe*, ed. N.R. Tanvir, A. Aragón–Salamanca, J.V. Wall (London: World Scientific), 67

Dalcanton, J.J., Spergel, D.N., Gunn, J.E., Schmidt, M. & Schneider, D.P. 1997, AJ, 114, 635

Danziger, J.J., Dennefeld, M., Kunth, D. & Schuster, H.E. 1974 AA, 37, 149

Deharveng, J.M., Sasseen, T.P., Buat, V., Bowyer, S., Lampton, M. & Wu, X. 1994, AA, 289, 715

Dermott, S.F., Jayaraman, S., Xu, Y.L., Grogan, K. & Gustafson, B.A.S. 1996, in AIP Conference Proceedings 348, *Unveiling the Cosmic Infrared Background*, ed. E. Dwek (Woodburry, NY: AIP Press), 25

de Vaucouleurs, G. 1955 Observatory 75, 129

de Vaucouleurs, G. & Freeman, K.C. 1972, Vistas Astr., 14, 163

Draine, B.T. & Lee, H.M. 1984, ApJ, 285, 89

Dubè, R.R., Wickes, W.C. & Wilkinson, D.T. 1977, ApJ, 215, L51

Dube, R.R., Wickes, W.C. & Wilkinson, D.T. 1979, ApJ, 232, 333

Fall, S.M., Charlot, S. & Pei, Y.C. 1996, ApJ, 464, L43

Fechtig, H., Hartung, J.B., Nagel, K., Neukum, G. & Storzer, D. 1974, *Proc. Fifth Lunar Sci. Conf.*, Geochem. Cosmochem. Sup., 5, 3, 2463

Filippenko, A.V. 1982, PASP, 94, 244

Freeman, K.C. 1970, ApJ, 160, 811

Frey, A., Hofmann, W., Lemke, D. & Thum, C. 1974, AA, 36, 447

Gilliland, R.L. 1992, in ASP Conference Series V23, *Astronomical CCD Observing and Reduction Techniques*, ed. S.B. Howell (San Fransisco: BookCrafters, Inc.), 68

Giovanelli, R. & Haynes, M.P. 1989, ApJ, 346, L5

Girard, T.M., Grundy, W.M., Lopez, C.E. & Van Altena, W.F. 1989, AJ, 98, 227

Graham, J.A. 1982, PASP, 94, 715

Guhathakurta, P. & Tyson, J.A. 1989, ApJ, 346, 773

Guhathakurta, P., Tyson, J.A., & Majewski, S.R. 1990 ApJ, 357, L9

Guiderdoni, B. 1991, Annales De Physique, 16, 235

Hamuy, M., Walker, A.R., Suntzeff, N.B., Gigoux, P., Heathcote, S.R. & Phillips, M.M. 1992, PASP, 104, 553

Hartmann, D. & Burton, W.B. 1995, Atlas of Galactic HI Emission, Cambridge University Press (under contract)

Harrison, E.R. 1964, Nature, 204, 271

Harrison, E.R. 1990, in IAU Symposium 139, *Galactic and Extragalactic Background Radiation*, ed. S. Bowyer & Ch. Leinert (Dordrecht: Kluwer), 3

Hauser, M.G. 1996, in AIP Conference Proceedings 348, *Unveiling the Cosmic Infrared Background*, ed. E. Dwek (Woodburry, NY: AIP Press), 11

Hayes, D.S. & Laytham, D.W. 1975, ApJ, 197, 587

Hayes, D.S. 1985, in IAU Symposium No. 111, *Calibration of Fundamental Quantities*, eds. D.S. Hayes, L.E. Pasinetti, & A.G. Davis Phillip (Reidel, Dordrecht), 225

Heckman, T.M. 1997, astro–ph/9708263

Henry, R.C. 1991, ARAA, 29, 89

Holtzman, J., Burrows, C.J. & Casertano, S. et al. 1995, PASP, 107, 1065 (H95b)

Holtzman, J., Hester, J.J. & Casertano, S. et al. 1995, PASP, 107, 156 (H95a)

Hurwitz, M., Bowyer, S. & Martin, C. 1991, ApJ, 372, 167

Hurwitz, M., Jelinsky, P. & Dixon, W. 1997, ApJ, 481, 31

Impey, C.D., Sprayberry, D., Irwin, M.J. & Bothun, G.D. 1996 ApJSS, 105,209

Impey, C.D. & Bothun, G.D. 1997, ARAA, in press

Jacobsen, P., de Vries, J.S. & Paresce, F. 1987, AA, 183, 335

Jarvis, J.F. & Tyson, J.A. 1981, AJ, 86, 476

Johnson, H.L. & Harris III, D.L. 1954, ApJ, 120, 196

Johnson, H.L., Mitchell, R.I., Iriarte, B. & Wisniewski, W.Z. 1966, Commun. Lunar Planet. Lab., 4, 99

de Jong, R.S. 1996, AA, 313,45

Jura, M. 1979, ApJ, 227, 798

Kauffmann, G., White, S.D.M., Guiderdoni, B. 1993, MN, 264, 201

King, D.J., Taylor, K.N.R. & Tritton, K.P. 1979, MN, 199, 719

Knapp, G.R. & Kerr, F.J. 1974, AA, 35, 271

Koo, D.C. & Kron, R.G. 1992, ARAA, 30, 613

Kron, R.G. 1980, ApJS, 43, 305

Kurucz, R.L., Furenlid, I., Brault, J. & Testerman, L. 1984, Solar Flux Atlas from 296 to 1300 nm, National Solar Observatory Atlas No.1

Landolt, A.U. 1992a, AJ, 104, 72

Landolt, A.U. 1992b, AJ, 104, 340

Lanzetta, K.M., Wolfe, A.M. & Turnsheck, D.A. 1995, ApJ, 440, 435

Laureijs, R.J., Mattila, K. & Schnur, G. 1987, AA, 184, 269

Leinert, Ch. 1977, SSR, 18, 281

Leinert, Ch., Richter, I., Pitz, E. & Planck B. 1981, AA, 103, 177

Levasseur-Regourd, A.C. & Dumont, R. 1980, AA, 84, 277

Lillie, C.F., 1968, PhD thesis, University of Wisconsin (unpublished)

Lilly, S.J. & Cowie, L.L. 1987, in *Infrared Astronomy with Arrays*, ed. C.G. Wynn-Williams and E. Becklin, Institute for Astronomy, Honolulu, Hawaii, 473

Lilly, S.J., Cowie, L.L. & Gardner, J.P. 1991, ApJ, 369, 79

Lilly, S.J., Le Fèvre, O., Hammer, F., Crampton, D. 1996, ApJ, 460, L1

Lin, H., Kirshner, R.P., Shectman, S.A., Landy, S.D., Oemler, A., Tucker, D.L., Shechter, P.L. 1996, ApJ, 464, 60

Loveday, J., Peterson, B.A., Efstathiou, G. & Maddox, S.J. 1992, ApJ, 390, 338

Madau, P. 1995, ApJ, 441, 18

Madau, P. 1997, astro–ph/9707141

Madau, P., Ferguson, H.C., Dickinson, M.E., Gaivalisco, M., Steidel, C.C. & Fruchter, A. 1995, MN, 283, 1388

Madau, P. & Phinney, E.S. 1996, ApJ, 456, 124

Madau, P., Pozzetti, L. & Dickinson, M. 1997, astro–ph/9708220

Madau, P. & Shull, J.M. 1996, ApJ, 457, 551

Martin, C., Hurwitz, M. & Bowyer, S. 1991, ApJ, 379, 549

Marzke, R.O., Huchra, J.P. & Geller, M.J. 1994, ApJ, 428, 43

Massey, P., Strobel, K., Barnes, J.V., & Anderson, E. 1988, ApJ, 328, 315

Mathis, J.S., Mezger, P.G. & Panagia, N. 1983, AA, 128, 212

Mathis, J.S., Rumpl, W. & Nordsieck, K.H. 1977, ApJ, 217, 425

Matsumoto, T., Akiba, M., Murakami, H. 1988, ApJ, 332, 575

Matsuura, S., Matsumoto, T. & Matsuhara, H. 1995, Icarus 115, 199

Mattila, K. 1976, AA, 47,44

Mattila, K. 1990, in IAU Symposium 139, *Galactic and Extragalactic Background Radation*, ed. S. Bowyer & Ch. Leinert (Dordrecht: Kluwer), 159

McDade, I.C. & Llewllyn, E.J. 1986, PSS, 34, 801

McGaugh, S.S. Bothun, G.D. & Schombert, J.M. 1995, AJ, 110, 573

McGaugh, S.S. 1996, MN, 280, 337

Menzies, J.W., Cousins, A.W.J., Banfield, R.M. & Laing, J.D. 1989, SAAO Circ., No. 13, 1

Milliard, B., Donas, J., Laget, M., Armand, C. & Vuillemin, A. 1992, AA, 257, 24

Murthy, J. & Henry, R.C. 1995, ApJ, 448, 848

Murthy, J., Henry, R.C., Geldman, P.D. & Tennyson, P.D. 1990, AA, 231, 187

Mushotzky, R.F. & Loewenstein, M. 1997, ApJ, 481, L63

Neckel, H. & Labs, D. 1984, Sol. Phys., 90, 205

Oke, J.B. 1990, AJ, 88, 1621

Olbers, H.W.M. 1826, Astrinomische Jahrbuch, 110, 26

Onaka, T. & Kadaira, K. 1991, ApJ, 379, 532

Paley, E.S., Low, F.J., McGraw, J.T., Cutri, R.M. & Rix, H.-W. 1991, ApJ, 376, 335

Partridge, R.B. & Peebles, P.J.E. 1967, ApJ, 148, 377

Pei, Y.C. & Fall, S.M. 1995, ApJ, 454, 69

Pettini, M., King, D.L., Smith, L.J. & Hunstead, R.W. 1997, ApJ, 478, 536 (1997a)

Pettini, M., Smith, L.J., King, D.L. & Hunstead, R.W. 1997, ApJ, 486, 665 (1997b)

Pitz, E., Leinert, Ch. & Schulz, A. & Link, H. 1979, AA, 74, 15

Poggianti, B.M. 1997, AAS, 122, 399

Pozzetti, L., Madau, P., Ferguson, H.C., Zamorani, G., & Bruzual, G.A. 1997, MN, submitted

Press, W., Teukolsky, S., Vetterling, W. & Flannery, B. 1992, *Numerical Recipes, 2nd. Edition* (Cambridge: Cabridge University Press)

Qi, J., Barnes, A.V., Espy, S.L., Riehl–Chudoba, M., Sun, C.–N., Albridge, R.G., Tolk, N.H. 1991, Appl. Phys. Let., 59, 16

Racine, R. 1996, PASP, 108, 699

Reach, W.T., Abergel, A., Boulanger, F., Désert, Perault, M., Bernard, J.P., Bloommaert, J., Desarsky, C.,Cesarsky, D., Metcalfe, L., Puget, J.L., Sibille, F., Vigroux, L. 1996, AA, 315, L381

Reach, W.T. 1988, ApJ, 335, 468

Reynolds, R.J. 1985, ApJ, 298, L27

Reynolds, R.J. 1990, in IAU Symposium 139, *Galactic and Extragalactic Background Radation*, ed. S. Bowyer & Ch. Leinert (Dordrecht: Kluwer), 159

Reynolds, R.J. 1992, ApJ, 392, L35

Richter, I., Leinert, Ch. & Planck, B. 1982, AA, 110, 115

Roach, F.E. & Smith, L.L. 1968, GJ, 15, 227

Roach, F.E. & Meinel, A. 1955, ApJ, 84, 120

Röser, S. & Staude, J. 1978, AA, 67, 381

Rowan–Robinson, M. et al. 1997, MN, 289, 490

Sandage, A. 1976, AJ, 81, 954

Sandage, A. & Tamman, G.A. 1965, 135, 302

Sasseen, T.P. & Deharveng, J.-M. ApJ, 1996, 469, 691

Savage, B.D. & Mathis, J.S. 1979, ARAA, 17, 73

Savage, B.D., Bohlin, R.C., Drake, J.F. & Budich, W. 1977, ApJ, 216, 291

Schiffer, R. 1985, AA, 148, 347

Shields, G.A. et al. 1981, ApJ, 248, 569

Smail, I., Hogg, D.W., Yan, L. & Cohen, J.G. 1995, ApJ, 449, L105

Smail, I., Ivison, R.J. & Blain, A.W. 1997, ApJ, submitted (astro-ph/9708135)

Songaila, A. & Cowie, L.L. 1996, AJ, 112, 335

Songaila, A., Cowie, L.L. & Lilly, S.J. 1990, ApJ, 348, 371

Spinrad, H. & Stone, R.P.S. 1978, ApJ, 226, 609

Sprayberry, D., Impey, C.D., Irwin, M.J. & Bothun, G.D. 1997, ApJ, 482, 104

Stark, R. et al. 1992, ApJS, 79, 77

Stark, R. 1995, AA, 301, 873

Steidel, C.C. & Hamilton, D. 1993, AJ, 105, 2017

Steidel, C.C., Pettini, M. & Hamilton, D. 1995, AJ, 110, 2519

Steidel, C.C., Giavalisco, M., Dickinson, M. & Adelberger, K.L. 1996, AJ, 112, 352

Stone, R.P.S. & Baldwin, J.A. 1983, MN, 204, 347

Takano, M., Watanabe, T., & Nakamura, M. 1990, JGG, 42, 1193

Taylor, B.J. 1984, ApJS, 54, 259

Tinsley, B.M. 1973, AA, 24, 89

Tinsley, B.M. 1977, ApJ, 211, 621

Tinsley, B.M. 1978, ApJ, 220, 816

Toller, G.N. 1983, ApJ, 266, L79

Tyson, J.A. 1990, in IAU Symposium 139, *The Galactic and Extragalactic Background Radiation*, eds. S. Bowyer and Ch. Leinert, (Dordrecht:Kluwer), 245-254

Väisänen, P. 1996, AA, 315, 21

Valdes, F. 1982, Faint Object Classification and Analysis System (KPNO Internal Publication)

van Rhijn, P.J. 1924, Bull Astr. Inst. Netherlands, 2, 75

van Rhijn, P.J. 1925, Pub. Gron. Ast. Obs., No. 43

Weiss–Wrana, K. 1983, AA, 126, 240

Wesson, P.S., Valle, K. & Stabell, R. 1987, AJ, 317, 601

Whitrow, G.J. & Yallop, B.D. 1963, MNRAS, 127, 301

Williams, R.E. et al. 1996, AJ, 112, 1335

Witt, A.N., Friedmann, B.C. & Sasseen, T.P 1997, ApJ 481, 809

Woods, T.N. et al. 1997 J. Geophys. Res. (in press)

Wright, E.L. 1992, ApJ, 391, 34

Yoshii, Y. & Takahara, F. 1988, ApJ, 326, 1

IRAS Explanatory Supplement. 1986, ed. C.A. Beichmann, G. Neugebauer, H.J. Habing, P.E. Clegg, & T.J. Chester (Washington: GPO)